Numerical modelling of low pressure plasmas for industrial and biomedical applications

Michel Osca Engelbrecht

Doctor of Philosophy

University of York
Physics, Engineering and Technology

April 2024

Abstract

The development of plasma technologies requires a deep understanding of the plasma physics, for which numerical methods are essential. In this thesis, two plasma-based industrial challenges are addressed using specifically developed numerical methods.

The use of dual-frequency, low (LF$\lesssim$ 1 MHz) and higher frequency (HF$\gtrsim$ 60 MHz), waveforms in capacitively coupled plasmas (CCPs) have important industrial applications. At HFs, inductive heating (IH) effects play an important role and, in view of current industrial needs, it is essential to understand these effects at the kinetic level. Therefore, a one-dimensional (1D) particle-in-cell model coupled to an IH model has been developed. This is a novel approach that enables 1D kinetic simulations of HF CCPs. The model was first used to simulate single HF CCPs, showing that IH couples most of its power to the bulk plasma-sheath interface. A further simulation shows a synergy between the HF and LF waveforms that enhances the inductive power coupling.

In the context of plasma sterilisation and materials processing, the control of vacuum ultraviolet (VUV) radiation is important. However, the understanding of the formation pathways of VUV photons remains limited and is restricted to a narrow range of operating parameters. In order to better understand radiation in plasma applications, a zero-dimensional global model (GM) and a self-consistent chemical-radiative reaction scheme for argon and oxygen have been developed and used to study VUV emission from oxygen atoms. The GM results have helped to identify the dominant reaction pathways leading to VUV emission, showing that it is dominated by the 130 nm resonance line. Furthermore, a parametric study over pressure (0.3-100 Pa), Ar/O_2 mixture (0-20 %) and power deposition (100-2000 W) has been carried out, which concludes that oxygen VUV emission increases with power and oxygen fraction, with peak emission intensities found for pressures between 5-50 Pa.

Contents

Author's declaration

I declare that this thesis is a presentation of original work and I am the sole author. This work has not previously been presented for a degree or other qualification at this University or elsewhere. All sources are acknowledged as references.

This thesis has resulted in a number of publications in peer reviewed journals, as listed below. Some of the results presented in the chapter have been adapted from the material in these publications:

- M. Osca Engelbrecht, J. Dedrick, C. Ridgers, R. Boswell, T. Goffrey. *EPOCH-LTP: Development and validation of an electrostatic particle-in-cell code with Monte Carlo collisions for low-pressure plasmas*, submitted to Computer Physics Communications (June 2024). DOI (Temp): 10.2139/ssrn.4959815

  The material presented in chapter 3 is heavily based on this publication.

- M. Osca Engelbrecht, C. P. Ridgers, J. Dedrick, and R. Boswell. *Particle-in-cell simulations of high frequency capacitively coupled plasmas including spatially localised inductive-like heating*, 2023, Plasma Sources Science and Technology, Volume 32, Number 12, 125003. DOI: 10.1088/1361-6595/ad0fb1

  The material presented in chapter 4 is heavily based on this publication.

- M. Osca Engelbrecht, J. Jenderny, H. Hylla, D. Filla, P. Awakowicz, I. Korolov, C. P. Ridgers, A. R. Gibson. *Numerical investigation of vacuum ultra-violet emission in Ar/O_2 inductively coupled plasmas*, submitted to Plasma Sources Science and Technology (Feb. 2024). ArXiv:2402.08092 [physics.plasm-ph]

  The material presented in chapters 5 and 6 are heavily based on this publication.

List of Figures

List of Tables

Acknowledgements

I would like to acknowledge the following people without whom this thesis would not have been possible:

Firstly, I would like to thank Chris Ridgers for giving me the opportunity to embark on this particular adventure. Thank you for the support I have received, not only academically but also in personal decisions, where the latter were very important and had a great impact on the development of the thesis.

Secondly, I would like to acknowledge the support and commitment of James Dedrick, who was so involved as a second supervisor, although he was not obliged to do so.

Thanks to Rod Boswell for his time and expertise from the other side of the globe. His knowledge and experience of plasma physics is immense and he inspired us with the idea of simulating inductive heating as presented in this thesis.

Many thanks to Andrew Gibson for hosting me in Bochum, introducing me to the field of plasma chemistry and carefully supervising all our work together.

Finally, I would like to thank my life partner Ana, aka Pepiti, for giving me all your love, affection and emotional intelligence. Without you I would not have survived 6 years of PhD, a pandemic, several moves and the birth and growing up of Lucas. I would also like to remember Lucas for just being there and giving our lives some perspective and meaning. Thank you to my parents and siblings for being an emotional support and for giving me the material conditions that allowed me to do a PhD.

Chapter 1

Introduction

This chapter introduces the concept of plasma, the challenges in its technological applications that motivate this thesis, and the numerical methods used to address these challenges.

In section 1.1, low temperature plasmas (LTPs) are briefly described, introducing their technological applications and the different operating pressure regimes. This is followed by the two technological challenges addressed in this thesis.

Firstly, in section 1.2, the challenges associated with plasma etching are described. In the semiconductor industry, plasma etching is used to create nm/atomic scale features on integrated circuits. This requires a high degree of control of high frequency (HF) capacitively coupled plasma (CCP) equipment. HF CCPs present transverse inductive currents that make plasma etching difficult to control. Therefore, studying the kinetic effects of inductive currents in HF CCPs would help to improve the etching process.

Secondly, in section 1.3, low-pressure LTPs are discussed as a source of vacuum ultraviolet (VUV) radiation. Understanding VUV radiation is of interest for the development of new sterilisation methods and for gaining more control in material processing techniques. However, this requires a detailed investigation of the mechanisms leading to the generation of VUV radiation and its behaviour under different operating conditions.

These challenges are addressed by numerical simulations, and therefore section 1.4 briefly introduces the use of numerical models for LTP research. This section describes the main methods and current challenges in developing and running simulation software.

Finally, section 1.5 summarises the aims and objectives of this thesis and outlines its structure.

1.1 Low temperature plasmas

Plasma can be defined as the fourth state of matter such that, if energy is added into a gaseous system, the neutral atoms will eventually dissociate into electrons and ions. It is this gaseous state of electrically charged particles that, under conditions of quasi-neutrality and collective behaviour [2], is considered a plasma.

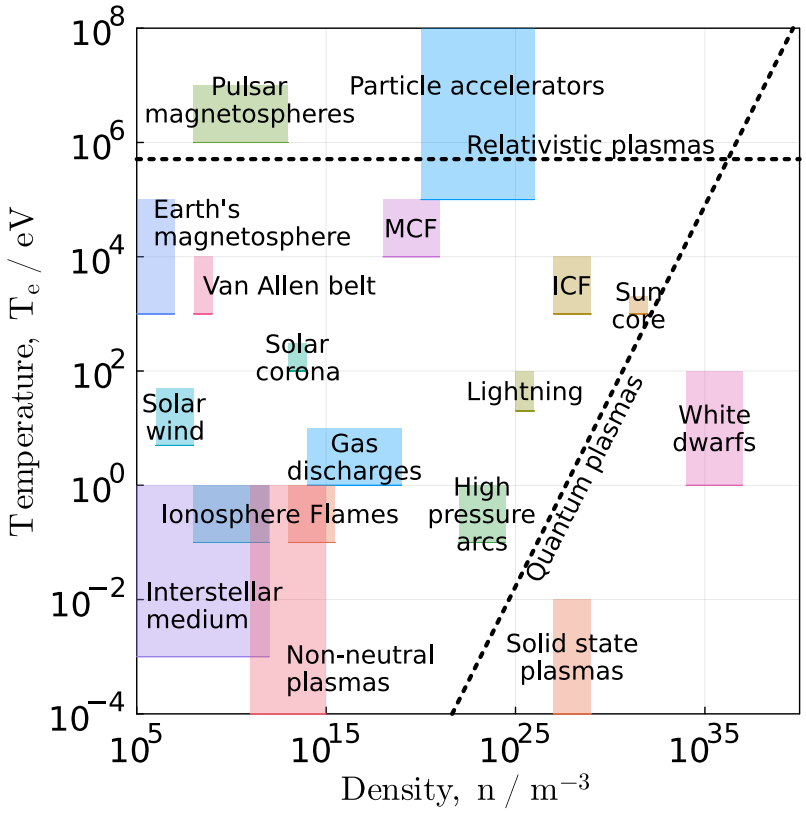

Figure 1.1: Plasmas that can occur naturally, or can be created in a laboratory or in technological applications are shown as a function of electron temperature and density. The boundaries are approximate and indicate ranges of plasma parameters. Note that flames are not always considered to be plasma due to their high collision frequency regime. Data collected from Refs. 1–5. MCF stands for magnetic confinement fusion and ICF stands for inertial confinement fusion.

Plasmas are the most abundant form of matter in the Universe [2, 23] and are found under a wide range of energy and density conditions, as shown in figure 1.1. Depending on the amount and type of energy transferred, the plasma will present different conditions. For instance, magnetic confinement fusion plasmas, heated with neutral beam injections and microwaves, reach higher temperatures but lower densities than the sun's core, where the plasma is gravitationally confined.

One important property to characterize the different plasmas is the ionisation degree

$$\chi_{iz} = \frac{n_i}{n_i + n_N}, \tag{1.1.1}$$

where n_i and n_N are the ion and neutral densities, respectively. This ratio indicates the amount of ions with respect to neutrals in a given plasma system. In local thermal equilibrium (LTE) plasmas, the ionisation degree depends on the temperature [24], so that at high temperatures, such as in fusion plasmas or the sun's core, the ionisation degree is large $\chi_{iz} \to 1$, while at lower temperatures we can expect neutral and charged species to coexist. In partially ionised plasmas ($\chi_{iz} < 1$) the interaction, i.e. the collisions, between electrically charged and neutral species becomes a key factor in characterising the plasma. In such a case, the mean free path λ_{mfp} and the collision frequency ν, i.e. the mean distance and time, respectively, that a particle moves freely before undergoing a collision, become two important plasma species parameters.

1.1.1 Technological applications of low temperature plasmas

Low temperature plasmas (LTPs), in particular gas discharges, are of special interest as they are widely used in industrial [7, 25–32], biomedical [19, 33–37], and space propulsion [38–42] applications. Gas discharge plasmas are sustained by electrical energy, which is mainly absorbed by electrons, due to their lower mass and therefore higher mobility, that generate new free electron-ion pairs by electron impact ionisation with neutrals. The resulting plasma consists of hot electrons and cold ions distributed in two main regions, a quasi-neutral bulk bounded by sheaths with strong density and electric field gradients. They present a low ionisation degree, $\chi_{iz} \ll 1$, such that collisions between charged and neutral particles are not only essential for the operation of the plasma but also act as a medium to stimulate chemical reactions.

The technological applications of LTPs exploit not only the tunability of this enhanced chemical medium, but also the plasma interaction with materials immersed in it. However LTPs are complex systems and thus controlling the plasma chemistry and ions is difficult, since different species of electrically charged and neutral particles interact with each other, through collisions and chemical reactions, with electric and magnetic fields, and with the system boundaries. Moreover, different physical and engineering aspects are involved, like electrodynamics, fluid mechanics, chemistry, atomic and molecular physics, radiation, and material science, that are closely intertwined with each other. Consequently, the use of plasmas in technological applications requires a detailed understanding not only of the physics of plasmas, but also of the specific application context, on spatial and temporal scales that can span several orders of magnitude. This presents a number of challenges for the LTP scientific community in order to further develop plasma technologies.

1.1.2 Operating pressure

In LTPs, the gas pressure, p_T, is an important operational factor as it has a major influence on the mean-free-path of particles and thus on the collision rates between neutral and charged particles and its impact on the plasma characteristics. Collisions largely determine plasma properties as they act as a heat transfer mechanism and induce plasma chemistry. Therefore p_T has led to the classification of LTPs into two main categories: low pressure plasmas and atmospheric pressure plasmas.

Atmospheric pressure plasmas

At atmospheric pressures, $p_T \sim 1\,\text{atm} \simeq 101325\,\text{Pa} \simeq 760\,\text{Torr}$, the gas density is higher, which increases the reactivity rate, so that not only higher plasma densities are achieved, but also higher neutral temperatures. This results in plasmas that although not necessarily in LTE, electron and heavy species temperatures are closer, or even in partial LTE [43]. Their main advantage is that they do not require vacuum systems, which are expensive, however they are more difficult to control, due to more complex chemistry and the presence of instabilities. Therefore atmospheric pressure applications are limited to smaller spatial regions. They have been used for decades in welding [44] and material processing [43], water treatment [45], and more recently for medical [46] and agricultural [47] applications.

Low pressure plasmas

At low pressure, $p_T < 10^3\,\text{Pa} \simeq 7500\,\text{mTorr}$, the collisional coupling between charged and neutral species is weak such that the heat transfer from electrons to neutrals is low. This results in a non-LTE plasma where electrons present high temperatures, $T_e \sim 10^4$-$10^5\,\text{K} \simeq$ 1-10 eV gained from the electric power, while the heavy species, i.e. ions and neutrals, remain at low temperature (usually room temperature $T_i \simeq T_N \sim$ 300-2000 K $\simeq$ 0.03-0.2 eV). They are used for atomic layer etching [48] and deposition [49] for the fabrication of microelectronics, photovoltaics and energy storage cells, in space thrusters [42] and for surface treatments in biomedicine such as sterilisation [50] or generation of biocompatible materials [51, 52]. In general terms, they allow a high degree of control on the production of heavy species over large areas, however they require vacuum equipment that have high costs associated.

The plasmas investigated in this thesis are in the low pressure regime, $p_T <$ 100 Pa. The study therefore focuses on plasmas generated in vacuum chambers used for material etching, mainly in the manufacture of integrated circuits, and as a source of VUV radiation.

1.2 Plasma etching

One of the most important applications of LTPs is the processing of materials for the semiconductor industry [53]. Plasma etching and deposition techniques are used to manufacture integrated circuits (ICs). This involves immersing a wafer on which the ICs are manufactured in the plasma, which generates the free radicals, etching atoms and deposition precursors required for processing the wafer [7, Ch. 1].

Plasma etching removes material from the wafer substrate to create trenches [54, 55]. The etching can be physical, when an incident atom transfers enough momentum and energy to a substrate particle to cause it to leave the surface; or chemical, when the incident atom reacts with the substrate to form a by-product that can eventually be pumped away [56]. In physical etching, ions are accelerated through the sheath gaining large amounts of energy before they impinge on the substrate. In chemical etching, reactive radicals generated in the bulk plasma diffuse and chemically interact with the substrate. The combination of physical and chemical etching is also possible, and has been shown to have synergies that significantly improve the etch rate [57].

The manufacture of ICs requires the carving of deep, straight trenches, which means that etching must be anisotropic, selective and uniform [7, Ch. 1]. In order to carve straight trenches, the etchants must impact the substrate surface in a preferred direction, hence the anisotropic conditions. The anisotropy is determined by the velocity vector of the etchant with respect to the substrate surface. While diffusion of neutral particles to the substrate results in isotropic etching, ions accelerated through the sheath impact perpendicular to the surface, resulting in anisotropic etching. Etching also requires the ability to select the materials to be etched while leaving other materials that compose the substrate intact. This involves careful control of the etchants production in the bulk plasma. The etching uniformity is also essential, since the carved trenches must be equal at any point of the wafer. To achieve this, the plasma must be homogeneous to ensure a spatially and energetically uniform etchant flux across the wafer.

In summary, plasma etching is a delicate process where the plasma must be able to generate a specific etchant species in the bulk that is accelerated through the sheath to impact the wafer surface at a specific energy and angle of incidence. This process must also be homogeneous across the wafer. One of the main plasma devices used for etching are capacitively coupled plasmas, which are described in the next section.

1.2.1 Etching with capacitively coupled plasmas

Capacitively coupled plasmas (CCPs) are one of the most widely used plasma devices for etching in the semiconductor industry. In CCPs an RF current is directly

applied to an electrode immersed in the plasma, as shown in figure 1.2. Conventional

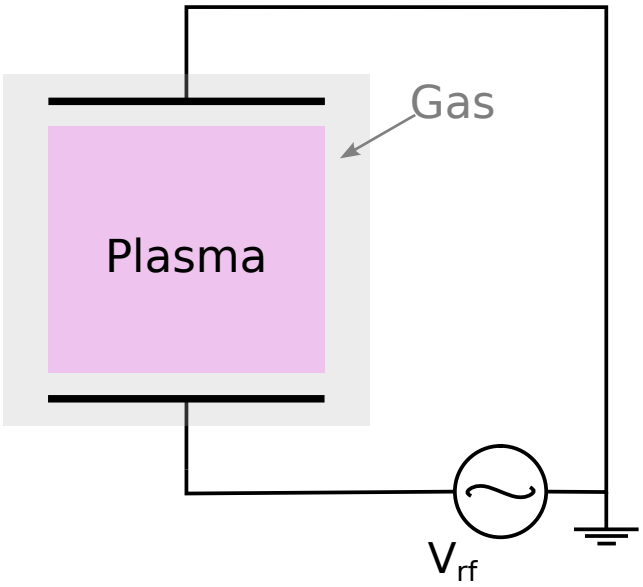

Figure 1.2: Schematic of a capacitively coupled plasma (CCP) reactor.

CCP reactors [58] consist of a cylindrical vacuum chamber with two planar parallel electrodes where a current is driven at 13.56 MHz[1]. The driving current forms a high voltage in the electrode that is shielded by the plasma, creating a high-voltage capacitive sheath between the electrode and the bulk plasma. This high-voltage sheath is used to accelerate ions towards the wafer for etching.

With capacitive power coupling, plasma generation and ion acceleration are interconnected and cannot be controlled independently [60]. The reason for this is that the driving frequency, ω, affects both the sheath formation and the power coupling to the plasma. On the one hand, the sheath impedance, and thus the sheath voltage, is inversely proportional to ω [7, Ch. 11]. On the other hand, power coupling to the plasma, and thus plasma density, are directly proportional to ω [7, Ch. 11]. Therefore, at low frequencies (LFs), i.e. $\omega \lesssim 1\,\text{MHz}$, CCPs present higher voltages across the sheath and relatively lower plasma densities, compared to high frequencies (HFs), i.e. $\omega \gtrsim 60\,\text{MHz}$, where sheath voltages are lower but plasma densities higher [61–63]. As a result, with increasing driving frequencies, the flux of ions to the electrodes increases due to higher densities at the bulk plasma, but the energy gained by the ions as they cross the sheath is lower. This is a disadvantage in material processing applications where absolute and precise control of both the ion energy and flux rate is required.

To gain control over both ion energy and flux, Goto *et al* [64, 65] proposed the use of two simultaneous voltage waveforms, a LF (ω_{LF}), and a HF (ω_{HF}). If

[1]The use of this arbitrary frequency has historical reasons. The 13.2 to 14 MHz band is internationally reserved for industrial, scientific and medical purposes to avoid interference with telecommunications [59].

$\omega_{HF} \gg \omega_{LF}$ the control of energy and fluxes would be decoupled such that the HF waveform regulates the plasma generation [66] and, the LF waveform controls the sheath formation, and thus the ion energy gain across the sheath [67, 68].

1.2.2 Current challenges in plasma etching

Current technologies require integrated circuits with electronic features of $\sim 7\,\text{nm}$, and atomic size is expected in the near future [53, 69–72]. Currently nm-sized trenches of large aspect ratios are required. This implies to carve features, with depth to width ratios of 10-100, straight profiles and smooth sidewalls [56, 71], on wafers with diameters of 300-450 mm [56, 71]. Achieving this requires a high degree of precision in etching anisotropy, selectivity and uniformity.

This high precision translates into a high degree of control over the plasma. Firstly, the bulk plasma must be spatially uniform, as the ion fluxes hitting the wafer depend on the local plasma density. Secondly, the sheath must be also spatially uniform and with the appropriate voltage drop so that the ions hit the wafer with the expected energy and angle of incidence. This is achieved through detailed understanding of the plasma physics, the chemical affinity between the plasma and the substrate and the effects of the etching process on the plasma.

The use of CCPs driven with two sinusoidal voltage waveforms (LF/HF) have been shown to be effective in the separate control of plasma density and ion energy. However with increasing driving frequencies electromagnetic effects, as depicted in figure 1.3, become significant if the excitation wavelength λ and the plasma skin depth δ[2] are of the order of magnitude of the plasma source [73, 74]. If the applied

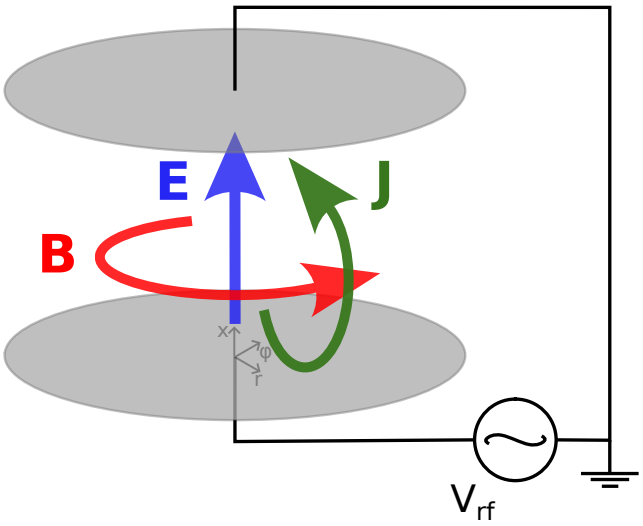

Figure 1.3: Schematic of a capacitively coupled plasma showing the induced electric field (E), magnetic field (B), and inductive current (J) present when driven at high frequency. Reproduced from 6.

[2]The plasma skin depth is described in section 2.1.5.

electric field (E) oscillates rapidly in the axial direction (x), it induces an oscillating magnetic field (B) in the azimuthal direction (φ), which, in turn, induces a current (J) opposing the axial E-field[3]. Therefore, the power coupling is not only capacitive, due to an oscillating E-field in the axial direction, but also inductive, due to induced currents in the radial (r) direction. This causes the power deposition to be non-homogeneous, with a complex transition from capacitive heating at the centre of the electrode, $r \to 0$, to inductive heating at outer radial positions of the electrode, which depends on the geometry and operating conditions of the CCP [73, 74]. This results in strong plasma inhomogeneities [75–78], which have a significant impact on the uniformity of the ion energy and fluxes [60, 79].

While there has been progress in studying the impact of electromagnetically induced currents on the ion kinetics [61, 80], further research is needed to understand these phenomena in detail and how it affects the etching processes.

1.3 Vacuum ultraviolet radiation in plasmas

The non-equilibrium nature of LTPs, with highly mobile electrons, makes plasmas an ideal medium for enhancing chemical-radiative processes. The most common

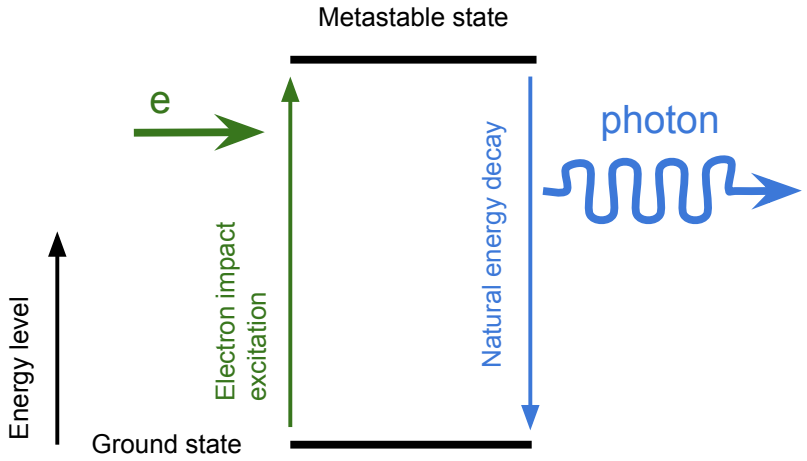

Figure 1.4: Schematic of the energy levels of a neutral species when i) electron impact increases the energy to a metastable state and ii) the gained energy is released in the form of radiation when decaying to a lower energy state, e.g. back to ground state.

radiative process, as sketched in figure 1.4, is the electron impact excitation of neutral species to a higher metastable energy state, which emits radiation when decaying to a lower energy level. Emission in the vacuum ultraviolet (VUV) spectrum, i.e. photon wavelengths $\sim 10 - 200\,\text{nm}$, can be used as a sterilisation method and must

[3] This is a direct application of Faraday's Law of Induction and Ampere's Circuital Law, equations 2.1.6 and 2.1.7 respectively in section 2.1.2

be controlled in material processing applications such as etching. It is therefore of interest to understand the main chemical pathways leading to VUV radiation in plasma sources and how these vary under different operating conditions, as this will allow greater control in their various applications.

1.3.1 Sterilisation

Sterilisation is an important part of the safety protocol in the medical, food, pharmaceutical and space industries to prevent infection and contamination due to the presence of microorganisms [33–37, 81–83]. There are several well-established sterilisation techniques such as autoclave, ionising and non-ionising radiation, dry and wet irradiation, electron beams and chemical solutions, but the development of new instruments and the use of new materials, such as advanced composites and biocompatible materials, creates a need for new techniques that can adapt to new surface requirements.

Conventional methods are widely used, but they have some drawbacks such as operating at high temperatures, surface damage, strict safety measures due to radiation or leaving dangerous by-products. Plasma sterilisation is seen as a promising technique for new materials and extremely resilient biological systems where conventional methods are not suited [50]. Low pressure plasmas have been shown to be effective in the microbial and molecular inactivation [84] and are suitable for sensitive equipment due to the low temperatures and highly tunable plasma chemistry. However, the high degree of complexity not only of the plasma but also of the surface being treated, especially biological tissues, requires a thorough knowledge of both to understand which inactivation method is most effective. This means that plasma cannot be a universal sterilisation method, but rather sterilisation systems optimised for specific applications.

Although it is difficult to generalise about the mechanisms of inactivation in plasmas, VUV radiation is one of the factors that plays an important role [50]. The presence of radicals can also be useful in sterilisation, as they can act as chemical etchants or sputtering agents. Moreover, synergistic effects can even be observed when VUV and radicals are combined.

In this context, VUV radiation for sterilisation purposes is of increasing interest as it is an effective mechanism on 3D, degradable and heat-sensitive objects and it enables sterilisation in non-wetting environments, with short exposure times and without toxic residues. Therefore, understanding VUV emission is of interest for plasma sterilisation applications [85].

1.3.2 Radiation in material processing

The control of VUV radiation is also important in material processing applications. Depending on the industrial process it is required to some degree [86–88] or unwanted [89, 90]. On the one hand, damage to the substrate by VUV radiation during plasma etching can be an important process in material processing applications and is therefore an active topic of research [91]. Otherwise, in some specific circumstances, VUV radiation can participate in synergistic processes [86, 87, 92], where they can be exploited for the benefit of materials processing.

1.3.3 State-of-the-art and current challenges

VUV emission has been investigated for different gas mixtures and under different operation conditions. Research has been carried out on VUV radiation in various gases, such as Ar [15, 93–97], N_2 [97, 98], O_2 [15, 97, 99], He [91], H_2 [97–100], Xe [91, 97], Cl_2 [101], Cl_2/BCl_3 [102] and fluorocarbon gases [93, 94], with either experimental or numerical methods in power ranges between 150 and 1100 W and total pressure ranges between 1 and 100 mTorr (0.13-13 Pa).

Of particular interest is the study of VUV radiation in oxygen plasmas, since oxygen is chemically highly reactive and has a variety of applications both in industry [99, 103–110] and biomedicine [19, 82, 85, 111]. Therefore, a comprehensive investigation of VUV emission that describes the pathways leading to emission over a wide range of operating parameters would be useful to better understand oxygen plasmas and their applications in the fields of industry and biomedicine. Despite the number of studies carried out, the understanding of the formation pathways of VUV photons remains relatively limited and the number of operating parameters studied is comparatively few.

The main reason for this is that the experimental diagnosis of both VUV emission and atomic oxygen densities is challenging [17–19, 50, 96, 97]. On the one hand, direct measurements of VUV are technically simple with optical emission spectroscopy (OES) [15], but there are only a few materials that transmit at VUV wavelengths, and detectors and windows are easily damaged by high reactive oxygen plasma exposure [96,97]. On the other hand, VUV emission can be determined indirectly from the concentrations of metastable states [97], but this also requires reliable information on oxygen atom densities, which increases the experimental complexity and difficulty. The measurement of oxygen plasma parameters is challenging because it requires a great deal of technical and theoretical effort, and existing techniques are limited to a certain operating regime. Moreover, indirect diagnostic techniques may also require additional numerical models to reproduce the atomic excitation and relaxation processes and these models in turn depend on other plasma parameters, such as electron density, gas temperature, electron energy distribution function

(EEDF), which also need to be diagnosed [15].

Numerical models are a suitable alternative for in-depth studies of oxygen VUV emission, as they can provide useful insights, such as chemical activity, that are otherwise not possible. The model of Gudmundsson *et al* [21, 112, 113] allows fast simulations of oxygen plasmas over wide range of parameters. The oxygen reaction scheme has been extended by Turner *et al* [114], but it does not include radiation processes. Nevertheless, Fiebrandt *et al* [15] has developed a collision-radiative model which includes the necessary oxygen metastable states and radiation processes to model VUV emission. Thus, the various pieces necessary to generate a self-consistent numerical model that both includes VUV radiation and allows fast simulation are already there in place, but are scattered and would need to be brought together into a single numerical model.

1.4 Numerical models for low temperature plasmas

The investigation of the kinetics of transverse inductive currents in HF CCPs, and the chemical kinetics leading to VUV radiation in LTPs, is difficult to be conducted by pure theoretical or experimental methods. The complexity of these plasma systems makes the analytical resolution of the mathematical models describing them extremely difficult, and the necessary experimental equipment, if available, would not only provide little information at the kinetic level, but would also require high operating costs and time. Instead, numerical models allow simulations that are cost-effective and provide insights of the physics that analytical theory and experimental work cannot. For this reason, the research carried out in this thesis is based on the simulation of numerical models.

1.4.1 Brief history review

The simulation of LTPs began in the late 1950s and early 1960s [115–118], and since then its importance has grown with the increase in computing power, making it key to the progress of LTP science and technology [72, 119, 120]. LTP modelling has enabled not only the description of new physics [121], but also the explanation of experimental data [12], the proposal of new experiments [4], the prediction of physical quantities that are difficult to measure [122], or the design of new plasma reactors [123].

Most of the computational work for LTPs has been conducted with numerical methods that have been established in the 1980s and 1990s [66, 124–135]. Two models have been established as the main plasma simulation methods, fluid and kinetic, which together cover an important part of the physics required for LTPs. The range of application of these models can be described using the Knudsen number, $\mathrm{Kn} = \lambda/L$, where λ is the mean-free-path of the plasma particles and L is the

representative physical length of the system of consideration.

1.4.2 Fluid methods

The fluid model assumes a low Knudsen number, Kn $\lesssim$ 0.1, i.e. the motion of particles is dominated by collisions and thus they can be considered in LTE. Under such consideration it is reasonable to assume a Maxwellian distribution function of particles, which enables solving for macroscopic quantities, like density, pressure and temperature. Some of the most important fluid-based techniques are, among others, hydrodynamics, magnetohydrodynamics and chemical-kinetics models. The main advantage of fluid models is that they provide fast simulations for larger space and time domains. However, they only work with averaged values and therefore effects resulting in non-Maxwellian distributions, i.e. kinetic effects, cannot be simulated. Therefore, fluid models have limited applications in low pressure plasmas, where strong non-equilibrium conditions are often present, especially at the sheath.

1.4.3 Kinetic methods

The simulation of non-equilibrium plasmas, usually with Kn $>$ 0.1, requires so called kinetic models, where the Boltzmann-Vlasov equation is solved for the particle distribution function, and this is an output of the simulation. Kinetic simulations are therefore more accurate than fluid simulations, and are of special importance in low pressure plasmas where the electron energy distribution is often non-Maxwellian [136, 137]. Nevertheless, they are computationally more expensive and are thus limited to smaller spatio-temporal scales. The most important kinetics models are, among others, Particle-In-Cell [129], Direct Simulation Monte Carlo [138], Direct Kinetic [139] and Boltzmann solver [140] codes.

1.4.4 Current challenges in LTP numerical modelling

One of the main challenges in simulating LTPs is the disparity in spatial and temporal scales. For example, etching plasmas require control of features on the nm scale, with the sheath on the mm scale and the wafer on the 10's cm scale. In addition, time scales range from ns response time of electrons, μs response time of ions, 10-100 ms residence time of heavy species chemistry and gases, to minutes duration of etching and deposition processes. Integrating these scale disparities into a single model is computationally intractable. Simulations therefore use models that describe simplified physics in order to be computationally feasible. This results in a tension between the accuracy of the simulation and its practicality, i.e. making the model as accurate as possible but simple enough to be handled by the available computing resources.

The rapid progress in computing technology over the last few decades has facilitated their development and utilisation not only in academia but also in the private sector and as commercial tools [72]. The different numerical models have been continuously developed with, for instance, the use of hybrid models, where some species (usually electrons) are treated with the fluid approach and other species (and neutrals) are treated with the kinetic approach, the implementation of adaptive mesh refinement methods, the integration of additional physics and the use of high performance computing and data-driven techniques.

Computation times have been reduced significantly with increasing use of CPU and GPU parallelisation methods for simulations in super-computer clusters [141–157]. This has expanded the scope of computer simulations for LTPs, enabling it to play an important role in the scientific progress of LTP physics and has enabled the development of models with increasing complexity. For instance, it is now more feasible to simulate systems over a wider parameter space, with complex geometries and boundaries, with larger chemical reaction schemes, and with an increasing number of spatial dimensions.

Modern computing offers many opportunities to develop increasingly complex numerical models that more accurately reproduce physical reality, but this brings with it three additional challenges [72]. Firstly, the need to develop more sophisticated codes that are computationally robust and efficient. Secondly, the validation and verification through rigorous comparison with theoretical, experimental and other numerical methods. This is key to ensuring the model's consistency and its correct implementation [72, 158]. Thirdly, additional input data that may be required, such as collision cross-sections, rate coefficients and/or surface coefficients, must be accurate, reliable and consistent, which is sometimes difficult to obtain.

These challenges are difficult to overcome and therefore the collaborative development of open source codes as an approach for the development of multiscale and multiphysics simulations is not only a viable but also a necessary approach for the development of numerical tools.

1.5 Objective and scope of this PhD thesis

This chapter has introduced LTPs and their uses in various technological applications. Within their industrial and biomedical applications, two research challenges have been identified that will be addressed in this thesis with numerical methods. On the one hand, the kinetics of inductive heating effects in HF CCPs needs to be studied in detail in order to gain further control over plasma-based material processing methods, such as etching. On the other hand, understanding VUV emission in LTPs is essential not only for the development of new sterilisation methods, but also for the control of VUV radiation in material processing applications.

These two specific problems found in plasma-based industrial and biomedical applications are addressed in this thesis using numerical simulations. For this purpose, two open-source numerical models for the simulation of LTPs are developed. The first is a one-dimensional (1D) particle-in-cell (PIC) model for the simulation of inductive heating effects in HC CCPs. The second is a zero-dimensional (0D) chemical kinetics global model (GM) for the simulation of VUV radiation in Ar/O_2 inductively coupled plasmas.

In this context, this thesis is structured in the following way:

- **Chapter 1** gives a brief introduction to LTPs and introduces the challenges that motivate this thesis.
- **Chapter 2** presents the theoretical framework that underpins the plasma physics employed in this thesis. This includes the physics of LTPs, the equations that describe its behaviour and the most fundamental concepts that sustain PIC and GMs.
- **Chapter 3** the development of the PIC model EPOCH-LTP is described in detail. This includes a description of the numerical model, its code implementation and a description of the validation tests performed.
- **Chapter 4** the simulation results of inductive heating-like effects in HF CCPs are presented and discussed.
- **Chapter 5** presents the development of the 0D GM and the reaction scheme for Ar/O_2.
- **Chapter 6** a characterisation of Ar/O_2 inductively coupled plasma followed by an extensive investigation of VUV in Ar/O_2 is conducted over a wide range of operating conditions.
- **Chapter 7** presents an overall summary.

Chapter 2

Background theory

This chapter provides the theoretical framework that underpins the plasma physics and numerical methods used in this thesis. This includes, in section 2.1, a formal definition of a plasma, the equations that describe the motion of the charged particles, Maxwell's equations for electromagnetics, and important plasma properties, such as the sheath and the skin depth. This is followed in section 2.2 by a presentation of the conservation equations that describe the behaviour of the plasma as a system. This includes the Boltzmann equation, which describes the systems down to the microscopic (kinetic) level, and fluid equations that describe averaged, i.e. macroscopic, quantities derived from Boltzmann-Vlasov equations. Both Boltzmann and the fluid equations are the basis of the numerical models developed later on, a particle-in-cell (PIC) and zero-dimensional (0D) chemical kinetics global models (GM) respectively. In section 2.3 the background and state-of-the-art of PIC models and 0D GM are described.

2.1 General description of a plasma

2.1.1 Plasma definition

A formal definition of plasma is that of an ionised gas, i.e. a collection of electrically charged and neutral particles, which exhibits collective behaviour and is quasi-neutral [2].

An important parameter in plasma physics is the Debye length, λ_D, which defines the distance over which electric potentials are shielded out. Under the assumption of static ions, given their larger mass relative to electrons, the field shielding is only due to the electrons and the Debye length can be defined as

$$\lambda_D = \sqrt{\frac{\varepsilon_0 k_B T_e}{n e^2}}, \tag{2.1.1}$$

where ε_0 is the vacuum permittivity, k_B the Boltzmann constant, e is the elementary charge, T_e the electron temperature, and n the plasma density. The Debye length helps to determine the conditions of quasi-neutrality and collective behaviour that define a plasma.

In plasmas, a distinction can be made between short and long-range interactions. On the one hand, short range interactions happen within λ_D and refer mainly to interparticle collisions. On the other hand, long-range range interactions occur at scales larger than λ_D where the plasma collectively interacts with electric and magnetic forces [2]. This allows the particles in a plasma to be interconnected so that local conditions are influenced by remote conditions, hence the collective behaviour of the plasma. This collective behaviour is the main difference between a gas and a plasma.

The condition for collective behaviour requires enough particles to respond to an external field without the states of the individual particles being important. This condition is satisfied if the number of charged particles within a Debye sphere is sufficiently large [2]

$$N_D = \frac{4}{3}\pi\lambda_D^2 n \gg 1. \tag{2.1.2}$$

The quasi-neutrality condition of a plasma is understood by its shielding property, which allows it to shield an externally applied electric potential within the Debye length λ_D. This enables the rest of the system to self-organise in a state of minimum potential, which results in a quasi-neutral charge distribution. In order for this to be possible, the characteristic system size L must be larger than λ_D,

$$L \gg \lambda_D. \tag{2.1.3}$$

A third condition must be met in the case of partially ionised plasmas ($\chi_{iz} < 1$) in order for them not to be considered a gas. The motion of charge particles must be

dominated by the collective behaviour and not by collisions with neutral particles. The most fundamental collective behaviour of the plasma, assuming static ions, is the oscillation of the electrons around their equilibrium position as they are displaced from a uniform background of ions. This oscillation is described by the electron plasma frequency,

$$\omega_{pe} = \sqrt{\frac{ne^2}{\varepsilon_0 m_e}} \tag{2.1.4}$$

and for a plasma to be dominated by its collective behaviour, collisions must be less frequent than the plasma frequency, i.e.

$$\frac{\omega_{pe}}{\nu} > 1, \tag{2.1.5}$$

where ν is the collision frequency between charged and neutral particles.

2.1.2 Field equations

The electric ($\boldsymbol{E}$) and magnetic ($\boldsymbol{B}$) fields present in plasmas are governed by Maxwell's equations

$$\nabla \times \boldsymbol{E} = -\frac{\partial \boldsymbol{B}}{\partial t}, \tag{2.1.6}$$

$$\nabla \times \boldsymbol{B} = \mu_0 \left(\varepsilon_0 \frac{\partial \boldsymbol{E}}{\partial t} + \boldsymbol{J} \right), \tag{2.1.7}$$

$$\nabla \cdot \boldsymbol{E} = \frac{\rho}{\varepsilon_0}, \tag{2.1.8}$$

$$\nabla \cdot \boldsymbol{B} = 0, \tag{2.1.9}$$

where $\mu_0 = 4\pi 10^{-7}\,\mathrm{N/A^2}$ is the vacuum permeability and $\varepsilon_0 \simeq 8.854 \cdot 10^{-12}\,\mathrm{F/m}$ is the vacuum permittivity, the charge density is

$$\rho = \sum_s q_s n_s, \tag{2.1.10}$$

the conduction current density is

$$\boldsymbol{J} = \sum_s q_s n_s \boldsymbol{u_s}, \tag{2.1.11}$$

where q, n, and $\boldsymbol{u}$ refer to the charge, density and macroscopic velocity of a given species s.

2.1.3 Equation of motion

Plasma particles can be tracked in space and time by their equations of motion

$$\frac{\partial \boldsymbol{x}}{\partial t} = \boldsymbol{v}, \tag{2.1.12}$$

$$m\frac{\partial \boldsymbol{v}}{\partial t} = \boldsymbol{F_L}, \tag{2.1.13}$$

where $\boldsymbol{x}$ and $\boldsymbol{v}$ are the position and velocity vectors of a given particle of mass m, and $\boldsymbol{F_L}$ are the electric and magnetic forces acting on the particle.

The force exerted by the electric and magnetic fields on charged particles are given by Lorentz force law

$$\boldsymbol{F_L} = q\left(\boldsymbol{E} + \boldsymbol{v} \times \boldsymbol{B}\right). \tag{2.1.14}$$

The moving charges contribute to ρ and $\boldsymbol{J}$, in equations 2.1.10 and 2.1.11 respectively, and these are linked to $\boldsymbol{E}$ and $\boldsymbol{B}$ by Maxwell's equations 2.1.6-2.1.9. Therefore they form a self-consistent system of equations.

Besides Lorentz forces, the momentum and energy of particles is affected also by collisions with other particles. However, incorporating a general expression for the collision force into equation 2.1.13 is not straightforward, and so collisions are treated as statistical phenomena later on, in section 2.2.1, when Boltzmann's equation is described.

2.1.4 Sheath and pre-sheath

Plasmas are connected to solid boundaries by thin layers called sheaths, which result from the quasi-neutrality property. In the bulk plasma, because of quasi-neutrality, the spatial distribution of charged particles is such that the average electric charge density, the electric potential and the electric field are close to zero. This means that charged particles are not confined and can escape, but the resulting flux leaving the bulk plasma should be zero. However, electrons escape faster due to their higher mobility, and to avoid this the plasma charges itself with a positive potential with respect to its boundaries, called plasma potential ϕ_P. This creates the sheaths, a space-charged region at the boundaries where ions are accelerated outwards while electrons are repelled into the plasma, ensuring that the charge flux is neutral.

The transition from the bulk plasma to the sheath is mediated by the pre-sheath, as shown in figure 2.1. The ions entering the sheath must satisfy the the Bohm sheath criterion, i.e. they must enter the sheath at a velocity greater than the Bohm (acoustic) velocity [2],

$$u_{is} > u_B \tag{2.1.15}$$

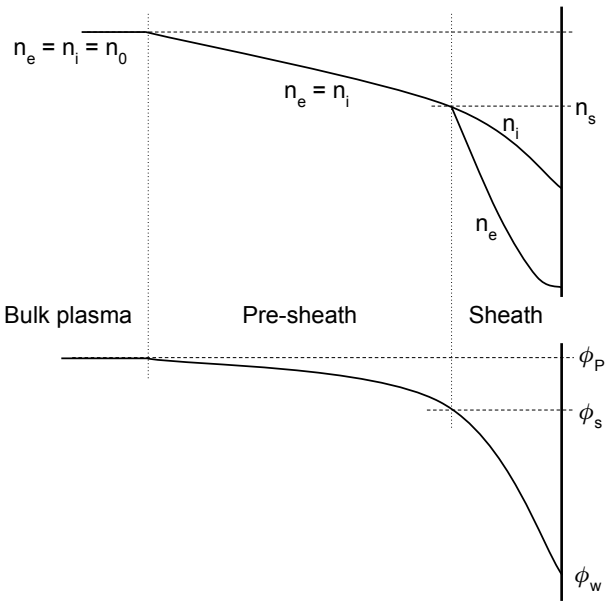

Figure 2.1: Qualitative behaviour of sheath and pre-sheath in contact with a wall. n_e and n_i stand for electron and ion density, respectively, n_0 is the density of the bulk plasma, n_s is the density at the sheath edge, ϕ_P is the plasma potential, ϕ_s is the potential at the sheath edge, and ϕ_w is the potential at the wall/boundary. Reproduced from [7, Ch. 6]

where u_{is} is the ion velocity at the sheath entrance, and

$$u_B = \sqrt{\frac{eT_e}{m_i}}, \tag{2.1.16}$$

is the Bohm velocity, where m_i is the ion mass. Therefore the presence of a pre-sheath region, where a finite electric field accelerates the ions from the bulk plasma, which is quasi-neutral and thus presents no electric fields, to the sheath into which they have to enter with the Bohm velocity.

The plasma at the pre-sheath can be considered quasi-neutral however it presents a plasma density and potential decrease. Under collisionless conditions, i.e. neutral collisions are neglected, the density decrease at the pre-sheath, i.e. between the bulk plasma (n_0) and the sheath edge (n_s) is given by the Boltzmann relation [7, Ch. 6]

$$\frac{n_s}{n_0} = \exp\left(\frac{-e\phi_P}{k_B T_e}\right), \tag{2.1.17}$$

and the electric potential drop at the pre-sheath is

$$\phi_P - \phi_s = \frac{k_B T_e}{2e}, \tag{2.1.18}$$

where ϕ_s is the potential at the sheath edge. Within this potential drop the ions gain enough energy to enter the sheath satisfying Bohm sheath criterion [7, Ch. 2].

The potential drop across the sheath, $\phi_s - \phi_w$, in case of a floating wall, i.e. the wall is grounded $\phi_w = 0\,\mathrm{V}$, can be determined by the condition of zero net charge flux at the sheath edge [7, Ch. 6]

$$\Gamma_e = \sum_i \Gamma_i \tag{2.1.19}$$

where

$$\Gamma_e = \frac{1}{4} n_s v_e \exp\left(-\frac{e\phi_s}{k_B T_e}\right) \tag{2.1.20}$$

is the electron particle flux and

$$\Gamma_i = n_{s,i} u_{B,i} \tag{2.1.21}$$

is the ion particle flux. From equation 2.1.19, assuming a single ion species, the potential at the sheath edge can be determined

$$\phi_s = \frac{k_B T_e}{e} \ln\left(\frac{m_i}{2\pi m_e}\right). \tag{2.1.22}$$

2.1.5 Wave propagation and skin effect

An important energy deposition mechanism in plasmas is via electromagnetic waves. Electromagnetic waves can be described using the dispersion relation, which relates the wavevector $\boldsymbol{k}$ to the frequency ω of the wave.

In uniform and isotropic plasmas the dispersion relation of an electromagnetic transverse wave is obtained by linearising Maxwell's equations (2.1.6-2.1.9) [7, Ch. 2],

$$k = \pm\frac{\omega}{c}\sqrt{1 - \frac{\omega_{pe}^2}{\omega(\omega - i\nu)}}. \tag{2.1.23}$$

where ν is the electron-neutral collision frequency. In the case of a collisionless plasma ($\nu \to 0$), it is shown that waves can propagate in the plasma only if $\omega > \omega_{pe}$ (k is real) and wave frequencies beyond that are cut off (k is pure imaginary). In LTPs, where collisions are not negligible and usually $\omega < \omega_{pe}$, waves do not present a cut off but instead decay exponentially when penetrating into the plasma. The imaginary part of k gives the wave decay rate

$$\alpha_{dec} = -\frac{\omega}{c}\mathrm{Im}\left(\sqrt{1 - \frac{\omega_{pe}^2}{\omega(\omega - i\nu)}}\right) \tag{2.1.24}$$

and provides information about the spatial scale at which the waves decays when

penetrating into the plasma. The inverse of α_{dec} is the skin depth

$$\delta = \alpha_{dec}^{-1}, \tag{2.1.25}$$

which is the characteristic length a wave can penetrate in a plasma. When $\nu \ll \omega$, the skin-depth can be approximated as

$$\delta_p = \frac{\omega_{pe}}{c}, \tag{2.1.26}$$

and is known as collisionless plasma skin-depth. In the opposite case, when $\nu \gg \omega_{pe}$,

$$\delta_c = \delta_p \sqrt{\frac{2\nu}{\omega}} \tag{2.1.27}$$

is the collisional skin-depth [7, Ch. 12].

2.1.6 Plasma reactors

Low pressure gas discharges are generated in a vacuum chamber by applying a radio frequency (RF) electrical power source. The free electrons absorb most of this power due to their higher mobility, and a plasma is created by a chain reaction of electron impact ionisation that creates new electron-ion pairs.

Collisions between charged and neutral particles therefore play an important role, not only electro-neutral but also ion-neutral interactions. The collisions can be elastic, which change the kinetic energy of the neutrals, or inelastic, which change both the kinetic energy and the internal energy state of the neutral particle. While elastic collisions act as a heat transfer mechanism between electrons and neutrals, inelastic collisions also induce plasma chemistry, i.e. excitation, ionisation, dissociation and other processes of neutral atoms and molecules. Therefore, although ionisation reactions are essential to maintain the plasma, other inelastic reactions are responsible for creating the chemically active medium that is of interest for the various technological applications.

The control of this chemically active medium is complex and depends on a large number of operating parameters. As already described in section 1.1.2, the gas pressure p_T is an important operating parameter. Another important operating parameter is the coupling of electrical energy to the gas. In this thesis, two of the most important plasma reactors, capacitively coupled and inductively coupled plasma devices, are studied.

Capacitively coupled plasmas

Capacitively coupled plasmas (CCPs) were already introduced in section 1.2.1 and in this thesis they are studied in the context of high frequency driving voltages.

One of the most important properties is the transient nature of the sheath, whose width and voltage change with the oscillating power supply [7, Ch. 11]. This leads to stochastic (collisionless) heating [7, Ch. 11], where electrons entering the oscillating sheath gain energy from a decelerating electric field in a similar way as a ball bouncing against a moving wall. The energy gained by the electrons in the oscillating electric field is transferred to the neutral gas by Ohmic heating, i.e. collisional energy transfer.

The plasma densities achieved in CCPs are between 10^{15}-$10^{17}\,\mathrm{m}^{-3}$ with operating pressures between 10 and 1000 mTorr ($\simeq$1-100 Pa) [56]. These densities are relatively low compared with, for example, inductively coupled plasmas or microwave discharges, because a larger fraction of the electrical energy supplied is used to raise the electrical potential of the plasma than to provide the kinetic energy for the particles to create new ion-electron pairs by impact collisions [7, Ch. 11].

Inductively coupled plasmas

In inductively coupled plasmas (ICPs), electrical energy is coupled by an antenna, or coil [76, 159, 160], across a dielectric window, as sketched in figure 2.2(a). The antenna drives an RF current, which induces a time-varying magnetic field. According to Ampere's law, the varying magnetic field produces an induced current in the plasma. The induced current accelerates the electrons which, through ohmic heating, transfer energy to the neutral gas and sustain the plasma. In essence, ICPs are like an electrical power transformer, with the antenna acting as the primary and the plasma as the secondary with a single loop.

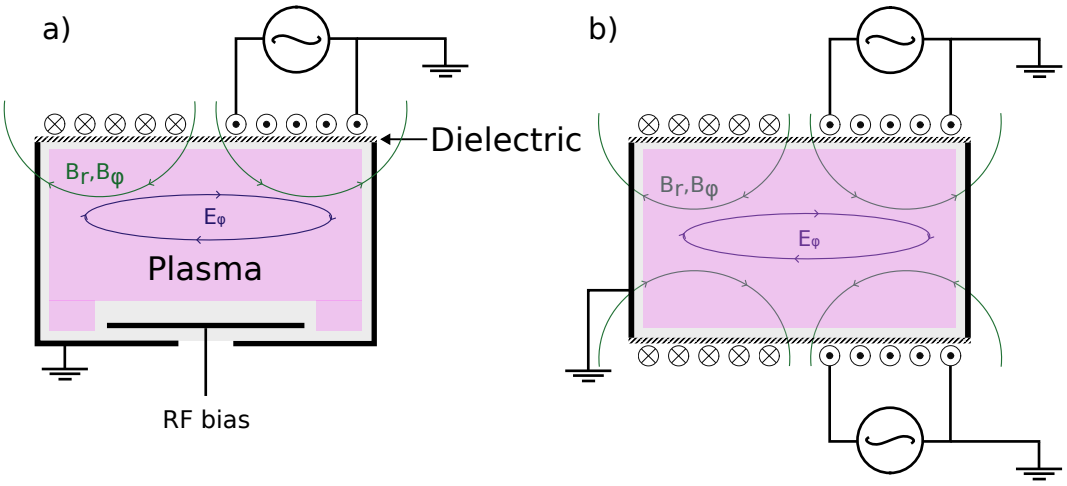

Figure 2.2: Schematic of a) planar inductively coupled plasma (ICP) and b) double inductively coupled plasma (DICP).

In ICPs the densities yielded are between 10^{16} - $10^{18}\,\mathrm{m}^{-3}$ and the plasma is operated with a low voltage across the sheaths. The voltage at the sheaths depends only on the plasma properties and not the generated power [7, Ch. 12].

Depending on the transferred power and plasma density ICPs present two operation modes, the capacitive E-mode and the inductive H-mode [7, 161]. At low densities, $\lesssim 10^{15}\,\mathrm{m}^{-3}$, the plasma does not contain enough particles to sustain an induced current and instead capacitive heating due to the electrostatic field formed across the antenna and the grounded walls is important. At higher densities the plasma operates at H-mode, where it suppresses the electrostatic field and can sustain an inductive current [76]. In H-mode the electromagnetic power penetrates a distance of the order of the skin-depth before decaying exponentially. With higher densities, the skin-depth might be smaller than the characteristic length of the plasma and thus the inductive power only penetrates to a fraction of the bulk plasma. In such cases larger density gradients are present as only the electrons within the skin-depth length gain energy from the inductive heating while further away from the antenna the plasma only gains energy via Ohmic heating.

A typical ICP device is the planar configuration, shown in figure 2.2(a), which consists of a cylindrical reactor chamber with a plane coil attached to one end of the chamber. There are several configurations possible, for instance with a cylindrical coil or ferrite immersed [76], that optimise the plasma generation in different aspects, such as power coupling efficiency in case of the ferrite immersed [162]. An alternative configuration proposed is the double inductively coupled plasma (DICP) source, shown in figure 2.2(b), where two planar coils are place at the top and bottom of a cylindrical reactor. The main advantage of DICPs is that they ensure a homogeneous plasma at higher densities [163, 164].

2.2 Conservation equations

2.2.1 Kinetic description: Boltzmann-Vlasov equation

A given species in a plasma system can be described by the distribution function $f = f(\boldsymbol{v}, \boldsymbol{x}, t)$, which provides information about particles per elementary unit volume $d^3x d^3v$ in six-dimensional space $\{\boldsymbol{x} = (x, y, z), \boldsymbol{v} = (v_x, v_y, v_z)\}$. The continuity equation of f, when it includes the Lorentz force (equation 2.1.14) and collisions, is known as Botlzmann equation

$$\frac{\mathrm{d}f}{\mathrm{d}t} = \frac{\partial f}{\partial t} + (\boldsymbol{v}\cdot\nabla)f - \frac{q}{m}(\boldsymbol{E} + \boldsymbol{v}\times\boldsymbol{B})\cdot\nabla_{\boldsymbol{v}} f = \left.\frac{\delta f}{\delta t}\right|_{coll}, \tag{2.2.1}$$

where $\nabla_{\boldsymbol{v}} = (\partial/\partial v_x, \partial/\partial v_y, \partial/\partial v_z)$, and $\delta f/\delta t|_{coll}$ is the term accounting for changes in f due to collisions with other species.

The collision term can be expressed with the Boltzmann collision operator [165]

$$\left.\frac{\delta f}{\delta t}\right|_{coll} = \int\int g\sigma(g,\chi,\psi)\left(f'f'_s - ff_s\right)d\Omega d^3\boldsymbol{v_s} \tag{2.2.2}$$

where the subscript s refers the colliding species, $'$ notes the post-collision state, $g = |\boldsymbol{v} - \boldsymbol{v_s}|$ is the impact velocity, χ and ψ are the polar and azimuthal scattering angles, respectively, of $\boldsymbol{v'}$ with respect to $\boldsymbol{v}$, $\sigma(g,\chi,\psi)$ is the collision cross-section, and $d\Omega = \sin\chi d\chi d\psi$ is the solid angle.

The Boltzmann equation accurately describes a plasma system, but a self-consistent analytical solution is difficult to obtain. Numerical methods are therefore well suited to solving this equation.

2.2.2 Macroscopic quantities: conservation equations

The complexity of the Boltzmann equation can be reduced by averaging over the velocity coordinates, also called velocity moments of f [7, Ch. 2]. The 0^{th} order moment provides number density values

$$n(\boldsymbol{x},t) = \int f d^3\boldsymbol{v}, \tag{2.2.3}$$

the 1^{st} order moment provides a particle flux values

$$\Gamma(\boldsymbol{x},t) = n\boldsymbol{u}(\boldsymbol{x},t) = \int \boldsymbol{v} f d^3\boldsymbol{v}, \tag{2.2.4}$$

and the 2^{nd} order moment provides energy density values

$$w(\boldsymbol{x},t) = \frac{3}{2}p(\boldsymbol{x},t) + \frac{1}{2}mu^2 n = \frac{1}{2}m\int v^2 f d^3\boldsymbol{v}, \tag{2.2.5}$$

where $\boldsymbol{u}(\boldsymbol{x},t)$ is the mean velocity and $p(\boldsymbol{x},t)$ is isotropic pressure.

Taking 0^{th} order moments on Boltzmann equation (2.2.1) we obtain the density (or mass) conservation equation

$$\frac{\partial n}{\partial t} + \nabla\cdot(n\boldsymbol{u}) = \left.\frac{\delta n}{\delta t}\right|_{coll} \tag{2.2.6}$$

where $\delta n/\delta t|_{coll}$ accounts for density gains and losses due to collisions.

Taking 1^{st} order moments, the momentum conservation equation is obtained

$$mn\left[\frac{\partial \boldsymbol{u}}{\partial t} + (\boldsymbol{u}\cdot\nabla)\boldsymbol{u}\right] = qn\left(\boldsymbol{E} + \boldsymbol{u}\times\boldsymbol{B}\right)) - \nabla\cdot\boldsymbol{\Pi} + \boldsymbol{f}\Big|_{coll}, \tag{2.2.7}$$

where Π is a pressure tensor and $\boldsymbol{f}$ is the momentum transfer rate per unit volume

due to collisions.

Taking 2^{nd} order moments the energy conservation equation is obtained

$$\frac{\partial}{\partial t}\left(\frac{3}{2}p\right) + \nabla \cdot \frac{3}{2}\left(p\boldsymbol{u}\right) + p\nabla \cdot \boldsymbol{u} + \nabla \cdot \boldsymbol{q} = \frac{\delta}{\delta t}\left(\frac{3}{2}p\right)\Bigg|_{coll} \tag{2.2.8}$$

where $\boldsymbol{q} = -\kappa\nabla T$ is the heat flow vector, κ the thermal conductivity, p is the scalar pressure, and $\delta/\delta t(3p/2)|_{coll}$ energy changes due to collisional processes.

The conservation equations, also called fluid equations, provide a macroscopic view of the system. This simplifies the problem with respect to Boltzmann's equation, however it only describes averaged values and therefore kinetic effects are lost. Moreover, the equations 2.2.6-2.2.8 are not self-consistent and require a closure equation. Typically, the isothermal relation for an equilibrium Maxwellian distribution

$$p = nk_BT, \tag{2.2.9}$$

where $k_B \simeq 1.381{\cdot}10^{-23}$ J/K is Boltzmann's constant, is an accurate closure equation as long as time variations are slower than thermal equilibrium times.

2.3 Numerical models for low temperature plasmas

Two different methods have been employed in this thesis. On the one hand, the particle-in-cell (PIC) method for kinetic simulations in which particles are tracked in phase-space. On the other hand, a fluid-based 0-dimensional global model (0D GM) that simulates the chemical kinetics of LTPs.

2.3.1 Particle-in-cell models

The particle-in-cell (PIC) model self-consistently solves the Boltzmann equation for a given system and provides information about the plasma in phase space. This is done by simulating the motion of individual particles under two system simplifications. Firstly, only a subset of the particles that constitute the plasma system is simulated. Each simulated particle is called a super-particle and represents a fraction of the real particles, determined by the super-particle weight W. The number of super-particles in the simulation, N_P, must be large enough to statistically represent the entire plasma system, i.e. the distribution function f is accurately resolved. Secondly, space is discretized into N_G grid points, where values of the electric and magnetic fields, as well as macroscopic parameters such as density and currents, are interpolated. The grid avoids solving an N-body problem for N_P super-particles, which has a high computational cost $C \sim O(N_P^2)$, and reduces it to $C \sim O(N_P \log N_P)$. The result of these simplifications is the simulation of a set of super-particles on a mesh that discretizes the space, as shown in figure 2.3.

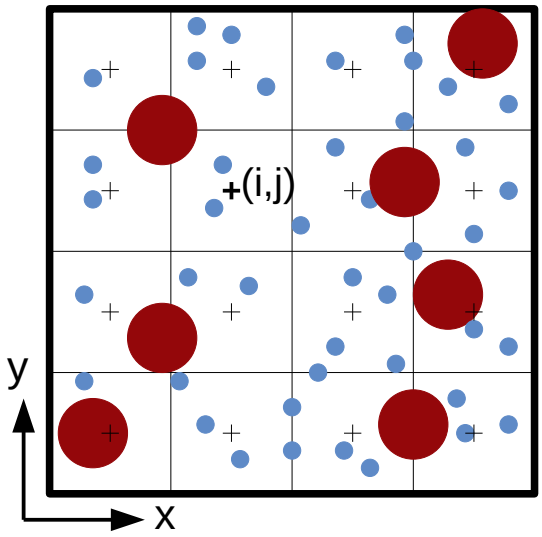

Figure 2.3: System environment of a two-dimensional (2D) particle-in-cell (PIC) model: super-particles are simulated in phase-space within a mesh that allows particle-grid interpolation.

PIC simulations are used to study most of the plasmas shown in figure 1.1, from inertial confinement fusion [166] and magnetic confinement fusion [167] to high intensity laser-plasma interactions [4], solar corona [168] and winds [169], the Earth's magnetosphere [170] and of course low pressure gas discharges. They have allowed the study of plasmas with strong non-Maxwellian distribution functions such as found in turbulent regimes [121], complex chemistries [171], strong non-linear particle-wave interactions [4], shock discontinuities [172] and non-local transport [173]. In low-pressure plasmas, PIC codes are of particular importance and have become a common method of numerical investigation, since they require few approximations and retain most of the non-linear behaviour that allows a precise study of the kinetic effects that characterise these plasmas.

Low pressure plasmas can be simulated with PIC codes from the initial gas breakdown [174] and can provide not only steady-state data, but also time-resolved information on plasma density, potential, charged-particle power absorption, current density, electron energy probability function (EEPF), energy and angle of incidence distribution of ion fluxes at the system boundaries, and collision reaction rates. They have been key to understanding the fundamental physics of low pressure plasmas, such as heating mechanisms [126, 127], interactions between charged and neutral particles [175] and particle-wall interactions [176], but they have also helped to investigate improvements in applications, such as tailored voltage waveforms [177], excitation of natural plasma modes [178] and high-frequency voltage sources [179].

The main drawback of PIC models is that they are computationally intensive for the following reasons: They require high resolution tracking of individual particles

in order to ensure an accurate statistical representation of the simulated system, this is particularly challenging at higher operating pressures where the plasma densities are higher; fine grid resolution for accurate field solutions, particularly at the sheath where field gradients are large, requiring grid cells that satisfy the condition $\Delta x \lesssim \lambda_D$; and constrained time steps dictated by the fastest timescale in the system, usually the electron plasma frequency, such that $\Delta t \leq 2\pi/\omega_{pe}$. Another limitation comes from using a limited number of super-particles, which may provide noisy results and can poorly reproduce the tails of the distribution function, where particle populations are generally low. Besides, the use of grid-cells, which smooths the fields, neglects Coulomb collisions [180,181]. This can be readily solved by explicitly adding Coulomb collision to the model [182]. This latter limitation is usually not an issue for low pressure plasmas as long as the ionisation degree is low [183].

The rapid progress in computing technology over the last couple decades has facilitated the development and utilisation of PIC codes, not only in academia [10, 130, 184–187] but also in the private sector [188] and as commercial tools [189–193]. Especially with increasing use of CPU [141–150] and GPU [151–157] parallelisation methods for simulations in super-computer clusters that significantly reduce computational times. This expands the simulation possibilities, for instance allowing simulations with an increasing number of spatial dimensions, complex geometries, chemistries and boundaries and higher pressure. Therefore, PIC models have great potential for the study not only of low-pressure plasmas, but of LTPs in general.

The vast majority of LTP PIC codes are developed by the scientific community and are not publicly available [130, 141, 143–157, 184–187], although they are often shared on request, and private sector codes are commercial tools with intellectual property and are only available for purchase [188–193]. Despite the wide range of existing codes, there is a notable absence of a collaborative open source framework to serve as a platform for LTP simulations. The implementation of such a project would bring significant benefits not only to academia but also to the private sector. It would facilitate the development of advanced and publicly available multiphysics tools. In addition, the open source nature of the code ensures that it can be reviewed by the wider community, improving validation and verification processes through a transparent methodology.

2.3.2 Zero dimensional plasma chemical-kinetics models

A zero-dimensional (0D) plasma chemical kinetics global model (GM) is a numerical method that solves the fluid-based conservation equations, described in section 2.2.2, and provides volume-averaged information about the simulated system, such as density and temperature. They are widely used in LTP research [7, 194] for investigating complex chemical reaction schemes, as simulations are fast and can provide robust insights into the scaling of important plasma parameters under variations of

external operating conditions [21, 112, 113].

Under the assumption that the plasma is homogeneously distributed in space, spatial gradients

$$\nabla = (\partial/\partial x, \partial/\partial y, \partial/\partial z) \to 0, \tag{2.3.1}$$

and drift velocities

$$\boldsymbol{u} \to 0, \tag{2.3.2}$$

are neglected in the continuity equations, so that only temporal variations are tracked by the model. This allows the plasma to be treated as a set of 0D point-like species contained in a reactor of volume V and surface area A, as shown in figure 2.4. The temporal variations in species densities and energies are caused only by

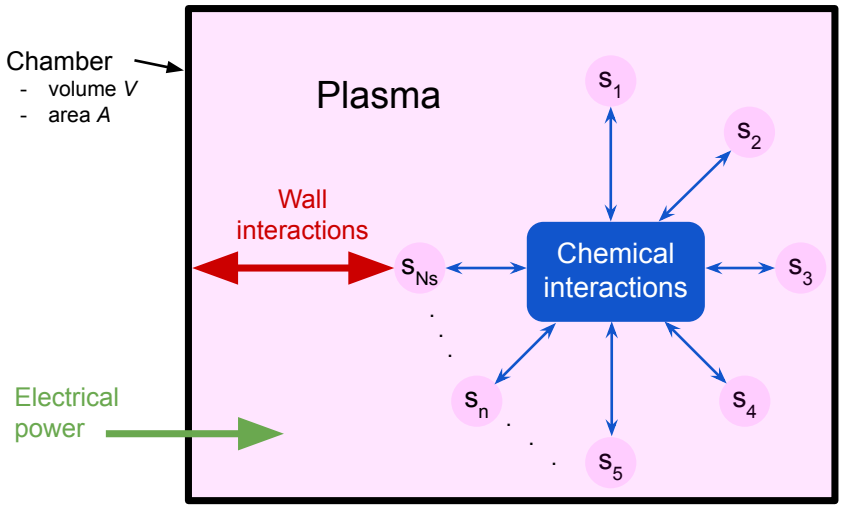

Figure 2.4: System environment of a 0-dimensional (0D) plasma chemical kinetics global model (GM): the plasma contained in a chamber of volume V and area A is formed by $s = 1, 2, 3, \cdots, N_S$ species. Each species s_n is considered a 0-dimensional (0D) system that interacts with other species and the boundary walls exchanging mass and energy.

chemical reactions, interactions with system boundaries and input power. This way each species s in the plasma can then be self-consistently described by their mass and energy continuity equations [7], equations 2.2.6 and 5.4.1 respectively, simplified by conditions 2.3.1 and 2.3.2

$$\frac{\partial n_s}{\partial t} = \left.\frac{\delta n_s}{\delta t}\right|_{coll}, \tag{2.3.3}$$

$$\frac{\partial}{\partial t}\left(\frac{3}{2}p_s\right) = \left.\frac{\delta}{\delta t}\left(\frac{3}{2}p_s\right)\right|_{coll}. \tag{2.3.4}$$

The 0D GM includes these first order ordinary differential equations (ODEs) for

each species in the plasma and forms a system of ODEs that can be readily solved.

The volume-averaged GM was first developed by Lieberman and Gottscho [195] for a monoatomic plasma and then extended to multi-species and molecular plasmas with more complicated chemistry [196, 197]. Since then, GMs have become an important numerical method for the study of LTPs [194], where complex chemistries play an important role [21,112,113,198–204]. They provide insight into the scaling of plasma parameters and information about the relationships between different parameters. The low computational cost of GMs allows broad parameter scans of system properties over several orders of magnitude, and the outputs serve as an important design tool for maximising a parameter of interest, such as energy efficiency [205] or by-product production [206].

Reducing the spatial dimensions to 0D greatly simplifies the system under consideration and makes the model compact and easy to understand, which has several advantages. The main advantage is the ability to add large chemical schemes that would not be feasible in more complex models. Another important advantage is the low computational cost, which allows fast simulations. In addition, the simplicity of the model also allows it to be developed relatively quickly and to be readily coupled to other models that incorporate the necessary spatial considerations [194]. There are a few well-known GMs, such as GlobalKin [207–209], Quantmol-p [210], ZDPlasKin [211] and PLASIMO [212], but it is common to find in-house models designed for a specific application.

The design of a GM requires consideration of the plasma and the system in which it is contained. The model requires information about the physical properties of the system, the energy coupling method, and a list of the species involved and the reactions between them. Due to the important simplifications made, the accuracy and robustness of these considerations is crucial, otherwise errors can be made that can easily lead to misleading results and large discrepancies between similar models and experimental data [213]. Particular attention must be paid to the implementation of analytical or semi-empirical assumptions and to inaccurate or unknown rate coefficients or cross sections [194]. The use of poor source data for reactions can lead to drastic differences in the resulting behaviour; in particular, it is important to take a critical view of reaction data that are estimated rather than measured experimentally. Furthermore, there may be limitations in the use of reaction rate coefficients, which require assumptions about the electron energy distribution function (EEDF) that can have a significant effect on the solution they produce [203,214–216]. Therefore, it should be noted that, due to the important simplifications made, GMs are not intended to provide exact values of plasma parameters, but rather estimates, and are useful for investigating plasma chemistry and how parameters depend on each other [21].

Chapter 3

EPOCH-LTP: particle-in-cell model for low temperature plasmas

This chapter presents the design and development of EPOCH-LTP, an open-source, highly parallelized, 1D3V (one-dimension in space and three-dimension in velocity) electrostatic particle-in-cell (PIC) code with Monte Carlo collisions (MCC) for the simulation of LTPs. EPOCH-LTP is developed from EPOCH, a collaborative code for high energy density plasma physics simulations that is widely used by the scientific community. Following the EPOCH approach, EPOCH-LTP is the basis for a collaborative and open source code initiative tailored for comprehensive LTP PIC simulations. It is important to note that the code is open source, as this allows it to be verified and validated by any user, and to be further developed to meet the needs of specific simulation projects.

First, in section 3.1, EPOCH, the code from which EPOCH-LTP has been developed, is presented. Secondly, in section 3.2, the simulation scheme implemented for EPOCH-LTP is outlined and, in section 3.3, a brief description of important concepts for the development of a PIC model are given, namely super-particles, shape functions and particle-grid interpolation. Thirdly, the different blocks of the main simulation scheme are described. These are the electrostatic field solver in 3.5, the integration of the equations of motion in 3.6, the particle boundary conditions in 3.7, the MCC algorithm in 3.8 and the inductive heating method in 3.10. Finally, section 3.9 describes the requirements that must be met by the spatio-temporal discretisation to ensure the accuracy and stability of the simulations, and section 3.11 presents the simulation results of a series of validation problems which show that EPOCH-LTP performs as expected.

3.1 EPOCH

EPOCH-LTP is developed from EPOCH [217, 218], an electromagnetic 3D3V (3-dimension in space and velocity) PIC code for high energy density plasma physics well established in the laser-plasma research community. EPOCH has a robust parallelisation architecture using Message Passing Interface (MPI) standards, allowing the use of supercomputers to significantly reduce simulation times. EPOCH is actively maintained, improved and developed by the Department of Physics at the University of Warwick, ensuring that it is a reliable and robust code. They have designed EPOCH to be extensible, using modern coding best practices, with a modular design that simplifies maintenance and facilitates further development. Therefore, EPOCH offers an ideal highly parallelized architecture for developing a PIC code for LTPs.

EPOCH uses an electromagnetic field solver for Maxwell's equations and the particle integrator includes relativistic effects. These methods are suitable for simulations involving high energy densities of fully ionised plasmas, but exceed the requirements for LTP simulations and show suboptimal performance in these contexts. Besides, EPOCH lacks a method of simulating collisions between neutral and charged particles. Consequently, while EPOCH's infrastructure offers immense potential for PIC simulations, it requires substantial development of the core physics modules for LTP applications.

3.2 EPOCH-LTP simulation scheme

The development of a 1D3V electrostatic PIC model for LTPs from EPOCH, involves the design and development of an electrostatic field solver, a non-relativistic Lorenz force particle integrator, and an MCC algorithm for interactions between charged and neutral particles. Additional adjustments, such as adaptations to boundary conditions, emanate from these core modifications and are also developed. Therefore, the necessary code development involves all of the simulation stages of an electrostatic PIC code [129, 175, 219], as shown in figure 3.1. Although it is necessary to develop most of the necessary simulation blocks, the great advantage of doing this in EPOCH is that we can take advantage of its already highly parallelised infrastructure. From EPOCH we use the input (definition of initial and boundary conditions) and output environment, the distribution of the grid and particles between the processors and their exchange of information (particles and fields).

Firstly, the simulation environment is initialised and super-particles are populated in phase-space following the inputs given in the input-deck. The system is set up as shown in figure 3.2, consisting of a 1D cartesian domain of length L placed between x_{min} and x_{max}. The domain is discretized into $N_G + 1$ grid cells of width Δx,

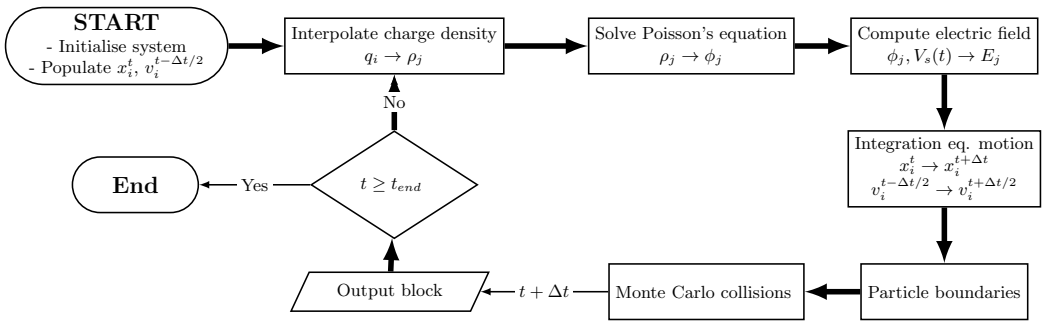

Figure 3.1: Simulation scheme of EPOCH-LTP.

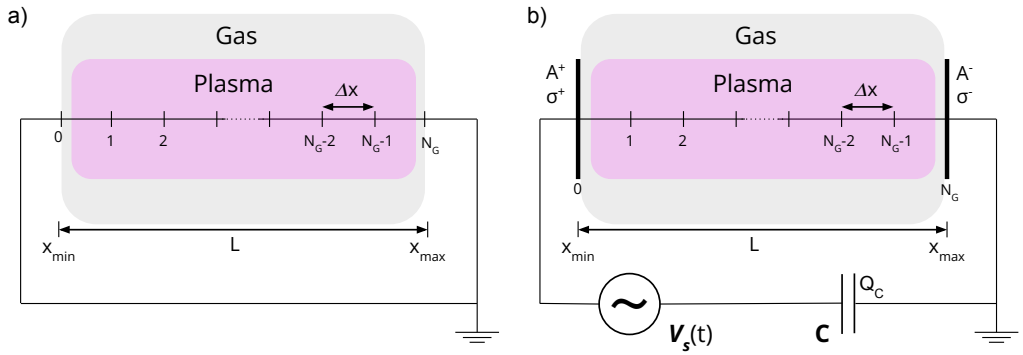

Figure 3.2: Simulation environment for a 1D PIC method in case of a) short circuit, or periodic boundaries and b) the case of a plasma bounded between two electrodes that are interconnected by an electric circuit which contains a voltage source $V_s(t)$ and a capacitor of capacitance C and charge Q_C. The electrodes have a surface $A^{\pm}$ and charge surface density $\sigma^{\pm}$. Note that the simulation domain is of length $L = x_{max} - x_{min}$ and is split into N_G cells of width Δx.

except the 0^{th} and the N_G^{th} grids that are $\Delta x/2$ wide. The plasma system may be defined with periodic boundary conditions, as in figure 3.2(a), or bounded between two electrodes of surfaces $A^{\pm}$ and charge density $\sigma^{\pm}$, as in figure 3.2(b). In both cases the simulation boundaries are connected by an electric circuit (described later on in section 3.5.2), which may including a voltage source $V_s(t)$ and a capacitor C.

After the initialisation the simulation iterates over a main loop that moves the system in time. The simulation cycle consists of a set of steps whose ultimate goal is to update the simulated particles in phase-space. These steps are summarised below and its corresponding code development is described in detail in the following sections:

1. Electrostatic solver that solves the electric field in the discretized grid, described in section 3.5, consist of

   (a) Charge density calculation that interpolates particle charge to grid points.

   (b) Electric potential computation solving Poisson's equation for electrostatics. Described in section 3.5.2.

(c) Electric field computation using the electric potential equation.

2. Integration of the Newton-Lorentz equations of motion that updates the position and velocity of the super-particles.

3. Application of super-particle spatial boundary conditions. Described in section 3.7.

4. Computation of super-particle collisions with Monte Carlo collision method. Described in section 3.8.

5. Time is moved forward $t \rightarrow t + \Delta t$ and, if required, output data is generated. Time dependent variables, like the voltage source $V_s(t)$, are updated.

These steps are repeated in a cyclic manner so that in each cycle time is advanced by a fraction Δt until the end time t_{end} is reached.

Before describing the outlined simulation blocks in more detail, three important concepts that are essential to making the PIC code computationally viable are explained in detail, namely the use of super-particles and shape functions, in section 3.3, and particle-grid interpolation, in section 3.4.

3.3 Super-particles and shape functions

The super-particles represent a subset of the real number of particles in the simulated system, and are assigned a weight W, which is the number of real particles they represent. They are not a point in space, but are distributed over a finite volume using a distribution function called the shape function $S(x)$, as shown in figure 3.3 (red shape). Similarly, the grid points used to discretise space are also associated

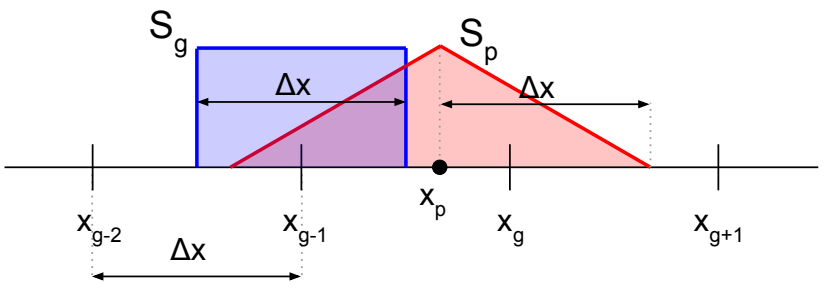

Figure 3.3: Triangular shape functions for a super-particle p at position x_p (red) and a top-hat shape function of a grid point at x_{g-1} (blue). The interpolation of the super-particle to the grid point x_{g-1} is the overlap between the two shape functions.

with a shape function that defines how a parameter, such as charge density, is distributed across the cell volume.

In PIC models, there is a constant transfer of data between super-particles and grid points, and vice versa, via particle-grid interpolation of their shape functions. The shape functions play a key role in this data transfer as they determine the smoothness of the interpolated data. However, while sophisticated shapes can improve noisy results, they also increase the computational cost. Therefore, the choice of shape functions for the grid points and super-particles is a trade-off between interpolation smoothness and computational efficiency.

The shape functions in EPOCH-LTP are reused from EPOCH. For super-particles there are three types: first order (top-hat, blue shape in figure 3.3), second order (triangle, red shape in figure 3.3) and third order b-spline. For grid cells, the top-hat shape function is available.

In general terms, the optimal combination of shape functions in terms of numerical noise and computational performance is, as in figure 3.3, the use of a triangular (second order b-spline) shape function for super-particles

$$S_p(x) = \begin{cases} 1 - |x_p - x|/\Delta x, & |x_p - x| \leq \Delta x \\ 0, & \text{otherwise} \end{cases} \tag{3.3.1}$$

and a top-hap shape function (first order b-spline) for the grid points

$$S_g(x) = \begin{cases} 1/\Delta x, & |x_g - x| \leq \Delta x/2 \\ 0, & \text{otherwise} \end{cases} \tag{3.3.2}$$

where x_p and x_g are the position of the particle and the grid, respectively. This choice is made after testing the different particle shape functions with problem 1 in Ref. 9. The test results with the top hat function differ significantly from the expected results, while the third order b-spline shape increases the computation time, but the results do not change significantly with respect to the triangle shape. Note, however, that the choice of shape functions also depends on the problem under study, and must therefore be considered on a case-by-case basis.

3.4 Particle-grid interpolation

The interpolation of shape functions is an important operation in the PIC method to share parameter quantities between super-particles and the grid.

The interpolation of a particle p (position x_p) to a grid point g (position x_g) is done with the convolution of the particle and grid shape functions, $S_p(x)$ and $S_g(x)$ respectively,

$$F_p(x_g) = (S_g * S_p)(x_g) = \int_{-\infty}^{\infty} S_g(x_g - x) S_p(x) dx, \tag{3.4.1}$$

which finds the area of overlap between the two shape functions.

The interpolation of the super-particle (triangular) shape function with the nearest grid point (top-hat) shape functions, at x_{g-1}, x_g, and x_g+1, is as sketched in figure 3.3, such that

$$\begin{aligned} F_p(x_{g-1}) &= \int_{x_p-\Delta x}^{x_g-\Delta x/2} S_g(x_{g-1}-x)S_p(x)dx \\ &= \frac{1}{8}+\frac{1}{2}\left(\frac{x_p-x_g}{\Delta x}\right)^2-\frac{1}{2}\frac{x_p-x_g}{\Delta x}, \end{aligned} \tag{3.4.2}$$

$$\begin{aligned} F_p(x_g) &= \int_{x_g-\Delta x/2}^{x_g+\Delta x/2} S_g(x_g-x)S_p(x)dx \\ &= \frac{3}{4}-\left(\frac{x_p-x_g}{\Delta x}\right)^2, \end{aligned} \tag{3.4.3}$$

$$\begin{aligned} F_p(x_{g+1}) &= \int_{x_g+\Delta x/2}^{x_p+\Delta x} S_g(x_{g+1}-x)S_p(x)dx \\ &= \frac{1}{8}+\frac{1}{2}\left(\frac{x_p-x_g}{\Delta x}\right)^2+\frac{1}{2}\frac{x_p-x_g}{\Delta x}, \end{aligned} \tag{3.4.4}$$

where $F_p(x_g)$ is the fraction of super-particle p that is interpolated to the grid point g. Note that $F_p(x_{g-1}) + F_p(x_g) + F_p(x_{g+1}) = 1$ and that the opposite process, i.e. the interpolation of grid cells to super-particles, will provide the same results, hence $F_p(x_g) = F_g(x_p)$.

3.4.1 Particle-grid interpolation at the boundaries

The interpolation of super-particle quantities to grid points, and vice-versa, as described in 3.4 is already implemented in EPOCH. However, the boundary conditions in EPOCH-LTP change and therefore the particle-grid interpolation at system boundaries requires a different treatment.

Under open boundary conditions, any particle whose position lies beyond the simulation domain is removed. However, particles close to the boundary whose shape functions fall partially outside the boundary, as shown in 3.4, must be treated with caution. In such cases, the fraction of the shape functions outside the simulation domain is folded back before the interpolation is performed. In this way, the shape function stays within the simulation domain and its corresponding quantity is conserved.

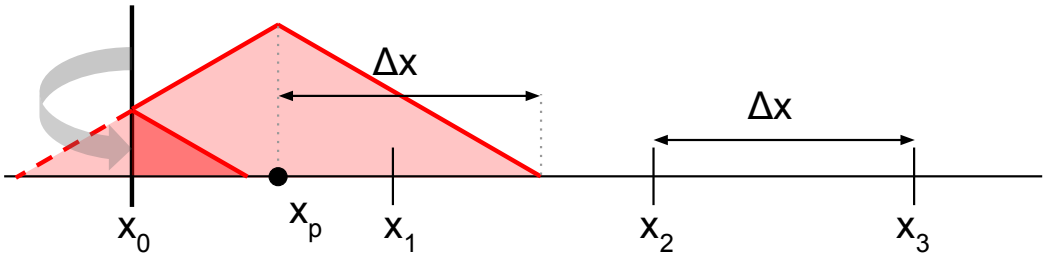

Figure 3.4: Shape functions that fall outside the system boundaries are folded back into the domain.

3.5 Field solver

The electric and magnetic fields must be solved as they are needed to integrate the equations of motion, which include the Lorentz force. This requires a numerical solution of Maxwell's equations however, in typical capacitively coupled plasma scenarios, these equations can be reduced to the electrostatic approximation, which simplifies the numerical method and significantly reduces the computational cost.

3.5.1 Electrostatic approximation

In LTPs the time variations of the magnetic field are generally negligible, i.e. $\partial \boldsymbol{B}/\partial t \simeq 0$. This assumption in Faraday's Law of induction (equation 2.1.6)

$$\nabla \times \boldsymbol{E} = -\frac{\partial \boldsymbol{B}}{\partial t} \simeq 0 \rightarrow \quad \nabla \times \boldsymbol{E} = 0 \tag{3.5.1}$$

implies that the electric field $\boldsymbol{E}$ is irrotational. With this $\boldsymbol{E}$ can be derived from the gradient of a scalar function

$$\boldsymbol{E} = -\nabla\phi, \tag{3.5.2}$$

which in this case is the electric potential, ϕ.

The potential equation 3.5.2 can in turn be substituted into Gauss Law for electricity (equation 2.1.8) such that ϕ is a function of the charge density ρ and is described by Poisson's equation

$$\nabla^2\phi = -\frac{\rho}{\varepsilon_0}. \tag{3.5.3}$$

With the electrostatic approximation, $\boldsymbol{E}$ and $\boldsymbol{B}$ are decoupled, with $\boldsymbol{E}$ being self-consistently described by equations 3.5.2 and 3.5.3, and $\boldsymbol{B}$ can be imposed arbitrary as an external source. Note that time variations in $\boldsymbol{B}$ are allowed as long as variations

are slower than the characteristic system speed.

3.5.2 Electrostatic field solver

In LTP simulation solving for electrostatic fields is preferable for two reasons. On the one hand, the numerical model is simpler, since it does not require the calculation of the electric current densities $\boldsymbol{J}$. On the other hand, the computational cost is lower since no currents need to be calculated and the simulation does not need to resolve to the speed of light c, which would otherwise imply more restrictive conditions on the cell width Δx and the time step Δt.

The numerical implementation of an electrostatic field solver consists of three steps. First, the interpolation of charged particles to the grid-points, obtaining a discretized, spatially distributed, charge density array $\boldsymbol{\rho}$. Second, with $\boldsymbol{\rho}$ as input, Poisson's equation is solved for the electric potential $\boldsymbol{\phi}$. Third, the electric field $\boldsymbol{E}$ is obtained by integrating the gradient in equation 3.5.2.

Note that $\boldsymbol{\rho}$, $\boldsymbol{\phi}$ and $\boldsymbol{E}$ are discretized values at the grid points $g = 0, 1, 2, \ldots, N_G$ and must be consistent between each other. In EPOCH-LTP these values are located at the centre of the cell.

Charge density interpolation

The charge density ρ is calculated by interpolating the charge of the super-particles onto the $N_G + 1$ grid points that discretize space [129]. The interpolation results in a charge density array

$$\boldsymbol{\rho} = \left[\rho_0, \rho_1, \ldots \rho_g \ldots, \rho_{N_G-1}, \rho_{N_G}\right] \tag{3.5.4}$$

where each value ρ_g represents the charge density at the grid point g.

The particle-grid interpolation is performed for each super-particle into its neighbouring grid points $g-1$, g and $g+1$ as follows

$$\rho_g = \frac{1}{\Delta x} \sum_{s=1}^{N_S} W_s q_s \sum_{p=1}^{N_P^s} F_p(x_g) \quad \Big/ \quad g = 0, 1, 2, \ldots, , N_G \tag{3.5.5}$$

where N_S is the number of species, N_P^s the number of particle of the given species s, and q_s and W_s are the species charge and super-particle weight, respectively.

The code implementation in EPOCH-LTP is presented in algorithm 1, where the shape functions described in equations 3.3.1 and 3.3.2 are used.

Algorithm 1 Computation of the charge density array

Define charge density array with zero values,
  $\boldsymbol{\rho} = \mathbf{0}$
for Every species $s = 1, 2, \ldots, N_S$ **do**
  Set super-particle weight, W_s
  Set charge, q_s
  for Every particle $p = 1, 2, \ldots, N_P^s$ **do**
    Get particle's grid location,
      $g = FLOOR\big[(x_p - x_{min})/\Delta x\big]$
    Particle-grid interpolation, eq. 3.4.2, 3.4.3, 3.4.4
    for $k = g - 1, g, g + 1$ **do**
      $\rho_k = \rho_k + F(x_k) W_s q_s / \Delta x$
    end for
  end for
end for

Poisson's solver for electrostatics

The electric potential is computed using Poisson's equation (equation 3.5.3) discretized around each cell g

$$\frac{\phi_{g+1} - 2\phi_g + \phi_{g-1}}{\Delta x^2} = \frac{\rho_g}{\varepsilon_0} \tag{3.5.6}$$

and solving the set of equations formed by the entire grid system [130]. The matrix form gathers the N_G discretized equations into one linear equation

$$\underline{\underline{M}}\boldsymbol{\phi} = -\frac{\Delta x^2}{\varepsilon_0}\boldsymbol{\rho}, \tag{3.5.7}$$

where $\boldsymbol{\phi}$, $\boldsymbol{\rho}$ have N_G components and $\underline{\underline{M}}$ is a matrix of size $N_G \times N_G$ such that

$$\begin{bmatrix} b_0 & c_0 & 0 & & & & \\ a_1 & b_1 & c_1 & 0 & & & \\ 0 & a_2 & b_2 & c_2 & & & \\ & & & \ldots & & & \\ & & & & a_{N_G-2} & b_{N_G-2} & c_{N_G-2} \\ & & & & 0 & a_{N_G-1} & b_{N_G-1} \end{bmatrix} \begin{bmatrix} \phi_0 \\ \phi_1 \\ \phi_2 \\ \vdots \\ \phi_{N_G-2} \\ \phi_{N_G-1} \end{bmatrix} = -\frac{\Delta x^2}{\epsilon_0} \begin{bmatrix} d_0 \\ d_1 \\ d_2 \\ \vdots \\ d_{N_G-2} \\ d_{N_G-1} \end{bmatrix} \tag{3.5.8}$$

where

$$\begin{aligned} a_i &= 1, \quad i = 1, 2, ..., N_G - 1 \\ b_0 = -1, \quad b_i &= -2, \quad i = 1, 2, ..., N_G - 1 \\ c_i &= 1, \quad i = 0, 1, ..., N_G - 2 \\ d_0 = \frac{\rho_0}{2} + \frac{\sigma_+}{\Delta x}, \quad d_i &= \rho_i, \quad i = 1, 2, ..., N_G - 1. \end{aligned} \tag{3.5.9}$$

This is a generalised expression that allows solutions of the form

$$\boldsymbol{\phi} = -\frac{\Delta x^2}{\varepsilon_0}\underline{\underline{M}}^{-1}\boldsymbol{\rho}, \tag{3.5.10}$$

for different electric circuit cases [130]. In EPOCH-LTP this can be solved using two different solving methods: i) a tri-diagonal method, or ii) using the Portable, Extensible Toolkit for Scientific Computation PETSc library [220], which makes use of a sparse matrix. The results presented in this thesis use the PETSc conjugate gradient method with an algebraic multigrid preconditioner.

Two different configurations are implemented in EPOCH-LTP that depend on the external electric circuit: i) the short circuit, in figure 3.2(a), which is equivalent to a system with periodic boundaries, and ii) the case where the plasma is bounded between two electrodes that are connected by an electric circuit that includes a voltage source and a blocking capacitor, as shown in figure 3.2(b).

Short circuit For the short circuit configuration, as in figure 3.2(a), there is no potential source, $V_s = 0$, and no capacitor, i.e. $C = \infty$, so that there is no potential drop between the simulation the boundaries,i.e. $\phi_0 = \phi_{N_g}$. With these conditions, the system of linear equations in 3.5.8 can be readily solved by removing the first row ($a_1 = b_0 = c_0 = d_0 = 0$) [129, 130].

In this configuration the left and right boundaries share the same electrical potential, which is an arbitrary value. Usually they are set to zero, $\phi_0 = \phi_{N_G} = 0$. Therefore, this circuit setup allows to simulate periodic boundaries when particles leaving one boundary are injected back on the opposite side.

Bounded plasma with voltage source and blocking capacitor. The configuration of a plasma bounded by two electrodes requires a closed electric circuit, as shown in figure 3.2(b). The electrodes are defined with a surface $A^{\pm}$ and charge density $\sigma^{\pm}$ and one of them acts as reference potential. The electric circuit also contains a voltage source $V_s(t)$ and a blocking capacitor of capacitance C, which are the control parameters of the external circuit. The presence of a capacitor is sometimes important as it causes a voltage drop which affects the voltage at the electrode. This is particularly important when simulating non-symmetrical voltage waveforms (see section 3.11.3).

In figure 3.2(b) the right electrode is grounded and acts as reference, i.e. $\phi_{N_G} = 0$ V, and therefore N_G^{th} row in equation 3.5.8 is not required. The opposite electrode is powered and requires knowing its charge surface density, σ^+. This is computed by applying charge continuity balance to its surface A^+ [130]

$$\sigma_+^t = \sigma_+^{t-\Delta t} + \frac{Q_{conv}^{\Delta t} + Q_C^t - Q_C^{t-\Delta t}}{A} \tag{3.5.11}$$

where, $Q_{conv}^{\Delta t}$ is the charge deposited by the convection current within a simulation time step, and Q_C^t is the charge deposited by the external circuit at a given time t.

The convection charge is the net electric charge deposition of super-particles, i.e. the super-particles crossing the simulation boundary in A^+,

$$Q_{conv}^{\Delta t} = \sum_{s}^{N_S} W_s \sum_{i \in x_i < x_{min}} q_s, \tag{3.5.12}$$

where subscript i refers to those super-particles reaching the powered electrode plate, i.e. their position is $x_i < x_{min}$.

The external circuit charge, Q_C^t, is determined by applying Kirchoff's Law to the circuit in figure 3.2(b)

$$V_s(t) = V_C + V_p = \frac{Q_c^t}{C} + \phi_0 - \phi_{N_G}, \tag{3.5.13}$$

i.e. the voltage across the source $V_s(t)$ (control parameter) is equal to the voltage drop across the plasma (simulation domain), $V_p = \phi_0 - \phi_{N_G}$, and the potential drop across the capacitor, $V_C = Q_C^t/C$. The charge accumulated on the capacitor Q_C^t is obtained by rearranging equation 3.5.13

$$Q_C^t = C\Big(V_s(t) + \phi_{N_G} - \phi_0\Big). \tag{3.5.14}$$

Substituting the convection charge, equation 3.5.11, and the external charge, equation 3.5.14, in the linear system of equation 3.5.8 enables a self-consistent solution of the plasma potential. After these substitutions, the coefficients b_0 and d_0 change to

$$\begin{aligned} b_0 =& -1 - \frac{\Delta x C}{A^+ \varepsilon_0} \\ d_0 =& \frac{\rho_0^t}{2} + \frac{\sigma_+^{t-\Delta t}}{\Delta_x} + \frac{Q_{conv}^{\Delta t} - Q_C^{t-\Delta t} + V_s(t)C}{A^+ \Delta x}. \end{aligned} \tag{3.5.15}$$

and only depend on parameters calculated within the current and previous simulation cycle.

The solver requires information from the previous simulation step, namely the charge surface density at the powered electrode $\sigma_+^{t-\Delta t}$ and the capacitor charge $Q_C^{t-\Delta t}$. Therefore, these two parameters must be initialised at the beginning of the simulation. The initial surface charge density on the electrode can be assumed to be zero, $\sigma^{t=0} = 0\,\mathrm{C/m^2}$, as initially no current is flowing across the circuit. The initial electric circuit charge is determined from Kirchoff's equation 3.5.13

$$Q^{t=0} = V_s(t=0)/(\frac{1}{C} + \frac{1}{C_v}). \tag{3.5.16}$$

where we assume that the simulation domain initially only contains a neutral gas and acts as capacitor C_v. The capacitance of the simulation domain depends on the neutral gases permittivity. This is usually close to the vacuum permittivity [221] and thus

$$C_v = \frac{\varepsilon_0}{L}. \tag{3.5.17}$$

Electric field solver

The electric field is computed from the discretized potential equation (equation 3.5.2) [129]

$$E_g = -\frac{\phi_{g+1} - \phi_{g-1}}{2\Delta x}. \tag{3.5.18}$$

The field values at the boundary grid points have to be treated in a special way, as the use of neighbouring points is tricky. In case of short circuits, the field values at grid point 0 and N_G are the equal adjacent potential points are taken from both sides of the simulation domain, such that

$$E_0 = E_{N_G} = -\frac{\phi_1 - \phi_{N_G-1}}{2\Delta x}. \tag{3.5.19}$$

In case of an electric circuit as in figure 3.2(b), the field values at the boundaries are obtained applying Gauss' law [130]

$$\begin{aligned} E_0 &= E_1 - \frac{\Delta x}{\varepsilon_0}\frac{\rho_0 + \rho_1}{2} \\ E_{N_G} &= E_{N_G-1} + \frac{\Delta x}{\varepsilon_0}\frac{\rho_{N_G} + \rho_{N_G-1}}{2}. \end{aligned} \tag{3.5.20}$$

3.6 Integration of the equations of motion

The equations of motion, described in section 2.1.3, are integrated to move the position $\boldsymbol{x_p}$ and velocity $\boldsymbol{v_p}$ of a super-particles p a fraction of time, $t \to t + \Delta t$. The integration method used in EPOCH-LTP is a time-centred finite-difference explicit method, also known as leap-frog method [129]. In the leap-frog method first velocity is moved in time $\boldsymbol{v_p^{t-\Delta t/2}} \to \boldsymbol{v_p^{t+\Delta t/2}}$ using a scheme developed by Boris [222], and then the position is integrated, $\boldsymbol{x_p^t} \to \boldsymbol{x_p^{t+\Delta t}}$ using $\boldsymbol{v_p^{t+\Delta t/2}}$. Note that $\boldsymbol{x_p}$ and $\boldsymbol{v_p}$ are moved in time with an offset of $\Delta t/2$ which is required for preserving energy conservation [129].

Firstly, the Boris scheme moves velocity in time by integrating the Newton-Lorentz equation 2.1.13. The scheme splits the velocity integration into four steps:

i) half time step linear acceleration due to the electric field

$$\boldsymbol{v_p^-} = \boldsymbol{v_p^{t-\Delta t/2}} + \boldsymbol{E_p^t}\frac{q_p}{m_p}\frac{\Delta t}{2}, \tag{3.6.1}$$

ii) rotation due to the magnetic field

$$\boldsymbol{v_p^*} = \boldsymbol{v_p^-} + \boldsymbol{v_p^-} \times \boldsymbol{t_p} \tag{3.6.2}$$

$$\boldsymbol{v_p^+} = \boldsymbol{v_p^*} + \boldsymbol{v_p^*} \times \boldsymbol{s_p} \tag{3.6.3}$$

where $\boldsymbol{t_p} = \boldsymbol{B_p^t} q_p \Delta t/(2m_p)$ and $\boldsymbol{s_p} = 2\boldsymbol{t}_p/(1+t_p^2)$

iii) half time step linear acceleration due to the electric field,

$$\boldsymbol{v_p^{t+\Delta t/2}} = \boldsymbol{v_p^+} + \boldsymbol{E_p^t} \frac{q_p}{m_p} \frac{\Delta t}{2}. \tag{3.6.4}$$

Secondly, the particle position is integrated in time using the new velocity value,

$$\boldsymbol{x_p^{t+\Delta t}} = \boldsymbol{x_p^t} + \boldsymbol{v_p^{t+\Delta t/2}} \Delta t. \tag{3.6.5}$$

Code implementation

The integration of the equations of motion described above is implemented in EPOCH-LTP as outlined in algorithm 2. Two comments are worth making about the implementation.

The equations 3.6.1 to 3.6.4 that push the velocity in time require the field values $\boldsymbol{E_p^t} = \boldsymbol{E}(\boldsymbol{x_p}, t)$ and $\boldsymbol{B_p^t} = \boldsymbol{B}(\boldsymbol{x_p}, t)$. The magnetic field is readily obtained from a predefined continuous function, $\boldsymbol{B}(x,t)$, however the electric field is discretized into grid points and thus grid-to-particle interpolation, as described in section 3.4, is required. Considering a 1D space with a top-hat shape function for grid points, equation 3.3.2, and a triangular shape function for super-particles, equation 3.3.1, the electric field at x_p is the sum of the electric field in the surrounding cells, $g-1$, g and $g+1$, weighted by the corresponding factors given in equations 3.4.2, 3.4.3 and 3.4.4,

$$E_p = F_{g-1}(x_p)E_{g-1} + F_g(x_p)E_g + F_{g+1}(x_p)E_{g+1}. \tag{3.6.6}$$

The evaluation of the boundary conditions on each super-particle is done within the loop of the integration of the equations of motion. This avoids looping twice over all simulated super-particles and is therefore computationally more efficient.

Initialisation of particles momenta

The leap-frog method requires that the Newton-Lorentz equations use time-centred values of velocity and force [129]. As the equations are interdependent, the position and velocity of the super-particles are out of phase by $\Delta t/2$. For this reason the velocity is moved back half a time step at the beginning of the simulation. This is done by executing the algorithm 2 but with $\Delta t \to -\Delta t/2$. This causes a time offset

Algorithm 2 Integration of Newton-Lorentz equation of motion

for Every species $s = 1, 2, \ldots, N_S$ **do**
  Set species charge q_s and mass m_s
  for Every particle $i = 1, 2, \ldots, N_P^s$ **do**
    Get particle's grid location, $g = FLOOR\big[(x_p - x_{min})/\Delta x\big]$
    E-field grid-to-particle interpolation, E_p, eq. 3.6.6,
    B-field, from function defined in advance $\boldsymbol{B_p} = \boldsymbol{B}(x_p, t)$
    $\boldsymbol{v_p}^{\boldsymbol{t-\Delta t/2}} \rightarrow \boldsymbol{v_p}^{\boldsymbol{t+\Delta t/2}}$ using eqs. 3.6.1 to 3.6.4
    $x_p^t \rightarrow x_p^{t+\Delta t}$ using eq. 3.6.5
    Apply boundary conditions, section 3.7
  end for
end for

of $\Delta t/2$ between position and velocity which allows time-centred integration of the equations of motion.

3.7 Particle boundary conditions

After integrating the equations of motion, the new position of the super-particles must be compared with the spatial boundaries of the system. Any particle beyond these boundaries must be treated according to the boundary conditions. In the 1D case, where the system is spatially delimited by x_{min} and x_{max} (see figure 3.2), boundary conditions must be applied to super-particles when $x_p > x_{max}$ or $x_p < x_{min}$.

Three types of conditions are considered in this thesis: periodic boundaries, perfect absorbing walls and non-perfect absorbing walls.

3.7.1 Periodic boundaries

Super-particles leaving the simulation domain are introduced back at the opposite boundary

$$\text{if} \quad x_p < x_{min} \quad \text{then} \quad x_p \rightarrow x_p + L, \tag{3.7.1}$$

$$\text{if} \quad x_p > x_{max} \quad \text{then} \quad x_p \rightarrow x_p - L, \tag{3.7.2}$$

where $L = x_{max} - x_{min}$ is the system length. Note that only position is changed while velocity is conserved.

3.7.2 Perfect absorbing walls

For the conditions of perfect absorbing walls any super-particle moving beyond the simulation domain limits is removed from the simulation environment. The code implementation in EPOCH-LTP is shown in algorithm 3.

Algorithm 3 Particle boundary condition: perfect absorbing walls.

for Every species $s = 1, 2, \ldots, N_S$ **do**
  for Every particle $p = 1, 2, \ldots, N_P^s$ **do**
    if $x_p > x_{max}$ or $x_p < x_{min}$ **then**
      Remove particle
    end if
  end for
end for

3.7.3 Non-perfect absorbing walls

In the case of non-perfect absorbing walls, super-particles moving beyond the simulation domain trigger a particle-wall interaction process, which in this case consists of secondary electron emission due to ion bombardment or electron reflection.

These processes are modelled using a Monte Carlo method, as described in algorithm 4. This consists of injecting an electron with a given probability $0 \leq P < 1$ when a charged species leaves the simulation domain. In case of a leaving ion, a secondary electron is injected with a probability P_{SEE}, and in case of an electron, it reflects with a probability P_{ER}.

Algorithm 4 Particle boundary condition: non-perfect absorbing walls.

for Every species $s = 1, 2, \ldots, N_S$ **do**
  for Every particle $p = 1, 2, \ldots, N_P^s$ **do**
    if $x_p > x_{max}$ or $x_p < x_{min}$ **then**
      Generate random uniform number, R_0
      if p is *electron* **then**
        if $P_{SEE} > R_0$ **then**
          Electron re-injected. Equations 3.7.3, 3.7.4
        else
          Remove particle
        end if
      else if p is *ion* **then**
        Remove particle
        if $P_{ER} > R_0$ **then**
          New electron injection. Equations 3.7.3, 3.7.4
        end if
      else
        Remove particle
      end if
    end if
  end for
end for

The velocity and position of the injected electron is defined as [223, 224]

$$\boldsymbol{v}_e = v_{e,th} \begin{bmatrix} \pm\sqrt{-2ln(R_1)} \\ \sqrt{-2ln(R_2)}\sin(2\pi R_3) \\ \sqrt{-2ln(R_2)}\cos(2\pi R_3) \end{bmatrix} \tag{3.7.3}$$

$$x_e = x_{min/max} + v_{e,x} R_4 \Delta t \tag{3.7.4}$$

where $v_{e,th} = \sqrt{k_B T_e / m_e}$ is a predefined electron thermal speed and R_1-R_4 are uniformly distributed random numbers. The injection velocity perpendicular to the boundary wall ($v_{e,x}$) follows a Maxwellian flux probability function [223] of the form

$$f(v) \propto v \exp\left(-\frac{v^2}{2v_{th}^2}\right), \tag{3.7.5}$$

with a $\pm$ sign depending on whether the electron is injected from x_{min} or x_{max}, which ensures that the velocity vector points into the simulation domain. The velocity terms parallel to the boundary wall ($v_{e,y}$, $v_{e,z}$) have simply a Gaussian (normal) distribution

$$f(v) \propto \exp\left(-\frac{v^2}{2v_{th}^2}\right). \tag{3.7.6}$$

The injection position is not set exactly at the boundary but at a random position as defined in equation 3.7.4. This random placement is an artefact to account for the motion of the injected electron within the given time-step Δt, otherwise non-physical effects would appear [223, 224].

3.8 Monte Carlo Collision algorithm

After the integration of the equations of motions the super-particles are "corrected" in velocity space in order to account for collisions. Collisions between neutral and charged particles are modelled as a statistical Monte Carlo process. In this section the Monte Carlo collision (MCC) method and its implementation in EPOCH-LTP is described.

3.8.1 Collision probability theory

Let us consider a volume fraction V that contains N^A super-particles of species A and N^B super-particles of species B, with particle weight W^A and W^B, respectively. The collision frequency of a particle i of species A with particles j of species B in a volume V is given by [165]

$$\nu_{ij}^{AB} = \frac{W^B}{V} g_{ij} \sigma_T^{AB}(g_{ij}) \tag{3.8.1}$$

where $g_{ij} = |\boldsymbol{v_i} - \boldsymbol{v_j}|$ is the impact speed between particles, and $\sigma_T^{AB}(g_{ij})$ is the total collision cross-section between two particles of species A and B. Note that the total collision cross-section between species A and B

$$\sigma_T^{AB}(g_{ij}) = \sum_{k=1}^{N_{CT}} \sigma_k^{AB}(g_{ij}), \tag{3.8.2}$$

is the sum of the N_{CT} collision types possible between these species, e.g. elastic scattering, excitation, ionisation, etc., and is a function of g_{ij} [165]. The collision frequency of i with any particle of species B is the sum of the collision frequencies of i with each of the j particles

$$\nu_i^{AB} = \sum_{j=1}^{N^B} \nu_{ij}^{AB} = \frac{W^B}{V} \sum_{j=1}^{N^B} g_{ij} \sigma_T^{AB}(g_{ij}). \tag{3.8.3}$$

The collision frequency ν_i^{AB} is of special interest as it is used to calculate the collision probabilities in the MCC algorithm.

The collision probability for particle i can be estimated with a Taylor expansion for a given time fraction Δt [165] as

$$P_i^{AB} = \exp\left(- \int_0^{\Delta t} \nu_i^{AB} dt \right) \simeq \nu_i^{AB} \Delta t = \frac{W^B}{V} \sum_{j=1}^{N^B} g_{ij} \sigma_T^{AB}(g_{ij}) \Delta t, \tag{3.8.4}$$

as long as the time fraction is small enough

$$\Delta t \ll 1/\nu_i^{AB}. \tag{3.8.5}$$

The equation 3.8.4 allows the numerical evaluation of the collision event undergone by particle i within Δt using a Monte Carlo statistics. This requires the evaluation of all possible combinations g_{ij} that constitute the total collision frequency, which can be computationally expensive. Nevertheless, the computational cost can be reduced using the null collision method.

3.8.2 Null collision method

The null collision method, first proposed by Vahedi *et al* [175] for LTP simulations, includes an additional null collision type to the collision set such that the total collision frequency is energy independent, i.e. it does not depend on the impact velocity g. This allows an estimate of the collision events that can occur in Δt without evaluating every super-particle in the system, and reduces this evaluation to just a small fraction of all possible ij interactions.

A null collision type, with cross-section $\sigma_{null}^{AB}(g)$, can be added to the total colli-

sion cross section, in equation 3.8.2, such that the product of g and σ_T^{AB} is constant for any value of g_{ij},

$$g_{ij}\sigma_T^{AB}(g_{ij}) = (g\sigma)_{max}^{AB} = \text{constant}. \tag{3.8.6}$$

The value of $(g\sigma)_{max}^{AB}$ must be estimated in advance, and is usually determined from the collision cross-section data. The resulting collision probability, described in equation 3.8.4, is then valid for any particle of species A without having to calculate every g_{ij},

$$P_{max}^{AB} = \nu_{max}^{AB}\Delta t = n_B(g\sigma)_{max}^{AB}\Delta t, \tag{3.8.7}$$

where $n_B = N^B W^B/V$ is the number density of species B in the volume fraction V. This allows to estimate the number of collision events that will happen between species A and B within Δt

$$N_{max}^{AB} = P_{max}^{AB} N_A. \tag{3.8.8}$$

Once N_{max}^{AB} is established, the next step is to determine what type of collisions take place. For this, N_{max}^{AB} pairs of species A (subscript i) and B (subscript j) are randomly selected and, for each of these pairs, the impact speed g_{ij} and the cross-sections for the different collision types, σ_k^{AB} in $k = 1, 2, \ldots, N_{CT}$, are computed. Each k-th collision type has a probability

$$P_k^{AB} = g_{ij}\sigma_k^{AB}(g_{ij})/(g\sigma)_{max}^{AB}. \tag{3.8.9}$$

As the last step, the collision dynamics of the ij pair undergoing the k-th collision type are executed. In case the selected collision type is the null collision, the ij particles do not undergo a collision, and so the overestimation caused by adding σ_{null}^{AB} to σ_T^{AB} is compensated. The dynamics of the remaining collision types, e.g. elastic scattering, or excitation and ionisation processes, are treated in the following sections.

3.8.3 Hard-sphere collision dynamics

In this thesis the colliding particles are treated as perfect solid spheres. The system of two particles i and j with momenta $\boldsymbol{p_i} = m_A\boldsymbol{v_i}$ and $\boldsymbol{p_i} = m_B\boldsymbol{v_i}$, is studied from the centre-of-mass (CM) frame of reference

$$\boldsymbol{p_{i/j}} = m_{A/B}\boldsymbol{u_{CM}} \pm \boldsymbol{p_{i/j}^{CM}} = m_{A/B}\boldsymbol{u_{CM}} \pm \mu\boldsymbol{g_{ij}} \tag{3.8.10}$$

where $\boldsymbol{p^{CM}} = \mu\boldsymbol{g_{ij}}$ is the momentum with respect to the CM frame of reference, $\mu = m_A m_B/(m_A+m_B)$ is the reduced mass, and $\boldsymbol{u_{CM}}$ is the CM velocity. The CM frame of reference is convenient because the colliding particles have the same magnitude but opposite directions, $\boldsymbol{p_i^{CM}} = -\boldsymbol{p_j^{CM}}$, and $\boldsymbol{u_{CM}}$ is invariant. Therefore, the

change in momentum $\boldsymbol{p} \rightarrow \boldsymbol{p'}$ caused by a collision

$$\boldsymbol{p'_{i/j}} = m_{A/B}\boldsymbol{u_{CM}} \pm \boldsymbol{p'^{CM}_{i/j}} = m_{A/B}\boldsymbol{u_{CM}} \pm \mu \boldsymbol{g'_{ij}} \tag{3.8.11}$$

is only reflected in $\boldsymbol{p^{CM}}$ and thus only requires the post-collision impact speed vector $\boldsymbol{g'_{ij}}$. The magnitude of $\boldsymbol{g'_{ij}}$ is determined by solving the energy conservation equation

$$\frac{1}{2}(m_A + m_B)u_{CM}^2 + \frac{1}{2}\mu g_{ij}^2 = \frac{1}{2}(m_A + m_B)u_{CM}^{2'} + \frac{1}{2}\mu g_{ij}^{2'} + E, \tag{3.8.12}$$

so that

$$g'_{ij} = \sqrt{g_{ij}^2 - \frac{2E}{\mu}}, \tag{3.8.13}$$

where E is the energy consumed during an inelastic process, e.g. excitation or ionisation. The scattering direction of $\boldsymbol{g'} = g'\hat{\boldsymbol{R}}$ is determined by an unit random vector [165]

$$\hat{\boldsymbol{R}} = \frac{\boldsymbol{R}}{|\boldsymbol{R}|}, \quad \boldsymbol{R} = (2R_1 - 1, 2R_2 - 1, 2R_3 - 1), \tag{3.8.14}$$

where $0 \leq R_1, R_2, R_3 < 1$ are uniform random numbers. Note that $\hat{\boldsymbol{R}}$ only applies to isotropic scattering.

The post-collision momentum is obtained replacing $\boldsymbol{g'} = g'\hat{\boldsymbol{R}}$ in 3.8.11

$$p'_{i/j} = m_{i/j}\boldsymbol{u}_{CM} \pm \hat{\boldsymbol{R}}\sqrt{g^2 - \frac{2E}{\mu}}. \tag{3.8.15}$$

This expression is valid for any two-body collision and is applied to the collision types described in the following section.

3.8.4 Collisions types

The collision types considered in this thesis are elastic scattering, electron impact excitation, electron impact ionisation, and ion-neutral charge-exchange.

Elastic scatterings, can occur between electrons and neutrals, $e + N \rightarrow e + N$, and between ions and neutrals, $i^+ + N \rightarrow i^+ + N$, where e refers to electrons, i^+ to ions and N to neutral species. These reactions only transfer momentum and total energy is conserved, thus $E = 0$.

Electron impact excitation, $e + N \rightarrow e + N'$. The neutral N transits to a higher energy state N', and thus $E > 0$. Only pairs with kinetic energy $\frac{1}{2}\mu g^2 \geq E$ are able to undergo this process.

Electron impact ionisation, $e + N \rightarrow 2e + i^+$. An electron is ripped off the neutral causing a loss of kinetic energy. Therefore an energy threshold, $E > 0$, is required for the ionisation process to happen and only pairs with a kinetic energy $\frac{1}{2}\mu g^2 \geq E$ are able to undergo this process. In the post-collision state, the momentum and energy balance must account for a new electron [165]

$$\boldsymbol{v}_{\boldsymbol{e_1}}^{\boldsymbol{CM'}} m_e + \boldsymbol{v}_{\boldsymbol{e_2}}^{\boldsymbol{CM'}} m_e + (m_i - m_e)\boldsymbol{v}_{\boldsymbol{i}}^{\boldsymbol{CM'}} = 0 \tag{3.8.16}$$

$$\frac{1}{2}m_e(v_{e_1}^{CM'})^2 + \frac{1}{2}m_e(v_{e_2}^{CM'})^2 + E = \frac{1}{2}\mu g^2, \tag{3.8.17}$$

where the subscripts e_1, e_2, and i refer to the impacting electron, the new electron-ion pair, respectively, and the superscript CM denotes vectors in the CM frame of reference. Note that the ion energy in equation 3.8.17 is neglected under the assumption that $m_e \gg m_i$ [165].

The electron post-collision energy is split randomly between the two electrons

$$\begin{aligned} \frac{1}{2}m_e(v_{e_1}^{CM'})^2 &= R(\frac{1}{2}\mu g^2 - E) \\ \frac{1}{2}m_e(v_{e_2}^{CM'})^2 &= (1-R)(\frac{1}{2}\mu g^2 - E), \end{aligned} \tag{3.8.18}$$

where $0 \leq R < 1$ is a random number. Assuming isotropic scattering, the velocity vectors in the rest frame are formed in the same way as in equations 3.8.14 and 3.8.15

$$\begin{aligned} \boldsymbol{v}'_{\boldsymbol{e_1}} &= \boldsymbol{u_{CM}} + v_{e_1}^{CM'}\hat{\boldsymbol{R}}_{\boldsymbol{1}} \\ \boldsymbol{v}'_{\boldsymbol{e_2}} &= \boldsymbol{u_{CM}} + v_{e_2}^{CM'}\hat{\boldsymbol{R}}_{\boldsymbol{2}} \\ \boldsymbol{v}_{\boldsymbol{i'}} &= \boldsymbol{u_{CM}} - \frac{(\boldsymbol{v}'_{\boldsymbol{e_1}} + \boldsymbol{v}'_{\boldsymbol{e_2}})m_e}{m_i - m_e}, \end{aligned} \tag{3.8.19}$$

where $\hat{\boldsymbol{R}}_{\boldsymbol{1}}$ and $\hat{\boldsymbol{R}}_{\boldsymbol{2}}$ random unitary vectors. The post-collision ion velocity vector is given by the equation 3.8.16.

Ion-neutral charge-exchange, or backscattering, $i^+ + N \rightarrow N + i^+$. The ion and neutral exchange an electron so that the ion becomes the neutral and vice-versa. This collision is simplified as an elastic process in which the ion and the neutral exchange their momentum vectors, but without any energy loss due to the exchange of the electron, and therefore $E = 0$.

3.8.5 Cold gas approximation

For collision between electrons and neutrals, where typically $m_e \gg m_N$ and $v_e \gg v_N$, the neutral velocity can be neglected, such that the impact speed $\boldsymbol{g} \simeq \boldsymbol{v_e}$. This assumption is called the *cold gas approximation* approximation, as it assumes that

neutrals are at $T_N \simeq 0\,\mathrm{K}$. Its main advantage is that it simplifies the computation of the collision dynamics, as electron-neutral collisions can be treated at the laboratory frame of reference and no information of the neutral is required.

The numerical method for electron-neutral collision dynamics with the cold gas approximation is briefly described here. A more detailed description can be found in [174, 175].

Electron-neutral elastic collision. The scattering of an incident electron can be described by two angles, as shown in figure 3.5 for χ and ψ. The first angle, χ,

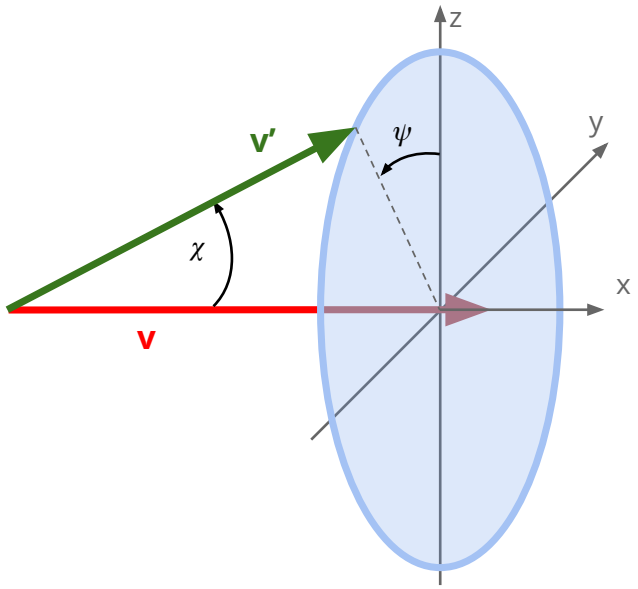

Figure 3.5: Sketch of the electron incident (red) and scattering (green) vectors. The direction of the scattering vector can be defined with respect to the incident vector by the angles χ and ψ.

sets the angle between the incident and scattering velocity vectors, and the second, ψ, determines the azimuthal position of the scattered vector around the incident angle. If the collision is isotropic the scattering angles are uniformly distributed, so that

$$\begin{aligned} \chi &= 2\pi R_1 \\ \psi &= 2\pi R_2 \end{aligned} \tag{3.8.20}$$

where $R_{1/2}$ are random uniform numbers. With χ and ψ defined the electron scattering unit vector is determined geometrically

$$\hat{\boldsymbol{v}}' = \frac{\boldsymbol{v}'}{|\boldsymbol{v}'|} = \hat{\boldsymbol{v}}\cos\chi + \hat{\boldsymbol{v}} \times \hat{\boldsymbol{i}}\frac{\sin\chi\sin\psi}{\sin\theta} + \hat{\boldsymbol{v}} \times (\hat{\boldsymbol{i}} \times \hat{\boldsymbol{v}})\frac{\sin\chi\sin\psi}{\sin\theta} \tag{3.8.21}$$

where $\hat{\boldsymbol{v}} = \boldsymbol{v}/|\boldsymbol{v}|$ is the electron incident unit vector, $\hat{\boldsymbol{i}}$ is a reference frame unit vector, e.g. Cartesian x-direction, and θ is the angle between $\hat{\boldsymbol{v}}$ and $\hat{\boldsymbol{i}}$.After determining the

scattering vector the post-collision electron energy is

$$E_{scat} = \left[1 - \frac{2m_e}{m_N}(1 - cos\chi)\right] E_{inc}, \tag{3.8.22}$$

where $E_{inc} = 1/2 m_e v_e^2$ is the incident electron energy. Finally, the velocity of the post-collision electron is

$$\boldsymbol{v'} = \sqrt{\frac{2E_{scat}}{m_e}}\hat{\boldsymbol{v}}' \tag{3.8.23}$$

Electron impact excitation and ionisation. The calculation is similar to the elastic scattering described with equations 3.8.20 to 3.8.23. The energy balance however only accounts for excitation and ionisation losses, E,

$$E_{scat} = E_{inc} - E \tag{3.8.24}$$

and neglects losses due to spatial scattering factors as the former dominate. In case of an ionisation process the post-collision energy is split randomly between the two electrons, as described in equation 3.8.18. The vector of the new ion is generated from the background gas energy distribution function.

3.8.6 Simulation of the neutral species

EPOCH-LTP implements neutral species in two different ways, as a continuous background field and as super-particles.

Neutral background field, the species is described by a density function $n_N = n_N(\boldsymbol{x}, t)$ and a velocity distribution function, $f_N = f_N(\boldsymbol{v}, t)$ which are called when necessary. The number density function is used to estimate collision events, in equation 3.8.7, and the velocity distribution function is used to generate velocity vectors that are required in the evaluation of collision events. The use of the neutral background field is well established in LTP PIC simulations [9, 10, 12, 174, 175, 177, 225], as it avoids simulating neutral species and provides accurate results as long as the neutral gas density is significantly larger than the plasma density, $n_N \gg n_p$.

Neutral super-particles, in this case the neutral gas is simulated with super-particles, where each super-particle represents a fraction W of the gas. Because of the low ionisation degree of LTPs, $\chi_{iz} \ll 1$, the neutral gas density is much higher than the plasma and therefore it is convenient to simulate the former with larger super-particle weights, as this reduces the computational costs. However, in such cases the collision dynamics must account for this weight difference.

When the particle weight of the colliding species is equal, $W^A = W^B$, the collision frequency of a super-particle i (species A) interacting with a super-particle

j (species B) is the same as of the super-particle j colliding with i, $\nu_{ij}^{AB} = \nu_{ji}^{BA}$ (see equation 3.8.1), and thus the estimation of collision events for species A and B is equal, $N_{max}^{AB} = N_{max}^{BA}$. However, when the species have different particle weights, $W^A \neq W^B$, the estimation of collision events is different, $N_{max}^{AB} \neq N_{max}^{BA}$. This inconsistency is resolved by selecting the highest number of collision events, $N_{max} = \max(N_{max}^{AB}, N_{max}^{BA})$, and, for each event, performing an additional Monte Carlo evaluation on each particle involved in the collision.

After calculating the post-collision momentum vectors, the momentum of the involved super-particles changes according to the probability given by the super-particle weight ratio [165]

$$P_i^A = \frac{W^B}{W_{max}^{AB}} \tag{3.8.25}$$

$$P_j^B = \frac{W^A}{W_{max}^{AB}}. \tag{3.8.26}$$

where $W_{max}^{AB} = \max(W^A, W^B)$. This additional evaluation balances out the overestimation of collision events on the species with super-particle of larger weight.

3.8.7 Monte Carlo collision implementation in EPOCH-LTP

The MCC algorithm is implemented in two steps in EPOCH-LTP. The first step consists of preparing the MCC method and loading it for optimal use in the main simulation loop. The second part executes the MCC algorithm within the main simulation loop, as shown in figure 3.1.

Initialisation of the MCC method

The initialisation of the MCC method, as described in algorithm 5, loops through the colliding species pairs A-B and for each collision type k it loads data from an input file. The input file contains the required data for defining the collision process:

Algorithm 5 Setup Monte Carlo collision method in EPOCH-LTP

```
for Species A = 1, 2, ..., N_S do
    for Species B = A, ..., N_S do
        for Collision type k = 1, ..., N_CT^AB do
            Identify collision type
            Identify reactants and products
            Read threshold energy, E_k^AB
            Read cross-section data table, (E^AB, σ_k^AB)_i ∈ i = 1, 2, ... N_table^k
            Read various: data units, output name, etc.
            Convert energy into impact speed data, E → g^AB = √(2E^AB/μ)
            Prepare cross-section data, (g^AB, g^AB σ_k^AB)_i ∈ i = 1, 2, ... N_table^k
        end for
        Set max. super-particle weight, W_max^AB
        Compute (gσ)_max^AB
    end for
end for
```

the collision type, the reacting and product species, the collision threshold energy; data tables for cross-section with respect to energy, and some additional data such as units of the data and output label. The energy and cross section data, are converted into impact speed $E^{AB} \rightarrow g^{AB} = \sqrt{2E/\mu}$, and $\sigma^{AB} \rightarrow g^{AB}\sigma^{AB}$ as these forms are more convenient for data interpolation and probability calculations (equation 3.8.9) required during the simulation. Once all collision data for a given species pair A-B is loaded, W^{AB}_{max} is set, and $(g\sigma)^{AB}_{max}$ is computed, using the available data tables $(g^{AB}, g^{AB}\sigma^{AB}_k)_i \in i = 1, 2, \ldots N^k_{table}, k = 1, 2 \cdots N^{AB}_{CT}$, where N^k_{table} is the number of data points in the cross-section data table of collision type k.

Algorithm 6 Monte Carlo collision algorithm in EPOCH-LTP

Sort super-particles by position in grid cells
for Species $A = 1, 2, \ldots, N_S$ **do**
  for Species $B = A, \ldots, N_S$ **do**
    for Grid cell $c = 1, 2, \ldots, N_G$ **do**
      Species densities, $n_c^A = N_c^A W^A / \Delta x$, and $n_c^B = N_c^B W^B / \Delta x$
      Max. collision events (real), $N_{max,c}^{AB^{\mathbb{R}}} = n_c^A n_c^B (g\sigma)_{max}^{AB} \Delta t / W_{max}^{AB}$
      Max. collision events (integer), $N_{max,c}^{AB} = \text{ceiling}(N_{max,c}^{AB^{\mathbb{R}}})$
      Boyd factor, $f_B = N_{max,c}^{AB^{\mathbb{R}}} / N_{max,c}^{AB}$
      for each collision pair $1, 2, \ldots, N_c^{AB}$ **do**
        Random particle i from species A in cell c, $\boldsymbol{v_i^A}$
        Random particle j from species B in cell c, $\boldsymbol{v_j^B}$
        Impact speed, $g_{ij}^{AB} = |\boldsymbol{v_i^A} - \boldsymbol{v_j^B}|$
        for each collision type $k = 1, 2, \ldots, N_{CT}^{AB}$ **do**
          Interpolate $g_{ij}^{AB} \sigma_k^{AB}(g_{ij}^{AB})$ from tabular data
          Collision probability, $P_k^{AB} = f_B g_{ij}^{AB} \sigma_k^{AB}(g_{ij}^{AB}) / (g\sigma)_{max}^{AB}$
        end for collision types k
        Uniform random number, R_1
        for each collision type $k = 1, 2, \ldots, N_{CT}^{AB}$ **do**
          if $\sum_{t=1}^{k} P_t^{AB} > R_1 > \sum_{t=1}^{k-1} P_t^{AB}$ **then**
            Uniform random number, R_2
            if $W^B / W_{max}^{AB} > R_2$ (eq. 3.8.25) **then**
              Execute collision type k on particle i (species A)
            end if
            if $W^A / W_{max}^{AB} > R_2$ (eq. 3.8.26) **then**
              Execute collision type k on particle j (species B)
            end if
            Exit collision type k for-loop
          end if
        end for collision type k
      end for collision pairs
    end for grid cell g
  end for species B
end for species A

MCC method in the main simulation loop

The implementation of the MCC algorithm in the main simulation loop is described in algorithm 6. The execution of the MCC algorithm has been extensively described in section 3.8, which consists of estimating a number of collision events and, for each collision event, selecting random pairs of superparticles, interpolating their corresponding cross section value, determining the collision type and calculating the collision dynamics. However, there are some computational aspects that are worth highlighting.

Before the MCC algorithm is actually executed, the super-particles are sorted by their position in the grid cells so that density calculations and super-particle selection can be performed quickly and efficiently.

Once the super-particles are sorted, the estimation of collision events is conducted on each grid cell c

$$N_{max,c}^{AB^{\mathbb{R}}} = \frac{n_c^A n_c^B}{W_{max}^{AB}} (g\sigma)_{max} \Delta t \tag{3.8.27}$$

is conducted using W_{max}^{AB} to account for different super-particles weights. In case the neutral species, for instance species B, is defined as a background field the density is obtained from a density function, $n_c^B = n^B(x_c)$, and $W_{max}^{AB} = W^A$. Because $N_{max}^{AB^{\mathbb{R}}}$ is a real number it must be rounded to an integer

$$N_{max}^{AB} = \text{ceiling}(N_{max}^{AB^R}) \tag{3.8.28}$$

and this implies that the number of collision events is slightly overestimated. Therefore, the real-to-integer conversion rate is stored in the factor

$$f_B = \frac{N_{max}^{AB^{\mathbb{R}}}}{N_{max}^{AB}}, \tag{3.8.29}$$

called here *Boyd factor*, which is used later to compensate for the rounding error [226].

Once N_{max}^{AB} is determined, collisions are executed in randomly selected ij super-particle pairs. For each ij pair, the impact speed g_{ij} is computed and used to linearly interpolate the $g^{AB}\sigma^{AB}(g_{ij})_k$ values for each $k = 1, 2, \ldots, N_{CT}^{AB}$ collision type. The $g^{AB}\sigma^{AB}(g_{ij})_k$ values are used to determine the probability of each k-th collision type, P_k^{AB}, using equation 3.8.9, however P_k^{AB} must be rated with the Boyd factor [226]

$$P_k^{AB} = f_B \frac{g_{ij}^{AB} \sigma_k^{AB}(g_{ij}^{AB})}{(g\sigma)_{max}^{AB}}. \tag{3.8.30}$$

Whether the collision type k will be executed for the given ij pair is given by

the following condition

$$\sum_{t=1}^{k-1} P_t^{AB} \leq R < \sum_{t=1}^{k} P_t^{AB} \tag{3.8.31}$$

where R is a uniform random number generated to evaluate this expression. Once the k-th collision type is determined the corresponding subroutine is called to compute the collision dynamics.

In the distinct cases where both species are super-particles, and not a background field, each particle is evaluated with the probabilities described in equations 3.8.25 and 3.8.26.

3.9 Simulation stability and accuracy conditions

Spatial and temporal discretization are essential in PIC methods to obtain a numerical solution. However, discretization cannot be arbitrary, but has a number of constraints to ensure that the numerical results are stable and physically accurate. Here we describe the main constraints that must be taken into account when performing simulations with a PIC model.

3.9.1 Grid cell constraints

The spatial discretization of space must ensure that the cell width Δx is smaller than the Debye length, $\Delta x < \lambda_D$. This ensures that the smallest features in a plasma, such as sheaths, are resolved.

It is also important to note that both the length of the simulation domain L and Δx limit the wavelengths that can be resolved. The smallest wavelength that can be solved is $\lambda_{min} = 2\Delta x$, while the longest wavelength is $\lambda_{max} = L$ [129].

3.9.2 Time step constraints

The following time step restriction must be fulfilled:

- The Courant-Friedrichs-Lewy (CLF) condition

$$\Delta t < \frac{\Delta x}{v_{max}}, \tag{3.9.1}$$

  ensures that simulated particles do not move more than a one grid cell within a time step.

- Plasma characteristic frequencies must be resolved [129],

$$\Delta t < \frac{\pi}{\omega_p} \tag{3.9.2}$$

where ω_p should be the natural mode with the highest frequency that may be present in a plasma: the electron plasma frequency $\omega_{pe} = \sqrt{e^2 n_e / m_e \varepsilon_0}$, the electron cyclotron frequency $\Omega_e = eB/m_e$, the upper hybrid frequency $\omega_{UH} = \sqrt{\omega_{pe}^2 + \Omega_e^2}$, the upper cut-off frequency $\omega_1 = \sqrt{\Omega_e^2/4 + \omega_{pe}^2} + \Omega_e/2$, etc. [227]. Any other externally driven excitation frequency ω_d should be also resolved following the condition in 3.9.2.

Similar to the grid discretisation, the time discretisation imposes constraints on the range of frequencies that can be resolved. The lowest frequency resolved is given by the simulation time $f_{low} = 1/t_{end}$, while the highest frequency is given by the time step $f_{high} = 1/2\Delta t$.

3.9.3 Accuracy conditions for collision modelling

In PIC models the MCC method is applied as a separate step in the simulation cycle, after the integration of motion, as shown in figure 3.1. This decoupled implementation of collisions is physically accurate only if [165]

- $\Delta t \ll \nu^{-1}$,
- the CFL condition described in section 3.9.2 is fulfilled, and
- changes in the super-particle speed are much smaller that the original speed, $\Delta t |\boldsymbol{F_L}|/m \ll |\boldsymbol{v}|$.

3.10 Inductive heating method

3.10.1 Inductive heating method from Meige *et al*

The use of electrostatic field solvers has several advantages for the simulation of LTPs, but its main limitation is that the electric and magnetic fields are not self-consistely solved. This hinders the simulation of, for instance ICPs, as they are heated by currents induced by an oscillating magnetic field, which are assumed to be negligible in electrostatic solvers as described in section 3.5.1.

To overcome this limitation, Meige *et al* developed a heating method that replaces the currents induced by a magnetic field and allows inductive-like heating effects in 1D3V electrostatic PIC simulations. This method has proved useful and has been implemented in the context of inductively coupled plasma research [228,229] and space propulsion research [230]. Therefore a similar method is implemented in EPOCH-LTP to investigate inductive currents in HF CCPs.

The inductive heating model from Meige *et al* is based on Ampere-Maxwell's law (equation 2.1.7), which describes that the total induced current density

$$J(x,t) = J_{disp}(x,t) + J_{cond}(x,t), \tag{3.10.1}$$

is composed of a displacement current

$$J_{disp}(x,t) = \varepsilon_0 \frac{\partial E_y(x,t)}{\partial t}, \tag{3.10.2}$$

caused by time variations in the electric field $E_y(x,t)$, and by conduction current

$$J_{cond}(x,t) = \sum_s q_s \Gamma_{y,s}(x,t), \tag{3.10.3}$$

caused by transport of electric charges. Note that ε_0 is the vacuum permittivity, E_y is the electric field responsible for the displacement current, and the subscript s refers to a given species that carries an electric charge q_s, has a particle flux $\Gamma_{y,s} = n_s \bar{v}_{y,s}$, a number density n_s and a mean velocity $\bar{v}_{y,s}$ in the perpendicular direction.

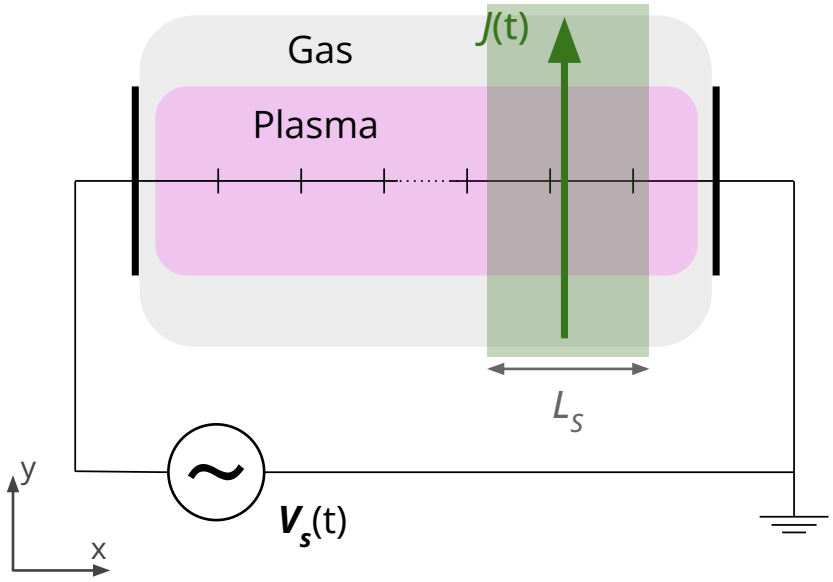

Figure 3.6: Simulation environment for a 1D PIC method with the inductive heating method developed by Meige *et al* [8].

The implementation of the inductive heating method in a 1D3V PIC model as in [8] is sketched in figure 3.6. It consists of imposing a sinusoidal current density function $J(t) = J_0 \sin(\omega t)$ over an arbitrary spatial extent L_S and computing E_y from equation 3.10.1 using 3.10.2 and 3.10.3

$$\int E_y dt = \frac{1}{\varepsilon_0} \int \left[J(x,t) - \sum_s q_s \Gamma_{y,s}(x,t) \right] dt. \tag{3.10.4}$$

The discretization of equation 3.10.4 for its numerical implementation is

$$E_y^{t+\Delta t} = E_y^t + \Delta t \left[J(t) - \frac{eW^e}{L_S} \sum_{i \in source} v_{e,y,i} \right] \tag{3.10.5}$$

where W^e is the weight of electron super-particles and $v^e y, i$ is the velocity term in the y-direction of i-th electron within the source region L_S. The resulting E_y is then used in the integration of the particle equations of motion such that inductive heating effects are reflected in the particle kinetics.

Although induction heating can be simulated with this method, the electromagnetic field is not self-consistently resolved and therefore electrostatic approximations prevail. Therefore, electromagnetic effects such as the skin depth effect cannot be observed with this method.

3.10.2 Inductive heating method in EPOCH-LTP

The heating method implemented in EPOCH-LTP is based on the work of Meige *et al* [8] described in section 3.10.1, but has been further developed to improve spatial resolution.

In the work of Meige *et al* [8] E_y is calculated globally over the whole inductive source length L_S, whereas the method implemented in EPOCH-LTP executes Meige's model on each grid cell i. This improves the spatial resolution, enabling interactions between plasma and induced currents to be taken into account when there are large spatial variations in the plasma, such as in the case of sheaths.

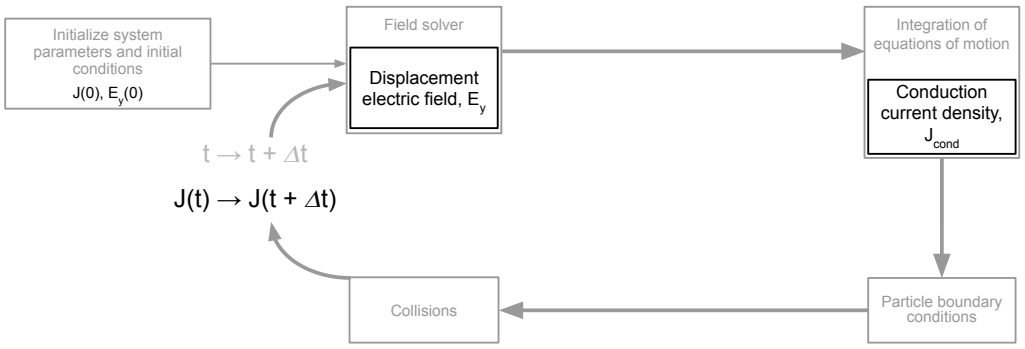

Figure 3.7: The implementation scheme of the inductive heating method (black blocks and text) within EPOCH-LTP's simulation loop (grey).

The implementation of the heating method in the main simulation loop of EPOCH-LTP is as shown in figure 3.7. For each time step $t \rightarrow t + \Delta t$ and for each grid cell i, it does as follows:

1. Computation of the plasma conduction current, making use of equation 3.10.3

$$J_{cond}(x_i,t) = \sum_s q_s \Gamma_{y,s}(x,t) = \sum_s q_s \frac{W^s}{\Delta x} \sum_{j \in x_i} v^s_{y,j}. \tag{3.10.6}$$

2. Computation of the perpendicular electric field time differential, using equations 3.10.1 and 3.10.2

$$\frac{\partial E_y(x_i,t)}{\partial t} = \frac{1}{\varepsilon_0}\left[J(x_i,t) - J_{cond}(x_i,t)\right]. \tag{3.10.7}$$

3. Integration of the electric field applying an implicit Euler method

$$E_y(x_i,t) = E_y(x_i,t-\Delta t) + \frac{\partial E_y(x_i,t)}{\partial t}\Delta t. \tag{3.10.8}$$

   Note that the time integration of E_y requires an initial condition at $t = 0$ which, assuming no initial induced field, is set to $E_y(x_i, t = 0) = 0$.

With regards to the time resolution, the numerical implementation is executed for each simulation cycle, $t \to t + \Delta t$, and the CFL time restriction (see section 3.9) is considered to ensure sufficient accuracy and stability.

3.11 Validation problems

EPOCH-LTP has been validated with four different test problems that ensure the code is working as expected. The test cases have been selected from the existing literature on problems that are considered to be well known. The test problems proposed are: CCPs operated in helium, between 4-133 Pa, and 450-120 V, from Turner *et al* [9] where the most important plasma physics blocks and diagnostics are tested; a CCP operated in argon, at 10 Pa, and 250 V, from Donko *et al* [10] which is a similar problem to the previous ones but operated in argon; CCPs operated in argon, between 1-10 Pa, and 350 V from Schulenberg *et al* [11] that includes non-perfect absorbing walls and compares against numerical and experimental data; a non-sinusoidal CCP operated in argon, 10 Pa and 300 V from Refs. 12, 13, that is used to test the effects of an external blocking capacitor; and an ICP operated in argon at 10 Pa from [8] to test the inductive heating method.

The test problems presented have similar simulation setups and execution methods. The simulation setup consists of a 1D domain bounded between two electrodes. In the case of the CCPs, the simulation setup is as sketched in 3.2(b), with the left electrode powered by an oscillating potential source, $V_s(t)$, and the right boundary grounded. In case of the ICP, the simulation setup is as sketched in 3.7, with both electrodes grounded. The initial super-particles loaded follow a uniform spatial distribution and a Maxwellian energy distribution. The simulations are run until the

problem converges to a steady state condition where the bulk plasma and sheath regions are identified. The steady state is reached when there is an equilibrium between particles lost across boundaries and particles gained through ionisation processes. Therefore, the convergence of the simulation can be assessed by following the evolution of the number of super-particles present with time. Once the number of super-particles is constant over time, the plasma has reached a steady state and can be diagnosed. The results collected from the simulations are taken once the plasma has reached steady state and averaged over a time defined as *average time* in the tables listing the simulation parameters.

3.11.1 Helium capacitively coupled plasmas

Four different CCP cases operated in helium, based on the experimental work in Ref. 137, are defined by Turner *et al* [9] as benchmark problems to test 1D3V electrostatic PIC codes with MCC. The validation is conducted by comparing the ion (He^+) density simulation results, n_i, with mean $\bar{n}_i$ and standard deviation σ data, that is provided in Ref. 9. This data enables a quantitative evaluation using a χ^2 distribution function. The validation is considered to be successful if the corresponding χ^2 value

$$\chi^2 = \sum_g \frac{|n_i(x_g) - \bar{n}_i(x_g)|^2}{\sigma_i(x_g)^2}, \tag{3.11.1}$$

is within the given confidence range, listed in the first two lines of table 3.1. If the χ^2 values are within these ranges, there is a high probability that the code is consistent with PIC codes already established in the LTP research community.

Table 3.1: Ion density spatial profile χ^2 values for the helium CCP test cases 1 to 4. The first two rows are the confidence ranges provided in Ref. 9. The following two rows list the results from EPOCH-LTP with the MCC method described in section 3.8 and with the cold gas approximation (section 3.8.5), respectively.

Case	**1**	**2**	**3**	**4**
95%	55-303	177-435	405-693	417-665
99%	48-405	160-548	382-798	392-730
EPOCH-LTP	807	4427	7153	2946
EPOCH-LTP (Cold gas approx.)	116	362	530	586

The simulation parameters for the cases 1 to 4 are detailed in Ref. 9 and listed in table 3.2 as they are used in EPOCH-LTP. They also including the collision set listed in table 3.3, and using the cross-section data provided in Ref. 9, which are plotted in figure 3.8. The benchmarking problems are executed twice: a first run using the MCC method described in section 3.8; and a second run implementing the MCC cold gas approximation (described in section 3.8.5), as used in Turner *et al* [9].

Table 3.2: Simulation parameters for helium CCP test cases which are similar to that in Ref. 9. The corresponding results are shown in figures 3.9 and 3.10.

Simulation parameters	**Value**			
Case	1	2	3	4
Gas species	Helium			
Gas pressure, P [Pa]	4	13	40	129
Gas density, n_N [10^{20}m^{-3}]	9.64	32.1	96.4	321
Gas temperature, T_N [K]	300			
Voltage waveform	$\sin(2\pi ft)$			
Voltage amplitude, V_s [V]	450	200	150	120
Frequency, f [MHz]	13.56			
Blocking capacitor, C [nF/m^2]	N/A			
Electrode gap, L [m]	0.067			
Grid cells, N_G	128	256	512	512
Time step, Δt [s]	$400/f$	$800/f$	$1600/f$	$3200/f$
Simulation time [s]	$1280/f$	$5120/f$	$5120/f$	$15360/f$
Average time [s]	$32/f$			
Init. super-part./species/cell	512	256	128	64
Initial plasma density, n_P [10^{14}m^{-3}]	2.56	5.12	5.12	3.84
Initial T_i [K]	300			
Initial T_e [K]	30.000			
Boundary conditions	Perfect abs. walls			

Table 3.3: Helium collisions implemented in the MCC model. E_{exc} and E_{ion} are the excitation and ionisation energy thresholds, respectively.

	Reaction	Description	Ref.
1	$e + \mathrm{He} \rightarrow e + \mathrm{He}$	Electron-neutral elastic collisions	9, 231
2	$e + \mathrm{He} \rightarrow e + \mathrm{He}$	Electron impact excitation ($E_{exc} = 19.82\,\mathrm{eV}$)	9, 231
2	$e + \mathrm{He} \rightarrow e + \mathrm{He}$	Electron impact excitation ($E_{exc} = 20.61\,\mathrm{eV}$)	9, 231
3	$e + \mathrm{He} \rightarrow 2e + \mathrm{He}^+$	Electron impact ionisation ($E_{ion} = 24.587\,\mathrm{eV}$)	9, 231
4	$\mathrm{He} + \mathrm{He}^+ \rightarrow \mathrm{He} + \mathrm{He}^+$	Ion-neutral elastic collision	9, 232
5	$\mathrm{He} + \mathrm{He}^+ \rightarrow \mathrm{He}^+ + \mathrm{He}$	Ion-neutral charge exchange	9, 232

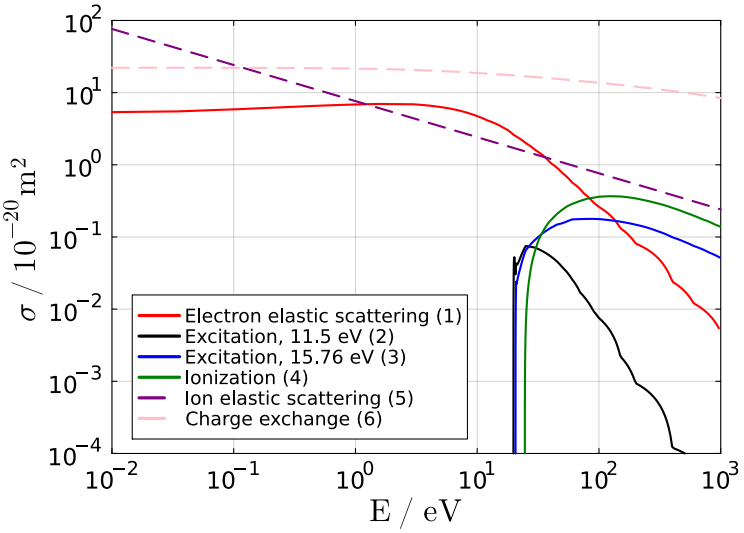

Figure 3.8: Cross sections of e + He and He^++ He collisions. The number in brackets in the legend corresponds to the reaction number in Table 3.3.

The simulation results for the spatial ion density profile are shown in figure 3.9a). The density peaks between 10^{14} and $3 \cdot 10^{16}\,\mathrm{m}^{-3}$ show that the plasma is

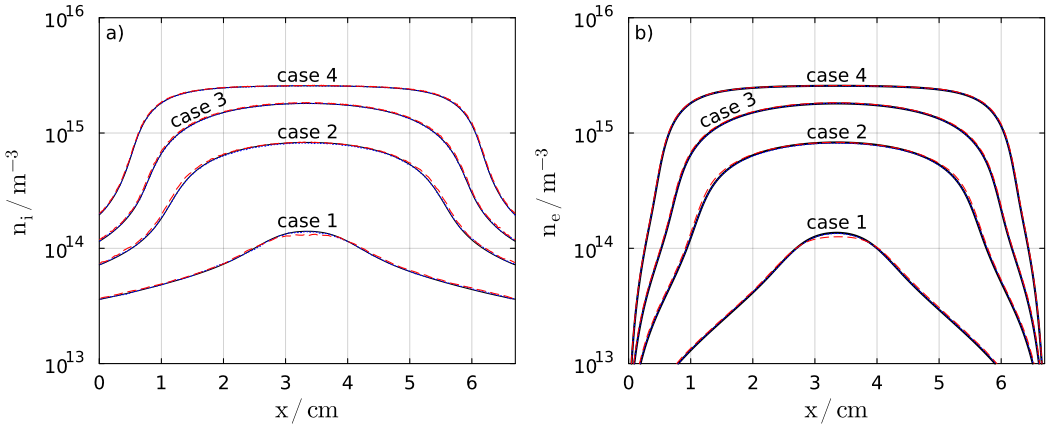

Figure 3.9: Spatial variation in the ion (a) and electron (b) density for the helium CCP test problems defined in table 3.2. The red-dashed lines are EPOCH-LTP results, and the blue-dotted lines are EPOCH-LTP with the cold-gas approximation. Black-solid lines are the results from Ref. 9.

formed by a central bulk region of higher density surrounded by two sheaths, where the plasma density drops by up to an order of magnitude at the electrodes. The simulation results for the spatial electron density profile are shown in figure 3.9b). As expected, they are in good agreement with the results in Ref. [9].

The results with both MCC implementations, with and without cold gas approximation, are qualitatively in excellent agreement with the results in Ref. 9. There is however a better agreement of the results with the cold gas approximation (blue-dotted lines) that is confirmed when applying equation 3.11.1 to the results. This is expected as the benchmarking problems are designed using the cold gas approximation. The χ^2 results are listed in table 3.1 and these show that simulations with the cold gas approximation are within the 95% confidence range provided in Ref. 9.

Results of the electron and ion power absorption, and ionisation rate spatial profiles, and the electron energy distribution function (EEDF) at the mid-plane are shown in figure 3.10. The electron power absorption, $P_{abs,e} = \langle J_{x,e} E_x \rangle$ in figure 3.10(a), peaks at the interface between the sheath and the bulk of the plasma. The ion power absorption, $P_{abs,i} = \langle J_{x,i} E_x \rangle$ in figure 3.10(b), shows large energy gains in the regions of the sheath where the ions are accelerated by the large potential gradients. The ionisation rate, $R_{ion} = n_e \langle \nu_{ion}^{eN} \rangle$ in figure 3.10(c), is most important where the electrons gain the most energy and, therefore, these regions coincide with the electron power absorption peaks. The EEPF results, in figure 3.10(d), show that the stochastic heating leading to high-energy tails is of less importance with increasing pressure, decreasing applied voltage amplitude, and wider bulk plasma regions. In general, the results presented in figure 3.10 are as expected and are in good qualitative agreement with the results presented in Ref. 9 (black lines). There

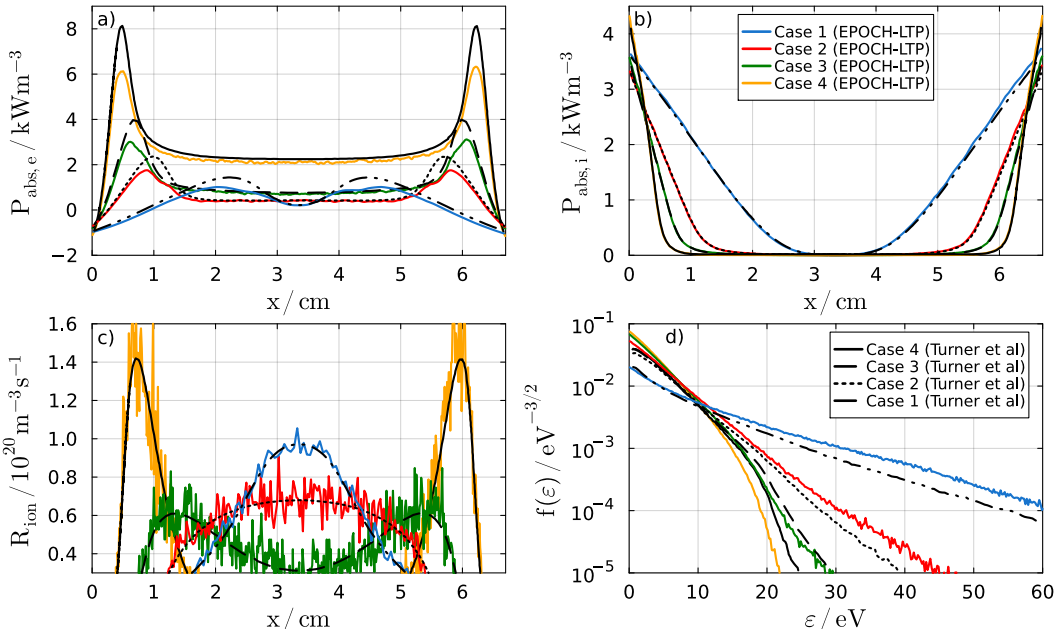

Figure 3.10: Spatial variation in the (a) electron power absorption, (b) ion power absorption, and (c) ionisation rate for the helium CCP test problems defined in table 3.2. Correspondingly in (d) the EEPF measured at the midplane ($x = 3.35\,\mathrm{cm}$). As described in the legend to figure b, case 1 is shown in blue, case 2 in red, case 3 in green and case 4 in yellow. The results of Turner *et al*9 (black lines) are described in the legend to figure (d).

are some discrepancies between the results of EPOCH-LTP and Ref. 9, mainly in the electron power absorption peaks and in the EEPF at higher energies, but these are considered to be small and are mainly related to the fact that EPOCH-LTP does not use the cold gas approximation.

In summary, the results presented in figure 3.9 and in table 3.1 show that the simulation results of the benchmarking problems proposed by Turner *et al* [9] are satisfactory and bring EPOCH-LTP in line with well-established PIC models. The diagnostics of ion density, electron and ion power absorption, ionization rate and EEPF, shown in figure 3.10, confirm that EPOCH-LTP is performing as expected. Therefore, it can be confirmed that the field solver, the integrator of equations of motion and the MCC algorithm, with a helium background field, in EPOCH-LTP are performing as expected.

3.11.2 Argon capacitively coupled plasmas

The validation process of EPOCH-LTP is extended by simulating argon CCPs studied by Donko *et al* [10] and Schulenberg *et al* [11]. These test cases are used to verify three aspects of the code. Firstly, to ensure that argon plasmas are simulated correctly. Secondly, to validate non-perfect absorbing wall boundaries. Thirdly, to validate ion flux energy distribution function (IF-EDF) on electrodes and phase-resolved plasma parameters, as these are important diagnostics in research on plasmas with

industrial applications.

The following simulations use the collision set listed in table 3.4 and plotted in figure 3.11.

Table 3.4: Argon collisions implemented in MCC model. E_{exc} and E_{ion} are the excitation and ionisation energy thresholds, respectively.

	Reaction	Description	Ref.
1	$e + \mathrm{Ar} \rightarrow e + \mathrm{Ar}$	Electron-neutral elastic collisions	233
2	$e + \mathrm{Ar} \rightarrow e + \mathrm{Ar}$	Electron impact excitation ($E_{exc} = 11.5\,\mathrm{eV}$)	234
3	$e + \mathrm{Ar} \rightarrow 2e + \mathrm{Ar}^+$	Electron impact ionisation ($E_{ion} = 15.76\,\mathrm{eV}$)	233
4	$\mathrm{Ar} + \mathrm{Ar}^+ \rightarrow \mathrm{Ar} + \mathrm{Ar}^+$	Ion-neutral elastic collision	232
5	$\mathrm{Ar} + \mathrm{Ar}^+ \rightarrow \mathrm{Ar}^+ + \mathrm{Ar}$	Ion-neutral charge exchange	232

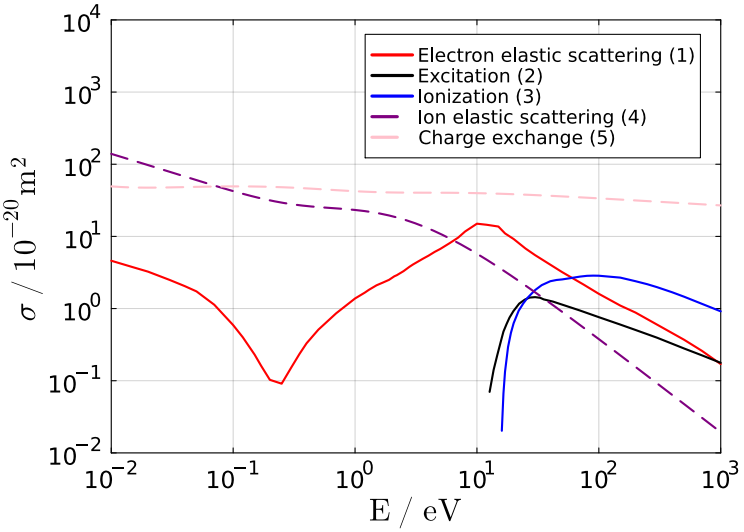

Figure 3.11: Cross sections of e + Ar and He^+ + Ar collisions. The number in brackets in the legend corresponds to the reaction number in Table 3.4.

Characterization of an argon capacitively coupled plasma

The problem proposed in Ref. 10 is simulated to characterise an argon CCP. The simulation parameters are described in table 3.5.

The results of the steady state electron and ion (Ar^+) densities and plasma potential, in figure 3.12, show a symmetrical plasma surrounded by two sheaths. The densities, in figure 3.12(a), are equal at the bulk plasma and peak at $n_e \simeq n_i \sim 7 \cdot 10^{15}\,\mathrm{m}^{-3}$. At the sheaths, quasi-neutrality is broken and electrons and ions present different density drop rates, as expected. The EPOCH-LTP density results (coloured lines) show a discrepancy of $\approx .7\%$ with the results presented in Ref. [10]. Considering that there are significant differences between the codes, e.g. differences in the collision method, in the cross section data, in the field solver method, and

Table 3.5: Simulation parameters for argon CCP test case which is similar to that in Ref. 10. The corresponding results are shown in 3.12.

Simulation parameter	**Value**
Gas species	Argon
Gas pressure, P [Pa]	10
Gas temperature, T_N [K]	350
Voltage waveform, $V_s(t)$	$V_0 \sin(2\pi f t)$
Voltage amplitude, V_0 [V]	250
Frequency, f [MHz]	13.56
Blocking capacitor, C [nF/m^2]	N/A
Electrode gap, L [m]	0.025
Grid cells, N_G	400
Time step, Δt [s]	$1.2 \cdot 10^{-11}$
Simulation time [s]	$4000/f$
Average time [s]	$1000/f$
Initial super-part./species/cell	32
Weight, W [part./m^2]	$7 \cdot 10^8$
Initial T_i [K]	350
Initial T_e [eV]	2
Boundary conditions	Perfect abs. walls

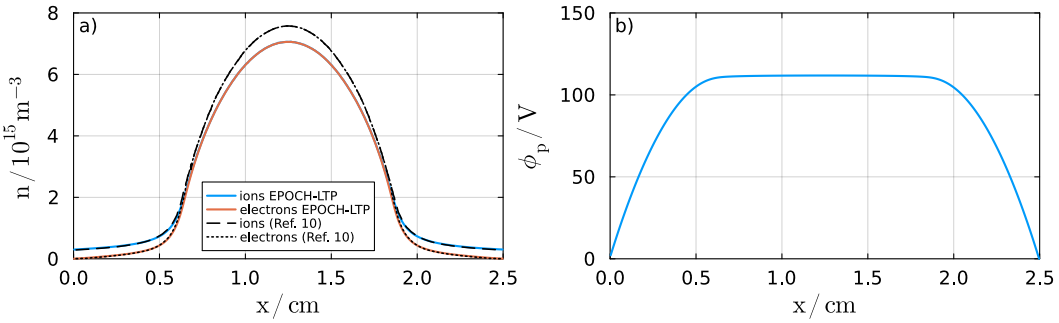

Figure 3.12: Spatial variation in the (a) electron and ion (Ar^+) densities and (b) plasma potential for the test problem based on Ref. 10. Operation parameters are described in table 3.5.

that small variations in the definition of the simulation parameters have an impact on the final results, as shown in [235], the results are considered satisfactory.

The plasma potential, in figure 3.12(b), is consistent with the density profiles and presents a flat potential, of about $\sim 112\,\mathrm{V}$, in the quasi-neutral region and a symmetrical potential drop at the sheath to match the 0 V time-averaged potential at the electrodes. These results are consistent with those of Refs. 7, 10, 219, 225.

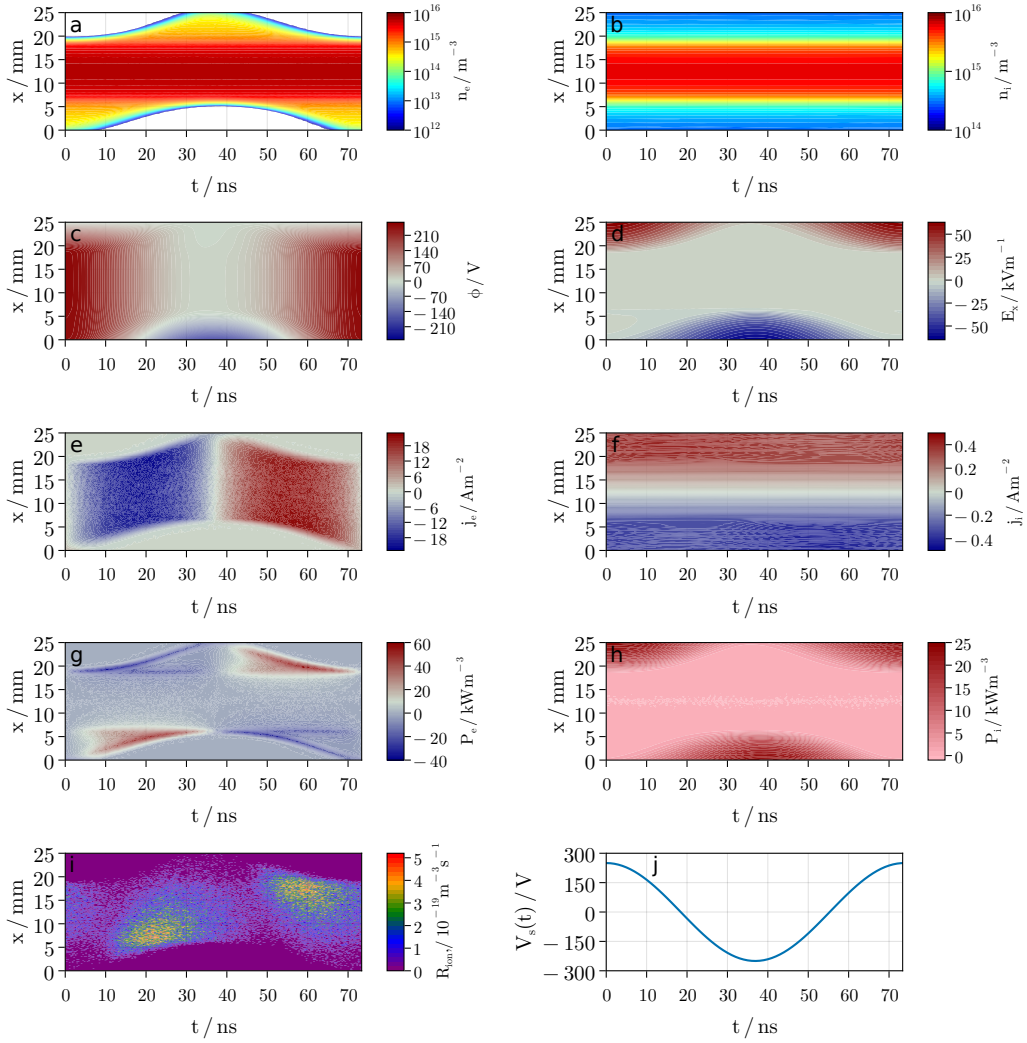

Figure 3.13: Spatially and temporally resolved distributions of (a) electron density, (b) ion (Ar^+) density, (c) plasma potential, (d) electric field, (e) electron current density, (f) ion current density, (g) electron power absorption, (h) ion power absorption, and (i) ionisation rate. The horizontal axis shows the time of one RF (13.56 MHz) cycle, and the vertical axis shows the space between electrodes. In (j) the potential waveform, $V_s(t)$, is applied to the left electrode (x=0 mm). Simulation conditions are described in table 3.5. This figure is intended to reproduce some of the data shown in Figure 11 of Ref. [10].

The phase-resolved plasma parameters within one 13.56 MHz radio frequency (RF) cycle are presented in figure 3.13. The plasma is characterised within one oscillation of the potential source, $V_s(t)$, applied at the electrode in x=0 mm and shown in figure 3.13(j). The electron density, in figure 3.13(a), shows that electrons at the sheath are subjected to oscillations of $V_s(t)$, that cause expansion and contraction of the sheath. When the sheath expands the electrons are ejected and the sheath is depleted (white areas). The ion density however, in figure 3.13(b), does not react to the variations of $V_s(t)$ because of their larger mass. The plasma potential, in figure 3.13(c), shows that the potential in the sheath at the powered electrode oscillates between $\pm V_0$. This sheath shields the remaining plasma, which oscillates between 0 and V_0. The electric field, in figure 3.13(d), shows large field gradients of opposite signs in the sheaths. The electron current density, in figure 3.13(e), shows the electron displacement towards the powered electrode in the first half of the RF cycle. This is followed by a sudden reversal at half cycle, and the displacement towards the grounded electrode in the second half of the RF cycle. The ion current density, in figure 3.13(f), shows that ions do not react to the RF oscillations but flow to the closest electrode. The electron power absorption, in figure 3.13(g), shows that most of the power absorption occurs in the sheath. When the sheaths expand, the electrons are accelerated, and thus gain power (red features), and when the sheaths contract, the electrons are decelerated and lose power (blue features). Note that the power gains are greater than the losses and that this positive balance allows the plasma to be sustained. The ion power absorption, in figure 3.13(h), shows that ions gain most of their energy when they are accelerated by the high electric fields present in the sheath. The ionisation rate, in figure 3.13(i), shows that ionisation is most frequent when electrons gain most of their energy during the expansion of the sheath. These highly energetic electrons are accelerated into the bulk plasma, so that a bright ionisation trail is observed moving inwards and along the sheath.

In summary, the phase-resolved results are in qualitative good agreement with the results presented in Ref. 10 and are consistent with results presented in Refs. 126, 225, 236, 237.

Non-perfect absorbing walls and IF-EDF

The argon CCP cases of study proposed by Schulenberg et al [11] are used to validate both the non-perfect absorbing wall conditions implemented in EPOCH-LTP as well as the IF-EDF diagnostics. These consist of four test cases where pressure is varied between 1 and 10 Pa. The simulation results from EPOCH-LTP are compared with PIC simulations and experimental results from Ref. 11.

The non-perfect absorbing walls boundary conditions are defined with an ion-impact secondary electron emission (SEE) rate of $P_{SEE} = 0.07$ and an electron reflection rate $P_{ER} = 0.7$. The remaining simulation parameters are listed in table

3.6. The electron density and IF-EDF results of these test cases are shown in figures 3.14 and 3.15.

Table 3.6: Simulation parameters for argon CCP test cases which are similar to that in Ref. 11. The corresponding results are shown in figures 3.14 and 3.15

Simulation parameters	**Value**			
Gas species	Argon			
Gas pressure, P [Pa]	10	5	2	1
Gas temperature, T_N [K]	315	305	302	295
Voltage waveform	$\cos(2\pi ft)$			
Voltage amplitude, V_s [V]	350			
Frequency, f [MHz]	13.56			
Blocking capacitor, C [nF/m^2]	N/A			
Electrode gap, L [m]	0.04			
Grid cells, N_G	1800			
Time step, Δt [s]	$6.15 \cdot 10^{-12}$			
Simulation time [s]	$2000/f$			
Average time [s]	$100/f$			
Init. super-part./species/cell	32			
Weight, W [10^8part./m^2]	10	10	5	0.6
Initial T_i [K]	315	305	302	295
Initial T_e [eV]	2			
Boundary conditions	Non-perfect abs. walls			
Ion-impact SEE rate, P_{SEE}	0.07			
Electron reflection rate, P_{ER}	0.7			

The electron density results at the CCP midplane ($x = 2\,\text{cm}$), in figure 3.14, show an increase of n_e with pressure. This is associated with higher collision rates,

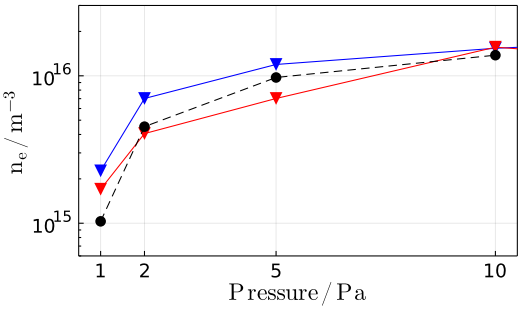

Figure 3.14: Electron density at the midplane ($x = 2\,\text{cm}$) of argon CCPs. Black circles are EPOCH-LTP simulation results, and blue and red triangles are PIC simulations and experimental results in Ref. 11, respectively. Operation conditions and EPOCH-LTP simulation parameters are listed in table 3.6.

and hence ionisation, between electrons and neutrals. The EPOCH-LTP results are in good agreement with the Langmuir measurements and PIC results in Ref. 11,

The IF-EDF results, in figure 3.15, show the strong influence of the gas pressure on ion fluxes. At lower pressure, 1-2 Pa, the low collision rate between ions and

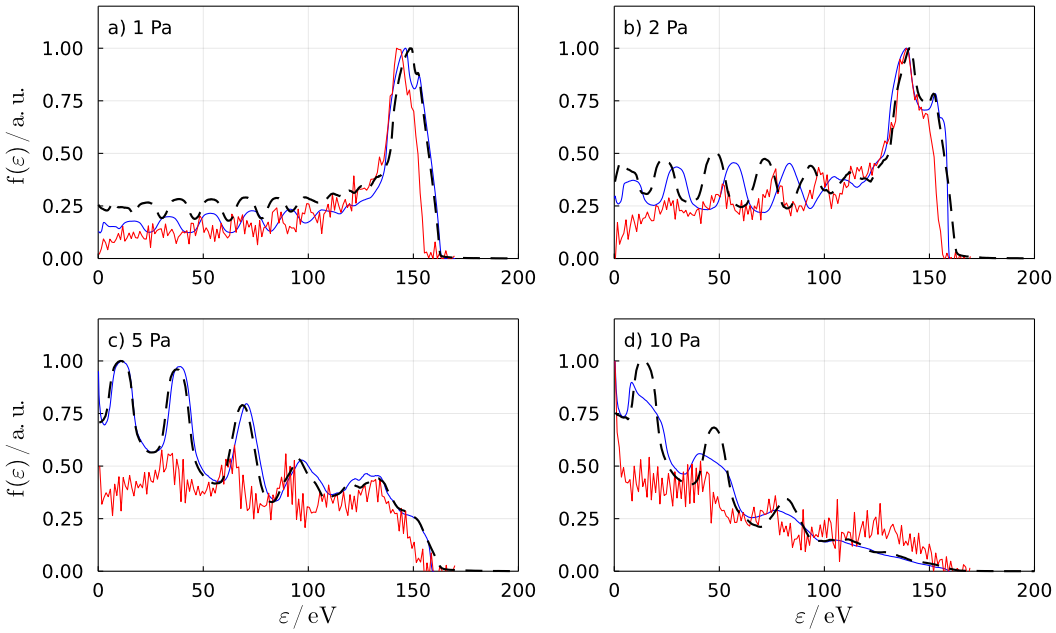

Figure 3.15: IF-EDF at both electrodes for argon CCPs at different pressures. The black-dashed lines are EPOCH-LTP results, and blue-solid and red-solid lines are PIC simulations and experimental results in Ref. 11, respectively. Operation conditions and EPOCH-LTP simulation parameters are listed in table 3.6.

neutrals allows most of the ions to cross the sheath without undergoing any collision. Therefore, most of the ions at the electrodes have gained and energy equivalent to the potential drop between the bulk plasma and the electrodes, about 150 eV. At higher pressure, 5-10 Pa, the collision frequency increases and ions are more likely to lose energy due to elastic scattering and charge-exchange interactions, reactions 4 and 5 in table 3.4 respectively. Therefore contact between relatively high-energy ions and the electrode surface occurs less frequently and characteristic peaks at energies below the plasma potential are observed [238, 239]. In summary, the IF-EDF results obtained with EPOCH-LTP agree well with the PIC simulations results and retarding field energy analyzer measurements carried out in Ref. 11.

3.11.3 Argon capacitively coupled plasma with blocking capacitor

An argon CCP operated with multi-frequency tailored voltage waveform as investigated in Donko *et al* [12], is proposed as a problem to test the blocking capacitor implemented EPOCH-LTP. The waveform,

$$V_s(t) = V_0 \left[\cos(2\pi f_1 t + \pi/2) + \cos(2\pi f_2 t)\right],$$

causes an asymmetrical voltage drop across the plasma sheaths such that a DC bias, V_{DC}, is self-induced across the discharge and absorbed by an external blocking capacitor [240]. This is only observed if a blocking capacitor is present in the electric

circuit and, therefore, this case is a suitable test problem. Therefore the simulation setup is as shown in figure 3.2(b), with the parameters listed in table 3.7. Results for steady state spatial variations in density and potential, and IF-EDF are presented in figure 3.16, and voltage temporal variations are presented in 3.17.

Table 3.7: Simulation parameters for argon CCP test case similar to that in Refs. 12, 13.

Simulation parameters	**Value**
Gas species	Argon
Gas pressure, P [Pa]	10
Gas temperature, T_N [K]	350
Driving voltage, V_s [V]	300
Frequencies, f_1/f_2 [MHz]	13.56/27.12
Voltage waveform	$\cos(2\pi f_1 t + \pi/2) + \cos(2\pi f_2 t)$
Blocking capacitor, C [nF/m^2]	30
Super-particle weight, W [part./m^2]	$3{\cdot}10^8$
Electrode gap, L [m]	0.02
Grid cells, N_G	512
Time step, Δt [s]	10^{-11}
Simulation time, [s]	$2000/f_1$
Average time [s]	$100/f_1$
Init. super-part./species/cell	32
Initial T_i [eV]	0.03
Initial T_e [eV]	2
Boundary conditions	Non-perfect abs. walls
Ion-impact SEE rate, P_{SEE}	0.1
Electron reflection rate, P_{ER}	0.2

The spatial variations in density and potential, in figure 3.16(a) and b) respectively, show an asymmetry caused by a self-induced $V_{DC} = 150\,\mathrm{V}$. This asymmetry causes the IF-EDF at the powered and grounded electrode to be different, as shown in figure 3.16(c) and (d). The EPOCH-LTP results show good agreement with results from similar simulations in [12, 13]. The electron density results and the IF-EDF at the driven electrode show good agreement. There is a notable offset in the IF-EDF at the grounded electrode (Figure 3.16(c)) due to the use of different field solver methods. While EPOCH-LTP self-consistently solves Poisson's equation along with the external circuit, Donko *et al* and Lafleur *et al* use an iterative method that, instead of solving for the blocking capacitor in the external circuit, readjusts the average potential after a certain number of RF cycles. As a result, the potential solved at the grounded electrode is different, resulting in a consistent energy offset in the IF-EDF, but the curve characteristics are the same.

The phase-resolved voltage in figure 3.17 show that the voltage drop across the sheath at the grounded and powered electrode, V_{gs} and V_{ps} respectively, are different and this is the reason for $V_{DC} \neq 0\,\mathrm{V}$ [240]. Applying Kirchoff's voltage law, in equation 3.5.13, the total voltage across the electrodes is $V_p = V_s(t) + V_C$, where

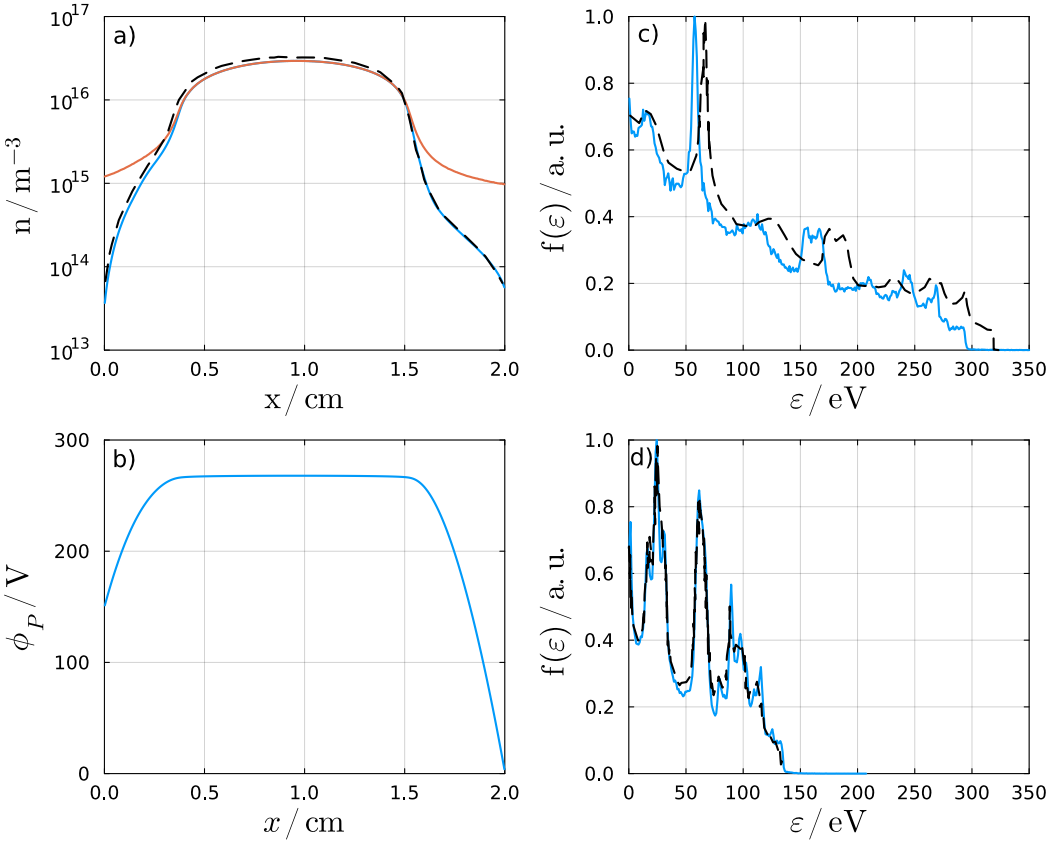

Figure 3.16: Spatial variation of electron (blue) and ion (red) density in figure (a) and plasma potential in figure (b) for the non-sinusoidal argon CCP test case based on Ref. 12,13. In figure (c) the IF-EDF of the grounded electrode and in (d) the IF-EDF of the powered electrode. The black dashed lines correspond to the results in 12,13. The operating parameters are described in Table 3.7.

any self-bias is absorbed by the capacitor, i.e. $V_C = V_{DC}$. Kirchoff's definition of V_p is compared with $V_p \simeq V_{gs} + V_{ps}$ [7, Ch. 11] in figure 3.17, and both are in good agreement.

The results presented are consistent with the numerical results presented in Refs. 12,13 and with the theoretical results from Kirchoff's voltage law. Therefore it can be conclude that EPOCH-LTP is performing as expected with an external blocking capacitor.

3.11.4 Argon inductively coupled plasma

The inductive heating method has been tested reproducing four simulation cases, labelled A to D, from Meige *et al* [8]. These test problems consist of a 1D inter-electrode gap of 10 cm, containing an argon at 1 mTorr (0.13 Pa) and 297 K, and grounded electrodes, as shown in figure 3.18.

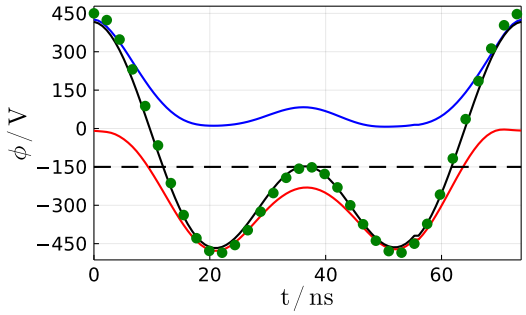

Figure 3.17: Temporal variation within one 13.56 MHz cycle of the voltage across the sheath at the grounded electrode, V_{gs}, (solid-blue line), the sheath at the powered electrode, V_{ps}, (solid-red), and the total voltage across the discharge, $V_p \simeq V_{gs} + V_{ps}$ (solid-black) and $V_T = V_s(t) + V_DC$ (green circles). The dashed-black line shows the self-induced DC bias, V_DC. Operation conditions are described in table 3.7.

The inductive current source,

$$J(x,t) = \begin{cases} J_0 \sin(2\pi f t), & x_{min} \leq x \leq x_{max} \\ 0, & \text{otherwise} \end{cases} \tag{3.11.2}$$

is driven at $f = 10\,\text{MHz}$ and $J_0 = 100\,\text{Am}^{-2}$ and placed between x_{min} and x_{max} in space. The simulations run for 1000 cycles, with a time step resolving the CFL condition for 100 eV electrons and a grid width that ensures the Debye length is resolved, $\Delta x < \lambda_D$. The reaction set included is as described in section 3.11.2 and the simulation parameters are listed in table 3.8.

Figure 3.19 shows the resulting spatial profiles for ions (Ar^+) and the plasma potential, where the spatial extents for the application of inductive heating corresponding to case A-D are shown in figure 3.19(a). The resulting plasma density and potential for these tests are shown in figures 3.19(b) and c), respectively. The inductive heating method is performing as expected, generating an homogeneous plasma independent from the location and extent of the inductive source. Even though the heating source is not symmetrically located, the resulting spatial profile is quasi-symmetric. This is because electron mean-free-path is larger than the reactor characteristic length, $\lambda_{mfp,e} > L$ and thus ionisation processes are non-local and are found in the entire simulation domain.

The plasma potential, $\phi_P \sim 17\,\text{V}$, is as expected for a plasma generated between floating walls with collisionless sheaths [7]. The plasma potential profiles are in good agreement not only with the results in Ref. 8 but also with theoretical analysis described in section 2.1.4, such that

$$\phi_P \sim \frac{k_B T_e}{e} \ln\left(\frac{m_i}{2\pi m_e}\right) + \frac{k_B T_e}{2e}, \tag{3.11.3}$$

where $T_e = 3.3\,\text{eV}$. There is however a difference between applying the inductive

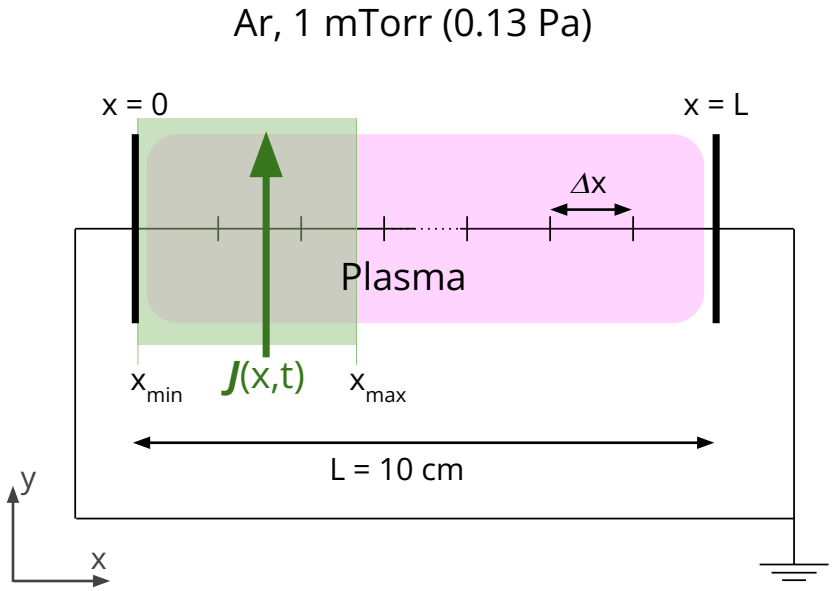

Figure 3.18: Simulation setup for an argon plasma driven with a inductive current, $J(x,t)$, that is applied in the y-direction between x_{min} and x_{max} (green shaded area).

source at the edge (cases A and B) or in the bulk plasma (cases C and D), that lead to different plasma densities. which results in different peak values of the plasma density: $\sim 2 \cdot 10^{16}\,\mathrm{m}^{-3}$ and $\sim 3 \cdot 10^{15}\,\mathrm{m}^{-3}$, respectively.

On the one hand, when the inductive source is placed at the bulk plasma (C and D) the density results, shown in figure 3.19(b), are in good agreement with results in Ref. 8, which present plasma density peaks of $\sim 2 \cdot 10^{16}\,\mathrm{m}^{-3}$. Note that the peak density in case C is slightly higher than in case D because longer inductive sources couple more power to electrons.

On the other hand, cases A and B show densities that are an order of magnitude higher than in cases C and D. This is caused by enhanced power absorption within the sheath that underpins ionization and thereby the plasma density. In these cases the penetration of the heating source into the bulk plasma does not play an important role and therefore the density for cases A and B are similar. This behaviour, discussed in detail in section 4.3, is not observed in Ref. 8, and this can reasonably be attributed to the relatively high spatial resolution implemented in EPOCH-LTP, which is not included in Meige's work.

Previous work using the inductive heating method did not observe enhanced power deposition within the sheath because the resulting displacement currents were averaged over the entire heating region, instead of being discretized into grid cells, and therefore regions with high displacement currents were smoothed out [8]. Nevertheless, these preliminary simulations show that the inductive heating method implemented in EPOCH-LTP produces plasmas similar to those expected in ICPs,

Table 3.8: Simulation parameters for an inductively heated argon plasmas proposed in Ref. 8 and sketched in figure 3.18. The corresponding results are shown in figure 3.19.

Simulation parameter	**A**	**B**	**C**	**D**
Electrode gap, L [cm]		10		
Gas species		Argon		
Gas pressure, P [mTorr/Pa]		1/0.13		
Gas temperature, T_N [K]		297		
Inductive waveform, $J(x,t)$		equation 3.11.2		
Amplitude, J_0 $[A/m^{-2}]$		100		
Frequency, f [MHz]		10		
$J(x,t)$ left bound, x_{min} [cm]	0	0	2.5	3.2
$J(x,t)$ right bound, x_{max} [cm]	5	2.5	5	4
Weight, W [10^9 part./m^2]	1	1	4	4
Grid cells, N_g		1500		
Time step, Δt [s]		10^{-11}		
Simulation time [s]		$1000/f$		
Average time [s]		$100/f$		
Initial super-part./species/cell		64		
Initial T_i [K]		297		
Initial T_e [eV]		2		
Boundary conditions		Perfect abs. walls		

i.e. constant sheaths, homogeneous density distributions and plasma potential at its floating potential, which is consistent with previous literature results using a similar inductive heating method [8, 228–230].

3.12 Parallel scalability

A strong scalability test has been carried out following Amdahl's method [241] to test the degree of parallelisation of EPOCH-LTP. For this purpose, a test problem is run varying the number of processors, N, and the wall clock time, t_N, of each simulation is measured to estimate the parallelisation speedup. The speedup of a problem running on N processors is given by

$$S_N = \frac{t_1}{t_N}, \tag{3.12.1}$$

where t_1 is the simulation time when running on one processor. The speedup can be evaluated with Amdahl's law,

$$S_A = \frac{1}{s + \frac{p}{N}} \tag{3.12.2}$$

which formulates that only the parallelised fraction of a code, p, can be reduced but not its serial fraction, s, and both fractions $s + p = 1$. This allows us to compare

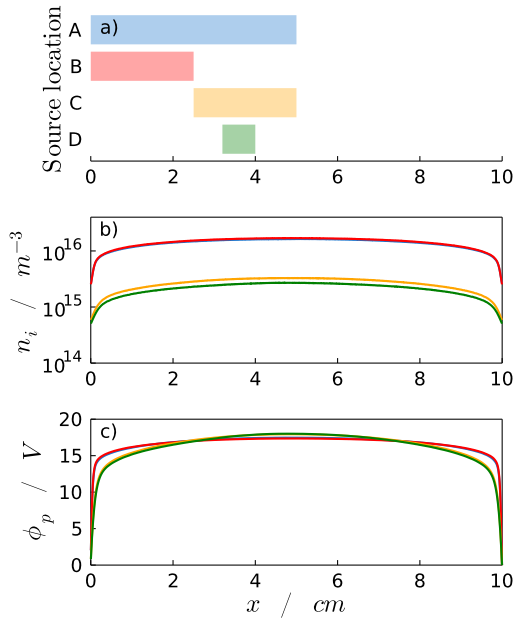

Figure 3.19: Steady state parameters for an argon plasmas test problem described in Ref. 8. In (a) the spatial extent of the inductive source $J(x,t)$, and the corresponding spatial variations of (b) ion density and (c) plasma potential. Simulation parameters listed in table 3.8.

the simulation results of S_N with S_A and to estimate the degree of parallelisation of EPOCH-LTP.

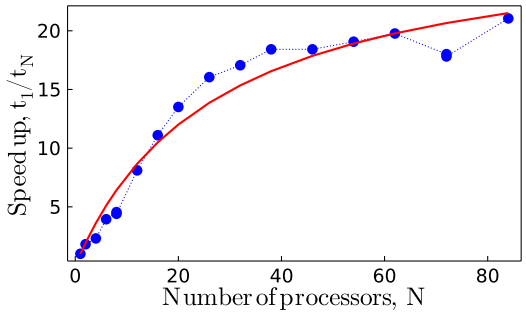

Figure 3.20: Scalability test conducted for from case 2 described in table 3.2. In blue, the results obtained with EPOCH-LTP and, in red, Amdahl's law with a 97.5% parallelization degree.

The case chosen for the scalability test is problem 2 of Ref. 9 which is described in section 3.11.1 and whose simulation parameters are listed in 3.2. This problem has been run with a number of processors between 1 and 84 on the University of York's *Viking* linux computer cluster, which runs on Intel Xeon 6138 nodes, with 40 threads on each node operating at 2 GHz, and 192 GB of RAM. The results obtained, presented in figure 3.20, show a speedup of up 21 times with N=84. The problem run at N=1 has a simulation time of t_1=1 day, 3 hours and 1 min, while for $N = 84$, t_{84} = 1 hour and 17 min. Fitting Amdahl's law, equation 3.12.2, to the speedup obtained gives a degree of parallelisation of $p = 97.5\,\%$.

3.13 Concluding remarks

In this chapter the PIC 1D model EPOCH-LTP has been developed and successfully validated.

The model has taken advantage of the highly parallelized structure of the EPOCH [217] code and has implemented the additional blocks necessary for the simulation of LTPs, namely an electrostatic field solver, a particle phase-space integrator and a Monte Carlo collision algorithm. In addition, an inductive heating method based on the work in [8] was implemented and further developed to improve its spatial resolution. In order to ensure the correct performance of the various code blocks, an extensive set of simulation test problems has been run, showing that EPOCH-LTP performs as expected.

The code development of EPOCH-LTP follows modern coding standards and a modular architecture to allow for easy expansion and flexible use. The version presented in this thesis can simulate CCPs and ICPs with different boundary configurations and allows the use of arbitrary charged and neutral species, where the latter can be modelled as background field but also as super-particles. The neutral-charged collision types included are elastic scattering, electron impact excitation and ionisation and charge-exchange, but this can readily be extended to other binary collisions.

Chapter 4

Kinetic effects of inductive heating in capacitively coupled plasmas

Capacitively coupled plasmas (CCPs) driven by two sinusoidal waveforms, a low frequency (LF) and a high frequency (HF), are commonly used for materials processing, particularly for the fabrication of integrated circuits in the semiconductor industry at the nm/atomic scale. Operating at these scales requires a high degree of control over the plasma and therefore an accurate understanding of the induced heating (IH) effects that are present when operating at HF. However, IH effects are still not well understood at the kinetic level, particularly in regard to the ion flux, its energy distribution and the angle of incidence on the target electrode, being these key parameters in material processing applications. It is therefore of interest to develop a kinetic model that helps to understand IH in order to gain further control over materials processing operations.

In this chapter, the IH model in EPOCH-LTP, described in section 3.10, is proposed as a numerical method to study the kinetic effects of IH in HF CCPs. For this purpose a HF (60 MHz) CCP operated in argon at low pressure (1 mTorr=0.13 Pa) is proposed as a case of study. Considerations about why this specific case of study are given in section 4.1 and a detailed description of the simulation setup is given in 4.2. In section 4.3, the results of a first simulation are used not only to characterise the main features of a plasma sustained by HF inductive currents, but also to understand the behaviour of the IH model. This preliminary characterisation is expanded by a parametric investigation that, in section 4.4, varies the amplitude of the inductive current and, in section 4.5, applies an additional direct current (DC) voltage bias to the target electrode. These studies build sufficient confidence to present, in 4.6, the simulation results for a dual-frequency driven CCP with an HF inductive current and a LF voltage waveform.

4.1 Considerations for 1D electrostatic simulations

The presence of inductive currents in HF CCPs, as sketched in figure 4.1, is a multi-dimensional and electromagnetic problem. Therefore, the design of a 1D simulation problem that models IH with an electrostatic solver requires some important preliminary considerations.

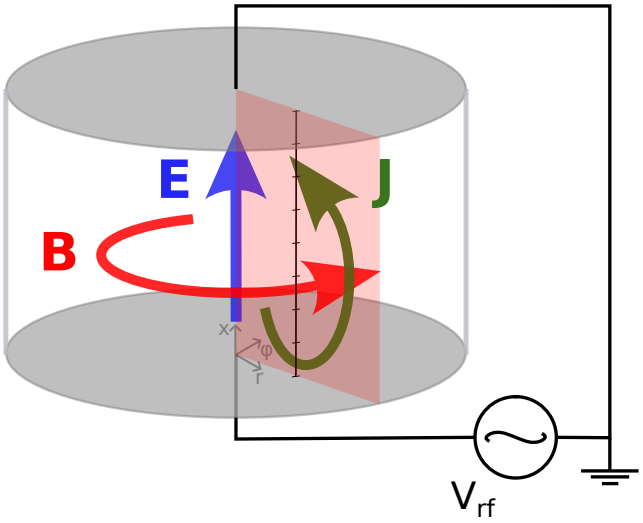

Figure 4.1: Schematic of a HF CCP simulation setup. The 1D simulation domain is the black marked line. The blue arrow is the induced electric field (E), the red arrow is the induced magnetic field (B), and the green arrow is the inductive current (J).

Firstly, the generated plasma is assumed to be axially symmetric with the inductive current pointing in the radial direction. This assumption is reasonable [73] and allows the problem to be reduced to a 2D radial section of the cylindrical reactor (red area in figure 4.1).

Secondly, the transition from capacitive to inductive heating in HF CCPs is caused by standing wave effects (SWEs) in the radial direction [73, 74]. For weak SWEs, i.e. waves with wavelengths $\lambda \sim R$, capacitive heating is maximum at the centre ($r \to 0$) and decays in the radial direction, and inductive heating is near zero at the centre and peaks at outer radial positions ($r \to R$) [74]. This cause non-homogeneous power deposition, however at low pressure, e.g. $\leq 30\,\mathrm{mTorr}$, the electron mean free path, $\lambda_{mfp,e}$, is typically larger than the reactor size, $\lambda_{mpe,e} \gg R$, and so the density profile is spatially homogeneous as it is determined by diffusion rather than by power deposition [74].

Thirdly, the sheath impedance in CCPs is inversely proportional to the driving frequency [7, Ch. 11] and, at a certain threshold frequency, $\geq 60\,\mathrm{MHz}$, the impedance reaches a minimum [61, 62]. At the limit of minimum sheath impedance, the radio frequency potential amplitude can be neglected and the plasma reactor walls can be defined as floating walls [61].

Based on these considerations, it is reasonable to model a HF (60 MHz) CCP

operated at low pressure, where inductive currents are the dominant heating mechanism, in a 1D space bounded by grounded electrodes and a perpendicular inductive current.

4.2 Simulation setup

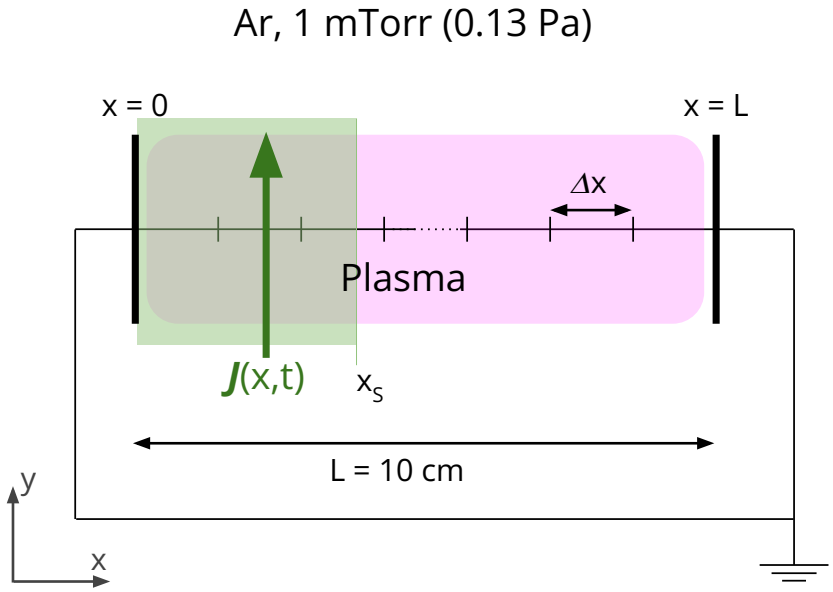

Figure 4.2: Simulation setup for a 1D HF CCP operated with argon at 1 mTorr and driven by an inductive current, $J(x,t)$, next to the left electrode.

The simulation setup consists of a 1D domain bounded by two grounded electrodes containing argon at 1 mTorr (0.13 Pa) with a perpendicular inductive heating source, as sketched in figure 4.2. Note that the simulation setup is designed to study the effects of inductive heating in isolation and therefore other effects that may be important, such as secondary electron emission, are neglected.

The heating source is defined as

$$J(x,t) = J_0(x)\sin(2\pi f t), \tag{4.2.1}$$

with driving frequency $f = 60\,\mathrm{MHz}$, and amplitude

$$J_0(x) = J_0\frac{1}{2}\left[1 - \tanh(8\pi\frac{x - x_S}{L})\right], \tag{4.2.2}$$

also profiled in figure 4.3, is applied uniformly from the left electrode until about $x_S = 2\,\mathrm{cm}$, where a hyperbolic tangent function avoids a sharp discontinuity that would otherwise cause unexpected electron heating. The penetration depth $x_S = 2\,\mathrm{cm}$ has been chosen after testing how the penetration of the source into the plasma

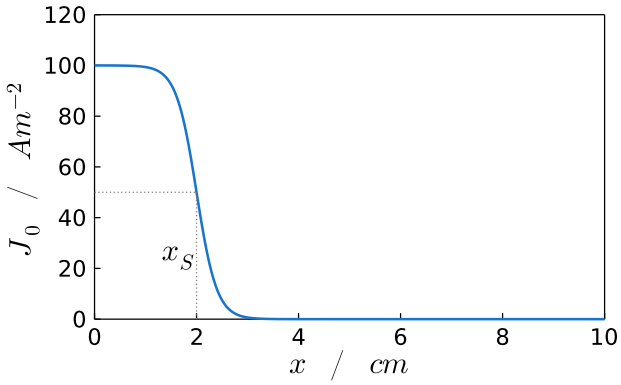

Figure 4.3: Spatial profile of the inductive current amplitude $J_0(x)$. The grey dotted line denotes the position of x_S, where J_0 falls to half its amplitude.

bulk affects the resulting plasma. It turns out that power deposition is dominated by the interaction of the displacement current with the sheath and, as described section 4.3, the source penetration into the bulk plasma plays a minor role. After this we selected an inductive heating source long enough to cover the plasma sheath. We observe that the perpendicular electric field penetrates a limited distance into the plasma edge, as expected, and its penetration depth, L_p, does not go beyond an hypothetical skin depth $\delta = c/\omega_{pe} > L_p$ for any of the cases of study.

Table 4.1: Simulation setup for a HF CCP.

Physical parameter	**Value**
Electrode gap, L [cm]	10
Gas species	Argon
Gas pressure, P [mTorr/Pa]	1/0.13
Gas temperature, T_N [K]	297
Inductive waveform, $J(x,t)$	equation 4.2.1
Amplitude, J_0 [A/m^{-2}]	100
Frequency, f [MHz]	60
Inductive source length, x_S [cm]	2
Weight, W [part./m^2]	10^9
Grid cells, N_g	2500
Time step, Δt [s]	$6 \cdot 10^{-12}$
Simulation time [s]	$7000/f$
Average time [s]	$1000/f$
Initial super-part./species/cell	256
Initial T_i [K]	297
Initial T_e [eV]	2
Boundary conditions	Perfect abs. walls

Further simulation parameters are listed in table 4.1, and the argon collisions included are as described in section 3.11.2. The simulation domain is split into 2500 cells, ensuring enough resolution for resolving the plasma Debye length, i.e. $\lambda_D \gg \Delta x$. The simulations run for 7000 cycles with a time step that satisfies the

CFL condition for electrons at 100 eV. The simulation run time is about 12 hours on 70 cores. The simulations converge after about 3000 cycles. The convergence criterion is that the number of super-particles is stable over time. The steady state and phase resolved data is extracted over the last 500-1000 cycles. These simulation parameters are used in the following sections unless otherwise explicitly stated.

4.3 Characterisation of inductive heating effects

Kinetic effects of inductive heating in HF CCPs have been characterised with the results of the simulation setup described in section 4.2. Steady state results are presented in figures 4.4, 4.5 and 4.6, and phase-resolved results, within a single 60 MHz cycle, in figures 4.7 and 4.8.

4.3.1 Steady state results

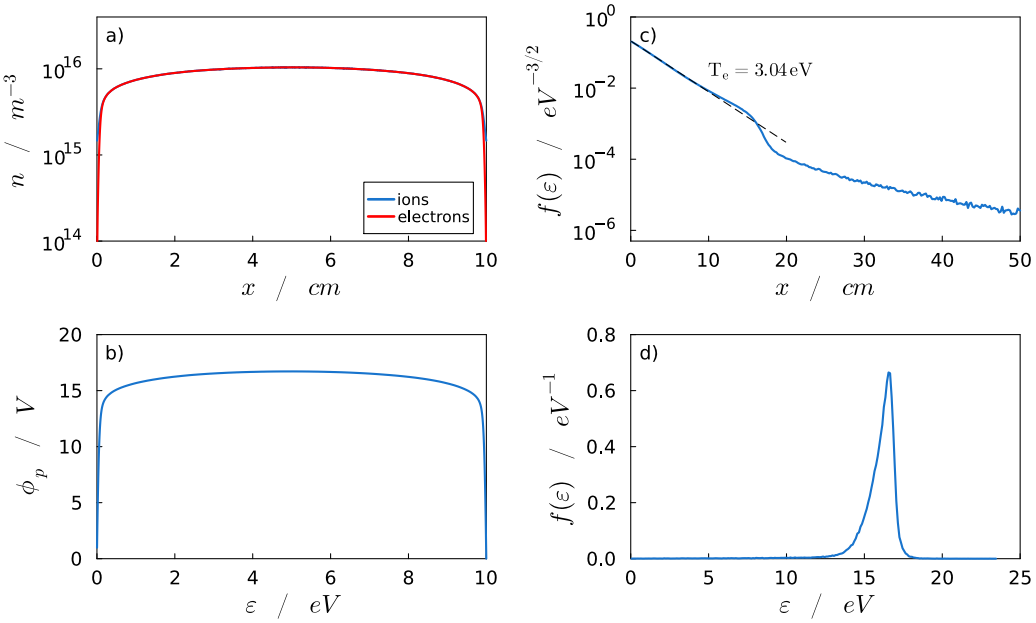

Figure 4.4: Spatial variation in the (a) electron and ion density and (b) plasma potential for the simulation setup described in section 4.2, parameters listed in table 4.1, and sketched in figure 3.18. Corresponding (c) EEPF at midplane ($x = 5\,\text{cm}$) and (d) IF-EDF at the left electrode ($x = 0\,\text{cm}$).

The steady state results, in figure 4.4(a), show an homogeneous and symmetrical plasma density distribution, with $n_e \sim 10^{16}\,\text{m}^{-3}$ at the midplane and a sheath width of about 1 mm. As observed in section 3.11.4, the profile is symmetric because of the non-local nature of electron impact ionisation processes with respect to the heating source, $\lambda_{mfp,e} > L$, and the plasma potential, in figure 4.4(b), is determined by the floating wall boundaries, $\phi_P \sim 17\,\text{V}$. The EEPF, in figure 4.4(c), shows the electron population crossing the midplane (x=5 cm) from left to right, i.e. electrons

moving away from the inductive source. Most of the electrons are found below the ionisation threshold, $\varepsilon < \varepsilon_{ion}$. These electrons are in thermal equilibrium following a Maxwellian distribution with $T_e = 3.04\,\text{eV}$. The electrons that are at higher energies, $\varepsilon > \phi_P$, present populations several orders of magnitude lower. This indicates that electrons in the bulk plasma either rapidly dissipate energy via electron-neutral collisions or are lost across the sheaths. The ion flux energy distribution function (IF-EDF) at the left electrode ($x = 0\,\text{cm}$), figure 4.4(d), shows a single peak at $\varepsilon \sim \phi_P$, indicating that the ion acceleration across the sheath is collisionless and is not significantly affected by displacement currents, which is in accordance with the experimental observations of Ref. 60.

Ion impact angle

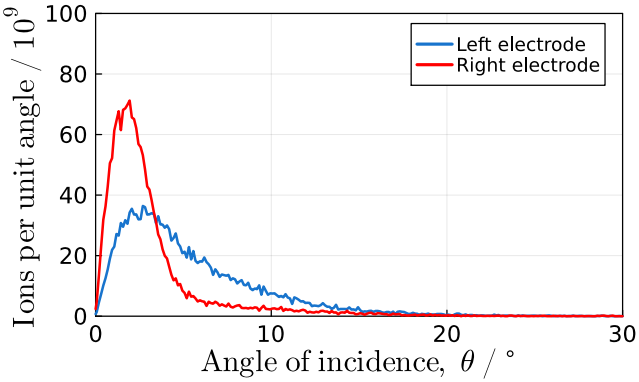

Figure 4.5: Ion flux angular distribution function (IF-ADF) at the electrodes. The angle of incidence θ is with respect to the normal direction of the electrode surface.

The ion flux angular distribution function (IF-ADF), in figure 4.5, shows the probability function of the angle of incidence θ of the ions with respect to the normal direction of the electrode surface. This shows that at the left electrode, where the inductive current is present, the ions have a larger impact angle θ than at the right electrode, indicating that the transverse inductive current has a small but non-negligible effect on the ion impact velocity.

Inductive power absorption

The inductive power, $P_{e,y} = E_y J_{e,y}$, is mostly coupled to the electrons due to its lower inertia. This is particularly high in the sheath, as shown in figure 4.6, and thus the inductive power absorption in this region determines the plasma formation. The power coupling in the bulk plasma, compared to the sheath, is negligible and therefore the penetration of the inductive current into the plasma does not play an important role in the plasma formation.

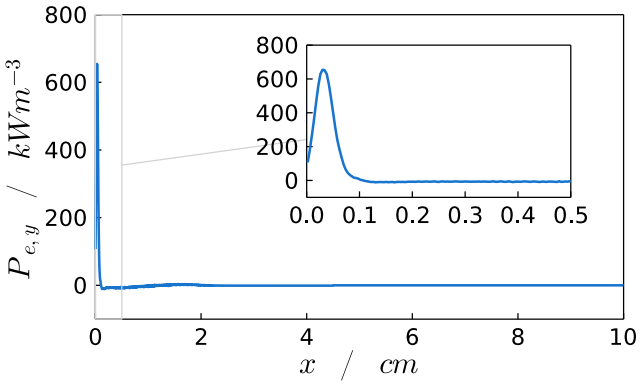

Figure 4.6: Spatial variation in the steady state electron power absorption for the simulation setup described in section 4.2.

4.3.2 Phase-resolved results

The phase-resolved results are helpful to understand the kinetic effects of IH in more detail. Therefore phase-resolved results near the left electrode ($0 \leq x \leq 5\,\text{mm}$) are shown in figure 4.7. The electron density, in figure 4.7(b), shows that the plasma sheath is steady in time and thus not perturbed by the inductive current, displayed in figure 4.7(a). The sheath is $\sim 1\,\text{mm}$ wide and, as expected, presents a sharp density drop. It is this density drop that causes the high inductive power coupling in the sheath.

Spatially localised values of the plasma density play an important role in power absorption because the response of the plasma to the inductive current $J(x,t)$ depends strongly on the number of particles present per unit volume. The interaction between the inductive current $J(x,t)$ and the plasma can be described as the plasma conduction current J_{cond} constantly adjusting to the inductive current. This adjustment is carried out by the displacement current J_{disp} which generates the electric field E_y needed to redirect the particle velocity. In case there are many particles present per unit volume, i.e. high density, the velocity redirection required at each particle is small and therefore a smaller E_y is generated. However, when there are fewer particles (lower density), the change in particle velocity is more important and higher E_y is required. It is in this case when the induced E_y field is high and the inductive power absorption $P_{e,y}$ becomes maximum. When the limit $x \to 0\,\text{mm}$ is approached, E_y grows exponentially, but n_e and $J_{e,y}$ are zero, and therefore the absorbed power decays to zero.

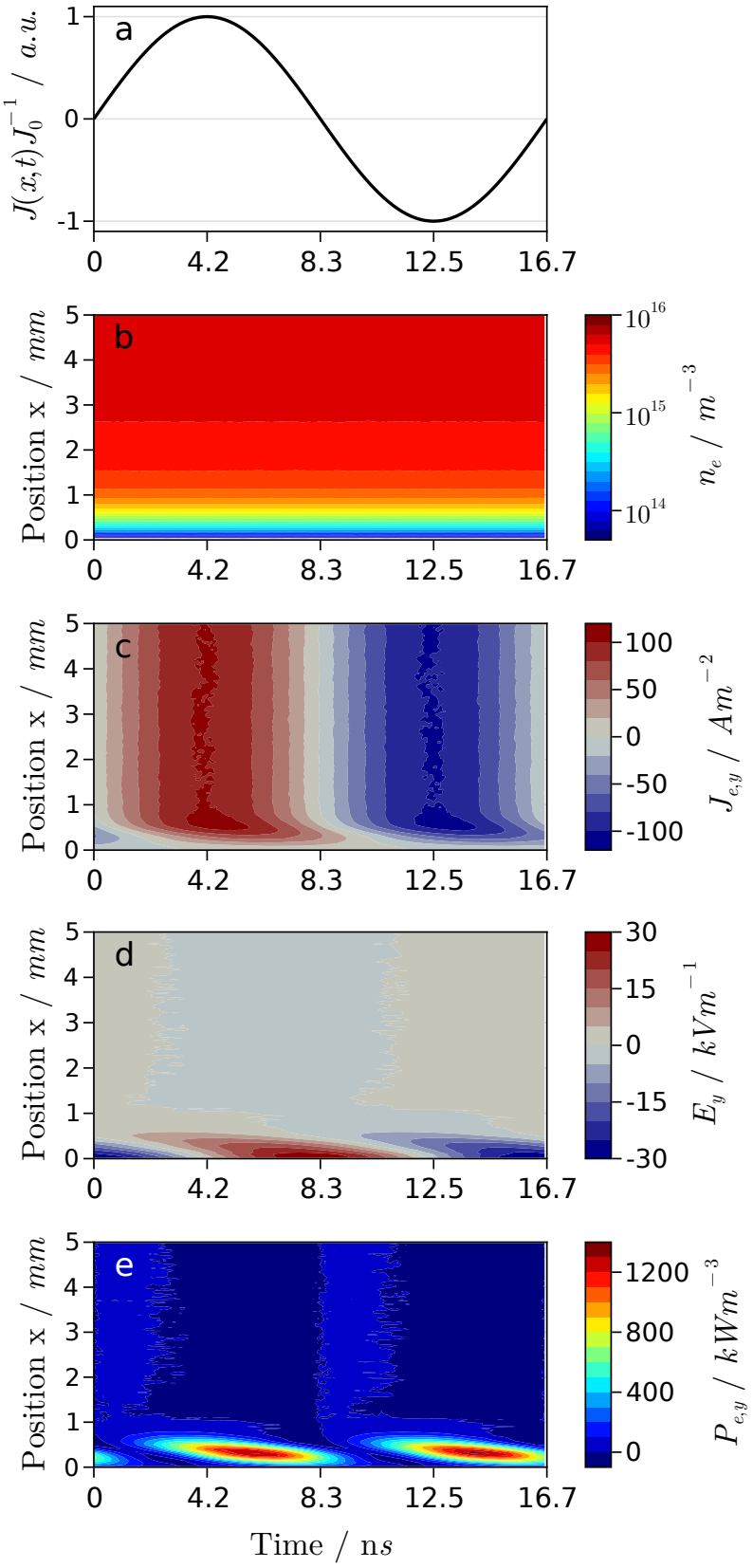

Figure 4.7: Phase resolved (a) normalised inductive current $J(x,t)$, (b) electron density n_e, (c) perpendicular electron current density $J_{e,y}$, (d) perpendicular electron field E_y, and (e) perpendicular electron power absorption $P_{e,y}$ for the simulation setup described in section 4.3. The vertical axis in panels (b)-(e) presents the first 5 mm next to the left electrode ($x = 0$ cm), as sketched in figure 3.18.

Inductive power absorption

The density in the bulk plasma, $x > 1\,\text{mm}$ in figure 4.7(b), is high enough for $J_{e,y}$ to respond rapidly to variations in $J(x,t)$. Consequently small E_y fields are induced. The temporal variation of $J_{e,y}$, shown in figure 4.7(c), presents an oscillating behaviour very similar to $J(x,t)$, and E_y, in figure 4.7(d), is small. This is confirmed in figure 4.8 where $J_{e,y}$ (red dashed line) and E_y (blue dashed line) at $x = 4\,\text{mm}$ are plotted in time. These curves show that $J_{e,y}$ in the bulk plasma responds quickly to $J(x,t)$ with little aid from E_y.

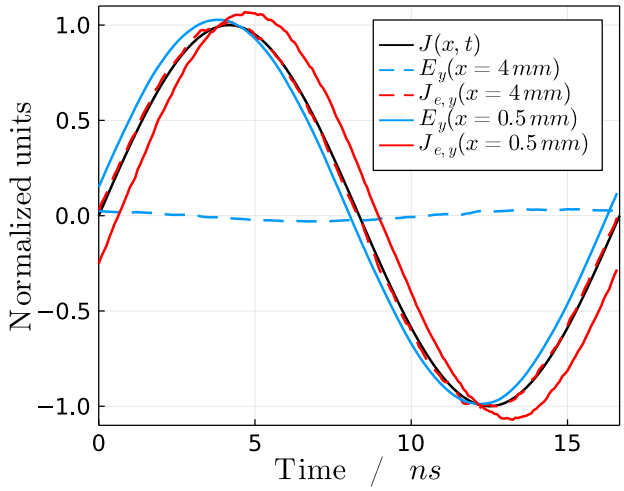

Figure 4.8: Phase resolved inductive current density (black), electron current density (red), and induced electric field (blue) at different locations. Current densities and electric fields are normalised with $J_0 = 100\,\text{A/m}^2$ and $E_0 = 8 \cdot 10^3\,\text{V/m}$, respectively.

The density in the sheath ($x < 1\,\text{mm}$) is much lower than in the bulk plasma and thus variations in $J(x,t)$ have a bigger impact on the particle velocity. Figure 4.7(d) shows that stronger E_y are formed and accelerate the electrons until $J_{e,y}$ matches $J(x,t)$. The required velocity change is large enough that the current match is not instantaneous, but a de-phase is observed between the inductive and the conduction current. The de-phase is inversely proportional to the density, as can be seen in 4.7(c) where $J_{e,y}$ reaches its maximum later in time the closer it is to the electrode, where $n_e \to 0$. This trend also correlates with the induced E_y, which is stronger with decreasing density, as shown in figure 4.7(d). Curves for $J_{e,y}$ and E_y at $x = 0.5\,\text{mm}$ are plotted in figure 4.8, showing that $J_{e,y}$ not only presents a delay with respect to $J(x,t)$ but also a slight amplitude over-shoot that is caused by the electron inertia. It is also observed that E_y is much larger than in the bulk plasma and therefore the inductive power coupling is much more efficient in the sheath, as shown in figure 4.7(e). These results are in agreement with results presented in Refs. 77, 78, where large radial electric fields and power absorption rates near the sheath were also observed.

Ion impact angle

The transit time of the ions across the sheath, $\sim 1-3\,\mu$s, is greater than the period of the drive frequency, $\sim 0.2\,\mu$s, and therefore one would expect the net transverse force exerted on the ion by E_y to average zero. However, as the ion approaches the sheath, E_y increases exponentially and so the transverse forces do not average to zero and cause a momentum deviation which affects the ion impact angle on the electrode, as shown in figure 4.5.

4.4 Current amplitude variation

This section investigates how variations in the inductive current amplitude, J_0 in equation 4.2.2, influence the plasma. A set of simulations have been undertaken where J_0 has been varied from 1 to 500 A/m^2. The super-particle weight has also been adjusted between $W = 2 \cdot 10^7$-10^{10} in order to find a balance between ensuring good statistical values [129, 174] and a reasonable computation performance. The remaining simulation parameters are as described in table 4.1 and results are shown in figures 4.9 and 4.10.

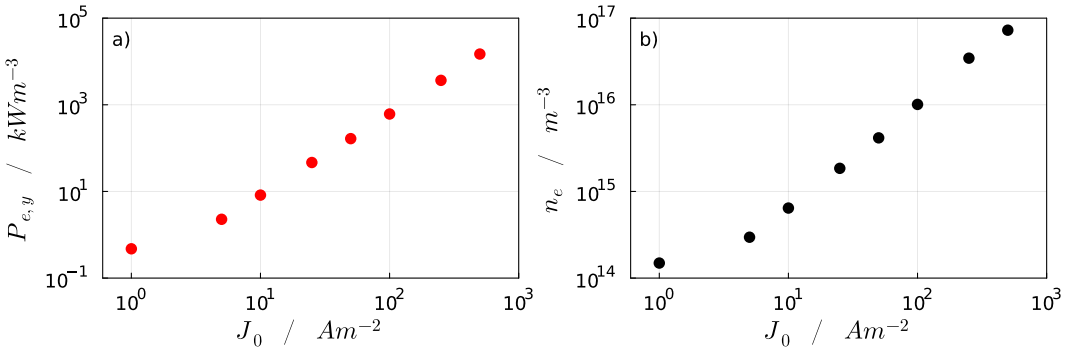

Figure 4.9: (a) Peak electron power absorption in the sheath and (b) electron density at the simulation midplane ($x = 5$ cm) under variations of J_0 for the operation conditions listed in table 4.1.

Variations of J_0 are reflected in the peak plasma density and the peak electron power absorption, as shown in figure 4.9. The remaining plasma parameters are quantitatively similar to those shown in figures 4.4 and 4.6, i.e. uniform spatial distribution, plasma potential $\phi_P \sim 17$ V, and EEPF and IF-EDF with similar features.

The electron power absorption is dominated by inductive heating at the sheath, as observed in section 4.3. Increasing J_0 however leads to larger induced displacement currents, and thus to larger induced E_y fields. Therefore higher electron power coupling rates are found in the sheath, as shown in figure 4.9(a), allowing for higher ionisation rates and a correspondingly denser plasma, as shown in figure 4.9(b).

The variation of the E_y peak values at the sheath also have an impact on the IF-ADF, as shown in figure 4.9. With increasing J_0, and thus E_y, the ion transverse acceleration is larger and therefore the impact angle θ on the electrode surface is larger.

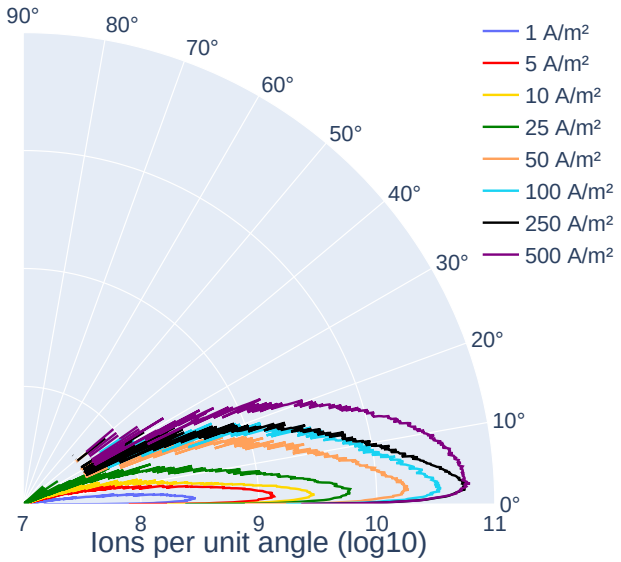

Figure 4.10: Ion flux angular distribution function (IF-ADF) at the left electrode under variations of J_0 for the operation conditions listed in table 4.1. The angle of incidence is with respect to the normal direction of the electrode surface.

Therefore, J_0 is a parameter that controls the power coupled to the plasma, with a direct impact on the electron power absorption rate and the plasma density but also on the IF-ADF.

4.5 Direct current bias variation

In plasma-based material processing applications the substrate is usually biased [7]. Therefore, in this section the combination of a DC bias voltage and HF inductive currents are investigated. For this, the left electrode is powered with a DC voltage, as sketched in figure 4.11, and has been varied between $V_{DC} = 0\,\mathrm{V}$ and $-300\,\mathrm{V}$. The simulation parameters are as listed in table 4.1 and results are shown in figures 4.12, 4.14 and 4.13.

The resulting plasmas present an asymmetry with a wider sheath at the powered electrode, as shown in figure 4.12(a). The plasma potential is $\phi_P \sim 17$ V, as in previous cases, however the sheath width grows with V_{DC} because larger potential drops must be shielded at the powered electrode, as shown in figure 4.12(b). This has an impact on the maximum energy that electrons can gain, and is reflected in the high energy tails of the EEPFs, shown in figure 4.12(c). Because of the wider

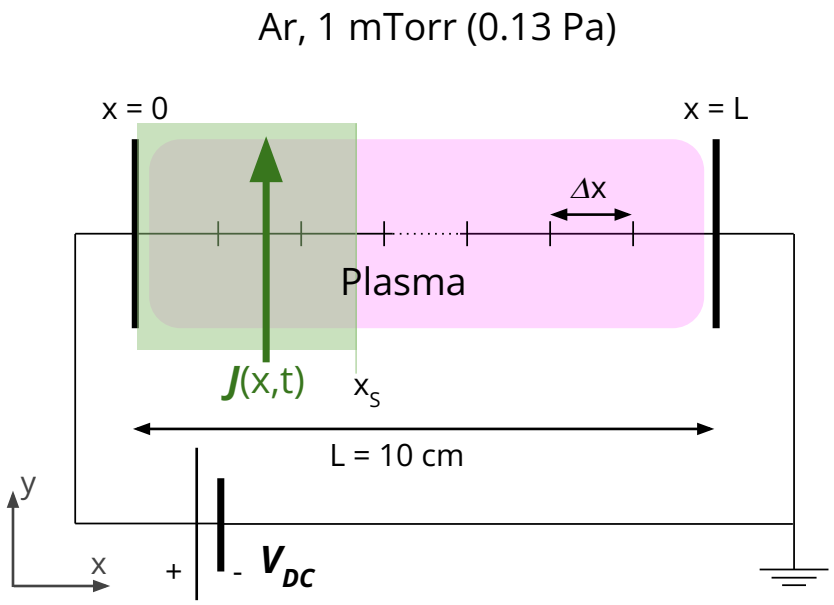

Figure 4.11: Simulation setup for an argon plasma driven with a HF inductive current $J(x,t)$ and a powered electrode with a DC voltage V_{DC}.

sheath electrons are able to penetrate deeper into the sheath, where the displacement currents are larger, and thus gain more energy from the inductive heating. This results in a population increase for $\varepsilon > \phi_P$ although it does not significantly affect the plasma production rate as these electrons are more likely to escape the plasma through the opposite sheath before undergoing any collision. The IF-EDFs, shown in figure 4.12(d), present peaks at $\varepsilon \sim \phi_P + V_{DC}$ and with lower peak population for increasing V_{DC}. This decrease in the peak population is caused by the broadening of the peak, i.e. ions crossing the sheath gain or lose a small fraction of energy because of the large displacement currents present near the electrode. The higher the V_{DC} applied the longer the ion exposure to high inductive fields while crossing the sheath and thus the wider the IF-EDF peak broadening is. However, the total ion flux at the electrode is equal for the four cases shown in figure 4.12(d) and is therefore independent from V_{DC} as expected.

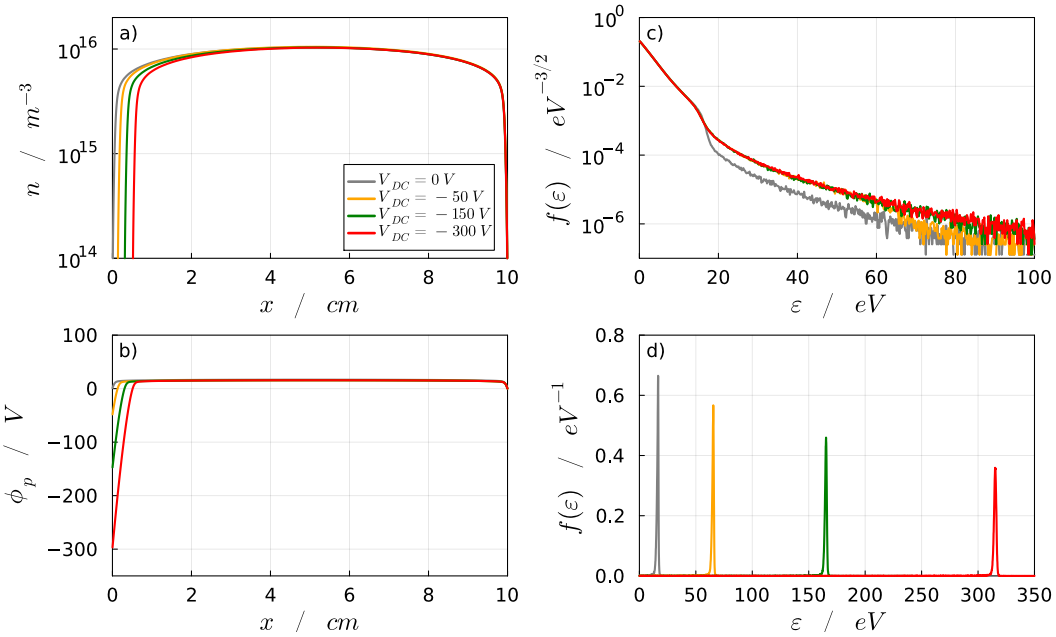

Figure 4.12: Spatial variation in the (a) electron density and (b) plasma potential for a plasma driven by HF inductive current with a DC voltage, as described in section 4.5 and sketched in figure 4.11. Corresponding (c) EEPF at the midplane ($x = 5$ cm) and (d) IF-EDF at the powered electrode.

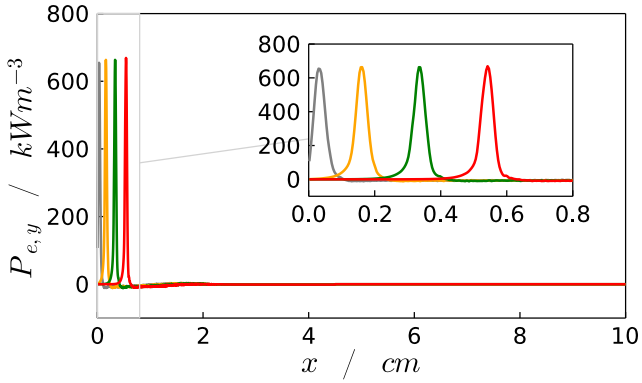

Figure 4.13: Spatial variation in the time-averaged electron power absorption under different applied V_{DC} bias voltages. The colour code is as in figure 4.12.

The electron power absorption $P_{e,y}$, as shown in figure 4.13, presents a peak in the sheath as observed before. The peak value is constant, as expected because this depends on J_0. However its location varies with V_{DC}, shifting inwards with increasing V_{DC}. This shows that the most effective power absorption location is found at the interface between the sheath and the bulk plasma, where the density is relatively low, but non-zero.

The presence of V_{DC} increases the perpendicularity of the ion impact on the electrodes, as shown in figure 4.14. This is simply due to an increase in the axial (x) direction of the ion due to larger potential drops across the sheath.

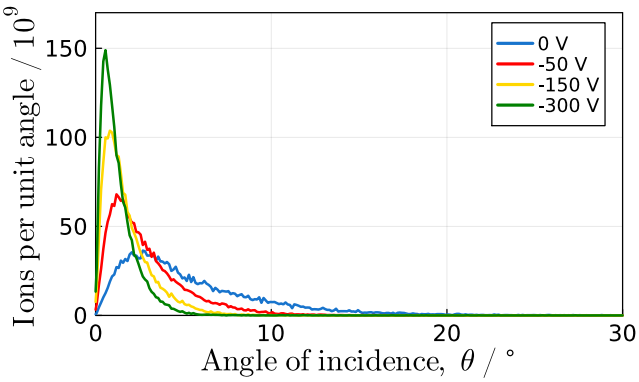

Figure 4.14: Ion flux angular distribution function (IF-ADF) at the left electrode under variations of a DC voltage bias for the operation conditions listed in table 4.1. The angle of incidence is with respect to the normal direction of the electrode surface.

In summary, the application of a DC bias introduces an asymmetry into the plasma, with a wider sheath at the driven electrode, which shifts the electron power absorption peak and improves the perpendicularity of the ion angle of impact on the electrode.

4.6 Dual-frequency capacitively coupled plasmas

In plasma-based material processing applications, HF voltage waveforms are usually combined with a low frequency (LF) voltage waveform. Therefore, in this section, the combination of a LF voltage waveform and a HF inductive current is examined. On the one hand, the LF waveform is assumed to be of sufficiently low frequency

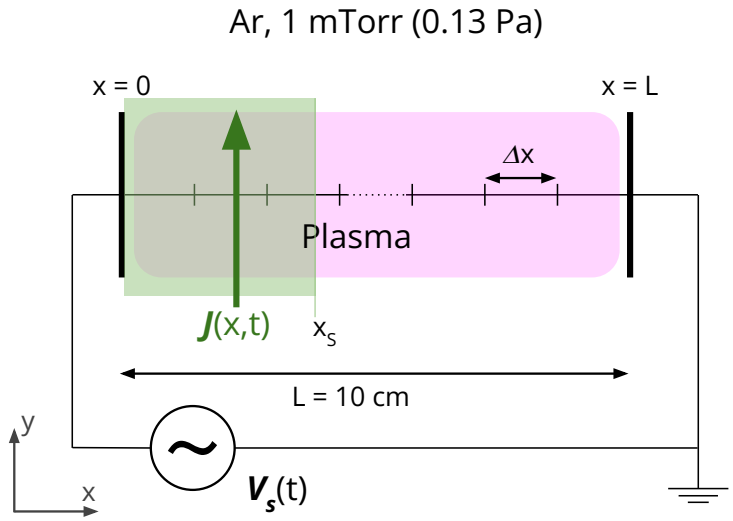

Figure 4.15: Simulation configuration for an argon plasma driven with a HF inductive current $J(x,t)$ and a LF voltage $V_s(t)$.

that its inductive heating component is negligible, i.e. purely capacitive heating. On

the other hand, the HF waveform is assumed to be of sufficiently high frequency that its capacitive heating component is negligible, i.e. a purely inductive heating source. Please note that the aim of this problem is not to make a detailed reproduction of physical reality, but to investigate the interaction between a low frequency capacitive source and a high frequency purely inductive source.

The simulation, as sketched in figure 4.15, is configured to apply, in addition to the HF IH source described in section 4.2, an oscillating voltage source to the left electrode

$$V_s(t) = V_0 \left[-1 + \sin(2\pi f_L t)\right], \tag{4.6.1}$$

at a frequency $f_L = 400\,\mathrm{kHz}$ and amplitude $V_0 = 300\,\mathrm{V}$. Note that the -1 term introduces a negative DC bias $V_{DC} = -V_0$. The remaining simulation parameters are as described in table 4.1. Steady state simulation results are presented in figures 4.16 and 4.17 and phase resolved results in figure 4.18.

4.6.1 Steady state results

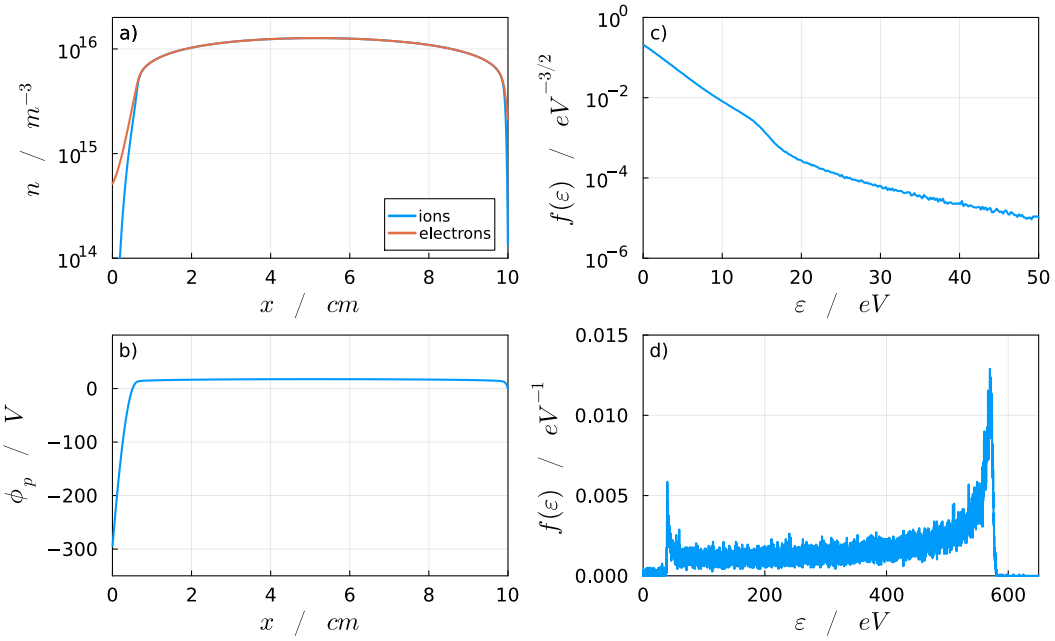

Figure 4.16: Spatial variation in the (a) electron and ion density and (b) plasma potential for an argon plasma driven by a HF (60 MHz) inductive current and a LF (400 kHz) voltage waveform. Operation conditions are listed in table 4.1 and the simulation configuration is sketched in figure 4.15. Corresponding (c) EEPF at midplane ($x = 5\,\mathrm{cm}$) and (d) IF-EDF at the powered electrode ($x = 0\,\mathrm{cm}$).

The resulting plasma presents an asymmetry, as shown in figure 4.16(a) that is caused by the DC bias term in $V_s(t)$. The plasma potential, as shown in figure 4.16(b), is $\phi_P \sim 17\,\mathrm{V}$, as in the cases presented in previous sections. The EEPF, shown in figure 4.16(c), is very similar to the distributions shown for cases with a

DC bias applied. This, as described in section 4.5, is caused by the presence of a wider sheath. The IF-EDF presents a two-peak distribution as typically found in low frequency driven CCPs [7, Ch. 11]. The IF-ADF is very similar to the case of $V_{DC} = -V_0$ in figure 4.14, showing small θ due to the bias voltage applied.

The inductive power absorbed by the electrons, the blue curve in figure 4.17, does not show the sharp peak observed in the previous cases (red curve), but is now more evenly distributed over a wider range of space. As a result, the total inductive power absorbed

$$P_{e,y}^{T} = \int P_{e,y}(x)\mathrm{d}x \tag{4.6.2}$$

is ∼10 % higher in the dual drive case. This is due to the expansion/contraction motion of the sheath induced by the LF waveform, as shown in the phase space results below.

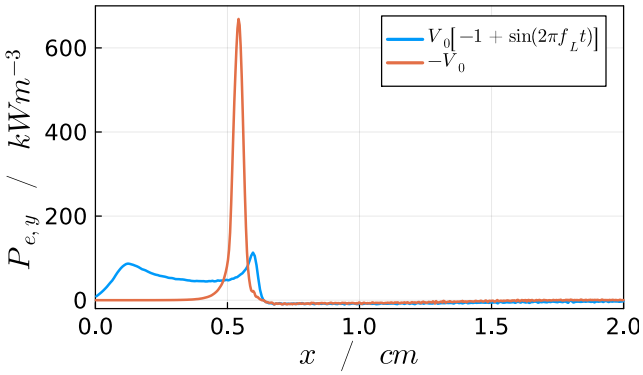

Figure 4.17: Spatial variation in the time-averaged electron power absorption for the dual LF/HF case (blue) and the HF case with a V_{DC} bias voltage (red) described in section 4.5.

4.6.2 Phase-resolved results

The phase-resolved results show that the LF voltage waveform, black line in figure 4.18(a), is responsible for the expansion and collapse of the sheath. The electron density, presented in figure 4.18(b), shows that the sheath is completely expanded when $V_s(t)$ is at its minimum ($t = 0$ and $2.5\,\mu$s), and collapses when $V_s(t) = 0$ V ($t = 1.25\,\mu$s). The inductive power absorption peaks at the sheath edge, as described in section 4.5, and therefore a high power absorption trace that follows the sheath motion is observed in figure 4.18(c).

The total inductive power absorbed $P_{e,y}^{T}$ is especially high when the sheath is collapsed, as shown in figure 4.18(a) (red solid line) where $P_{e,y}^{T}$ is integrated between the limits $x = 0\,$mm and $x = 8\,$mm. When the sheath shrinks ($0 < t < 1.25\,\mu$s) it allows a plasma expansion that lowers the plasma density near the sheath. This widens the extent over which the displacement current is important, and thus inductive power absorption becomes more effective. When the sheath is fully collapsed

($t \sim 1.25\,\mu$s), the extension over which the power absorption is important is at its maximum, and the electrons gain most of their energy. The mean electron energy, shown in figure 4.18(d), shows that electrons gain more energy while the sheath is collapsing and peak when the sheath is fully collapsed. This causes an increase in the ionisation rate, by a factor of about ~ 5, as shown in figure 4.18(e). When the sheath begins to expand ($t > 1.25\,\mu$s), the opposite effect occurs, i.e. the plasma contracts, the density increases and the effective power absorption length narrows and thus the inductive current couples less energy.

To sum up, the interaction of a HF inductive current and a LF voltage demonstrates interesting behaviour as dynamics at very different time scales are able to create synergies that enhance the inductive power coupling and plasma generation. This is clear when comparing results with the $V_{DC} = -300\,\mathrm{V}$ case in section 4.5. The presence of a LF voltage increases the total power absorption by 30% and the plasma density increases by approximately 20%.

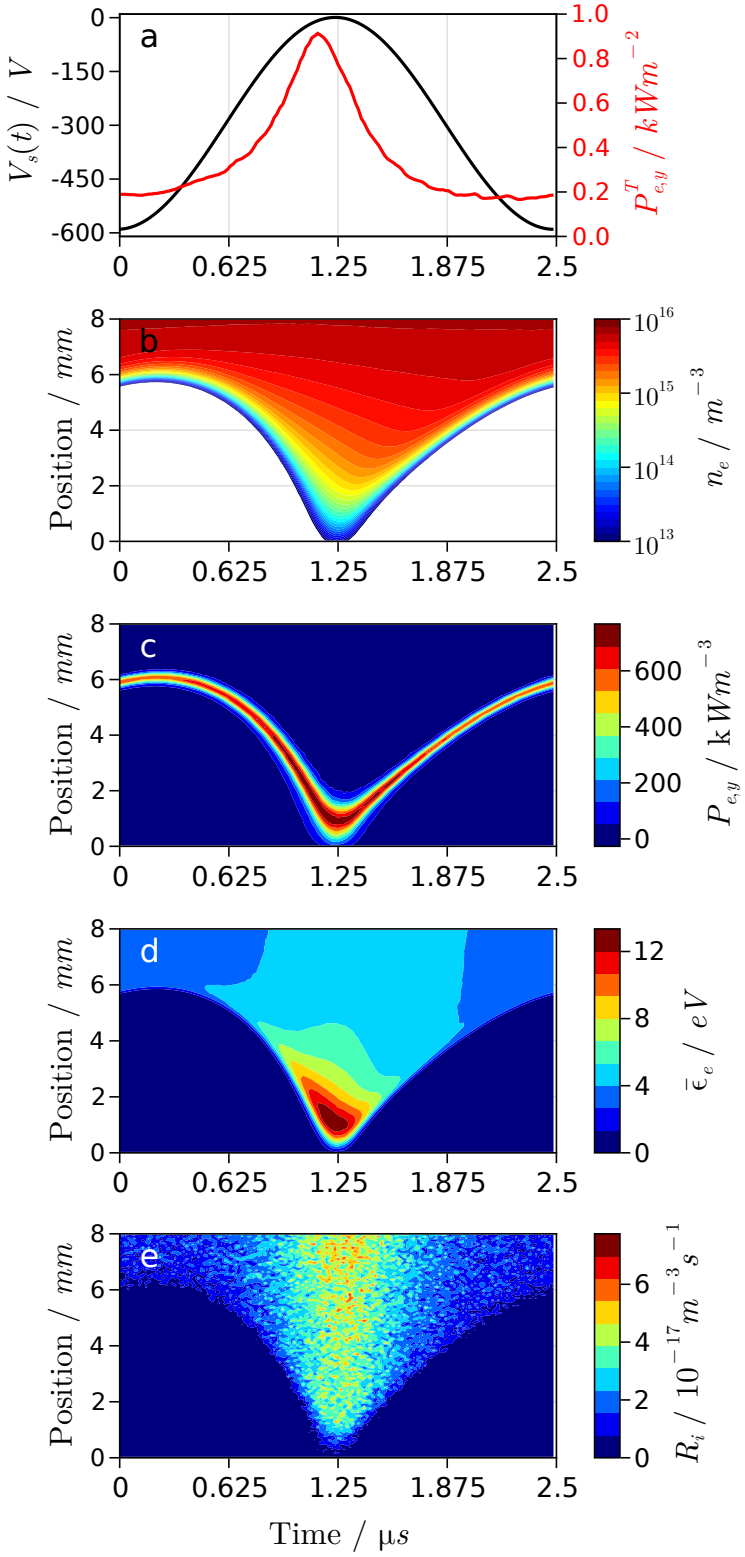

Figure 4.18: Phase resolved (a) LF voltage waveform $V_s(t)$ (black) and total electron power absorption $P^T_{e,y}$ (red), (b) electron density n_e, (c) electron perpendicular power absorption $P_{e,y}$, (d) electron mean energy $\bar{\varepsilon}_e$, and (e) ionisation rates R_i for a plasma driven by a HF inductive current and a LF voltage waveform, as described in section 4.6 and sketched in figure 4.15. The vertical axis in the heatmap plots present the first 8 mm next to the powered electrode.

4.7 Concluding remarks

The IH model implemented in EPOCH-LTP is proposed to study kinetic inductive heating effects in HF CCPs. EPOCH-LTP has been used to simulate a CCP operated in argon at 1 mTorr and driven at 60 MHz. The simulation results show that transverse inductive currents in the sheath dominate the inductive heating and thus the plasma formation. The plasma density is directly proportional to the size of the inductive current. The application of a DC bias shifts the location of the inductive heating peak. When the HF inductive current is combined with a LF voltage waveform the inductive heating is controlled by the sheath dynamics and this improves the plasma generation efficiency. This is an interesting result as dynamics at very different time scales are able to create synergies that enhance the inductive power coupling and thus the plasma density.

These results can serve as a basis for further investigation of kinetic inductive heating effects using 1D electrostatic PIC codes. Apart from the parameters studied in this work, there is a wide range of parameters that would be useful to investigate to understand inductive heating in more detail, such as the driving frequency, the gas pressure, the spatial distribution of the inductive source, and the synergies between LF and HF waveforms.

Chapter 5

Zero-dimensional chemical kinetics global model for argon and oxygen

This chapter presents the design and development of a zero-dimensional (0D) chemical kinetics global model (GM) with collisional and radiative processes for argon (Ar) and oxygen (O_2). This 0D GM allows computationally inexpensive self-consistent simulations of Ar/O_2 plasma chemical and radiative processes, which is used in the following chapter for the investigation of vacuum ultraviolet (VUV) radiation.

The main features and structure of the GM model is described in section 5.1. This is followed in section 5.2 by a description of the species and reaction scheme implemented in the GM. In sections 5.3 the mass continuity equation is described and, in section 5.4 the electron energy continuity equation. The continuity equations require considerations about the ion flux interaction with the reactor walls, which is described in section 5.5, the diffusion of neutral species to the walls, described in section 5.6, and atomic energy transitions and radiative processes, which are described in section 5.7.

5.1 Main features and structure of the global model

The GM of this thesis has been designed and developed for modelling cylindrical plasma reactors, of length L and radius R, to which power P_{in} is coupled inductively. Although this work only considers argon and oxygen plasmas, the code can work with any species and associated chemical reactions provided in advance. As a complimentary note, the model is coded with the programming language Julia [242].

The numerical execution structure consists of an initialization of the simulation environment and a five-step cycle, shown in figure 5.1, that updates the simulation system in time.

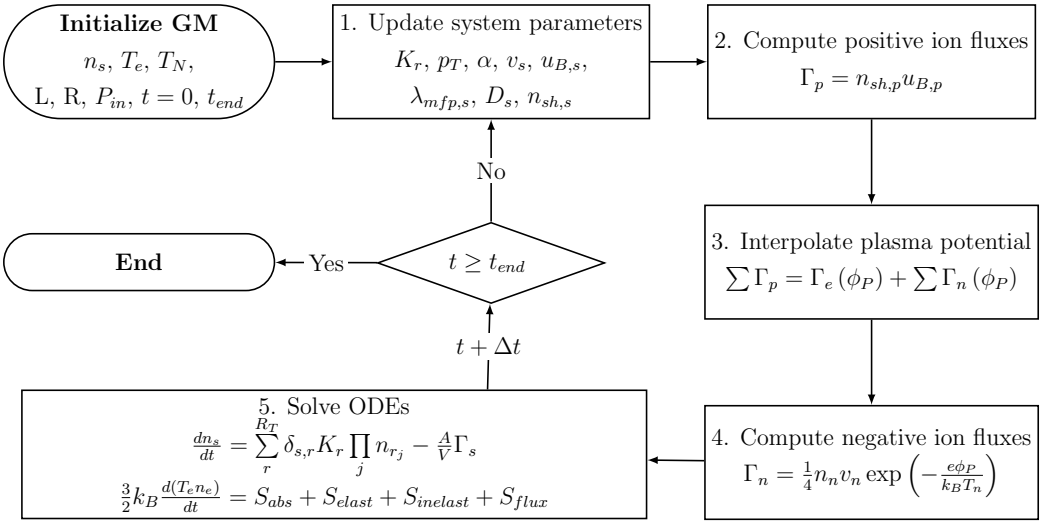

Figure 5.1: Flowchart of the 0D plasma-chemical kinetics GM. Steps 2-4 are described in section 5.5 and step 5 in sections 5.3 and 5.4.

The initial conditions for the density and temperature of each species, as well as the length L and radius R of the reactor, the applied power P_{in} and the simulation time length t_{end} must be defined in advance. After initialising the simulation parameters, the execution of the cycle computes a new electron temperature and species densities values and advances in time by Δt. The simulation ends when the final time condition is reached, $t \geq t_{end}$. The cycle consists of the following steps

1.- Computation of system parameters necessary for later steps: reaction rate coefficients K_r, species mean-free-path $\lambda_{mfp,s}$, diffusion coefficients D_s, electronegativity α, total pressure p_T, thermal speed v_s, Bohm velocity $u_{B,s}$ and number density at the plasma sheath edge $n_{sh,s}$.

2-4.- Computation of charged particle fluxes to the system walls, Γ, and plasma potential, ϕ_P. This is described in more detail in section 5.5.

5.- Solve the system of first-order ordinary differential equations (ODEs) formed by mass and energy continuity equations. The ODE solver *Rosenbrock23* in

the *DifferentialEquations* library [243] is used for this purpose. A detailed description of the mass and energy equations is found in sections 5.3 and 5.4, respectively.

5.2 Species and plasma-chemical reaction scheme

The species list included in the model is based on previous works on the simulation of argon and oxygen containing plasmas [15, 21, 114], and is listed in table 5.1.

Table 5.1: Species included in the numerical model.

Species	**Atomic level**
e	
Ar	
Ar^+	
Ar(4p)	$3s^2\ 3p^5(2P^0_{3/2})4p$, $3s^2\ 3p^5(2P^0_{1/2})4p$
Ar^m	$3s^2\ 3p^5(2P^0_{3/2})4s_2$, $3s^2\ 3p^5(2P^0_{1/2})4s_0$
Ar^r	$3s^2\ 3p^5(2P^0_{3/2})4s_1$, $3s^2\ 3p^5(2P^0_{1/2})4s_1$
O_2	
O_2^+	
O_2^-	
$O_2(a^1\Delta_u)$	
$O_2(b^1\Sigma_u^+)$	
O	$2s^2\ 2p^4\ {}^3P_{2,1,0}$
O^+	
O^-	
$O(^1D)$	$2s^2\ 2p^4\ {}^1D_0$
$O(^1S)$	$2s^2\ 2p^4\ {}^1S_0$
$O(^3S)$	$2s^2\ 2p^3\ (^3S^0)\ 3s\ {}^3S^0_1$
$O(^5S)$	$2s^2\ 2p^3\ (^3S^0)\ 3s\ {}^5S^0_2$
$O(^3P)$	$2s^2\ 2p^3\ (^3S^0)\ 3p\ {}^3P_{1,2,0}$
$O(^5P)$	$2s^2\ 2p^3\ (^3S^0)\ 3p\ {}^5P_{1,2,3}$
O_3	
$O_3(\nu)$	
O_3^+	
O_3^-	
O_4	
O_4^+	
O_4^-	

The plasma-chemical reaction scheme included in the GM is a compendium of reactions used in [15, 194, 244] and the references therein. The reaction scheme con-

sists of a set of electron-oxygen reactions, in table A.1, electron-argon, in table A.2, oxygen-oxygen, in table A.3, argon-argon, in table A.4, oxygen-argon, in table A.5, and recombination reactions, in table A.6. Moreover, additional reactions are included for ion-wall interactions, in table 5.2, neutral-wall interactions, in table 5.3, atomic level transitions, in table 5.4, and oxygen reactions with radiative cascading processes, in table A.7. Altogether there are a total of $R_T = 393$ reactions included. As is noted in the appendices, reaction rate coefficients for electron impact reactions are implemented as functions of electron temperature, assuming a Maxwellian electron energy distribution function.

Reactions #13, 31, 50 (in table A.1) and 106 (table A.2) are electron-neutral elastic collisions. Reactions #14, 32 and 51 (table A.1) are rotational excitations, and #15-20, #33-38, and #52-57 (table A.1) are vibrational excitations [114], whose products are not explicitly simulated and therefore these reactions only act as an energy gain or loss mechanism. The reactions #62 (table A.1) and #141 (table A.2) has as product the vibrational state of O_2 but this is not included in the model and is replaced by the O_2 ground state.

The interactions between electrically charged particles and the reactor walls are described in more detail in section 5.5 and neutral-wall reactions are described in section 5.6. Besides, atomic level transitions and radiative processes, especially in oxygen, are described in section 5.7.

5.3 Mass balance equations

The basic formulation of the equations used in the model is adapted from Refs. [21, 194]. The GM includes a mass balance equation for each species s, in table 5.1,

$$\frac{dn_s}{dt} = \sum_{r}^{R_T} \delta_{s,r} K_r \prod_j n_{r_j} - \frac{A}{V}\Gamma_s. \tag{5.3.1}$$

where the term on the left hand side (lhs) represents the time variations of the density of the s-th species, n_s, the first term on the right hand side (rhs) accounts for density variations caused by collisional reactions, and a second term is added to account for mass variations due to interactions with the wall.

The first term on the rhs is obtained taking the 0^{th} momentum of equation 2.2.2 and accounts for the particle gain, or loss, due to the collisions with other species. In the model described here this includes the R_T reactions listed in tables A.1, A.2, A.3, A.4, A.5, A.6, 5.3, 5.4 and A.7. The mass variation caused by the r-th reaction is the product of the rate coefficient K_r with the densities of the j reacting species, n_{r_j}. The factor $\delta_{s,r}$ is an integer that reflects the particle balance of species s in reaction r. For instance, in reaction #1 ($e + O \rightarrow 2e + O^+$ in table A.1) electrons

have a positive balance $\delta_{1,e} = 1$, atomic oxygen a negative balance $\delta_{1,\mathrm{O}} = -1$, and oxygen ions a positive balance $\delta_{1,\mathrm{O}^+} = 1$. Essentially, $\delta_{s,r} < 0$ represents a mass loss, $\delta_{s,r} > 0$ gain, and $\delta_{s,r} = 0$ equilibrium.

The second term on the rhs is an additional term that accounts for mass variations caused by particle fluxes of charged particles to the system walls, Γ_s, that are described in more detail in section 5.5. The surface area A and system volume V are determined by the cylindrical shape of the reactor, i.e. $A = 2\pi(R^2 + RL)$ and $V = \pi R^2 L$.

5.4 Electron energy conservation equation

The energy balance equation accounts for changes in species temperatures as a function of time. The energy balance equation is only solved for electrons, while the temperatures of heavy particles are assumed to be constant in time. Here, the shape of the energy distribution function (EDF) of electrons is assumed to be Maxwellian. The potential limitations of this assumption are discussed further later. The energy equation for electrons takes the following form

$$\frac{3}{2}k_B\frac{d(T_e n_e)}{dt} = S_{abs} + S_{elast} + S_{inelast} + S_{flux}, \tag{5.4.1}$$

where the electron temperature T_e is used as energy reference parameter, k_B is the Boltzmann constant, n_e is the electron density, S_{abs} is the input power absorbed per unit volume, S_{elast} represents energy changes caused by elastic collision processes, $S_{inelast}$ are energy changes caused by inelastic and superelastic collision processes, and S_{flux} is related to the kinetic energy lost by electron and ion fluxes through the plasma sheath.

The input power absorption rate in equation 5.4.1

$$S_{abs} = \frac{P_{in}}{V}, \tag{5.4.2}$$

represents the external inductive power P_{in} that is coupled to the electrons.

The term S_{elast} represents the electron energy gains and losses caused by elastic collisions, of the type $e + N \rightarrow e + N$ where N is a neutral species,

$$S_{elastic} = -3\sum_{l}^{R_{elast}} \frac{m_e}{m_{N_l}} k_B \left(T_e - T_{N_l}\right) K_l n_e n_{N_l}, \tag{5.4.3}$$

where R_{elast} is the set of elastic collisions present in the collision model, K_l is the rate coefficient of the l-th elastic scattering process, N_l is the neutral species involved in the process, and m_N and T_{N_l} its mass and temperature, respectively.

Gains or losses of energy caused by inelastic and superelastic collision processes

are accounted as

$$S_{inelast} = -\sum_{r} E_{thr,r} K_r \prod_{r_j} n_j. \tag{5.4.4}$$

where $E_{thr,r}$ is the energy released, or absorbed, by the r-th collision.

The last term in equation 5.4.1 accounts for the kinetic energy of electrons and positive ions that pass through the sheath and are lost at surfaces [7]

$$S_{Flux} = -\frac{A}{V}\left[2k_B T_e \Gamma_e + \sum_{p} \Gamma_p \left(\frac{1}{2} k_B T_e + q_p \phi_P\right)\right], \tag{5.4.5}$$

where Γ is the particle flux at the system walls, the subscript p is for positive ions, ϕ_P is the plasma potential, and q_p is electric charge. The first term on the right hand side accounts for the kinetic energy taken to surfaces by electrons that have passed through the sheath and the second term accounts for the kinetic energy taken to surfaces by positive ions that have passed across the sheath [7, Ch. 6]. How particle fluxes crossing the sheath are handled in the GM is described in more detail in the following section.

5.5 Ion fluxes to the reactor walls

Ion fluxes crossing the plasma sheaths and reaching the reactor walls play an important role in the mass and energy balance equations. Moreover, ion fluxes are also important to compute the plasma potential ϕ_P, which is required for the electron energy equation and for fluxes of negatively charged species. Positive ion (subscript p) fluxes are computed differently from negative ion (subscript n) and electron (subscript e) fluxes.

Positive ions, whose fluxes are given by

$$\Gamma_p = n_{sh,p} u_{B,p}, \tag{5.5.1}$$

where $n_{sp,p}$ is the density at the sheath, need to enter the sheath with the Bohm velocity $u_{B,p} = \sqrt{k_B T_e / m_p}$ in order to be able to reach the walls. The effective density at the sheath edge [7, 112]

$$n_{sh,p} = \frac{R^2 h_{L,p} + RL h_{R,p}}{R^2 + RL} n_p \tag{5.5.2}$$

is determined from bulk plasma densities, n_p using geometrical factors R and L as well as the parameters [199]

$$h_{\{R,L\},p} = \left[\left(\frac{h_{\{R,L\}0}}{1 + 3\alpha/2}\right)^2 + h_c^2\right]^{1/2} \tag{5.5.3}$$

where

$$h_{R0,p} = 0.8\left[4 + \frac{\eta R}{\lambda_{mfp,p}} + \left(\frac{0.8Ru_{B,p}}{\chi_{01}J_1(\chi_{01})D_{a,p}}\right)^2\right]^{-1/2}, \tag{5.5.4}$$

$$h_{L0,p} = 0.86\left[3 + \frac{\eta L}{2\lambda_{mfp,p}} + \left(\frac{0.86Lu_{B,p}}{\pi D_{a,p}}\right)^2\right]^{-1/2}, \tag{5.5.5}$$

$$h_c = \frac{1}{\gamma_-^{1/2} + \gamma_+^{1/2}[n_{*,p}^{1/2}n_+/n_-^{3/2}]}. \tag{5.5.6}$$

These parameters enable the computation of the sheath edge density from very low pressure regimes, where the ion mean free path is much larger than the system dimensions $\lambda_{mfp,p} \gg (L, R)$, to high pressures, where $\lambda_{mfp} \ll T_e/T_p(R, L)$ [7, 197]. The $h_{\{R,L\}0}$ parameters make use of $\chi_{01} \simeq 2.405$, the first zero of the zero order Bessel function J_0, and the Bessel function 1 of the first kind J_1. The plasma electronegativity is given by

$$\alpha = \frac{1}{n_e}\sum_n n_n. \tag{5.5.7}$$

The temperature ratio between positive and negative ions is given by

$$\eta = \frac{2T_+}{T_+ + T_-}, \tag{5.5.8}$$

where the subscript $+$ and $-$ refer to all positive and negative ion species, respectively. The ambipolar diffusion coefficient is calculated as

$$D_{a,p} = D_p\frac{1 + \gamma_p + \gamma_p\alpha}{1 + \gamma_p\alpha} \tag{5.5.9}$$

where

$$\gamma_p = T_e/T_p, \tag{5.5.10}$$

is the temperature ratio between electrons and the ion species.

The diffusion coefficient for ions (and also for neutrals, as discussed in the next section) is defined as

$$D_p = \left(\sum_s \frac{1}{D_{ps}}\right)^{-1} \tag{5.5.11}$$

which represents an approximation for the diffusion of a species in a multicomponent mixture. Here, $D_{ps} = k_B T_N/\mu_{ps}\nu_{ps}$ is the binary diffusion coefficient [7, Ch. 9] between the given ion p and the s-th heavy mass species in the system, i.e. species with $m_s \gg m_e$. Besides, $\nu_{ps} = n_s\sum_r K_r$ is the total collision frequency between p and s, and μ_{ps} is the reduced mass.

The h_c parameter makes use of $\gamma_- = T_e/T_-$ and $\gamma_+ = T_e/T_+$, which in our case

are the same as the temperature of ions and neutrals are equal $T_- = T_+ = T_N$, and

$$n_{*,p} = \frac{15}{56}\frac{\eta^2}{K_{rec}\lambda_{mfp,p}}v_p, \tag{5.5.12}$$

where K_{rec} is the total rate coefficient of the recombination reactions listed in table A.6.

The total mean-free-path is estimated as

$$\lambda_{mfp,p} = \frac{1}{\sum_s n_s \sigma_{ps}^T} \tag{5.5.13}$$

where $\lambda_{mfp,ps} = 1/n_s\sigma_{ps}^T$ and σ_{ps}^T is the total collision cross-section between species p and s. Please note that s refers only to heavy mass species, and therefore the corresponding neutral-ion and ion-ion collisions listed in tables A.3-A.6, as well as elastic scattering, resonant charge-exchange and Coulomb collision processes are included in the calculation of the mean-free-path. The cross-section of the reactions in the above-mentioned tables are approximated with $\sigma_{ps} \simeq K_r/v_{ps}$ [7, Ch. 3] where $v_{ps} = \sqrt{8k_BT_N/\pi\mu_{ps}}$ is the mean speed of relative motion [7, Ch. 9]. The cross-section of elastic scattering and resonant charge-exchange are extracted from [7, 21, 245], if available, otherwise they are calculated using the hard sphere model, $\sigma_{ps} = \pi(r_p + r_s)^2$, using the following atomic, and molecular, radii: $r_{\mathrm{Ar}} = 188\,\mathrm{pm}$, $r_{\mathrm{O}} = 152\,\mathrm{pm}$, $r_{\mathrm{O}_2} = r_{\mathrm{O}_3} = r_{\mathrm{O}_4} = 197\,\mathrm{pm}$. For Coulomb collisions, a constant cross-section estimate of $5 \cdot 10^{-19}\,\mathrm{m}^2$ is used [199].

Negative ion fluxes to surfaces are described by the expression given in [113]

$$\Gamma_n = \frac{1}{4}n_n v_n \exp\left(-\frac{e\phi_P}{k_BT_n}\right), \tag{5.5.14}$$

where the subscript n refers to negative ion species. The flux of these species are restricted to those particles with energies high enough to overcome the potential barrier of the plasma sheath, which is determined in ICPs by the plasma potential with respect to a floating wall. Note that $v_n = \sqrt{8k_BT_n/\pi m_n}$ is the thermal speed of the n-th negative ion. The same expression as in equation 5.5.14 is valid for the electron flux, Γ_e. To determine Γ_n and Γ_e the plasma potential ϕ_P must be known, which is obtained by solving the flux balance equation

$$\sum_p q_p\Gamma_p + q_e\Gamma_e + \sum_n q_n\Gamma_n = 0, \tag{5.5.15}$$

which states that the total particle flux, of positive, negative ions and electrons, must balance to ensure quasi-neutrality. The flux balance equation is solved for ϕ_P using an iterative method. ϕ_P is then used in the flux term of the energy balance

equation, equation 5.4.5, and for computing the flux of negative ions and electrons, equation 5.5.14.

In order to maintain mass conservation in the system, both positive and negative ions are considered to be neutralised when they get in contact with the wall [21]. These reactions are listen in table 5.2, such that $A/V\Gamma_s = \delta_{s,r} n_s K_r$ [21], and are included in the mass balance (second term on rhs of equation 5.3.1) for the species on both left and right sides of the neutralisation reactions. Note that the ion-wall neutralisation reactions in Ref. [21] have been extended to the ion species included in this work.

Table 5.2: Ion-wall reactions.

#	**Process**	K_r [s^{-1}]	**Ref.**
343	$O^+ \rightarrow O$	$2u_{B,O^+}\left(R^2 h_{L,O^+} + RLh_{R,O^+}\right)/\left(R^2 L\right)$	21
344	$O_2^+ \rightarrow O_2$	$2u_{B,O_2^+}\left(R^2 h_{L,O_2^+} + RLh_{R,O_2^+}\right)/\left(R^2 L\right)$	21
345	$O_3^+ \rightarrow O_3$	$2u_{B,O_3^+}\left(R^2 h_{L,O_3^+} + RLh_{R,O_3^+}\right)/\left(R^2 L\right)$	21[a]
346	$O_4^+ \rightarrow 2O_2$	$2u_{B,O_4^+}\left(R^2 h_{L,O_4^+} + RLh_{R,O_4^+}\right)/\left(R^2 L\right)$	21[a]
347	$Ar^+ \rightarrow Ar$	$2u_{B,Ar^+}\left(R^2 h_{L,Ar^+} + RLh_{R,Ar^+}\right)/\left(R^2 L\right)$	21
348	$O^- \rightarrow O$	$(A/4V)v_{O^-} \exp\left(-e\phi_P/k_B T_{O^-}\right)$	113
349	$O_2^- \rightarrow O_2$	$(A/4V)v_{O_2^-} \exp\left(-e\phi_P/k_B T_{O_2^-}\right)$	113[b]
350	$O_3^- \rightarrow O_3$	$(A/4V)v_{O_3^-} \exp\left(-e\phi_P/k_B T_{O_3^-}\right)$	113[b]
351	$O_4^- \rightarrow 2O_2$	$(A/4V)v_{O_4^-} \exp\left(-e\phi_P/k_B T_{O_4^-}\right)$	113[b]

[a] The expression is of the same form given in Ref. 21, but is extended here to all positively charged species.
[b] The expression is of the same form given in Ref. 113, but is extended here to all negatively charged species.

5.6 Neutral particle diffusion to the reactor walls

Neutral particle diffusion within the plasma reactor plays an important role as it determines the flux of neutral species that interact with the reactor walls [7, 112]. This is important because metastable species reaching the walls are de-excited to ground state, and atomic oxygen recombines into molecular oxygen. Therefore, neutral-wall interactions depend on the species diffusion properties. These types of reactions are included in the GM, and listed in table 5.3.

The effective loss-rate coefficient for a neutral species N to the wall is given by [247, 248]

$$K_{D,N} = \left[\frac{\Lambda^2}{D_N} + \frac{2V(2-\gamma_N)}{A v_N \gamma_N}\right]^{-1} \tag{5.6.1}$$

Table 5.3: Neutral-wall reactions. γ is the sticking coefficient.

#	Process	γ	K_r [s^{-1}]	Ref.
352	$O \rightarrow \frac{1}{2}O_2$	equation 5.6.3	$\left[\frac{\Lambda^2}{D_O} + \frac{2V(2-\gamma_O)}{Av_O\gamma_O}\right]^{-1}$	21
353	$O(^1D) \rightarrow O$	1.0	$\left[\frac{\Lambda^2}{D_{O(^1D)}} + \frac{2V(2-\gamma_{O(^1D)})}{Av_{O(^1D)}\gamma_{O(^1D)}}\right]^{-1}$	15
354	$O(^1S) \rightarrow O$	1.0	$\left[\frac{\Lambda^2}{D_{O(^1S)}} + \frac{2V(2-\gamma_{O(^1S)})}{Av_{O(^1S)}\gamma_{O(^1S)}}\right]^{-1}$	15
355	$O(^3S) \rightarrow O$	1.0	$\left[\frac{\Lambda^2}{D_{O(^3S)}} + \frac{2V(2-\gamma_{O(^3S)})}{Av_{O(^3S)}\gamma_{O(^3S)}}\right]^{-1}$	15
356	$O(^5S) \rightarrow O$	1.0	$\left[\frac{\Lambda^2}{D_{O(^5S)}} + \frac{2V(2-\gamma_{O(^5S)})}{Av_{O(^5S)}\gamma_{O(^5S)}}\right]^{-1}$	15
357	$O(^3P) \rightarrow O$	1.0	$\left[\frac{\Lambda^2}{D_{O(^3P)}} + \frac{2V(2-\gamma_{O(^3P)})}{Av_{O(^3P)}\gamma_{O(^3P)}}\right]^{-1}$	15
358	$O(^5P) \rightarrow O$	1.0	$\left[\frac{\Lambda^2}{D_{O(^5P)}} + \frac{2V(2-\gamma_{O(^5P)})}{Av_{O(^5P)}\gamma_{O(^5P)}}\right]^{-1}$	15
359	$O_2(a^1\Delta_u) \rightarrow O_2$	0.007	$\left[\frac{\Lambda^2}{D_{O_2(a^1\Delta_u)}} + \frac{2V(2-\gamma_{O_2(a^1\Delta_u)})}{Av_{O_2(a^1\Delta_u)}\gamma_{O_2(a^1\Delta_u)}}\right]^{-1}$	21, 246
360	$O_2(b^1\Sigma_u^+) \rightarrow O_2$	0.007	$\left[\frac{\Lambda^2}{D_{O_2(b^1\Sigma_u^+)}} + \frac{2V(2-\gamma_{O_2(b^1\Sigma_u^+)})}{Av_{O_2(b^1\Sigma_u^+)}\gamma_{O_2(b^1\Sigma_u^+)}}\right]^{-1}$	21, 246
361	$Ar^m \rightarrow Ar$	1.0	$\left[\frac{\Lambda^2}{D_{Ar^m}} + \frac{2V(2-\gamma_{Ar^m})}{Av_{Ar^m}\gamma_{Ar^m})}\right]^{-1}$	21
362	$Ar^r \rightarrow Ar$	1.0	$\left[\frac{\Lambda^2}{D_{Ar^r}} + \frac{2V(2-\gamma_{Ar^r})}{Av_{Ar^r}\gamma_{Ar^r})}\right]^{-1}$	21
363	$Ar(4p) \rightarrow Ar$	1.0	$\left[\frac{\Lambda^2}{D_{Ar(4p)}} + \frac{2V(2-\gamma_{Ar(4p)})}{Av_{Ar(4p)}\gamma_{Ar(4p))}}\right]^{-1}$	21

where the first term in the right hand side (rhs) accounts for the diffusion of particles from the bulk plasma to the walls and the second term in the rhs is a correction factor due to particles reflecting at the reactor walls [247]. In equation 5.6.1

$$\Lambda = \left[(\frac{\pi}{L})^2 + (\frac{2.405}{R})^2\right]^{-1/2} \tag{5.6.2}$$

is the effective diffusion length for a cylindrical reactor [247], D_N is the diffusion coefficient for neutrals, $v_N = \sqrt{8k_BT_N/\pi m_N}$ is the thermal speed and γ_N is the sticking coefficient. D_N and the mean free path $\lambda_{mfp,N}$ are defined as in equations 5.5.11 and 5.5.13 respectively, but for neutrals instead of ions. The sticking coefficient depends, among other parameters, on the wall material and operating pressure [21, 112]. The GM uses γ_N values taken from [15, 21] that conducted simulations under similar operating conditions. The γ_N values used, listed in table 5.3, are constant parameters except for atomic oxygen [21], which is pressure dependent

based on the following expression

$$\gamma_O = \begin{cases} 1 - p_{O_2}[\text{mTorr}]/4), & p_{O_2} < 2\,\text{mTorr} \\ 0.1438 \exp\left(2.5069/p_{O_2}[\text{mTorr}]\right), & \text{otherwise.} \end{cases} \tag{5.6.3}$$

5.7 Atomic energy transitions and radiative processes

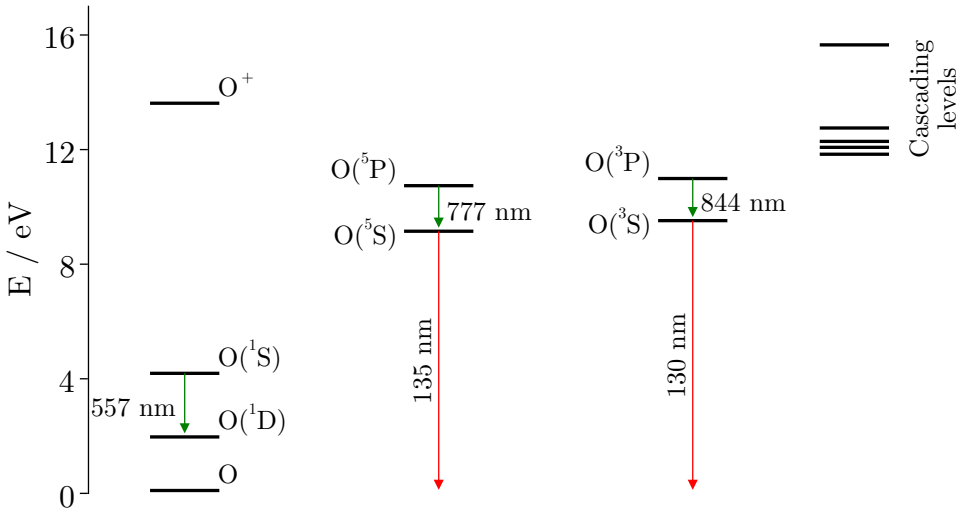

Figure 5.2: Energy diagram of atomic oxygen and radiative transitions taken into account in the numerical model. The cascading levels shown are only a representative subset of the existing high energy levels [14]. Figure adapted from Ref. [15].

Radiation processes from certain excited states when they decay to lower energy levels are included in the GM. The natural decay of excited species at energy level a to a lower energy level b emitting radiation at a wavelength λ_{ab} is a well-known physical phenomenon whose rates are described by Einstein coefficients for spontaneous emission. The radiative reactions included in the GM are sketched in figure 5.2 and listed in table 5.4. The most important transitions for VUV emission are from the $O(^5S)$ and $O(^3S)$ states, as they emit photons at ∼135 and ∼130 nm when decaying to ground state. Other transitions between excited states of oxygen atoms defined in table 5.1, are included for completeness of the physical model. However, including all possible energy transitions would add significant complexity to the collisional radiative scheme, so instead, energy transitions at higher energy levels are simplified with so-called *cascade processes* [15].

Cascading processes gather several energy transition steps into one single reaction without needing to know the intermediate states. This usually includes electron impact excitation of O atoms, or dissociative excitation during electron collisions with O_2 molecules, that lead to the formation of high energy levels that subsequently decay to lower energy levels that are considered as species in the numerical model.

Table 5.4: Atomic transitions from state $a \rightarrow b$. λ_{ab} is the radiation wavelength, A_{ab} is the Einstein coefficient for spontaneous emission, g_a and g_b are the statistical weights of the a and b levels, respectively, and γ_{ab} is the escape factor.

#	**Process**	K_r [s^{-1}]	λ_{ab} [**nm**]	A_{ab} [s^{-1}]	g_a	g_b	**Ref.**
364	$O(^1S) \rightarrow O(^1D)$	$\gamma_{ab}A_{ab}$	557.7	1.26	1.0	5.0	14, 15
365	$O(^5S) \rightarrow O$	$0.5\gamma_{ab}A_{ab}$	135.6	$4.2{\cdot}10^3$	5.0	5.0	14, 15
366	$O(^5S) \rightarrow O$	$0.5\gamma_{ab}A_{ab}$	135.9	$1.4{\cdot}10^3$	5.0	3.0	14, 15
367	$O(^3S) \rightarrow O$	$0.33\gamma_{ab}A_{ab}$	130.2	$3.4{\cdot}10^8$	3.0	5.0	14, 15
368	$O(^3S) \rightarrow O$	$0.33\gamma_{ab}A_{ab}$	130.5	$2.0{\cdot}10^8$	3.0	3.0	14, 15
369	$O(^3S) \rightarrow O$	$0.33\gamma_{ab}A_{ab}$	130.6	$6.8{\cdot}10^7$	3.0	1.0	14, 15
370	$O(^5P) \rightarrow O(^5S)$	$0.47\gamma_{ab}A_{ab}$	777.2	$3.7{\cdot}10^7$	7.0	5.0	14, 15
371	$O(^5P) \rightarrow O(^5S)$	$0.33\gamma_{ab}A_{ab}$	777.4	$3.7{\cdot}10^7$	5.0	5.0	14, 15
372	$O(^5P) \rightarrow O(^5S)$	$0.2\gamma_{ab}A_{ab}$	777.5	$3.7{\cdot}10^7$	3.0	5.0	14, 15
373	$O(^3P) \rightarrow O(^3S)$	$0.11\gamma_{ab}A_{ab}$	844.6	$9.2{\cdot}10^7$	1.0	3.0	14, 15
374	$O(^3P) \rightarrow O(^3S)$	$0.56\gamma_{ab}A_{ab}$	844.6	$9.2{\cdot}10^7$	5.0	3.0	14, 15
375	$O(^3P) \rightarrow O(^3S)$	$0.33\gamma_{ab}A_{ab}$	844.7	$9.2{\cdot}10^7$	3.0	3.0	14, 15
376	$Ar^r \rightarrow Ar$	A_{ab}		10^5			21, 249
377	$Ar(4p) \rightarrow Ar$	A_{ab}		$3.2{\cdot}10^7$			21, 250
378	$Ar(4p) \rightarrow Ar^m$	A_{ab}		$3{\cdot}10^7$			21, 171
379	$Ar(4p) \rightarrow Ar^r$	A_{ab}		$3{\cdot}10^7$			21, 171

The decay of high energy levels may occur in a stepwise manner, called cascading, and modelling this using Einstein coefficients would add significant complexity to the species and chemistry schemes.

A number of processes including cascades are included in the current model in different ways. In the case of electron impact excitation of oxygen atoms, direct excitation from the ground state to the $O(^3S)$, $O(^3P)$, $O(^5S)$ and $O(^5P)$ states are all included (reactions #86-89). In addition, the excitation of ground state oxygen atoms to triplet levels above $O(^3P)$ is assumed to populate $O(^3P)$ via cascade processes (reaction #90). A number of electron impact collisions with excited O atoms, leading to the formation of different excited levels are also included (reactions #91-102)

A number of processes based on emission cross sections, which inherently include cascading processes, are also incorporated into the GM based on Ref. 15 and are listed in table A.7. The first of these reactions (#380) is used to account for the contribution of cascade processes towards the formation of $O(^5S)$ and ~777 nm

radiation during electron impact excitation of ground state oxygen atoms. This represents a different way of including cascades compared to that used for the O(^{3}P) state. This is motivated by the availability of an experimentally measured emission cross section for the 777 nm line. Similarly, experimentally measured emission cross sections have been used for the formation of photons at 130.4 nm, 135.6 nm, 777 nm and 844 nm, from electron impact excitation. The way in which rate constants have been calculated based on these emission cross sections, and what these represent specifically, is described in detail in the footnotes of table A.7.

Self absorption of the emission line by the lower state of the given transition can be an important effect that has an impact on the population of the emitting species and the intensity of radiation leaving the plasma. Therefore it is important to account for this phenomena in the model. This is modelled by adding a so-called escape factor γ_{ab}, as a correction to the Einstein coefficient for spontaneous emission. To do this, we follow the approach described in [15]. In general, the emission rate, K_{ab}, and intensity per unit volume, I_{ab} for atomic transitions affected by self absorption are given by

$$K_{ab} = \gamma_{ab} A_{ab} \tag{5.7.1}$$

$$I_{ab} = K_{ab} n_a. \tag{5.7.2}$$

The definition of the escape factor used is the empirical formula given in [251]

$$\gamma_{ab} = \frac{2 - \exp\left(-10^{-3} \kappa_{ab,0} R\right)}{1 + \kappa_{ab,0} R} \tag{5.7.3}$$

Under conditions where Doppler broadening is the dominant line broadening mechanism, as is the case for the low pressure conditions of interest in this work, the absorption coefficient at the centre of the emission line is given by [252]

$$\kappa_{ab,0} = n_b A_{ab} \frac{g_p}{g_b} \frac{\lambda_{ab,0}^3}{8\pi} \sqrt{\frac{m_b}{2 k_B T_b \pi}} \tag{5.7.4}$$

where $\lambda_{ab,0}$ is the central wavelength of the emission line.

As described in table 5.1, a number of the species considered in the model consist of grouped states. While the choice to group states whose energies are very similar is convenient for the plasma-chemical model, the fact that these states emit radiation at slightly different wavelengths needs to be accounted for to properly describe the line emission and self absorption. To do this, the density distribution of individual states within a grouped state needs to be estimated. For the wavelength ranges of interest in this work, two cases can be distinguished: (1) the upper state of the transition is represented in the model by a grouped state and the lower state is not and (2) the

lower state is represented in the model by a grouped state and the upper state is not. The first case applies to emission around 777 nm (three emission lines, individual upper states: $2s^2\ 2p^3\ (^3S^0)\ 3p\ ^5P_{1,2,3}$, grouped state: $O(^5P)$) and 844 nm (three emission lines individual upper states $2s^2\ 2p^3\ (^3S^0)\ 3p\ ^3P_{1,2,0}$, grouped state: $O(^3P)$). The second case applies to emission around 130 (two emission lines individual lower states $2s^2\ 2p^4\ ^3P_{2,1}$, grouped state: O) and 135 nm (three emission lines, individual lower states $2s^2\ 2p^4\ ^3P_{2,1,0}$, grouped state: O). We follow the approach used in [15] to estimate the densities of individual multiplet states within each grouped state. Here, the density of each multiplet level is estimated using the statistical weights of each level

$$n_m = \frac{g_m}{\sum_i g_{m_i}} n_g \tag{5.7.5}$$

where g_m are the statistical weights of each multiplet level within a grouped state with density n_g and $\sum_i g_{m_i}$ is the sum of the statistical weights of each multiplet level within the grouped state.

For emission around 777 and 844 nm, where the upper state is the grouped state, the densities of the individual upper states, n_a, used to calculate the emission intensity in equation 5.7.2 are determined using equation 5.7.5. On the other hand, for emission around 130 and 135 nm, where the lower state is the grouped state, the densities of the individual lower states, n_b required for the calculation of $\kappa_{ab,0}$ in equation 5.7.4 are determined by equation 5.7.5.

The small differences in emission wavelength of each multiplet are not relevant for the aims of the model and therefore, when presenting results, the emission intensities of the multiplet emission lines are added together. Specifically, the 135 nm emission line, I_{135}, is the sum of reactions #365 and 366 (in table 5.4) and reactions #384-386 (in table A.7), the 130 nm line, I_{130}, is the sum of reactions #367-369 (in table 5.4) and reactions #381-383 (in table A.7), and the 777 nm line, I_{777}, is the sum of reactions #370-372 (in table 5.4) and reactions #380 and #387-389 (in table A.7).

5.8 Concluding remarks

The development of a 0D plasma chemical kinetics GM implementing an extended chemical-radiative reaction scheme for Ar and O_2 species has been described. The model includes a mass balance equation for each species in the model and an energy balance equation for electrons, which are assumed to have a Maxwellian EDF. Heavy species (neutrals and ions) are assumed to have a constant temperature.

The mass balance equation accounts for mass variations due to chemical reactions and fluxes of particles interacting with the reactor walls. The electron energy continuity equation accounts for energy changes due to power input, particle reactions

and fluxes of particles interacting with the walls. In addition, the reaction scheme of Ar/O_2 and the physics of the flux of particles (ions and neutrals) to the walls have been described. Special attention has been paid to radiative transitions and radiation self-absorption, since the first goal of the GM is to model VUV radiation.

Finally, it is worth mentioning that the GM described in this chapter has been developed following modern coding standards and a modular architecture to allow easy extension and flexible use. Therefore, the GM could be used to simulate inductively coupled plasmas using any species and reaction scheme that may be available by simply describing it in the input deck.

Chapter 6

Vacuum ultraviolet emission in oxygen species

Controlling vacuum ultraviolet (VUV) emission in low pressure plasmas is essential not only for the development of new sterilisation methods [50, 85], but also for the control of VUV radiation in materials processing applications [86–90]. It is therefore of interest to have a detailed understanding of the chemical pathways leading to VUV in low pressure plasma applications.

For this reason, a numerical investigation of oxygen atom VUV emission in low pressure Ar/O_2 double inductively coupled plasmas (DICPs) is carried out in this chapter. Oxygen containing plasmas are widely used in industrial [104–110] and biomedical [19, 85, 111] applications and thus providing a detailed understanding of VUV radiation formed from O atoms in Ar/O_2 ICPs and the plasma-chemical pathways leading to it could be useful to improve plasma performance in these applications.

This investigation uses the GM and reaction scheme for Ar/O_2 presented in chapter 5. The simulation conditions are described in section 6.1. The GM results are first compared against experimental measurements, in section 6.2, not only to provide confidence in the numerical model and the reaction scheme used but also to characterise Ar/O_2 DICPs.

Following comparison with experimental data, a more extensive numerical investigation is carried out over a wide range of operating conditions. In section 6.3 variations of the operating parameters of total pressure (p_T = 0.3-100 Pa), input power (P_{in} = 100-2000 W) and oxygen fraction (χ_{O_2} = 0-0.2) are conducted and oxygen VUV emission and its formation pathways investigated. For the first time, the VUV emission from oxygen atoms is studied consistently over a wide range of operating parameters, and is described not only in absolute terms, but also in comparison with ion and oxygen atom fluxes at the reactor walls, to provide a broad context for regimes of interest to plasma process optimisation, which may depend

on the fluxes of the various components to the surfaces.

6.1 Initial simulation conditions

The simulation results presented in this chapter use the following initial conditions, unless explicitly stated otherwise.

The GM simulates a double inductively coupled plasma (DICP) in a cylindrical reactor of axial length $L = 0.2\,\mathrm{m}$ and radius $R = 0.2\,\mathrm{m}$, with stainless steel walls, as illustrated in figure 6.1. The reason for simulating DICPs rather than conventional

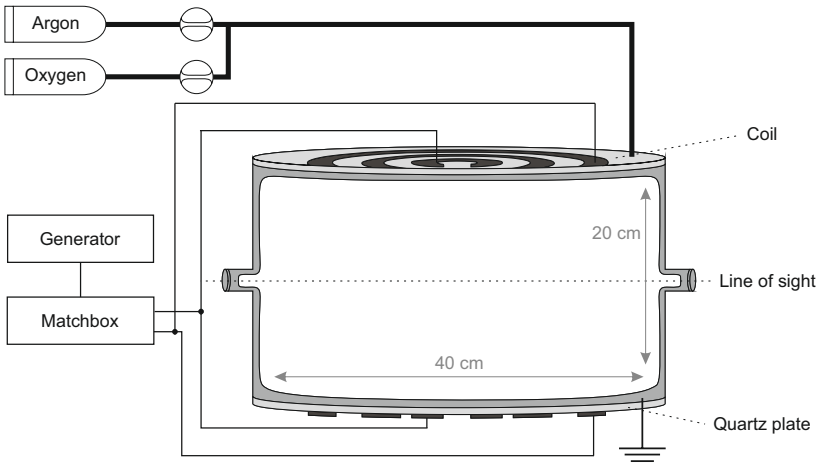

Figure 6.1: Schematic of the double inductively coupled plasma (DICP) simulated in the 0D GM and used for experimental verification of the simulation results.

ICPs is that the former generate better spatially homogeneous plasmas [163,164] and are therefore more appropriate for comparing experimental results with the GM.

The plasma reactor is initially filled with a partially ionised plasma, where the neutral gas is formed only by ground state Ar and O_2 at total pressure p_T and with an arbitrary oxygen fraction $0 \leq \chi_{O_2} \leq 1$. The initial charged species are electrons, O_2^+ and Ar^+ with an initial plasma density $n_P = 10^{14}\,\mathrm{m}^{-3}$. The initial density of the plasma species fulfils quasi-neutrality, and thus $n_P = n_e = n_{O_2^+} + n_{Ar^+}$, where $n_{Ar^+} = (1 - \chi_{O_2})n_P$ and $n_{O_2^+} = \chi_{O_2} n_P$ are in the same ratio as the Ar/O_2 gas mixture. The remaining neutral and charged species have an initial density of zero. The initial electron temperature is set to $T_e = 1.5\,\mathrm{eV}$ and neutral and ion species have a fixed temperature T_N. Different values of T_N are used depending on the conditions, as discussed in more detail later. The simulation time is $t_{end} = 1\,\mathrm{s}$, which has been tested to be long enough for the simulations to converge to a stable solution in all the results presented. The stability of the solution is defined when the variations in the electron density and temperature, the argon density and the atomic oxygen density are less than 1% with respect to the previous time step result.

6.2 Characterisation of argon oxygen double inductively coupled plasma

In this first section, the Ar/O_2 DICP is described by performing a small parametric study where the total gas pressure, p_T, the input power, P_{in}, and the oxygen fraction, χ_{O_2}, are varied. The results presented in this section are not only used to provide a general characterisation of Ar/O_2 plasmas and its radiation behaviour of oxygen species, but also to validate the numerical results. An important part of the experimental results presented in this study were carried out specifically for this research and are described in more detail in [16].

The total pressure is varied between $p_T = 2$ - 20 Pa the input power $P_{in} = 200$ - 800 W and the oxygen fraction $\chi_{O_2} = 0$ - 0.20. However, since the temperature of ions and neutrals, T_N, may change significantly under variations of p_T, P_{in}, and χ_{O_2} [18], and this is a fixed parameter in the GM, simulations are run with various values of T_N to ensure that variations of this parameter have been taken into account in the final results. On the one hand, simulations have been performed varying T_N between 400 - 2000K in order to understand the impact of T_N on the plasma parameters. On the other hand, a second set of simulations has also been run using values of

Table 6.1: Neutral temperature experimental measurements, in K.

	5 Pa			**500 W**		
χ_{O_2}	200 W	500 W	800 W	2 Pa	10 Pa	20 Pa
0.0	425±11	513± 8	569± 3	413±55	632± 5	787±12
0.04	567±11	657± 6	722±16	459± 5	680±10	780± 9
0.08	615±16	743±12	843±49	501± 8	675±31	446[a]
0.12	626±36	801±10	862±10	538± 7	654±22	587±68[b]
0.16	617±35	784±12	931±25	534± 7	661±12	
0.2	596± 7	793± 9	930± 1	526±22	726±22[b]	

[a] This reaction is given in Ref. [15] for electron collisions with ground state O_2 and is used here for electron collisions with excited states of O_2 with the same rate constant.
[b] The constants were obtained from the polynomial fit to the data in the supplementary information in Ref. [244].

T_N measured experimentally using a tunable diode laser absorption spectroscopy (TDLAS), listed in table 6.1, in order to better compare experiment and simulation.

The results are compared with the experimental work described in [15–18]. The experimental work from Fiebrandt *et al* [15,17,18] is conducted on the same plasma reactor and in similar operating conditions and thus its results are a useful reference. However, in the time since the earlier works of Fiebrandt *et al*, the reactor has

undergone several changes including the replacement of the quartz plates separating the coils from the plasma. While these changes would not necessarily be expected to significantly affect the plasma properties, since the design of the reactor has not changed, the more recent measurements are generally not in exact agreement with the earlier data for otherwise identical operating conditions. This should also be kept in mind when interpreting the level of agreement between experiment and simulation.

6.2.1 Electron density and temperature

The electron density n_e, in figure 6.2, and temperature T_e, in figure 6.3, are the first parameters to evaluate the plasma results. The numerical results for n_e are compared with multipole resonance probe (MRP) measurements described in [16] and also conducted in [17]. Numerical results for T_e are compared with Langmuir probe data from [17].

Electron density

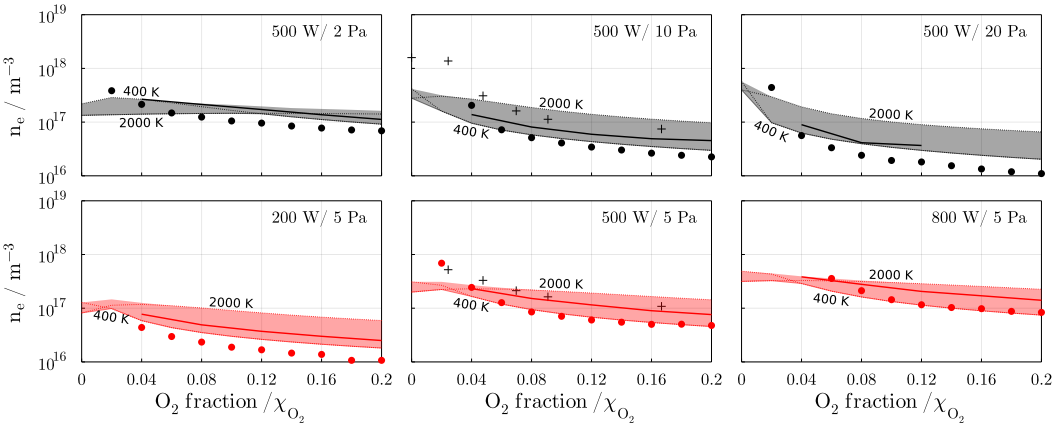

Figure 6.2: Electron density, n_e, for variations of p_T (top row), P_{in} (bottom row) and χ_{O_2}. Circle (•) markers are experimental data described in [16], and + markers are experimental MRP results from [17]. The shaded areas cover the model results when the neutral gas temperature, T_N, is varied between 400 and 2000 K (dotted lines). The solid lines are numerical results using the T_N experimental data listed in table 6.1.

Electron density values, n_e, are found between 10^{16} and $10^{18}\,\mathrm{m}^{-3}$ and present decreasing trends with χ_{O_2}, as observed in [21], as well as with p_T. These trends are caused by a constant growth of dissociative attachment

$$e + O_2 \rightarrow O + O^-$$

$$e + O_2(a^1\Delta_u) \rightarrow O + O^-$$

$$e + O_2(b^1\Sigma_u^+) \rightarrow O + O^-$$

(reactions #25, 42 and 60 in table A.1, respectively) acting as the main electron loss mechanism, while the main production mechanism transits from argon ionisation

$$e + \mathrm{Ar} \rightarrow \mathrm{Ar}^+ + 2e$$

(reaction #107 in table A.2), dominant at low χ_{O_2} and p_T, to the detachment of $\mathrm{O}_2((\mathrm{a}^1\Delta_u)$ and $\mathrm{O}_2(\mathrm{b}^1\Sigma_u^+)$ with O_2^-

$$\mathrm{O}_2(\mathrm{a}^1\Delta_u) + \mathrm{O}_2^- \rightarrow e + 2\mathrm{O}_2$$

$$\mathrm{O}_2(\mathrm{b}^1\Sigma_u^+) + \mathrm{O}_2^- \rightarrow e + 2\mathrm{O}_2$$

(reactions #226 and 230 in table A.3), and O with O^-

$$\mathrm{O} + \mathrm{O}^- \rightarrow e + \mathrm{O}_2$$

(reaction #176 in table A.3), at low χ_{O_2} and higher p_T.

Besides, a positive trend in n_e with P_{in} is observed that is in line with the results in [112]. This is caused by a significant increase of argon ionisation with increasing P_{in}.

The simulation results and the experimental data are in good agreement, with both showing similar trends for variations of p_T, P_{in} and χ_{O_2}. There is however a consistent difference between numerical and experimental results (circle markers), with the latter generally being slightly lower. A potential explanation for this may lie in the fact that the power defined for the simulation is that coupled into the plasma, that defined for the experiment is measured at the RF generator. It is generally well known that there can be significant differences between the power provided at the RF generator and the power coupled into the plasma in ICP systems [253–258]. Since the electron density is strongly power dependent, any deviation between generator power and that coupled into the plasma would tend to decrease the experimentally measured electron density in comparison to the simulated electron density. However, since we are currently unable to characterise the power coupling efficiency in detail, the extent to which this effect can explain the differences between experiment and simulation is currently not known.

Electron temperature

The electron temperature data T_e, in figure 6.3, show values between approximately 2 and 3 eV for variations in χ_{O_2}. Both numerical and experimental values show a slight positive trend that plateaus with increasing values of χ_{O_2}. The absolute T_e values between experimental and numerical data differs less than 1 eV and therefore results are in reasonably good agreement. The assumption of a Maxwellian electron

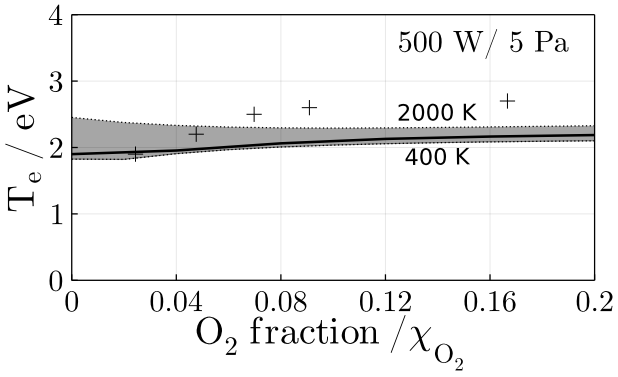

Figure 6.3: Electron temperature, T_e, for variations of O_2 fraction. The + markers are LP experimental results in [17]. The shaded areas cover the model results when the neutral gas temperature, T_N, is varied between 400 and 2000 K (dotted lines). The solid lines are numerical results using the T_N experimental data listed in table 6.1.

EDF, which does not hold for increasing χ_{O_2} [17,89,112], is likely to be an important reason for the differences that do exist between experiment and simulation. While this is a weakness in the model formulation, the effect on the comparison between experimentally measured and simulated electron densities and temperatures is not severe for the cases compared here. A detailed study on the effects of the EDF shape on the properties of oxygen discharges for similar conditions has previously been carried out in [203]. In general, EDFs of different shapes were found to change the absolute values of species densities and electron temperatures predicted by the global model used in that work, without strongly affecting the observed trends.

Given this context and the n_e and T_e comparisons obtained here it can be concluded that the physics and chemistry modelled by the GM is as expected and is in good agreement with experimental work and previous literature.

6.2.2 Neutral temperature variations

The variations of n_e and T_e caused by variations of T_N, shown in the figures by the shaded areas, are considerable but do not have a determining effect on the trends observed. The resulting plasma parameters remain within an order of magnitude for variations between 400 and 2000 K. Similar variations are observed for the other parameters described in this section, so it can be concluded that T_N has an important influence on the plasma properties, but does not have a strong influence on the qualitative trends presented in this work.

6.2.3 Neutral species densities

With respect to neutral species densities, measured and simulated densities of Ar^m, n_{Ar^m}, and the O_2 dissociation fraction are compared.

Argon metastable density

In the GM, the species Ar^m represents an effective metastable state that includes the states $Ar(1s_3)$ and $Ar(1s_5)$ [21]. However, the experimental measurements performed with TDLAS, described in [16], measure only the $Ar(1s_5)$ state. Still, the comparison between the experimental and GM results is considered reasonable since the work performed in [18] with optical emission spectroscopy (OES), under similar operating conditions, infers the densities of both $Ar(1s_3)$ and $Ar(1s_5)$ states and shows that the former is typically an order of magnitude lower in density.

The results for n_{Ar^m}, in figure 6.4, show values between 10^{15} and $10^{17}\,m^{-3}$. The production of Ar^m is sustained by electron impact excitation from ground and

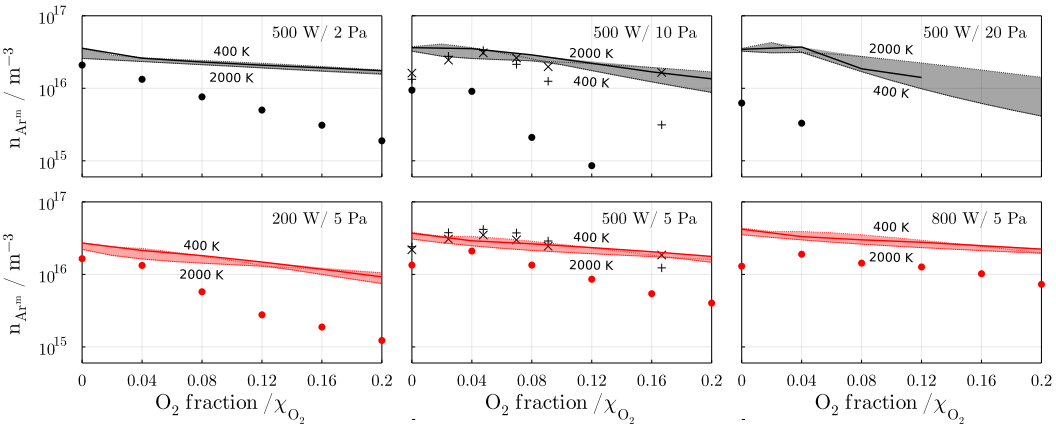

Figure 6.4: Ar^m density, n_{Ar^m}, for variations of p_T (top row), P_{in} (bottom row) and χ_{O_2}. Circle (•) markers are experimental TDLAS data described in [16], + and × markers are TDLAS and OES results in [18], respectively. The shaded areas cover the model results when the neutral gas temperature, T_N, is varied between 400 and 2000 K (dotted lines). The solid lines are numerical results using the T_N experimental data listed in table 6.1. It should be noted that TDLAS measurements refer to the density of the $Ar(1s_5)$ state, while the simulated densities and OES measurements represent an effective metastable state comprising the densities of both $Ar(1s_3)$ and $Ar(1s_5)$.

radiative Ar^r states,

$$e + Ar \rightarrow Ar^m + e$$

$$e + Ar^r \rightarrow Ar^m + e$$

(reactions #108-109 and 122 in table A.2 respectively), and the decay

$$Ar(4p) \rightarrow Ar^m$$

, reaction #378 in table 5.4. These three reactions are of similar importance in the range of parameters studied. The loss mechanisms of Ar^m are dominated by electron impact collisions forming Ar^r and $Ar(4p)$

$$e + Ar^m \rightarrow Ar^r + e$$

$$e + \mathrm{Ar}^m \rightarrow \mathrm{Ar(4p)} + e$$

(#115-116 in table A.2), and the dissociation of O_2 by Ar^m impact

$$\mathrm{O_2} + \mathrm{Ar}^m \rightarrow \mathrm{O} + \mathrm{O} + \mathrm{Ar}$$

$$\mathrm{O_2} + \mathrm{Ar}^m \rightarrow \mathrm{O} + \mathrm{O}(^1\mathrm{S}) + \mathrm{Ar}$$

(#275 and 281 in table A.5), which is expected to be important when $\chi_{O_2} \rightarrow 1$ [21, 259–261], is only relevant for $P_{in} = 200\,\mathrm{W}$ and $\chi_{O_2} \simeq 0.2$.

The GM results and the experimental measurements carried out in [16] (circle markers) show reasonable agreement as they share similar trends and results are, mostly, within an order of magnitude in terms of absolute values. The differences between GM and experimental work become more pronounced for increasing p_T and χ_{O_2}. The reason for these divergences are not fully clear as there are many factors that could be involved, both from the experimental and the computational perspectives. On the experimental side, note that measurements carried out in [18] using TDLAS and OES, + and × markers respectively in figure 6.4, show better agreement with the GM results than the measurements done in this investigation. This may reflect changes in the experimental system between now and when the work of Fiebrandt was carried out, as discussed earlier. On the simulation side, the GM results are consistently above the experimental data, as also observed for n_e in figure 6.2, and therefore a discrepancy with the experimental data due to a non-unity inductive power coupling efficiency cannot be discarded. Besides, the underestimation of argon quenching with oxygen atoms and non-Maxwellian EEDF could also be a reasonable explanation for the larger difference between numerical and experimental results with increasing χ_{O_2} and P_T.

Aside from comparing with experimental data, a series of simulations has also been carried out to compare with previous simulations of Ar excited state densities in Ar/O_2 plasmas with varying O_2 content [20, 21]. These additional results are presented in the appendices B.1, B.2 and B.3. In general, very good agreement is found in the excited state densities of Ar simulated in those previous works and using the GM developed here.

Oxygen dissociation percentage

The oxygen dissociation percentage

$$\mathrm{O_2\,diss.[\%]} = 100\frac{\frac{1}{2}n^*_{\mathrm{O}}}{\frac{1}{2}n^*_{\mathrm{O}} + n^*_{\mathrm{O_2}}}, \tag{6.2.1}$$

where n^*_{O}, and $n^*_{\mathrm{O_2}}$, are the sum of all atomic, and molecular, oxygen species in table 5.1, reflecting the ratio between atomic and molecular oxygen present in the system.

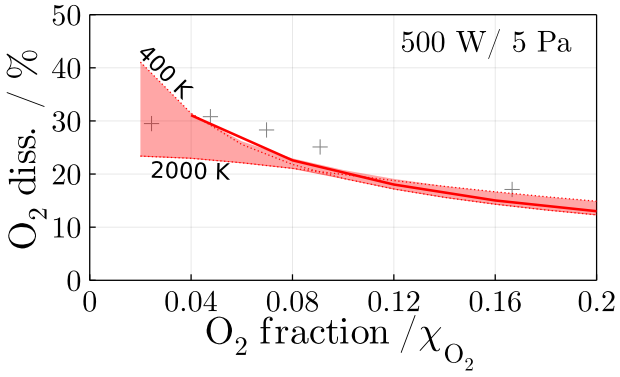

Figure 6.5: Oxygen dissociation percentage for variations of χ_{O_2}. The + markers are the collisional-radiative model results in [15]. The shaded areas cover the model results when the neutral gas temperature, T_N, is varied between 400 and 2000 K (dotted lines). The solid lines are numerical results using the T_N experimental data listed in table 6.1.

The dissociation percentage are shown in figure 6.5, where GM results are compared to the collisional-radiative model (CRM) results in [15]. The CRM estimates volume averaged atomic oxygen ground and excited state densities from experimental data. Both CRM and GM results are in good agreement, showing a decreasing trend for growing χ_{O_2}. This shows that GM results for the main oxygen species, i.e. the molecular and atomic species in the ground state, are computed as expected.

6.2.4 Oxygen radiation

The simulation of radiation from oxygen species is tested with the 777 nm emission line, I_{777}, from the $O(^5P) \rightarrow O(^5S)$ transition, and the VUV emission lines, $I_{VUV} = I_{130} + I_{135}$. The two most important VUV emission lines investigated are the 130 nm line, I_{130}, from the $O(^3S) \rightarrow O$ transition, and the 135 nm line, I_{135}, from the $O(^5S) \rightarrow O$ transition. These parameters are not only used to study the radiation of oxygen but also to verify the composition of excited states present in the gas.

The results for I_{777}, in figure 6.6, show emission intensities between 10^{19} and $10^{21}\,m^{-3}s^{-1}$. The production of $O(^5P)$ is mostly sustained by electron impact excitation from ground state

$$e + O \rightarrow e + O(^5P)$$

(reaction #88 in table A.1) and from $O(^5S)$

$$e + O(^5S) \rightarrow e + O(^5P)$$

(#98 in table A.1), where the latter is more important when P_{in} is larger, p_T is lower, and/or $\chi_{O_2} \rightarrow 0$. The main loss mechanism of $O(^5P)$ is the decay

$$O(^5P) \rightarrow O(^5S)$$

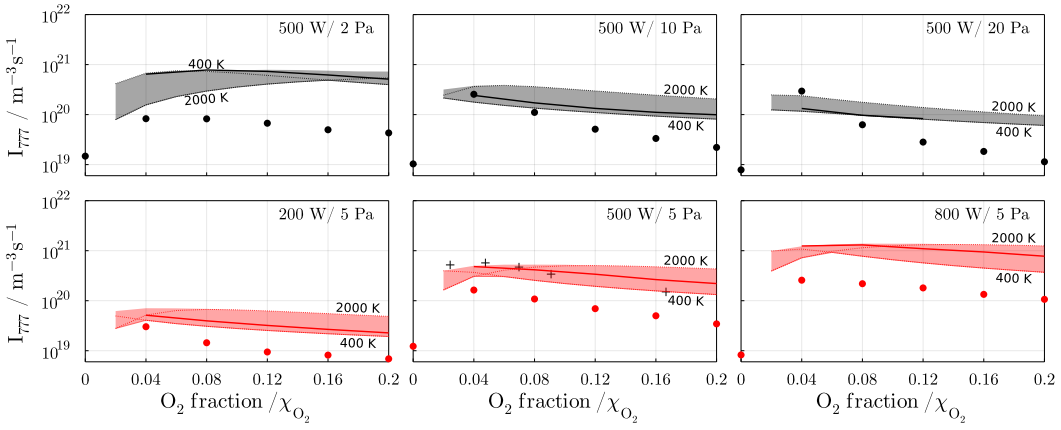

Figure 6.6: Emission intensity of the 777 nm line, from transition $O(^5P) \rightarrow O(^5S)$, for variations of p_T (top row), P_{in} (bottom row) and χ_{O_2}. Circle (•) markers are experimental spectrometer data described in [16], and + spectrometer results in Refs. [15, 19]. The shaded areas cover the model results when the neutral gas temperature, T_N, is varied between 400 and 2000 K (dotted lines). The solid lines are numerical results using the T_N experimental data listed in table 6.1.

(#370-372 in table 5.4) that emits at 777 nm. Although $O(^5P)$ is directly responsible for the 777 nm line, the concentration of $O(^5S)$ is also important as it is closely related to the creation and destruction of $O(^5P)$. As expected, $O(^5S)$ is mainly created by electron impact excitation

$$e + O \rightarrow e + O(^5S)$$

(reaction #86 in table A.1) and the transition $O(^5P) \rightarrow O(^5S)$. However, the destruction of $O(^5S)$ is not only determined by electron impact excitation to $O(^3P)$, $O(^3S)$ and $O(^5P)$ but also by quenching with Ar, O and O_2. Quenching reactions become more important at increasing p_T and χ_{O_2} and are thus responsible for the decreasing trends with respect to these parameters.

The results obtained with the GM are in reasonably good agreement with experimental measurements carried out in this work, as trends are similar and values differ less than an order of magnitude. The experimental data conducted in this investigation is systematically below the numerical data, and that of the previous work of Fiebrandt [15, 19], as observed above for n_e and n_{Ar^m}. Although it is not yet clear what the cause of this difference is, the low power coupling efficiency could be an important factor to take into account, as the coupling efficiency decreases with low pressure and high power [253], and this is in consistent with the observed differences between the experimental and numerical results. However, other factors must also be taken into account for the deviation between numerical and experimental data, such as the underestimation of quenching rates and the assumption of a Maxwellian EEDF. Therefore, bearing in mind the simplifications made, the results of the GM are taken as acceptable.

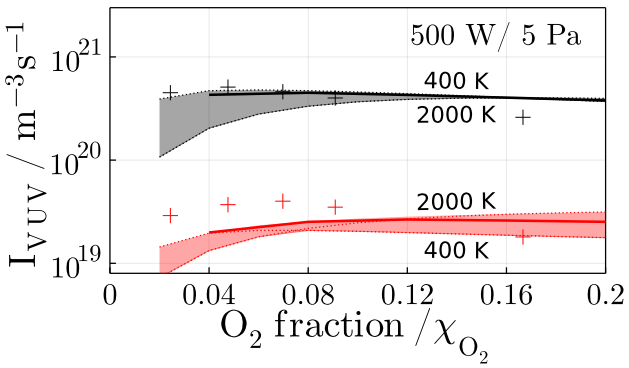

Figure 6.7: VUV emission intensities for variations of χ_{O_2}. In black, the 130 nm line transition $O(^3S) \rightarrow O$ and, in red, the 135 nm line transition $O(^5S) \rightarrow O$. The + markers are the results in [15]. The shaded areas cover the model results when the neutral gas temperature, T_N, is varied between 400 and 2000 K (dotted lines). The solid lines are numerical results using the T_N experimental data listed in table 6.1.

The VUV emission results, shown in figure 6.7, show good agreement between the GM results and the experimental data in [15]. The 130 nm emission line, $I_{130} \sim 5 \cdot 10^{20} \text{m}^{-3}\text{s}^{-1}$, dominates the oxygen VUV radiation as it is an order of magnitude higher than the 135 nm line, $I_{135} \sim 5 \cdot 10^{19} \text{m}^{-3}\text{s}^{-1}$. For both emission lines, radiation comes from the natural decay of excited species,

$$O(^3S) \rightarrow O$$

(reactions #367-369 in table 5.4) and

$$O(^5S) \rightarrow O$$

(reactions #365-366 in table 5.4) respectively, and the contribution from cascading reactions

$$e + O_2(X) \rightarrow e + 2O + \lambda_{130.4}$$

$$e + O_2(X) \rightarrow e + 2O + \lambda_{135.6}$$

(#381-386 in table A.7) is negligible. This is in line with the description given in [97]. Further analysis of oxygen VUV radiation is found in the following section.

6.3 Vacuum ultraviolet emission in oxygen species

After confirming that the GM results are in agreement with experimental reality and after characterising the main properties of the Ar/O_2 DICPs, this second part of the results presents an extended numerical investigation of the VUV radiation in Ar/O_2 DICPs. This section presents results over a wider range of operating conditions, P_T = 0.3-100 Pa and p_T = 100-2000 W. The simulations in this section

use a constant neutral gas temperature of $T_N = 700\,\mathrm{K}$. The analysis of the results focuses on the VUV emission intensity of oxygen species, in absolute terms, I_{VUV}, but also with respect to the flux of ions, $I_{VUV}/(\Gamma_+ A/V)$, and the diffusion of oxygen species, $I_{VUV}/R_{D,O}$, present in the DICP system.

6.3.1 Absolute VUV emission intensities

The total VUV emission intensity from oxygen species, I_{VUV}, is shown in figure 6.8. These results show that, in general terms, the VUV radiation is higher at higher P_{in}

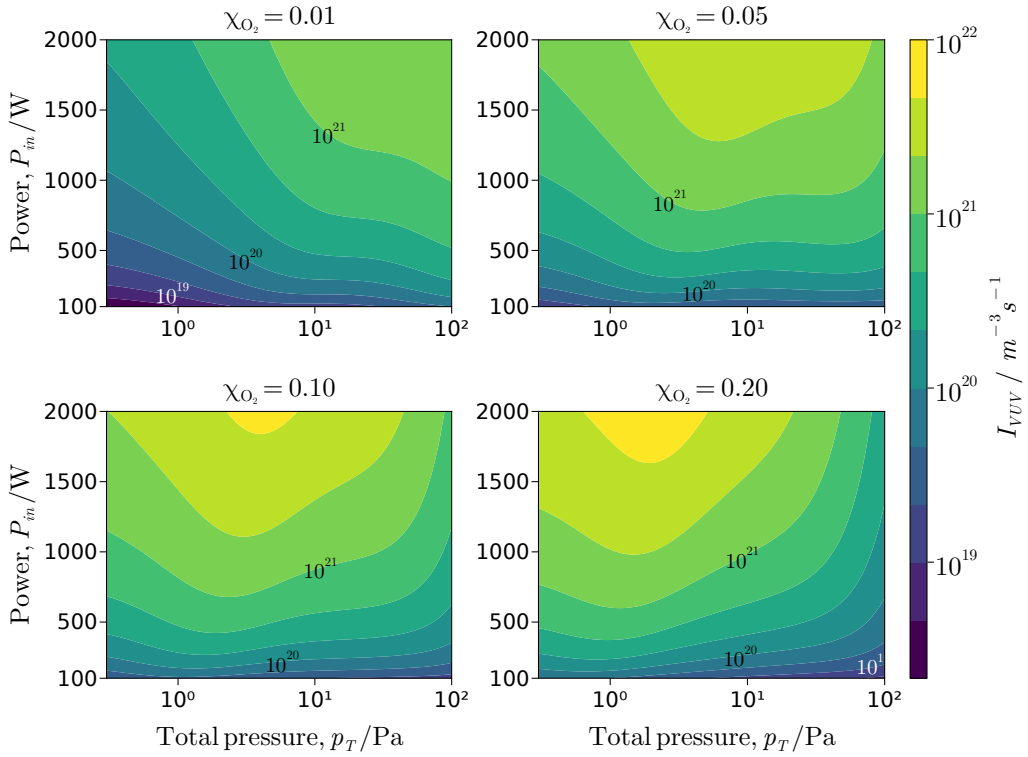

Figure 6.8: Absolute vacuum-ultraviolet (VUV) emission intensity, I_{VUV}, from oxygen species for variations of p_T, P_{in}, and χ_{O_2}.

and χ_{O_2} and finds a peak at a given range of p_T. This VUV peak with respect to p_T moves towards lower pressure values as the χ_{O_2} increases. The VUV emission, as noted in section 6.2.4 is dominated by the 130 nm line, specifically by the transition $O(^3S) \rightarrow O$.

The reaction pathways for the production of $O(^3S)$ species have been tracked to understand the most important source of oxygen VUV radiation. The main production mechanisms of $O(^3S)$ are electron impact excitation of atomic oxygen

$$e + O \rightarrow e + O(^3S)$$

(reaction #87 in table A.1), electron impact cross-excitation

$$e + \mathrm{O}(^5\mathrm{S}) \rightarrow e + \mathrm{O}(^3\mathrm{S})$$

(#97 in table A.1), and the radiative decay

$$\mathrm{O}(^3\mathrm{P}) \rightarrow \mathrm{O}(^3\mathrm{S})$$

(#373-375 in table 5.4). The % of $\mathrm{O}(^3\mathrm{S})$ produced by each of these reactions is shown in figure 6.9 for the case where $\chi_{\mathrm{O}_2} = 0.1$. Interestingly, the most frequent

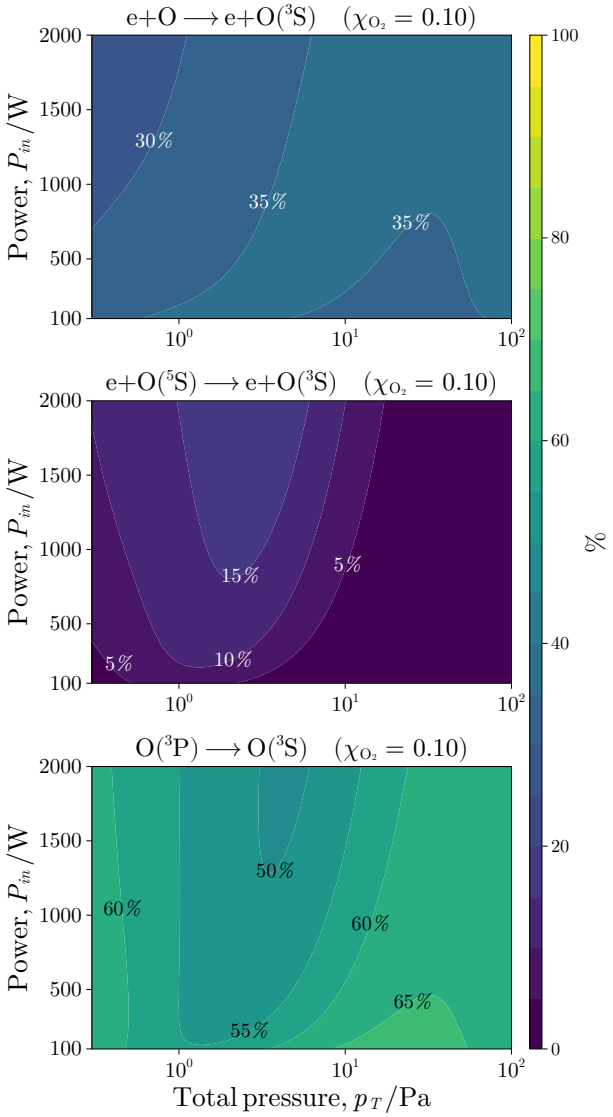

Figure 6.9: Most important $\mathrm{O}(^3\mathrm{S})$ production processes as a % of the overall $\mathrm{O}(^3\mathrm{S})$ production for $\chi_{\mathrm{O}_2} = 0.1$.

production mechanism of $\mathrm{O}(^3\mathrm{S})$ is via decay $\mathrm{O}(^3\mathrm{P})$, about 60-70%, instead of the di-

rect excitation through electron collision impact, 25-30%. This means that the most important oxygen VUV radiation mechanism is a three-step process that consist of

i electron impact excitation to O(^{3}P) state

ii radiative decay to O(^{3}S) (emission at 844 nm)

iii radiative decay to ground state and photon emission at 130 nm.

In fact, the distribution of I_{VUV} in the (p_T, P_{in}) parameter space in figure 6.8, is determined by the density of O(^3P). The reason for a peak in I_{VUV} is that electron impact excitation from ground state (reactions #89-90 in table A.1) dominates the production of O(^3P), and n_e presents a peak in that pressure range which is consistent with the results presented in [203]. With increasing p_T higher n_e are found. However, as the p_T increases further, negative ion production, mainly O^-, becomes more important at the expense of the electron population. Therefore at intermediate pressures, where electron impact ionisation is large and negative ion production is relatively low, the electron density finds its maximum.

6.3.2 VUV emission to ion flux rate

For some industrial processes it is of interest to know photon flux, $\frac{V}{A}I_{VUV}$, with respect to the ion fluxes reaching the reactor walls, Γ_+, and therefore

$$r_{\Gamma_+} = \frac{\frac{V}{A}I_{VUV}}{\Gamma_+}, \tag{6.3.1}$$

is a useful parameter to evaluate VUV emission. Note that $\Gamma_+ = \sum_p \Gamma_p$ is the sum of the positive ion fluxes resulting from the reactions #343-347 (in table 5.2). This rate is shown in figure 6.10. The ion and VUV-photon fluxes are in the same order of magnitude and therefore it is possible to find operating conditions where either VUV emission dominates, $r_{\Gamma_+} \gg 1$, or ion fluxes dominates, $r_{\Gamma_+} \ll 1$. Please note that r_{Γ_+} only takes into account VUV radiation from oxygen species, and that other sources of VUV radiation, e.g. from argon (reaction #376 in table 5.4), are not included in r_{Γ_+}.

The total positive ion flux, shown in figure 6.11, is strongly correlated with the plasma electronegativity $\alpha = n_-/n_e$ such that Γ_+ is largest when $\alpha \to 0$. In general terms at lower pressures, $p_T \leq 1$ Pa, Γ_+ is large and mostly dominated by Ar^+, and for $p_T > 10$ Pa the electronegativity is large, $\alpha > 1$, and Γ_+ drops more than an order of magnitude. Please refer to figures C.1 and C.2 in C for more detailed results on the fluxes of Ar^+, O^+, and O_2^+ respectively. This pressure dependence of Γ_+ has a significant impact on r_{Γ_+}, such that, in general terms, it grows with pressure. r_{Γ_+} becomes largest at high p_T and P_{in} as in these operating conditions

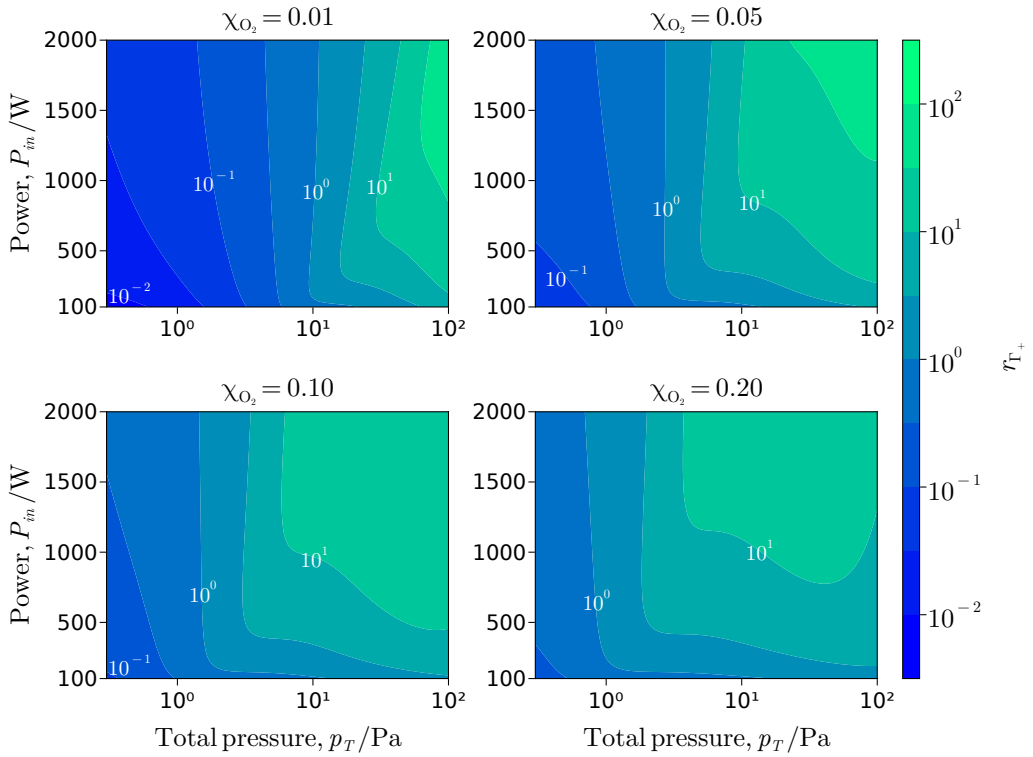

Figure 6.10: Vacuum-ultraviolet emission intensity to positive ion flux rate, r_{Γ_+}.

I_{VUV} is maximum and Γ_+ drops significantly. With increasing χ_{O_2} the peak VUV intensity is displaced towards lower p_T, whereas Γ_+ does not change significantly, and therefore larger r_{Γ_+} values, close to unity, are already found for $\chi_{O_2} \geq 0.1$ and $p_T \sim 1\,\text{Pa}$.

6.3.3 VUV emission to atomic oxygen diffusion to the wall

The ratio between I_{VUV} and atomic oxygen reaching the reactor walls may be of interest for industrial and biomedical applications as both oxygen radicals and VUV photons can readily interact with material leading to surface modifications. This ratio is defined as follow

$$r_{D,\text{O}} = \frac{I_{VUV}}{R_{D,\text{O}}}, \tag{6.3.2}$$

where $R_{D,\text{O}} = \sum_{\text{O(X)}} n_{\text{O(X)}} K_{D,\text{O(X)}}$ is the sum of neutral diffusion reaction rates of atomic oxygen species touching the walls, i.e. reactions #352-358 in table 5.3.

First, $R_{D,\text{O}}$ results are shown in figure 6.12. The flux of oxygen radicals to the wall due to diffusion is large, especially at $p_T > 10\,\text{Pa}$ and $P_{in} > 1000\,\text{W}$ and with increasing χ_{O_2}. Only at very low pressure, $< 0.6\,\text{Pa}$, these fluxes can be considered low. These trends correlate mainly with atomic oxygen density, which presents a similar distribution in the parameter space investigated.

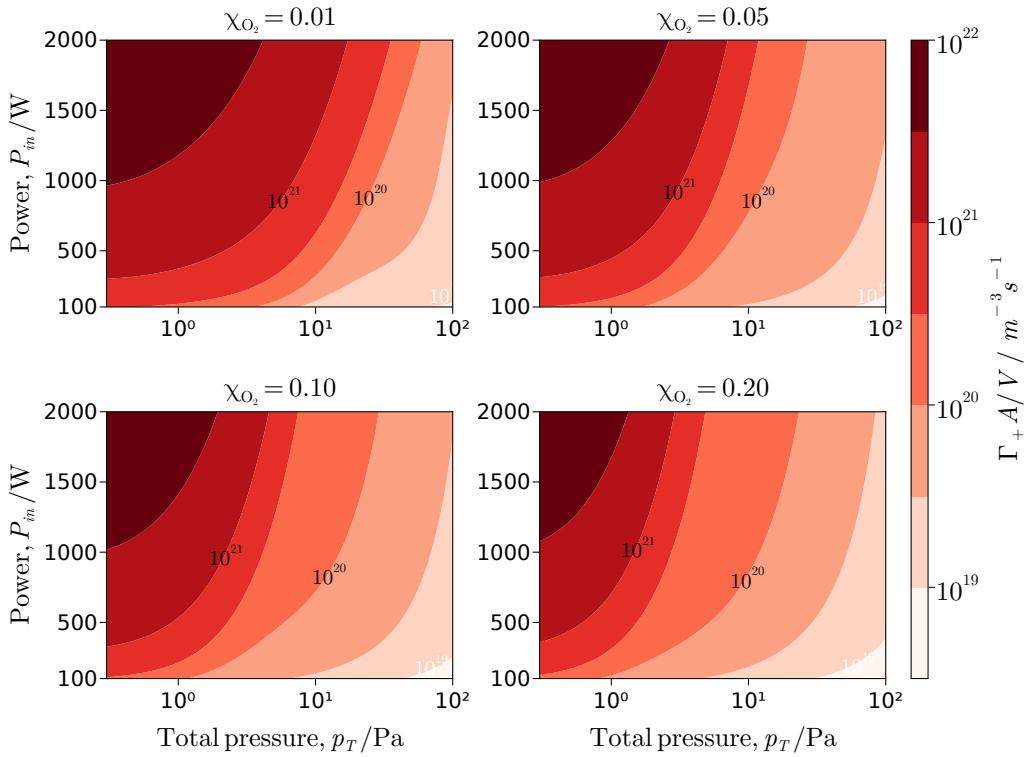

Figure 6.11: Total positive ion flux rate to the reactor walls.

The results for $r_{D,\mathrm{O}}$ are presented in figure 6.13. This data shows that I_{VUV} is always lower than $R_{D,\mathrm{O}}$. The maximum values, $r_{D,\mathrm{O}} \sim 0.4$, are found at minimum p_T ~0.3 Pa, and maximum power,P_{in} ~ 2000 W and decreases with increasing χ_{O_2}. The minimum values, $r_{D,\mathrm{O}} \to 0$, are found in a larger region of high p_T and low p_T.

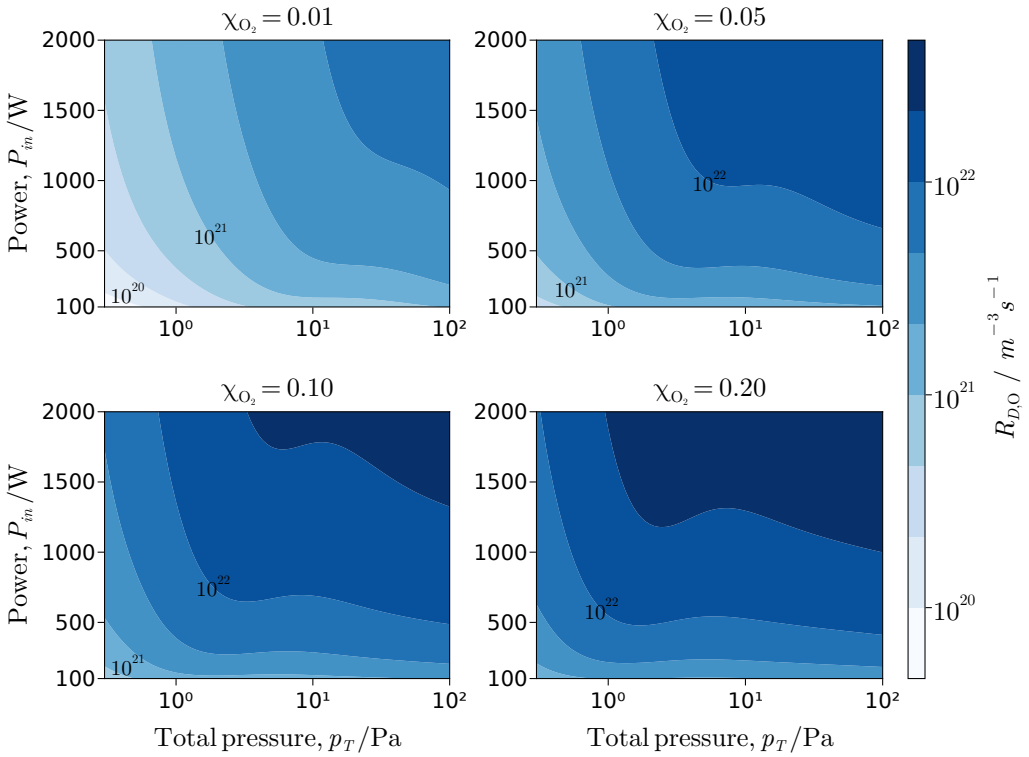

Figure 6.12: Atomic oxygen diffusion rate to the reactor walls.

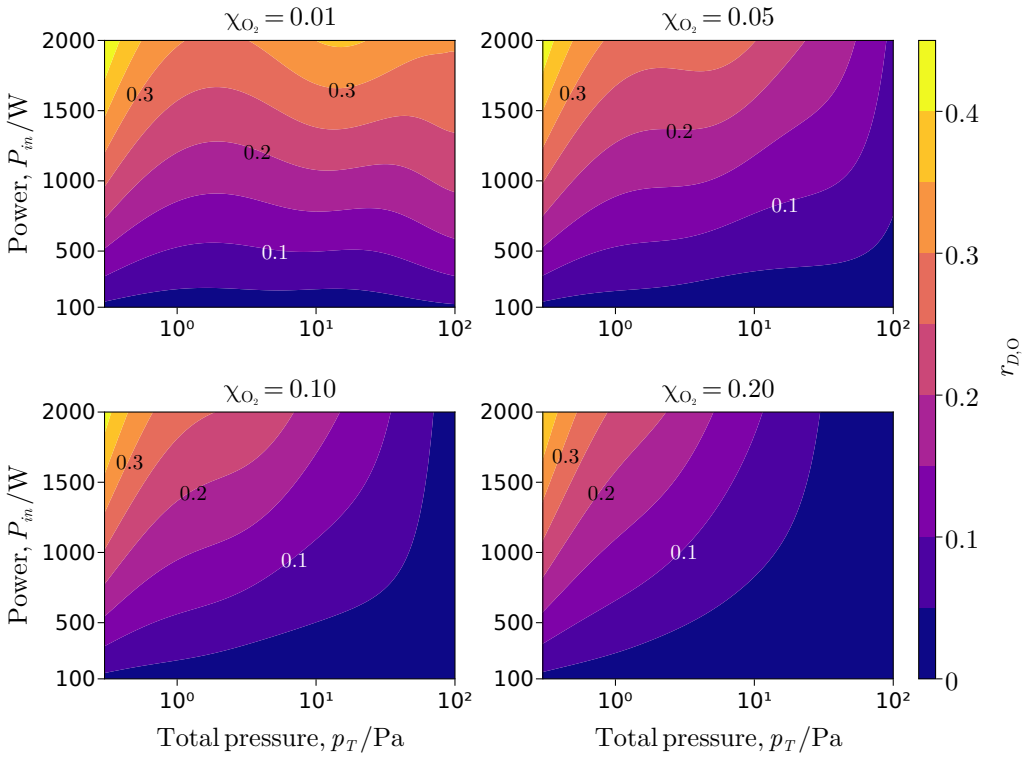

Figure 6.13: Vacuum-ultraviolet emission to atomic oxygen surface flux rate.

6.4 Concluding remarks

In this chapter a numerical investigation of the oxygen VUV emission in Ar/O_2 DICP is presented in two main parts.

The first part of the results investigates Ar/O_2 DICPs for operating parameters between 200-800 W, 2-20 Pa and 0-0.20 O_2 fractions. Moreover, because the GM works with a fixed temperature T_N for neutrals and ions, T_N has also been varied between 400 and 2000 K to test the impact of T_N on the plasma results. The numerical results have been presented alongside experimental work and show that the GM is performing correctly and that T_N does have an impact on the final results but within a relatively small range. The gas and plasma results, as well as the emission lines measured are as expected although some differences are observed for argon metastables. The source of these discrepancies is not yet clear, as they are not necessarily errors in the numerical method, and thus results are taken as valid. Oxygen VUV emission results show good agreement, with the 130 nm line, from the $O(^3S) \rightarrow O$ transition, clearly dominating. The 135 nm line, from the $O(^5S) \rightarrow O$ transition, is an order of magnitude lower and emission from cascading reactions is negligible.

The second part of results investigates oxygen VUV emission over a broader range of total pressure and power. The GM results for plasmas with χ_{O_2} =0-0.20, 0.3-100 Pa and 100-2000 W have shown that oxygen VUV emission, in general terms, increases within the investigated power and oxygen fraction and peak emission intensities are found for pressures between 5-50 Pa. The 130 nm line dominates for most of the parameter space investigated. Surprisingly the most frequent chemical pathway that generates $O(^3S)$ is not direct electron impact excitation from ground state, but excitation to $O(^3P)$ that then decays to $O(^3S)$.

Results of VUV emission intensities with respect to ion fluxes and oxygen diffusion to the reactor walls have also been presented. While VUV emission is largest with respect to ion fluxes at high pressures, oxygen diffusion is much larger than VUV emission for the parameter space investigated.

Chapter 7

Summary and future work

In this thesis, two challenges in plasma-based industrial and biomedical applications have been addressed using numerical methods. Firstly, inductive heating effects in high frequency (HF) capacitively coupled plasmas (CCPs) have been investigated using EPOCH-LTP, a particle-in-cell (PIC) model. EPOCH-LTP has been developed from the parent code EPOCH [217] and a new inductive heating (IH) model has been implemented that allows the simulation of transverse inductive currents. Secondly, vacuum ultraviolet (VUV) radiation has been studied in Ar/O_2 inductively coupled plasmas (ICPs) using a zero-dimensional (0D) chemical kinetics global model (GM). The 0D GM model was developed specifically for this investigation and the results are expected to contribute to the development of new sterilisation techniques and the control of VUV radiation in plasma-based materials processing.

The development of EPOCH-LTP is a one-dimensional (1D) PIC code with an electrostatic field solver and Monte Carlo collisions (MCCs). The main code blocks have been described, namely the electrostatic field solver, the integrator of the equations of motion in phase-space and the MCC algorithm. In addition, an IH block has been implemented, based on the work of Meige *et al* [8], with an improved spatial discretisation that allows the characterisation of inductive heating features down to the cell width scale. Furthermore, the MCC allows the simulation of neutral species as a continuous background gas or as super-particles.

The validation of EPOCH-LTP has been carried out with a proposed set of test problems, which show that the model performance is consistent with the results of already established PIC codes and with experimental work. The high degree of parallelism of EPOCH-LTP is also demonstrated, and it is shown that simulation times can be significantly reduced by using many processors.

As a result, EPOCH-LTP is capable of running not only capacitively coupled plasmas, but also inductively coupled plasmas with a user-defined waveform and the use of an external blocking capacitor, non-perfect absorbing walls and neutral-

charged collisions.

The modular design of EPOCH-LTP is intended to be easily extended, so the code offers great potential for development. Therefore, EPOCH-LTP is not only designed for the specific challenges addressed in this thesis, but is also intended to meet the needs of contemporary LTP research by serving as a platform for future numerical research projects.

Inductive heating effects in HF CCPs have been investigated for the first time with a 1D PIC model that implements an IH model. EPOCH-LTP has been used to simulate a CCP operated in argon at 1 mTorr and driven at 60 MHz, where IH effects are assumed to be the dominant heating mechanism. The simulation results show that transverse inductive currents in the sheath dominate the inductive heating and thus the plasma formation. The plasma density is directly proportional to the size of the inductive current, and the ion angle of incidence at the electrodes increases with increasing current amplitudes. The application of a direct current (DC) bias shifts the location of the inductive heating peak. When the HF inductive current is combined with a low frequency voltage waveform the inductive heating is controlled by the sheath dynamics and this improves the inductive power coupling, i.e. the plasma generation efficiency is increased. This is an interesting result as dynamics at very different time scales are able to create synergies that enhance the inductive power coupling and thus the plasma density.

The development of a 0D chemical kinetics GM with a chemical-radiative reaction scheme for Ar and O_2 species is presented. The model solves the mass continuity equations, for each species in the system, and the electron energy equation. Heavy species, i.e. neutrals and ions, are assumed to have constant temperature. Other important physical aspects that are modelled include the flux or ions and neutrals to the reactor walls. While the ion fluxes are modelled solving the flux balance equation, the diffusion of neutral species is modelled following the model from [199]. Another key aspects are the use of a self-consistent radiative reaction scheme, which has been developed from [15], and the implementation of self-absorption [251].

The primary goal of the GM in this thesis is the simulation of Ar/O_2 double ICPs for studying VUV radiation from atomic oxygen, nevertheless the software is designed with an flexible input deck such that other species and reaction schemes could readily be simulated. The code architecture is intended to be easily extended to provide scope for future development. Therefore, the 0D GM model presented is not only designed for the specific challenges addressed in this thesis, but is also intended to meet the needs of contemporary LTP research by serving as a platform for future numerical research projects.

Investigation of Ar/O_2 DICPs with a focus on VUV emission. The first part of this investigation simulates Ar/O_2 DICPs for operating parameters between 200-800 W, 2-20 Pa and 0-0.20 O_2 fractions. The numerical results have been presented alongside experimental work and show that the GM is performing correctly and that temperature of neutrals and ions does have an impact on the final results but within a relatively small range. The plasma results, as well as the emission lines measured, are as expected with minor differences for argon metastables and the 777 nm emission line. Oxygen VUV emission results show good agreement with experimental data, with the 130 nm line, from the $O(^3S) \rightarrow O$ transition, clearly dominating. The 135 nm line, from the $O(^5S) \rightarrow O$ transition, is an order of magnitude lower and emission from cascading reactions is negligible.

The second part of results investigates oxygen VUV emission over a broader range of total pressure and power. The GM results for plasmas with 0-0.2 O_2 fraction, 0.3-100 Pa and 100-2000 W have shown that oxygen VUV emission, in general terms, increases within the investigated power and oxygen fraction and peak emission intensities are found for pressures between 5-50 Pa. The 130 nm line dominates for most of the parameter space investigated and the most significant chemical pathway leading to $O(^3S)$ is the electron impact excitation to $O(^3P)$ that then naturally decays to $O(^3S)$.

Results of VUV emission intensities with respect to ion fluxes and oxygen diffusion to the reactor walls have also been presented. While VUV emission is largest with respect to ion fluxes at high pressures, oxygen diffusion is much larger than VUV emission for the parameter space investigated.

Future work Based on the numerical models developed and the results obtained in this thesis, several directions for future research are suggested.

- **Extend EPOCH-LTP to 2 and 3 dimensions.** This would allow the study of more complex physical phenomena. For example, inductive heating effects, which are inherently three-dimensional in nature, could be analysed more accurately in a multi-dimensional framework than in the current study. While an increase in dimensionality leads to a significant increase in computational requirements, EPOCH's efficient parallelization, designed for modern supercomputing architectures, significantly mitigates this challenge associated with particle-in-cell (PIC) models.

- **Application of MCC method for super-particle collisions.** EPOCH-LTP can be used to simulate collisions between super-particles, which would enable the study of density fluctuations in neutral species caused by interactions with plasmas. Nevertheless, this would first require a rigorous validation of the MCC method when applied to collisions between super-particles.

- **Expanding the reaction set of the MCC method.** The MCC method has been structured to allow easy extension of the reaction set. It currently includes elastic scattering, excitation, ionisation and charge exchange reactions, but an extension to include processes such as molecular recombination and dissociation would allow, for instace, the simulation of oxygen plasmas.

- **Further investigation of inductive heating effects in HF CCPs.** The investigation carried out in this thesis could be continued by developing simulations that more accurately replicate experimental setups. For example, by adding two inductive currents, each adjacent to the electrodes and with opposite flow directions. Such a setup in combination with a low frequency voltage source may also show similar synergistic phenomena as presented in Chapter 4.

- **Combine the MCC method in EPOCH-LTP with the electromagnetic solver in EPOCH.** The modular structure of EPOCH and EPOCH-LTP should allow this combination without much coding effort. This would allow the self-consistent simulations of electromagnetic effects in LTPs, such as those observed in ICPs and HF CCPs.

- **Hybrid PIC and 0D GM approaches.** In this thesis a PIC and GM model has been developed. The integration of the GM into EPOCH-LTP has the potential to improve collisional modelling in the EPOCH-LTP, reducing the need to simulate large quantities of neutral super-particles and thus reducing computational cost.

- **Study of VUV emission in oxygen plasmas under pulsed power conditions.** Building on preliminary studies [91, 101, 262], pulsed power operations can be used as an additional control parameter to tune the production of metastable species and consequently the VUV emission in oxygen. A first investigation in this direction could use the GM model developed in this thesis and study VUV emission under variation of power pulse frequency, and duty ratio.

Bibliography

[1] National Research Council 1995 *Plasma Science: From Fundamental Research to Technological Applications*(Washington, DC: The National Academies Press) ISBN 978-0-309-05231-3

[2] Chen F F 2016 *Introduction to Plasma Physics and Controlled Fusion*(Springer Cham) ISBN 978-3-319-22308-7

[3] Ferrière K M 2001 *Rev. Mod. Phys.* **73**(4) 1031–1066

[4] Ridgers C P, Brady C S, Duclous R, Kirk J G, Bennett K, Arber T D, Robinson A P L and Bell A R 2012 *Phys. Rev. Lett.* **108**(16) 165006

[5] Fridman A 2008 *Plasma chemistry*(Cambridge university press) ISBN 9780511546075

[6] Raizer Y, Shneider M and Yatsenko N 1995 *Radio-Frequency Capacitive Discharges*(CRC Press) ISBN 9780203741337

[7] Lieberman M A and Lichtenberg A J 2005 *Principles of Plasma Discharges and Materials Processing*(John Wiley & Sons, Ltd) ISBN 9780471724254

[8] Meige A, Boswell R W, Charles C and Turner M M 2005 *Physics of Plasmas* **12** 052317

[9] Turner M M, Derzsi A, Donkó Z, Eremin D, Kelly S J, Lafleur T and Mussenbrock T 2013 *Physics of Plasmas* **20** 013507

[10] Donkó Z, Derzsi A, Vass M, Horváth B, Wilczek S, Hartmann B and Hartmann P 2021 *Plasma Sources Science and Technology* **30** 095017

[11] Schulenberg D A, Korolov I, Donkó Z, Derzsi A and Schulze J 2021 *Plasma Sources Science and Technology* **30** 105003

[12] Donkó Z, Schulze J, Heil B G and Czarnetzki U 2008 *Journal of Physics D: Applied Physics* **42** 025205

[13] Lafleur T and Booth J P 2012 *Journal of Physics D: Applied Physics* **45** 395203

[14] Kramida A, Yu Ralchenko, Reader J and and NIST ASD Team *NIST Atomic Spectra Database (ver. 5.10) National Institute of Standards and Technology, Gaithersburg, MD.* Accessed Oct, 2023 URL https://physics.nist.gov/asd

[15] Fiebrandt M, Bibinov N and Awakowicz P 2020 *Plasma Sources Science and Technology* **29** 045018

[16] Engelbrecht M O, Jenderny J, Hylla H, Filla D, Awakowicz P, Korolov I, Ridgers C P and Gibson A R 2024 *Plasma Sources Science and Technology* **33** 095008

[17] Fiebrandt M, Oberberg M and Awakowicz P 2017 *Journal of Applied Physics* **122** 013302

[18] Fiebrandt M, Hillebrand B, Spiekermeier S, Bibinov N, Böke M and Awakowicz P 2017 *Journal of Physics D: Applied Physics* **50** 355202

[19] Fiebrandt M, Hillebrand B, Lackmann J W, Raguse M, Moeller R, Awakowicz P and Stapelmann K 2018 *Journal of Physics D: Applied Physics* **51** 045401

[20] Sato T and Makabe T 2008 *Journal of Physics D: Applied Physics* **41** 035211

[21] Gudmundsson J T and Thorsteinsson E G 2007 *Plasma Sources Science and Technology* **16** 399

[22] Hayashi Y, Hirao S, Zhang Y, Gans T, O'Connell D, Petrović Z L and Makabe T 2009 *Journal of Physics D: Applied Physics* **42** 145206

[23] Atzeni S and Meyer-ter Vehn J 2004 *The Physics of Inertial Fusion: Beam-Plasma Interaction, Hydrodynamics, Hot Dense Matter*(Oxford University Press) ISBN 9780198562641

[24] Saha M N 1920 *The London, Edinburgh, and Dublin Philosophical Magazine and Journal of Science* **40** 472–488

[25] Chabert P and Braithwaite N 2011 *Physics of Radio-Frequency Plasmas*(Cambridge University Press)

[26] Wang S B and Wendt A E 2001 *Journal of Vacuum Science & Technology A* **19** 2425–2432

[27] Athavale S D and Economou D J 1995 *Journal of Vacuum Science & Technology A* **13** 966–971

[28] Schaepkens M, Oehrlein G S and Cook J M 2000 *Journal of Vacuum Science & Technology B: Microelectronics and Nanometer Structures Processing, Measurement, and Phenomena* **18** 848–855

[29] Barela M J, Anderson H M and Oehrlein G S 2005 *Journal of Vacuum Science & Technology A* **23** 408–416

[30] Banna S, Agarwal A, Tokashiki K, Cho H, Rauf S, Todorow V, Ramaswamy K, Collins K, Stout P, Lee J Y, Yoon J, Shin K, Choi S J, Cho H S, Kim H J, Lee C and Lymberopoulos D 2009 *IEEE Transactions on Plasma Science* **37** 1730–1746

[31] Agarwal A, Stout P J, Banna S, Rauf S and Collins K 2011 *Journal of Vacuum Science & Technology A* **29** 011017

[32] Diomede P, Economou D J and Donnelly V M 2011 *Journal of Applied Physics* **109** 083302

[33] Abreu A C, Tavares R R, Borges A, Mergulhão F and Simões M 2013 *Journal of Antimicrobial Chemotherapy* **68** 2718–2732

[34] Gómez-López V M, Ragaert P, Debevere J and Devlieghere F 2008 *Critical Reviews in Food Science and Nutrition* **48** 487–495

[35] Denis B, Steves S, Semmler E, Bibinov N, Novak W and Awakowicz P 2012 *Plasma Processes and Polymers* **9** 619–629

[36] A F 2011 *Journal of Hospital Infection* **77**(3) 210–212

[37] Siani H and Maillard J Y 2015 *European Journal of Clinical Microbiology & Infectious Diseases* **34** 1–11

[38] Charles C 2009 *Journal of Physics D: Applied Physics* **42** 163001

[39] Chen F F 2008 *IEEE Transactions on Plasma Science* **36** 2095–2110

[40] Takahashi K, Oguni K, Yamada H and Fujiwara T 2008 *Physics of Plasmas* **15** 084501

[41] Zhurin V V, Kaufman H R and Robinson R S 1999 *Plasma Sources Science and Technology* **8** R1

[42] Goebel D M, Katz I and Mikellides I G 2008 *Fundamentals of electric propulsion*(John Wiley & Sons)

[43] Tendero C, Tixier C, Tristant P, Desmaison J and Leprince P 2006 *Spectrochimica Acta Part B: Atomic Spectroscopy* **61** 2–30

[44] Liu Z M, Cui S, Luo Z, Zhang C, Wang Z and Zhang Y 2016 *Journal of Manufacturing Processes* **23** 315–327

[45] Foster J E 2017 *Physics of Plasmas* **24** 055501

[46] Duarte S and Panariello B H 2020 *Archives of Biochemistry and Biophysics* **693** 108560

[47] Šimek M and Homola T 2021 *The European Physical Journal D* **75**(7) 210

[48] Kanarik K J, Lill T, Hudson E A, Sriraman S, Tan S, Marks J, Vahedi V and Gottscho R A 2015 *Journal of Vacuum Science & Technology A* **33** 020802

[49] Johnson R W, Hultqvist A and Bent S F 2014 *Materials Today* **17** 236–246

[50] Fiebrandt M, Lackmann J W and Stapelmann K 2018 *Plasma Processes and Polymers* **15** 1800139

[51] Zhianmanesh M, Gilmour A, Bilek M M M and Akhavan B 2023 *Applied Physics Reviews* **10** 021301

[52] Akdoğan E and Şirin H T 2021 *Materials Science and Engineering: C* **131** 112474

[53] Lee C G N, Kanarik K J and Gottscho R A 2014 *Journal of Physics D: Applied Physics* **47** 273001

[54] Arnold J C and Sawin H H 1991 *Journal of Applied Physics* **70** 5314–5317

[55] Jansen H, de Boer M, Wiegerink R, Tas N, Smulders E, Neagu C and Elwenspoek M 1997 *Microelectronic Engineering* **35** 45–50

[56] Darnon M 2017 2 - plasma etching in microelectronics *Plasma Etching Processes for CMOS Devices Realization* ed Posseme N(Elsevier) pp 23–58 ISBN 978-1-78548-096-6

[57] Coburn J W and Winters H F 1979 *Journal of Applied Physics* **50** 3189–3196

[58] Hargis P J J, Greenberg K E, Miller P A, Gerardo J B, Torczynski J R, Riley M E, Hebner G A, Roberts J R, Olthoff J K, Whetstone J R, Van Brunt R J, Sobolewski M A, Anderson H M, Splichal M P, Mock J L, Bletzinger P, Garscadden A, Gottscho R A, Selwyn G, Dalvie M, Heidenreich J E, Butterbaugh J W, Brake M L, Passow M L, Pender J, Lujan A, Elta M E, Graves D B, Sawin H H, Kushner M J, Verdeyen J T, Horwath R and Turner T R 1994 *Review of Scientific Instruments* **65** 140–154

[59] International Telecommunication Union *Documents of the International Radio Conference (Atlantic City, 1947) p. 650* Accessed Aug, 2024 URL https://search.itu.int/history/HistoryDigitalCollectionDocLibrary/4.62.51.en.101.pdf

[60] Perret A, Chabert P, Jolly J and Booth J P 2005 *Applied Physics Letters* **86**(2)

[61] Schwarzenbach W, Howling A A, Fivaz M, Brunner S and Hollenstein C 1996 *Journal of Vacuum Science & Technology A* **14** 132–138

[62] Yan M and Goedheer W J 1999 *Plasma Sources Science and Technology* **8**(3) 349–354

[63] Barnat E V, Miller P A, Hebner G A, Paterson A M, Panagopoulos T, Hammond E and Holland J 2007 *Applied Physics Letters* **90** 201503

[64] Goto H H, Löwe H and Ohmi T 1992 *Journal of Vacuum Science & Technology A* **10** 3048–3054

[65] Goto H, Lowe H D and Ohmi T 1993 *IEEE Transactions on Semiconductor Manufacturing* **6** 58–64

[66] Vahedi V, Birdsall C K, Lieberman M A, DiPeso G and Rognlien T D 1993 *Physics of Fluids B: Plasma Physics* **5** 2719–2729

[67] Kitajima T, Takeo Y, Petrović Z L and Makabe T 2000 *Applied Physics Letters* **77** 489–491

[68] Boyle P C, Ellingboe A R and Turner M M 2004 *Plasma Sources Science and Technology* **13** 493

[69] Oehrlein G S, Metzler D and Li C 2015 *ECS Journal of Solid State Science and Technology* **4** N5041

[70] Faraz T, Roozeboom F, Knoops H C M and Kessels W M M 2015 *ECS Journal of Solid State Science and Technology* **4** N5023

[71] Knoops H C M, Faraz T, Arts K and Kessels W M M E 2019 *Journal of Vacuum Science & Technology A* **37** 030902

[72] Adamovich I, Agarwal S, Ahedo E, Alves L L, Baalrud S, Babaeva N, Bogaerts A, Bourdon A, Bruggeman P J, Canal C, Choi E H, Coulombe S, Donkó Z, Graves D B, Hamaguchi S, Hegemann D, Hori M, Kim H H, Kroesen G M W, Kushner M J, Laricchiuta A, Li X, Magin T E, Thagard S M, Miller V, Murphy A B, Oehrlein G S, Puac N, Sankaran R M, Samukawa S, Shiratani M, Šimek M, Tarasenko N, Terashima K, Jr E T, Trieschmann J, Tsikata S, Turner M M, van der Walt I J, van de Sanden M C M and von Woedtke T 2022 *Journal of Physics D: Applied Physics* **55** 373001

[73] Lieberman M A, Booth J P, Chabert P, Rax J M and Turner M M 2002 *Plasma Sources Science and Technology* **11** 283

[74] Chabert P, Raimbault J L, Levif P, Rax J M and Lieberman M A 2006 *Plasma Sources Science and Technology* **15** S130

[75] Salabas A, Marques L, Jolly J, Gousset G and Alves L L 2004 *Journal of Applied Physics* **95**(9) 4605–4620

[76] Lee I, Graves D B and Lieberman M A 2008 *Plasma Sources Science and Technology* **17** 015018

[77] Yang Y and Kushner M J 2010 *Plasma Sources Science and Technology* **19** 055011

[78] Yang Y and Kushner M J 2010 *Plasma Sources Science and Technology* **19** 055012

[79] Perret A, Chabert P, Booth J P, Jolly J, Guillon J and Auvray P 2003 *Applied Physics Letters* **83** 243–245

[80] Kawamura E, Lieberman M A and Graves D B 2014 *Plasma Sources Science and Technology* **23** 064003

[81] Horneck G, Klaus D M and Mancinelli R L 2010 *Microbiology and Molecular Biology Reviews* **74** 121–156

[82] Kylián O, Denis B, Stapelmann K, Ruiz A, Rauscher H and Rossi F 2011 *Plasma Processes and Polymers* **8** 1137–1145

[83] Bartis E A J, Barrett C, Chung T Y, Ning N, Chu J W, Graves D B, Seog J and Oehrlein G S 2013 *Journal of Physics D: Applied Physics* **47** 045202

[84] von Keudell A, Awakowicz P, Benedikt J, Raballand V, Yanguas-Gil A, Opretzka J, Flötgen C, Reuter R, Byelykh L, Halfmann H, Stapelmann K, Denis B, Wunderlich J, Muranyi P, Rossi F, Kylián O, Hasiwa N, Ruiz A, Rauscher H, Sirghi L, Comoy E, Dehen C, Challier L and Deslys J P 2010 *Plasma Processes and Polymers* **7** 327–352

[85] Lerouge S, Fozza A C, Wertheimer M R, Marchand R and Yahia L 2000 *Plasmas and Polymers* **5** 31–46

[86] Nest D, Graves D B, Engelmann S, Bruce R L, Weilnboeck F, Oehrlein G S, Andes C and Hudson E A 2008 *Applied Physics Letters* **92** 153113

[87] Titus M J, Graves D B, Yamaguchi Y and Hudson E A 2011 *Journal of Physics D: Applied Physics* **44** 085204

[88] Shin H, Zhu W, Donnelly V M and Economou D J 2012 *Journal of Vacuum Science & Technology A* **30** 021306

[89] Lee H C, Hwang H J, Kim Y C, Kim J Y, Kim D H and Chung C W 2013 *Physics of Plasmas* **20** 033504

[90] Uchida S, Takashima S, Hori M, Fukasawa M, Ohshima K, Nagahata K and Tatsumi T 2008 *Journal of Applied Physics* **103** 073303

[91] Tian P and Kushner M J 2015 *Plasma Sources Science and Technology* **24** 034017

[92] Nakano T, Kumagai S and Samukawa S 2002 *Journal of Applied Physics* **92** 2990–2995

[93] Woodworth J R, Riley M E, Amatucci V A, Hamilton T W and Aragon B P 2001 *Journal of Vacuum Science & Technology A* **19** 45–55

[94] Jinnai B, Fukuda S, Ohtake H and Samukawa S 2010 *Journal of Applied Physics* **107** 043302

[95] Titus M J, Nest D G and Graves D B 2009 *Journal of Physics D: Applied Physics* **42**(15) 152001

[96] Boffard J B, Lin C C, Culver C, Wang S, Wendt A E, Radovanov S and Persing H 2014 *Journal of Vacuum Science & Technology A* **32** 021304

[97] Boffard J B, Lin C C, Wang S, Wendt A E, Culver C, Radovanov S and Persing H 2014 *Journal of Vacuum Science & Technology A* **33** 021306

[98] Fantz U, Briefi S, Rauner D and Wünderlich D 2016 *Plasma Sources Science and Technology* **25** 045006

[99] Fozza A C, Kruse A, Holländer A, Ricard A and Wertheimer M R 1998 *Journal of Vacuum Science & Technology A* **16** 72–77

[100] Wünderlich D, Briefi S, Friedl R and Fantz U 2021 *Review of Scientific Instruments* **92** 123510

[101] Tian P and Kushner M J 2017 *Plasma Sources Science and Technology* **26** 024005

[102] Woodworth J R, Blain M G, Jarecki R L, Hamilton T W and Aragon B P 1999 *Journal of Vacuum Science & Technology A* **17** 3209–3217

[103] Truica-Marasescu F E and Wertheimer M R 2005 *Macromolecular Chemistry and Physics* **206** 744–757

[104] Cook J G, LeBrun L, Zhongming L and Ogryzlo E A 1995 *Journal of Applied Physics* **77** 1690–1695

[105] Collart E J H, Baggerman J A G and Visser R J 1995 *Journal of Applied Physics* **78** 47–54

[106] Korzec D, Schott M and Engemann J 1995 *Journal of Vacuum Science & Technology A* **13** 843–848

[107] Kelly P and Arnell R 2000 *Vacuum* **56** 159–172

[108] Depla D, Mahieu S and De Gryse R 2009 *Thin Solid Films* **517** 2825–2839

[109] Mitschker F, Dietrich J, Ozkaya B, de los Arcos T, Giner I, Awakowicz P and Grundmeier G 2015 *Plasma Processes and Polymers* **12** 1002–1009

[110] Ries S, Bibinov N, Rudolph M, Schulze J, Mráz S, Schneider J M and Awakowicz P 2018 *Plasma Sources Science and Technology* **27** 094001

[111] Moisan, Michel, Boudam, Karim, Carignan, Denis, Kéroack, Danielle, Levif, Pierre, Barbeau, Jean, Séguin, Jacynthe, Kutasi, Kinga, Elmoualij, Benaïssa, Thellin, Olivier and Zorzi, Willy 2013 *Eur. Phys. J. Appl. Phys.* **63** 10001

[112] Gudmundsson J T, Kimura T and Lieberman M A 1999 *Plasma Sources Science and Technology* **8**(1) 22–30

[113] Gudmundsson J T, Marakhtanov A M, Patel K K, Gopinath V P and Lieberman M A 2000 *Journal of Physics D: Applied Physics* **33**(11) 1323–1331

[114] Turner M M 2015 *Plasma Sources Science and Technology* **24** 035027

[115] Tien P K and Moshman J 1956 *Journal of Applied Physics* **27** 1067–1078

[116] Buneman O 1959 *Phys. Rev.* **115**(3) 503–517

[117] Birdsall C K and Bridges W B 1961 *Journal of Applied Physics* **32** 2611–2618

[118] Dawson J 1962 *The Physics of Fluids* **5** 445–459

[119] National Academies of Sciences, Engineering, and Medicine 2021 *Plasma Science: Enabling Technology, Sustainability, Security, and Exploration*(Washington, DC: The National Academies Press) ISBN 978-0-309-67760-8

[120] US Department of Energy, Office of Science 2023 *Plasma Science for Microelectronics Nanofabrication* Accessed January, 2024 URL https://science.osti.gov/-/media/fes/pdf/2023/DOE_FES_PlasmaScience_Semiconductors_Final.pdf

[121] Lafleur T, Baalrud S D and Chabert P 2016 *Physics of Plasmas* **23** 053502

[122] Poder K, Tamburini M, Sarri G, Di Piazza A, Kuschel S, Baird C D, Behm K, Bohlen S, Cole J M, Corvan D J, Duff M, Gerstmayr E, Keitel C H, Krushelnick K, Mangles S P D, McKenna P, Murphy C D, Najmudin Z, Ridgers C P, Samarin G M, Symes D R, Thomas A G R, Warwick J and Zepf M 2018 *Phys. Rev. X* **8**(3) 031004

[123] Magazova A and Agar D W 2023 *Chemie Ingenieur Technik* **95** 780–784

[124] Boswell R W and Morey I J 1987 *Le Vide, Les Couches Minces* **237** 143–145

[125] Boswell R W and Morey I J 1988 *Applied Physics Letters* **52** 21–23

[126] Vender D and Boswell R 1990 *IEEE Transactions on Plasma Science* **18** 725–732

[127] Vender D and Boswell R W 1992 *Journal of Vacuum Science & Technology A* **10** 1331–1338

[128] Ventzek P L G, Hoekstra R J and Kushner M J 1994 *Journal of Vacuum Science & Technology B: Microelectronics and Nanometer Structures Processing, Measurement, and Phenomena* **12** 461–477

[129] Birdsall C K and Langdon A B 1991 *Plasma Physics via Computer Simulations*(CRC Press)

[130] Verboncoeur J, Alves M, Vahedi V and Birdsall C 1993 *Journal of Computational Physics* **104** 321–328

[131] Deshmukh S C and Economou D J 1993 *Journal of Vacuum Science & Technology B: Microelectronics and Nanometer Structures Processing, Measurement, and Phenomena* **11** 206–215

[132] Paranjpe A P 1994 *Journal of Vacuum Science & Technology A* **12** 1221–1228

[133] Kondo K, Kuroda H and Makabe T 1994 *Applied Physics Letters* **65** 31–33

[134] Surendra M and Graves D 1991 *IEEE Transactions on Plasma Science* **19** 144–157

[135] Turner M M and Hopkins M B 1992 *Phys. Rev. Lett.* **69**(24) 3511–3514

[136] Godyak V A and Piejak R B 1990 *Phys. Rev. Lett.* **65**(8) 996–999

[137] Godyak V A, Piejak R B and Alexandrovich B M 1992 *Plasma Sources Science and Technology* **1** 36

[138] Economou D, Bartel T, Wise R and Lymberopoulos D 1995 *IEEE Transactions on Plasma Science* **23** 581–590

[139] Hara K and Hanquist K 2018 *Plasma Sources Science and Technology* **27** 065004

[140] Hagelaar G J M and Pitchford L C 2005 *Plasma Sources Science and Technology* **14** 722

[141] Wang H Y, Jiang W and Wang Y N 2009 *Computer Physics Communications* **180** 1305–1314

[142] Kühn C and Groll R 2021 *Computer Physics Communications* **262** 107853

[143] Fubiani G, Garrigues L, Hagelaar G, Kohen N and Boeuf J P 2017 *New Journal of Physics* **19**(1) 015002

[144] Montellano I M, Wünderlich D, Mochalskyy S and Fantz U 2019 *Journal of Physics D: Applied Physics* **52** 235202

[145] Lafleur T and Chabert P 2017 *Plasma Sources Science and Technology* **27** 015003

[146] Villafana W 2021 *Numerical Particle-In-Cell studies of Hall thrusters using unstructured grids* Ph.D. thesis Centre Européen de Recherche et Formation Avancées en Calcul Scientifique (CERFACS) URL https://oatao.univ-toulouse.fr/28825/

[147] Charoy T, Boeuf J P, Bourdon A, Carlsson J A, Chabert P, Cuenot B, Eremin D, Garrigues L, Hara K, Kaganovich I D, Powis A T, Smolyakov A, Sydorenko D, Tavant A, Vermorel O and Villafana W 2019 *Plasma Sources Science and Technology* **28**(10) 105010

[148] Coche P and Garrigues L 2014 *Physics of Plasmas* **21**(2) 023503

[149] Taccogna F, Minelli P, Asadi Z and Bogopolsky G 2019 *Plasma Sources Science and Technology* **28**(6) 064002

[150] Janhunen S, Smolyakov A, Sydorenko D, Jimenez M, Kaganovich I and Raitses Y 2018 *Physics of Plasmas* **25**(8) 082308

[151] Hur M Y, Kim J S, Song I C, Verboncoeur J P and Lee H J 2019 *Plasma Research Express* **1** 015016

[152] Mertmann P, Eremin D, Mussenbrock T, Brinkmann R P and Awakowicz P 2011 *Computer Physics Communications* **182** 2161–2167

[153] Juhasz Z, Ďurian J, Derzsi A, Štefan Matejčík, Donkó Z and Hartmann P 2021 *Computer Physics Communications* **263** 107913

[154] Eremin D, Kemaneci E, Matsukuma M, Mussenbrock T and Brinkmann R P 2023 *Plasma Sources Science and Technology* **32**(4) 044007

[155] Kim J S, Hur M Y, Kim C H, Kim H J and Lee H J 2018 *Journal of Physics D: Applied Physics* **51**(10) 104004

[156] Wang L, Hartmann P, Donkó Z, Song Y H and Schulze J 2021 *Plasma Sources Science and Technology* **30**(8) 085011

[157] Park G, Kim J S, Kim C H, Kim H J and Lee H J 2022 *IEEE Transactions on Plasma Science* **50**(2) 540–549

[158] Turner M M 2017 *Plasma Processes and Polymers* **14** 1600121

[159] Piejak R B, Godyak V A and Alexandrovich B M 1992 *Plasma Sources Science and Technology* **1** 179

[160] El-Fayoumi I M and Jones I R 1998 *Plasma Sources Science and Technology* **7** 179

[161] Lee M H and Chung C W 2006 *Physics of Plasmas* **13** 063510

[162] Godyak V 2013 *Journal of Physics D: Applied Physics* **46** 283001

[163] Halfmann H, Bibinov N, Wunderlich J and Awakowicz P 2007 *Journal of Physics D: Applied Physics* **40** 4145

[164] Zhang Z L, Nie Q Y, Kong F R, Zhang X N, Jiang B H, Lim J M, Levchenko I and Xu S 2018 *IEEE Transactions on Plasma Science* **46** 954–961

[165] Nanbu K 2000 *IEEE Transactions on Plasma Science* **28** 971–990

[166] Chrisman B, Sentoku Y and Kemp A J 2008 *Physics of Plasmas* **15** 056309

[167] Cook J W S, Dendy R O and Chapman S C 2013 *Plasma Physics and Controlled Fusion* **55** 065003

[168] Baumann G and Nordlund A 2012 *The Astrophysical Journal Letters* **759** L9

[169] Deca J, Divin A, Lapenta G, Lembège B, Markidis S and Horányi M 2014 *Phys. Rev. Lett.* **112**(15) 151102

[170] Liu K, Gary S P and Winske D 2011 *Journal of Geophysical Research: Space Physics* **116**

[171] Lee S H, Iza F and Lee J K 2006 *Physics of Plasmas* **13** 057102

[172] Klimo O, Weber S, Tikhonchuk V T and Limpouch J 2010 *Plasma Physics and Controlled Fusion* **52** 055013

[173] Debayle A, Honrubia J J, d'Humières E and Tikhonchuk V T 2010 *Phys. Rev. E* **82**(3) 036405

[174] Donkó Z 2011 *Plasma Sources Science and Technology* **20** 024001

[175] Vahedi V and Surendra M 1995 *Computer Physics Communications* **87** 179–198 particle Simulation Methods

[176] Horváth B, Daksha M, Korolov I, Derzsi A and Schulze J 2017 *Plasma Sources Science and Technology* **26** 124001

[177] Lafleur T, Boswell R W and Booth J P 2012 *Applied Physics Letters* **100** 194101

[178] Schüngel E, Brandt S, Korolov I, Derzsi A, Donkó Z and Schulze J 2015 *Physics of Plasmas* **22** 043512

[179] Sharma S, Sirse N, Kaw P K, Turner M M and Ellingboe A R 2016 *Physics of Plasmas* **23** 110701

[180] Okuda H and Birdsall C K 1970 *The Physics of Fluids* **13** 2123–2134

[181] Langdon A 1970 *Journal of Computational Physics* **6** 247–267

[182] Weng Y and Kushner M J 1990 *Phys. Rev. A* **42**(10) 6192–6200

[183] Rockwood S D 1973 *Phys. Rev. A* **8**(5) 2348–2358

[184] Verboncoeur J P, Langdon A B and Gladd N T 1995 *Computer Physics Communications* **87**(1) 199–211

[185] Vahedi V and Dipeso G 1997 *Journal of Computational Physics* **131**(1) 149–163

[186] Donkó Z 2011 *Plasma Sources Science and Technology* **20**(2) 024001

[187] Princeton Plasma Physics Laboratory *Simulation tools for the modeling of low-temperature plasma devices* Accessed Nov, 2023 URL https://pcrf.princeton.edu/capabilities/modeling-tools-and-computer-codes/info/

[188] Rauf S 2020 *Plasma Sources Science and Technology* **29**(9) 095019

[189] Princeton Plasma Physics Laboratory *LSP Code* Accessed Nov, 2023 URL https://pcrf.princeton.edu/capabilities/modeling-tools-and-computer-codes/lsp-code/

[190] Particle In Cell Consulting LLC *CTSP (Contamination Transport Simulation Program)* Accessed Nov, 2023 URL https://www.particleincell.com/

[191] Boltzplatz *PICLas* Accessed Nov, 2023 URL https://boltzplatz.eu/plasma-simulation/

[192] Tech-X Corporation *VSimPlasma* Accessed Aug, 2024 URL https://txcorp.com/vsim-plasma/

[193] Dassault Systems *CST* Accessed Aug, 2024 URL https://www.cst.com/

[194] Hurlbatt A, Gibson A R, Schröter S, Bredin J, Foote A P S, Grondein P, O'Connell D and Gans T 2017 *Plasma Processes and Polymers* **14** 1600138

[195] Lieberman M A and Gottscho R A 1994 Design of high-density plasma sources for materials processing *Plasma Sources for Thin Film Deposition and Etching* (*Physics of Thin Films* vol 18)(Elsevier) pp 1–119

[196] Lee C, Graves D B, Lieberman M A and Hess D W 1994 *Journal of The Electrochemical Society* **141** 1546

[197] Lee C and Lieberman M A 1995 *Journal of Vacuum Science & Technology A* **13** 368–380

[198] Kim S, Lieberman M A, Lichtenberg A J and Gudmundsson J T 2006 *Journal of Vacuum Science & Technology A* **24** 2025–2040

[199] Thorsteinsson E G and Gudmundsson J T 2010 *Plasma Sources Science and Technology* **19** 055008

[200] Park G, Lee H, Kim G and Lee J K 2008 *Plasma Processes and Polymers* **5** 569–576

[201] Lieberman M A and Ashida S 1996 *Plasma Sources Science and Technology* **5** 145

[202] Monahan D D and Turner M M 2008 *Plasma Sources Science and Technology* **17** 045003

[203] Toneli D A, Pessoa R S, Roberto M and Gudmundsson J T 2015 *Journal of Physics D: Applied Physics* **48** 495203

[204] Grondein P, Lafleur T, Chabert P and Aanesland A 2016 *Physics of Plasmas* **23** 033514

[205] Berthelot A and Bogaerts A 2017 *The Journal of Physical Chemistry C* **121** 8236–8251

[206] Davies H L, Guerra V, van der Woude M, Gans T, O'Connell D and Gibson A R 2023 *Plasma Sources Science and Technology* **32** 014003

[207] Dorai R and Kushner M J 2003 *Journal of Physics D: Applied Physics* **36** 666

[208] Stafford D S and Kushner M J 2004 *Journal of Applied Physics* **96** 2451–2465

[209] Dorai R 2002 *Modeling of atmospheric pressure plasma processing of gases and surfaces* Phd thesis Department of Chemical and Biomolecular Engineering, University of Illinois

[210] Munro J J and Tennyson J 2008 *Journal of Vacuum Science & Technology A* **26** 865–869

[211] Pancheshnyi S, Eismann B, Hagelaar G and Pitchford L 2008 *Computer code ZDPlasKin* Accessed Jan, 2024 URL http://www.zdplaskin.laplace.univ-tlse.fr

[212] Dijk, van J, Peerenboom K, Jimenez-Diaz M, Mihailova D and Mullen, van der J 2009 *Journal of Physics D: Applied Physics* **42** 194012–1/14

[213] Alves L L, Becker M M, van Dijk J, Gans T, Go D B, Stapelmann K, Tennyson J, Turner M M and Kushner M J 2023 *Plasma Sources Science and Technology* **32** 023001

[214] Gudmundsson J T 2001 *Plasma Sources Science and Technology* **10** 76

[215] Monahan D D and Turner M M 2009 *Plasma Sources Science and Technology* **18** 045024

[216] Gudmundsson J, Hjartarson A and Thorsteinsson E 2012 *Vacuum* **86** 808–812

[217] Arber T D, Bennett K, Brady C S, Lawrence-Douglas A, Ramsay M G, Sircombe N J, Gillies P, Evans R G, Schmitz H, Bell A R and Ridgers C P 2015 *Plasma Physics and Controlled Fusion* **57** 113001

[218] University of Warwick *Extendable PIC Open Collaboration (EPOCH)* Accessed March, 2024 URL https://epochpic.github.io/

[219] Kawamura E, Birdsall C K and Vahedi V 2000 *Plasma Sources Science and Technology* **9** 413

[220] Balay S, Abhyankar S, Adams M F, Benson S, Brown J, Brune P, Buschelman K, Constantinescu E M, Dalcin L, Dener A, Eijkhout V, Faibussowitsch J, Gropp W D, Hapla V, Isaac T, Jolivet P, Karpeev D, Kaushik D, Knepley M G, Kong F, Kruger S, May D A, McInnes L C, Mills R T, Mitchell L, Munson T, Roman J E, Rupp K, Sanan P, Sarich J, Smith B F, Zampini

S, Zhang H, Zhang H and Zhang J *Portable, Extensible Toolkit for Scientific Computation (PETSc)* Accessed March, 2024 URL https://petsc.org/

[221] Schmidt J and Moldover M 2003 *International Journal of Thermophysics*

[222] Boris J P 1970 *Acceleration calculation from a scalar potential* URL https://www.osti.gov/biblio/4168374

[223] Cartwright K L, Verboncoeur J P and Birdsall C K 2000 *Journal of Computational Physics* **162**(2) 483–513

[224] Croes M V 2017 *Modélisation de la décharge plasma d'un propulseur à effet Hall* Ph.D. thesis École Polytechnique Université Paris-Saclay URL https://theses.hal.science/tel-01652098v2

[225] Lafleur T and Boswell R W 2012 *Physics of Plasmas* **19** 023508

[226] Boyd I D and Schwartzentruber T E 2017 *Direct Simulation Monte Carlo*(Cambridge University Press) p 183–251 Cambridge Aerospace Series

[227] Fitzpatrick R 2021 *Plasma Physics,* Accessed Jan, 2024. URL https://farside.ph.utexas.edu/teaching/plasma/lectures/Plasma2html.html

[228] Meige A and Boswell R W 2006 *Physics of Plasmas* **13** 092104

[229] Lafleur T and Chabert P 2015 *Plasma Sources Science and Technology* **24** 025017

[230] Baalrud S D, Lafleur T, Boswell R W and Charles C 2011 *Physics of Plasmas* **18** 063502

[231] 2004 Cross sections extracted from MAGBOLTZ (v7.1) Accessed Nov, 2012 URL www.lxcat.net/Biagi-v7.1

[232] Phelps A V 1994 *Journal of Applied Physics* **76**(2) 747–753

[233] Alves L L 2014 *Journal of Physics: Conference Series* **565** 012007

[234] Yamabe C, Buckman S J and Phelps A V 1983 *Phys. Rev. A* **27**(3) 1345–1352

[235] Vass M, Palla P and Hartmann P 2022 *Plasma Sources Science and Technology* **31** 064001

[236] Lafleur T 2015 *Plasma Sources Science and Technology* **25** 013001

[237] Wilczek S, Schulze J, Brinkmann R P, Donkó Z, Trieschmann J and Mussenbrock T 2020 *Journal of Applied Physics* **127** 181101

[238] Wild C and Koidl P 1991 *Journal of Applied Physics* **69** 2909–2922

[239] Schüngel E, Donkó Z and Schulze J 2017 *Plasma Processes and Polymers* **14** 1600117

[240] Heil B G, Czarnetzki U, Brinkmann R P and Mussenbrock T 2008 *Journal of Physics D: Applied Physics* **41** 165202

[241] Amdahl G M 1967 Validity of the single processor approach to achieving large scale computing capabilities *Proceedings of the April 18-20, 1967, Spring Joint Computer Conference*(New York, NY, USA: Association for Computing Machinery) p 483–485 ISBN 9781450378956

[242] Bezanson J, Edelman A, Karpinski S and Shah V B 2017 *SIAM Review* **59** 65–98

[243] Rackauckas C and Nie Q 2017 *Journal of Open Research Software* **5**

[244] Fiebrandt M 2018 *Influence of photon energy and photon / particle fluxes on the inactivation efficiency of B. subtilis spores in low-pressure plasmas* Ph.D. thesis Fakultiät für Elektrotechnik und Informationstechnik

[245] Smirnov B M 1977 *Introduction to Plasma Physics*(Mir Publishers Moscow) chap Appendix I & II, pp 169–170

[246] Sharpless R L and Slanger T G 1989 *The Journal of Chemical Physics* **91** 7947–7950

[247] Chantry P J 1987 *Journal of Applied Physics* **62** 1141–1148

[248] Booth J P and Sadeghi N 1991 *Journal of Applied Physics* **70** 611–620

[249] Hurst G S, Wagner E B and Payne M G 2003 *The Journal of Chemical Physics* **61** 3680–3685

[250] Ashida S, Lee C and Lieberman M A 1995 *Journal of Vacuum Science & Technology A* **13** 2498–2507

[251] Mewe R 1967 *British Journal of Applied Physics* **18** 107

[252] Holstein T 1947 *Phys. Rev.* **72**(12) 1212–1233

[253] Godyak V A 2011 *Plasma Sources Science and Technology* **20** 025004

[254] Zielke D, Briefi S and Fantz U 2021 *Journal of Physics D: Applied Physics* **54** 155202

[255] Rauner D, Briefi S and Fantz U 2019 *Plasma Sources Science and Technology* **28** 095011

[256] Elaissi S, Trabelsi A B G, Alkallas F H, Alrebdi T A and Charrada K 2022 *Materials* **15**

[257] Rauner D, Mattei S, Briefi S, Fantz U, Hatayama A, Lettry J, Nishida K and Tran M Q 2017 *AIP Conference Proceedings* **1869** 030035

[258] Schwabedissen A, Benck E C and Roberts J R 1997 *Phys. Rev. E* **55**(3) 3450–3459

[259] Agarwal S, Quax G W W, van de Sanden M C M, Maroudas D and Aydil E S 2003 *Journal of Vacuum Science & Technology A* **22** 71–81

[260] Takechi K and Lieberman M A 2001 *Journal of Applied Physics* **90** 3205–3211

[261] Kitajima T, Nakano T and Makabe T 2006 *Applied Physics Letters* **88** 091501

[262] Gibson A, Osca Engelbrecht M and Ridgers C 2024 Vacuum ultraviolet photon formation from oxygen atoms in pulsed inductively coupled plasmas(77th Gaseous Electronics Conference)

[263] Lawton S A and Phelps A V 2008 *The Journal of Chemical Physics* **69** 1055–1068

[264] Phelps A *Phelps Database* Accessed March, 2024 URL `https://www.lxcat.net/Phelps`

[265] Laher R R and Gilmore F R 1990 *Journal of Physical and Chemical Reference Data* **19** 277–305

[266] Deutsch H, Scheier P, Becker K and Märk T 2003 *Chemical Physics Letters* **382** 26–31

[267] McConkey J, Malone C, Johnson P, Winstead C, McKoy V and Kanik I 2008 *Physics Reports* **466** 1–103

[268] Straub H C, Renault P, Lindsay B G, Smith K A and Stebbings R F 1996 *Phys. Rev. A* **54**(3) 2146–2153

[269] Tashiro M, Morokuma K and Tennyson J 2006 *Phys. Rev. A* **73**(5) 052707

[270] Jaffke T, Meinke M, Hashemi R, Christophorou L G and Illenberger E 1992 *Chemical Physics Letters* **193** 62–68

[271] Hayashi D H D and Kadota K K K 1999 *Japanese Journal of Applied Physics* **38** 225

[272] Deutsch H, Becker K, Probst M, Zhu W and Märk T 2008 *International Journal of Mass Spectrometry* **277** 151–154

[273] Gupta M and Baluja K L 2005 *Journal of Physics B: Atomic, Molecular and Optical Physics* **38** 4057

[274] Rangwala S A, Kumar S V K, Krishnakumar E and Mason N J 1999 *Journal of Physics B: Atomic, Molecular and Optical Physics* **32** 3795

[275] Joshipura K N, Antony B K and Vinodkumar M 2002 *Journal of Physics B: Atomic, Molecular and Optical Physics* **35** 4211

[276] Zhaunerchyk V, Geppert W D, Österdahl F, Larsson M, Thomas R D, Bahati E, Bannister M E, Fogle M R and Vane C R 2008 *Phys. Rev. A* **77**(2) 022704

[277] Seiersen K, Bak J, Bluhme H, Jensen M J, Nielsen S B and Andersen L H 2003 *Phys. Chem. Chem. Phys.* **5**(21) 4814–4820

[278] Flannery M 1996 Electron-ion and ion-ion recombination Tech. Rep. p606–29 School of Physics, Georgia Institute of Technology Accessed March, 2024

[279] Bortner M and Baurer T 1972 Defense nuclear agency reaction rate handbook Tech. Rep. Second Edition. Revision number 1 Space Division, General Electric Company Accessed March, 2024

[280] Alge E, Adams N G and Smith D 1983 *Journal of Physics B: Atomic and Molecular Physics* **16** 1433

[281] Florescu-Mitchell A and Mitchell J 2006 *Physics Reports* **430** 277–374

[282] Queffelec J L, Rowe B R, Vallée F, Gomet J C and Morlais M 1989 *The Journal of Chemical Physics* **91** 5335–5342

[283] Dulaney J L, Biondi M A and Johnsen R 1988 *Phys. Rev. A* **37**(7) 2539–2542

[284] Gudmundsson J 2002 Notes on the electron excitation rate coefficients for argon and oxygen (Discharge-RH-21-2002) Tech. rep. Science Institute-University of Iceland

[285] Straub H C, Renault P, Lindsay B G, Smith K A and Stebbings R F 1995 *Phys. Rev. A* **52**(2) 1115–1124

[286] Tachibana K 1986 *Phys. Rev. A* **34**(2) 1007–1015

[287] Eggarter E 2008 *The Journal of Chemical Physics* **62** 833–847

[288] Kannari F, Obara M and Fujioka T 1985 *Journal of Applied Physics* **57** 4309–4322

[289] Ferreira C M, Loureiro J and Ricard A 1985 *Journal of Applied Physics* **57** 82–90

[290] Johnston H S 1968 Gas phase reaction kinetics of neutral oxygen species Tech. Rep. NSRDS-NBS 20 National Institute of Standards and Technology, Gaithersburg, MD Accessed March, 2024

[291] Rawlins W T, Caledonia G E and Armstrong R A 1987 *The Journal of Chemical Physics* **87** 5209–5221

[292] Slanger T G and Copeland R A 2003 *Chemical Reviews* **103** 4731–4766

[293] Sobral J H A, Takahashi H, Abdu M A, Muralikrishna P, Sahai Y, Zamlutti C J, de Paula E R and Batista P P 1993 *Journal of Geophysical Research: Space Physics* **98** 7791–7798

[294] Schofield K 1978 *Journal of Photochemistry* **9** 55–68

[295] Sander S, Burkholder J, Abbatt J, Barker J, Cappa C, Crounse J, Dibble T, Huie R, Kolb C, Kurylo M, Orkin V, Percival C, Wilmouth D and Wine P 2011 Chemical kinetics and photochemical data for use in atmospheric studies Tech. Rep. 10-6 NASA Jet Propulsion Laboratory

[296] Atkinson R, Baulch D L, Cox R A, Crowley J N, Hampson R F, Hynes R G, Jenkin M E, Rossi M J and Troe J 2004 *Atmospheric Chemistry and Physics* **4** 1461–1738

[297] Baulch D L, Cox R A, Hampson R F J, Kerr (Chairman) J A, Troe J and Watson R T 1984 *Journal of Physical and Chemical Reference Data* **13** 1259–1380

[298] Wine P H, Nicovich J M, Thompson R J and Ravishankara A R 1983 *The Journal of Physical Chemistry* **87** 3948–3954

[299] Steinfeld J I, Adler-Golden S M and Gallagher J W 1987 *Journal of Physical and Chemical Reference Data* **16** 911–951

[300] Demore W B, Sander S P, Golden D M, Hampson R F, Kurylo M J, Howard C J, Ravishankara A R, Kolb C E and Molina M J 1992 Chemical kinetics and photochemical data for use in stratospheric modeling Tech. Rep. NAS7-1260 NASA Jet Propulsion Laboratory

[301] Slanger T G and Black G 1978 *The Journal of Chemical Physics* **68** 998–1000

[302] Kenner R and Ogryzlo E 1982 *Journal of Photochemistry* **18** 379–382

[303] Slanger T G and Black G 1981 *The Journal of Chemical Physics* **75** 2247–2251

[304] Slanger T G and Black G 1981 *Geophysical Research Letters* **8** 535–538

[305] Knickelbein M B, Marsh K L, Ulrich O E and Busch G E 1987 *The Journal of Chemical Physics* **87** 2392–2393

[306] Lilenfeld H V, Carr P A G and Hovis F E 1984 *The Journal of Chemical Physics* **81** 5730–5736

[307] Ard S G, Melko J J, Jiang B, Li Y, Shuman N S, Guo H and Viggiano A A 2013 *The Journal of Chemical Physics* **139** 144302

[308] Belostotsky S G, Economou D J, Lopaev D V and Rakhimova T V 2005 *Plasma Sources Science and Technology* **14** 532

[309] Ikezoe Y 1987 Gas phase ion-molecule reaction rate constants Tech. rep. Ion Reaction Research Group of the Mass Spectroscopy Society of Japan

[310] Eichelberger B R, Snow T P and Bierbaum V M 2003 *Journal of the American Society for Mass Spectrometry* **14** 501–505 pMID: 12745219

[311] Langevin M 1905 Une formule fondamentale de théorie cinétique *Annales de chimie et de physique, Series* vol 5 pp 245–288

[312] Nesbet R K 1977 *Phys. Rev. A* **16**(1) 1–5

[313] Miller T M 2000 *CRC Handbook of Chemistry and Physics (Boca Raton, FL: CRC Press)* **77** 193–202

[314] Anicich V G 1993 *Journal of Physical and Chemical Reference Data* **22** 1469–1569

[315] Midey A, Dotan I and Viggiano A A 2008 *The Journal of Physical Chemistry A* **112** 3040–3045

[316] Lifshitz C, Wu R L C, Haartz J C and Tiernan T O 2008 *The Journal of Chemical Physics* **67** 2381–2382

[317] Böhringer H and Arnold F 1982 *The Journal of Chemical Physics* **77** 5534–5541

[318] de Petris G 2003 *Mass Spectrometry Reviews* **22** 251–271

[319] Niemi K, von der Gathen V S and Döbele H F 2005 *Plasma Sources Science and Technology* **14** 375

[320] Dagdigian P J, Forch B E and Miziolek A W 1988 *Chemical Physics Letters* **148** 299–308

[321] Roth E P, Perner D and Dreyer J W 1973 *Zeitschrift für Naturforschung A* **28** 725–729

[322] Bassett N L and Economou D J 1994 *Journal of Applied Physics* **75** 1931–1939

[323] King D L, Piper L G and Setser D W 1977 *J. Chem. Soc., Faraday Trans. 2* **73**(2) 177–200

[324] Midey A J and Viggiano A A 1998 *The Journal of Chemical Physics* **109** 5257–5263

[325] Gaucherel P and Rowe B 1977 *International Journal of Mass Spectrometry and Ion Physics* **25** 211–227

[326] Velazco J E, Kolts J H and Setser D W 2008 *The Journal of Chemical Physics* **69** 4357–4373

[327] Balamuta J and Golde M F 1982 *The Journal of Physical Chemistry* **86** 2765–2769

[328] Piper L G, Clyne M A A and Monkhouse P B 1982 *J. Chem. Soc., Faraday Trans. 2* **78**(8) 1373–1382

[329] Piper L G 1974 *Chemical Physics Letters* **28** 276–279

[330] Miller T M, Shuman N S and Viggiano A A 2012 *The Journal of Chemical Physics* **136** 204306

[331] Biondi M A 1969 *Canadian Journal of Chemistry* **47** 1711–1719

[332] Itikawa Y 2008 *Journal of Physical and Chemical Reference Data* **38** 1–20

Appendix A

Plasma-chemical reaction scheme

Please note that the rate coefficients for the reactions from [15, 244] were generated assuming a Maxwellian energy distribution function (EDF) for electrons with temperatures between 1.5 and 4 eV.

A.1 Electron-oxygen

Table A.1: Electron-oxygen reactions. Electron temperature, T_e, in eV and neutral temperature, T_N, in K. N_r is the number of reactants

#	**Reaction**	$\mathbf{E}_{thr}$ **[eV]**	K_r $[\mathbf{m}^{3+3(N_r-2)}\mathbf{s}^{-1}]$	**Ref.**
1	$e + \mathrm{O} \rightarrow 2e + \mathrm{O}^+$	13.6	$4.93 \cdot 10^{-15} T_e^{0.723} \exp(-13.20/T_e)$	[114, reaction 12], 265
2	$e + \mathrm{O} \rightarrow e + \mathrm{O}(^1\mathrm{D})$	1.96	$8.45 \cdot 10^{-15} T_e^{-0.306} \exp(-3.13/T_e)$	[114, reaction 13], 265
3	$e + \mathrm{O} \rightarrow e + \mathrm{O}(^1\mathrm{S})$	4.18	$1.04 \cdot 10^{-15} T_e^{-0.134} \exp(-4.19/T_e)$	[114, reaction 14], 265
4	$e + \mathrm{O}(^1\mathrm{D}) \rightarrow 2e + \mathrm{O}^+$	11.65	$4.93 \cdot 10^{-15} T_e^{0.723} \exp(-11.64/T_e)$	[114, reaction 15]
5	$e + \mathrm{O}(^1\mathrm{D}) \rightarrow e + \mathrm{O}$	-1.96	$8.45 \cdot 10^{-15} T_e^{0.306} \exp(-1.17/T_e)$	[114, reaction 16], 265
6	$e + \mathrm{O}(^1\mathrm{S}) \rightarrow 2e + \mathrm{O}^+$	9.43	$4.93 \cdot 10^{-15} T_e^{0.723} \exp(-9.42/T_e)$	[114, reaction 17]
7	$e + \mathrm{O}(^1\mathrm{S}) \rightarrow e + \mathrm{O}$	-4.18	$1.04 \cdot 10^{-15} T_e^{-0.134} \exp(-0.73/T_e)$	[114, reaction 18], 265
8	$e + \mathrm{O}^- \rightarrow 2e + \mathrm{O}$	3.44	$9.33 \cdot 10^{-14} T_e^{0.178} \exp(-3.13/T_e)$	[114, reaction 19], 266
9	$e + \mathrm{O}_2 \rightarrow 2e + \mathrm{O} + \mathrm{O}^+$	18.73	$8.60 \cdot 10^{-16} T_e^{1.110} \exp(-19.84/T_e)$	[114, reaction 20], 267,268
10	$e + \mathrm{O}_2 \rightarrow 2e + \mathrm{O}_2^+$	12.06	$2.32 \cdot 10^{-15} T_e^{0.990} \exp(-12.51/T_e)$	[114, reaction 21], 267,268
11	$e + \mathrm{O}_2 \rightarrow e + \mathrm{O} + \mathrm{O}(^1\mathrm{D})$	8.5	$3.12 \cdot 10^{-14} T_e^{0.017} \exp(-8.05/T_e)$	[114, reaction 22], 263
12	$e + \mathrm{O}_2 \rightarrow e + \mathrm{O} + \mathrm{O}(^1\mathrm{D})$	9.97	$1.56 \cdot 10^{-17} T_e^{1.500} \exp(-4.68/T_e)$	[114, reaction 23], 263
13	$e + \mathrm{O}_2 \rightarrow e + \mathrm{O}_2{}^a$	0.0	$4.15 \cdot 10^{-14} T_e^{0.599} \exp(-0.016/T_e)$	[114, reaction 24], 263,264

Continuation of table A.1: Electron-oxygen reactions.

#	**Reaction**	$\mathbf{E}_{thr}$ **[eV]**	K_r $[\mathbf{m}^{3+3(N_r-2)}\mathbf{s}^{-1}]$	**Ref.**
14	$e + O_2 \rightarrow e + O_2{}^b$	0.02	$3.88 \cdot 10^{-17} T_e^{-1.220} \exp(-0.55/T_e)$	[114, reaction 25], 263, 264
15	$e + O_2 \rightarrow e + O_2{}^c$	0.19	$4.32 \cdot 10^{-16} T_e^{-1.570} \exp(-0.586/T_e)$	[114, reaction 26], 263, 264
16	$e + O_2 \rightarrow e + O_2{}^d$	0.19	$2.76 \cdot 10^{-14} T_e^{-1.030} \exp(-6.96/T_e)$	[114, reaction 27], 263, 264
17	$e + O_2 \rightarrow e + O_2{}^e$	0.57	$5.40 \cdot 10^{-15} T_e^{-0.916} \exp(-6.6/T_e)$	[114, reaction 28], 263, 264
18	$e + O_2 \rightarrow e + O_2{}^f$	0.38	$1.64 \cdot 10^{-16} T_e^{-1.410} \exp(-0.723/T_e)$	[114, reaction 29], 263, 264
19	$e + O_2 \rightarrow e + O_2{}^g$	0.38	$1.20 \cdot 10^{-14} T_e^{-1.015} \exp(-6.9/T_e)$	[114, reaction 30], 263, 264
20	$e + O_2 \rightarrow e + O_2{}^h$	0.75	$5.27 \cdot 10^{-15} T_e^{-1.130} \exp(-7.57/T_e)$	[114, reaction 31], 263, 264
21	$e + O_2 \rightarrow e + O_2(a^1\Delta_u)$	0.977	$2.10 \cdot 10^{-15} T_e^{-0.232} \exp(-2.87/T_e)$	[114, reaction 32], 263, 264
22	$e + O_2 \rightarrow e + O_2(b^1\Sigma_u^+)$	1.627	$3.97 \cdot 10^{-16} T_e^{-0.089} \exp(-2.67/T_e)$	[114, reaction 33], 263, 264
23	$e + O_2 \rightarrow e + O_2(b^1\Sigma_u^+)$	4.5	$1.28 \cdot 10^{-14} T_e^{-1.160} \exp(-7.00/T_e)$	[114, reaction 34], 263, 264
24	$e + O_2 \rightarrow e + O_2(b^1\Sigma_u^+)$	6.0	$1.98 \cdot 10^{-14} T_e^{-0.779} \exp(-7.36/T_e)$	[114, reaction 35], 263, 264
25	$e + O_2 \rightarrow O + O^-$	0.0	$1.32 \cdot 10^{-15} T_e^{-1.400} \exp(-1.40/T_e)$	[114, reaction 36], 263, 264
26	$e + O_2(a^1\Delta_u) \rightarrow 2e + O + O^+$	17.75	$8.60 \cdot 10^{-16} T_e^{1.110} \exp(-18.86/T_e)$	[114, reaction 37]
27	$e + O_2(a^1\Delta_u) \rightarrow 2e + O_2^+$	11.08	$2.32 \cdot 10^{-15} T_e^{0.990} \exp(-11.53/T_e)$	[114, reaction 38]

Continuation of table A.1: Electron-oxygen reactions.

#	**Reaction**	$\mathbf{E}_{thr}$ **[eV]**	K_r $[\mathbf{m}^{3+3(N_r-2)}\mathbf{s}^{-1}]$	**Ref.**
28	$e + O_2(a^1\Delta_u) \rightarrow e + O + O(^1D)$	7.52	$3.12 \cdot 10^{-14} T_e^{0.017} \exp(-7.07/T_e)$	[114, reaction 39]
29	$e + O_2(a^1\Delta_u) \rightarrow e + O + O(^1D)$	9.0	$1.56 \cdot 10^{-17} T_e^{1.500} \exp(-3.70/T_e)$	[114, reaction 40]
30	$e + O_2(a^1\Delta_u) \rightarrow e + O_2$	-0.977	$2.10 \cdot 10^{-15} T_e^{-0.232} \exp(-1.89/T_e)$	[114, reaction 41], 263
31	$e + O_2(a^1\Delta_u) \rightarrow e + O_2(a^1\Delta_u)^a$	0.0	$4.15 \cdot 10^{-15} T_e^{0.599} \exp(-0.016/T_e)$	[114, reaction 42], 263, 269
32	$e + O_2(a^1\Delta_u) \rightarrow e + O_2(a^1\Delta_u)^b$	0.02	$3.88 \cdot 10^{-17} T_e^{-1.220} \exp(-0.55/T_e)$	[114, reaction 43]
33	$e + O_2(a^1\Delta_u) \rightarrow e + O_2(a^1\Delta_u)^c$	0.19	$4.32 \cdot 10^{-16} T_e^{-1.570} \exp(-0.586/T_e)$	[114, reaction 44]
34	$e + O_2(a^1\Delta_u) \rightarrow e + O_2(a^1\Delta_u)^d$	0.19	$2.76 \cdot 10^{-14} T_e^{-1.030} \exp(-6.96/T_e)$	[114, reaction 45]
35	$e + O_2(a^1\Delta_u) \rightarrow e + O_2(a^1\Delta_u)^e$	0.38	$1.64 \cdot 10^{-16} T_e^{-1.410} \exp(-0.723/T_e)$	[114, reaction 46]
36	$e + O_2(a^1\Delta_u) \rightarrow e + O_2(a^1\Delta_u)^f$	0.38	$1.20 \cdot 10^{-15} T_e^{-1.015} \exp(-6.9/T_e)$	[114, reaction 47]
37	$e + O_2(a^1\Delta_u) \rightarrow e + O_2(a^1\Delta_u)^g$	0.57	$5.40 \cdot 10^{-15} T_e^{-0.916} \exp(-6.6/T_e)$	[114, reaction 48]
38	$e + O_2(a^1\Delta_u) \rightarrow e + O_2(a^1\Delta_u)^h$	0.75	$5.27 \cdot 10^{-15} T_e^{-1.130} \exp(-7.57/T_e)$	[114, reaction 49]
39	$e + O_2(a^1\Delta_u) \rightarrow e + O_2(b^1\Sigma_u^+)$	0.657	$5.25 \cdot 10^{-15} T_e^{-0.440} \exp(-1.49/T_e)$	[114, reaction 50], 269
40	$e + O_2(a^1\Delta_u) \rightarrow e + O_2(b^1\Sigma_u^+)$	3.52	$1.28 \cdot 10^{-14} T_e^{-1.160} \exp(-6.02/T_e)$	[114, reaction 51]
41	$e + O_2(a^1\Delta_u) \rightarrow e + O_2(b^1\Sigma_u^+)$	5.02	$1.98 \cdot 10^{-14} T_e^{-0.779} \exp(-6.38/T_e)$	[114, reaction 52]

Continuation of table A.1: Electron-oxygen reactions.

#	**Reaction**	$\mathbf{E}_{thr}$ **[eV]**	K_r $[\mathbf{m}^{3+3(N_r-2)}\mathbf{s}^{-1}]$	**Ref.**
42	$e + O_2(a^1\Delta_u) \rightarrow O + O^-$	3.0	$4.14 \cdot 10^{-15} T_e^{-1.340} \exp(-5.15/T_e)$	[114, reaction 53], 270
43	$e + O_2(a^1\Delta_u) \rightarrow O(^1D) + O^-$	3.0	$9.20 \cdot 10^{-16} T_e^{-1.260} \exp(-6.55/T_e)$	[114, reaction 54], 270
44	$e + O_2(b^1\Sigma_u^+) \rightarrow 2e + O + O^+$	17.1	$8.60 \cdot 10^{-16} T_e^{1.110} \exp(-18.21/T_e)$	[114, reaction 55]
45	$e + O_2(b^1\Sigma_u^+) \rightarrow 2e + O_2^+$	10.43	$2.32 \cdot 10^{-15} T_e^{0.990} \exp(-10.88/T_e)$	[114, reaction 56]
46	$e + O_2(b^1\Sigma_u^+) \rightarrow e + O + O(^1D)$	6.87	$3.12 \cdot 10^{-14} T_e^{0.017} \exp(-6.42/T_e)$	[114, reaction 57]
47	$e + O_2(b^1\Sigma_u^+) \rightarrow e + O + O(^1D)$	8.34	$1.56 \cdot 10^{-17} T_e^{1.500} \exp(-3.05/T_e)$	[114, reaction 58]
48	$e + O_2(b^1\Sigma_u^+) \rightarrow e + O_2$	-1.627	$3.97 \cdot 10^{-16} T_e^{-0.089} \exp(-1.04/T_e)$	[114, reaction 59], 263
49	$e + O_2(b^1\Sigma_u^+) \rightarrow e + O_2(a^1\Delta_u)$	-0.657	$5.25 \cdot 10^{-15} T_e^{-0.440} \exp(-0.833/T_e)$	[114, reaction 60], 269
50	$e + O_2(b^1\Sigma_u^+) \rightarrow e + O_2(b^1\Sigma_u^+)^a$	0.0	$4.15 \cdot 10^{-14} T_e^{0.599} \exp(-0.016/T_e)$	[114, reaction 61], 263, 269
51	$e + O_2(b^1\Sigma_u^+) \rightarrow e + O_2(b^1\Sigma_u^+)^b$	0.02	$3.88 \cdot 10^{-17} T_e^{-1.220} \exp(-0.55/T_e)$	[114, reaction 62]
52	$e + O_2(b^1\Sigma_u^+) \rightarrow e + O_2(b^1\Sigma_u^+)^c$	0.19	$4.32 \cdot 10^{-16} T_e^{-1.570} \exp(-0.586/T_e)$	[114, reaction 63]
53	$e + O_2(b^1\Sigma_u^+) \rightarrow e + O_2(b^1\Sigma_u^+)^d$	0.19	$2.76 \cdot 10^{-14} T_e^{-1.030} \exp(-6.96/T_e)$	[114, reaction 64]
54	$e + O_2(b^1\Sigma_u^+) \rightarrow e + O_2(b^1\Sigma_u^+)^e$	0.38	$1.64 \cdot 10^{-16} T_e^{-1.410} \exp(-0.723/T_e)$	[114, reaction 65]
55	$e + O_2(b^1\Sigma_u^+) \rightarrow e + O_2(b^1\Sigma_u^+)^f$	0.38	$1.20 \cdot 10^{-15} T_e^{-1.015} \exp(-6.9/T_e)$	[114, reaction 66]

Continuation of table A.1: Electron-oxygen reactions.

#	**Reaction**	$\mathbf{E}_{thr}$ **[eV]**	K_r $[\mathbf{m}^{3+3(N_r-2)}\mathbf{s}^{-1}]$	**Ref.**
56	$e + O_2(b^1\Sigma_u^+) \rightarrow e + O_2(b^1\Sigma_u^+)^g$	0.57	$5.40 \cdot 10^{-15} T_e^{-0.916} \exp(-6.6/T_e)$	[114, reaction 67]
57	$e + O_2(b^1\Sigma_u^+) \rightarrow e + O_2(b^1\Sigma_u^+)^h$	0.75	$5.27 \cdot 10^{-15} T_e^{-1.130} \exp(-7.57/T_e)$	[114, reaction 68]
58	$e + O_2(b^1\Sigma_u^+) \rightarrow e + O_2(b^1\Sigma_u^+)$	2.87	$1.28 \cdot 10^{-14} T_e^{-1.160} \exp(-5.37/T_e)$	[114, reaction 69]
59	$e + O_2(b^1\Sigma_u^+) \rightarrow e + O_2(b^1\Sigma_u^+)$	4.37	$1.98 \cdot 10^{-14} T_e^{-0.779} \exp(-5.73/T_e)$	[114, reaction 70]
60	$e + O_2(b^1\Sigma_u^+) \rightarrow O + O^-$	0.0	$7.11 \cdot 10^{-16} T_e^{-1.040} \exp(-0.23/T_e)$	[114, reaction 71], 271
61	$e + O_2^- \rightarrow 2e + O_2$	4.68	$1.57 \cdot 10^{-14} T_e^{1.010} \exp(-1.77/T_e)$	[114, reaction 72], 272
62	$e + O_3 \rightarrow e + O + O_2$	2.6	$1.70 \cdot 10^{-14} T_e^{-0.570} \exp(-2.48/T_e)$	[114, reaction 73], 273
63	$e + O_3 \rightarrow e + O(^1D) + O_2(a^1\Delta_u)$	5.72	$3.22 \cdot 10^{-13} T_e^{-1.180} \exp(-9.17/T_e)$	[114, reaction 74], 273
64	$e + O_3 \rightarrow O + O_2^-$	0.0	$1.02 \cdot 10^{-15} T_e^{-1.300} \exp(-1.03/T_e)$	[114, reaction 75], 274
65	$e + O_3 \rightarrow O^- + O_2$	0.0	$3.45 \cdot 10^{-15} T_e^{-0.960} \exp(-1.00/T_e)$	[114, reaction 76], 274
66	$e + O_3 \rightarrow 2e + O_3^+$	12.43	$5.96 \cdot 10^{-15} T_e^{0.978} \exp(-12.55/T_e)$	[114, reaction 77], 267,275
67	$e + O_3^+ \rightarrow 3O$	-6.27	$2.07 \cdot 10^{-13} T_e^{-0.550}$	[114, reaction 78], 276
68	$e + O_3^+ \rightarrow 2O + O(^1D)$	-4.3	$6.69 \cdot 10^{-13} T_e^{-0.550}$	[114, reaction 79], 276
69	$e + O_3^+ \rightarrow O + 2O(^1D)$	-2.33	$1.55 \cdot 10^{-13} T_e^{-0.550}$	[114, reaction 80], 276

Continuation of table A.1: Electron-oxygen reactions.

#	**Reaction**	$\mathbf{E}_{thr}$ **[eV]**	K_r $[\mathbf{m}^{3+3(N_r-2)}\mathbf{s}^{-1}]$	**Ref.**
70	$e + O_3^- \rightarrow 2e + O_3$	2.1	$2.12 \cdot 10^{-14} T_e^{0.510} \exp(-5.87/T_e)$	[114, reaction 81], 277
71	$e + O_3^- \rightarrow 2e + O + O_2$	3.2	$7.12 \cdot 10^{-14} T_e^{-0.132} \exp(-5.94/T_e)$	[114, reaction 82], 277
72	$e + O_3^- \rightarrow 2e + 3O$	8.4	$1.42 \cdot 10^{-14} T_e^{-0.520} \exp(-9.3/T_e)$	[114, reaction 83], 277
73	$2e + O^+ \rightarrow e + O$	0.0	$2.00 \cdot 10^{-39} T_e^{-4.5}$	[114, reaction 142], 278
74	$2e + O_2^+ \rightarrow e + O_2$	0.0	$2.00 \cdot 10^{-39} T_e^{-4.5}$	[114, reaction 143], 278
75	$2e + O_4^+ \rightarrow e + 2O_2$	0.0	$2.00 \cdot 10^{-39} T_e^{-4.5}$	[114, reaction 144], 278
76	$e + O + O_2 \rightarrow O + O_2^-$	0.0	$1.00 \cdot 10^{-43}$	[114, reaction 145], 279
77	$e + O^+ \rightarrow O(^1D)$	0.0	$2.70 \cdot 10^{-19} T_e^{-0.7}$	[114, reaction 146], 279
78	$e + O^+ + O_2 \rightarrow O + O_2$	0.0	$3.30 \cdot 10^{-44} T_e^{-2.5}$	[114, reaction 147], 278
79	$e + 2O_2 \rightarrow O_2 + O_2^-$	0.0	$3.62 \cdot 10^{-43} T_e^{-1.0} \exp(-0.052/T_e)$	[114, reaction 148], 279
80	$e + O_2 + O_2^+ \rightarrow 2O_2$	0.0	$3.30 \cdot 10^{-44} T_e^{-2.5}$	[114, reaction 149], 278
81	$e + O_2 + O_3 \rightarrow O_2 + O_3^-$	0.0	$3.62 \cdot 10^{-43} T_e^{-1.0} \exp(-0.052/T_e)$	[114, reaction 150]
82	$e + O_2^+ \rightarrow O + O(^1D)$	0.0	$9.10 \cdot 10^{-15} T_e^{-0.7}$	[114, reaction 151], 280–282
83	$e + O_2^+ \rightarrow O(^1D) + O(^1S)$	0.0	$6.00 \cdot 10^{-15} T_e^{-0.7}$	[114, reaction 152], 280–282

Continuation of table A.1: Electron-oxygen reactions.

#	**Reaction**	$\mathbf{E}_{thr}$ **[eV]**	K_r $[\mathbf{m}^{3+3(N_r-2)}\mathbf{s}^{-1}]$	**Ref.**
84	$e + O_4^+ \rightarrow O + O(^1D) + O_2$	0.0	$2.02 \cdot 10^{-14} T_e^{-0.4}$	[114, reaction 153], 281, 283
85	$e + O_4^+ \rightarrow O(^1D) + O(^1S) + O_2$	0.0	$1.35 \cdot 10^{-14} T_e^{-0.4}$	[114, reaction 154], 281, 283
86	$e + O \rightarrow e + O(^5S)$	9.15	$2.84 \cdot 10^{-15} T_e^{-0.39} \exp(-8.75/T_e)$	[244, reaction 3]
87	$e + O \rightarrow e + O(^3S)$	9.52	$1.01 \cdot 10^{-15} T_e^{0.78} \exp(-7.33/T_e)$	[244, reaction 4]
88	$e + O \rightarrow e + O(^5P)$	10.74	$1.92 \cdot 10^{-15} T_e^{-0.12} \exp(-10.15/T_e)$	[244, reaction 5]
89	$e + O \rightarrow e + O(^3P)$	10.99	$1.93 \cdot 10^{-15} T_e^{0.38} \exp(-9.71/T_e)$	[244, reaction 6]
90	$e + O \rightarrow e + O(^3P)$	12.0	$2.96 \cdot 10^{-15} T_e^{0.80} \exp(-10.58/T_e)$	[244, reaction 8][i]
91	$e + O(^1D) \rightarrow e + O(^1S)$	2.22	$1.63 \cdot 10^{-15} T_e^{0.04} \exp(-2.28/T_e)$	[244, reaction 10]
92	$e + O(^1D) \rightarrow e + O(^3S)$	7.55	$1.57 \cdot 10^{-17} T_e^{0.17} \exp(-7.57/T_e)$	[244, reaction 11]
93	$e + O(^1D) \rightarrow e + O(^3P)$	9.02	$1.87 \cdot 10^{-16} T_e^{-0.18} \exp(-9.44/T_e)$	[244, reaction 12]
94	$e + O(^1D) \rightarrow e + O(^3P)$	11.03	$2.42 \cdot 10^{-15} T_e^{0.04} \exp(-10.08/T_e)$	[244, reaction 13]
95	$e + O(^1S) \rightarrow e + O(^3P)$	6.8	$9.54 \cdot 10^{-17} T_e^{-0.27} \exp(-6.74/T_e)$	[244, reaction 15]
96	$e + O(^1S) \rightarrow e + O(^3P)$	7.81	$3.08 \cdot 10^{-17} T_e^{0.70} \exp(-6.91/T_e)$	[244, reaction 16]
97	$e + O(^5S) \rightarrow e + O(^3S)$	0.37	$1.67 \cdot 10^{-13} T_e^{-1.09} \exp(-1.13/T_e)$	[244, reaction 17]

Continuation of table A.1: Electron-oxygen reactions.

#	**Reaction**	$\mathbf{E}_{thr}$ **[eV]**	K_r $[\mathbf{m}^{3+3(N_r-2)}\mathbf{s}^{-1}]$	**Ref.**
98	$e + \mathrm{O}(^5\mathrm{S}) \rightarrow e + \mathrm{O}(^5\mathrm{P})$	1.59	$8.17 \cdot 10^{-13} T_e^{-0.16} \exp(-1.96/T_e)$	[244, reaction 18]
99	$e + \mathrm{O}(^5\mathrm{S}) \rightarrow e + \mathrm{O}(^3\mathrm{P})$	1.84	$1.29 \cdot 10^{-13} T_e^{-1.07} \exp(-2.76/T_e)$	[244, reaction 19]
100	$e + \mathrm{O}(^3\mathrm{S}) \rightarrow e + \mathrm{O}(^5\mathrm{P})$	1.22	$3.24 \cdot 10^{-13} T_e^{-1.05} \exp(-1.90/T_e)$	[244, reaction 20]
101	$e + \mathrm{O}(^3\mathrm{S}) \rightarrow e + \mathrm{O}(^3\mathrm{P})$	1.47	$6.27 \cdot 10^{-13} T_e^{-0.44} \exp(-1.58/T_e)$	[244, reaction 21]
102	$e + \mathrm{O}(^5\mathrm{P}) \rightarrow e + \mathrm{O}(^3\mathrm{P})$	0.25	$2.09 \cdot 10^{-13} T_e^{-0.99} \exp(-1.14/T_e)$	[244, reaction 22]
103	$e + \mathrm{O}_2 \rightarrow e + \mathrm{O} + \mathrm{O}(^1\mathrm{S})$	0.0	$2.89 \cdot 10^{-16} T_e^{0.36} \exp(-15.22/T_e)$	[244, reaction 26]
104	$e + \mathrm{O}_2(\mathrm{a}^1\Delta_u) \rightarrow e + \mathrm{O} + \mathrm{O}(^1\mathrm{S})$	0.0	$2.89 \cdot 10^{-16} T_e^{0.36} \exp(-15.22/T_e)$	[244, reaction 26]
105	$e + \mathrm{O}_2(\mathrm{b}^1\Sigma_u^+) \rightarrow e + \mathrm{O} + \mathrm{O}(^1\mathrm{S})$	0.0	$2.89 \cdot 10^{-16} T_e^{0.36} \exp(-15.22/T_e)$	[244, reaction 26]

Continuation of table A.1: Electron-oxygen reactions.

#	Reaction	$\mathbf{E}_{thr}$ [eV]	K_r [$\mathbf{m}^{3+3(N_r-2)}\mathbf{s}^{-1}$]	Ref.

[a] Elastic scattering

[b] Rotational excitation

[c] Vibrational excitation: from "v1" in Phelps database [263, 264]

[d] Vibrational excitation: from "v1res" in Phelps database [263, 264]

[e] Vibrational excitation: from "v3" in Phelps database [263, 264]

[f] Vibrational excitation: from "v2" in Phelps database [263, 264]

[g] Vibrational excitation: from "v2res" in Phelps database [263, 264]

[h] Vibrational excitation: from "v4" in Phelps database [263, 264]

[i] Excitation to triplet states above the ^3P level are assumed to cascade down into the ^3P level

A.2 Electron-argon

Table A.2: Electron-argon reactions. Electron temperature, T_e, in eV.

#	Process	$\mathbf{E}_{thr}$ [eV]	K_r [$\mathbf{m^3 s^{-1}}$]	Ref.
106	$e + \mathrm{Ar} \rightarrow e + \mathrm{Ar}$	0.0	$2.336 \cdot 10^{-14} T_e^{1.609} \cdot \exp\left[0.0618(\log T_e)^2 - 0.1171(\log T_e)^3\right]$	194, 284
107	$e + \mathrm{Ar} \rightarrow \mathrm{Ar}^+ + 2e$	15.76	$2.3 \cdot 10^{-14} T_e^{0.59} \exp(-17.44/T_e)$	21, 285
108	$e + \mathrm{Ar} \rightarrow \mathrm{Ar}^m + e$	11.55	$5.0 \cdot 10^{-15} \exp(-12.64/T_e)$	21, 286
109	$e + \mathrm{Ar} \rightarrow \mathrm{Ar}^m + e$	11.72	$1.4 \cdot 10^{-15} \exp(-12.42/T_e)$	21, 286
110	$e + \mathrm{Ar} \rightarrow \mathrm{Ar}^r + e$	11.62	$1.9 \cdot 10^{-15} \exp(-12.60/T_e)$	21, 286
111	$e + \mathrm{Ar} \rightarrow \mathrm{Ar}^r + e$	11.83	$2.7 \cdot 10^{-16} \exp(-12.14/T_e)$	21, 286
112	$e + \mathrm{Ar} \rightarrow \mathrm{Ar(4p)} + e$	13.22	$2.1 \cdot 10^{-14} \exp(-13.13/T_e)$	21, 287
113	$e + \mathrm{Ar}^m \rightarrow \mathrm{Ar} + e$	0.0	$4.3 \cdot 10^{-16} T_e^{0.74}$	21, 250
114	$e + \mathrm{Ar}^m \rightarrow \mathrm{Ar}^+ + 2e$	4.12	$6.8 \cdot 10^{-15} T_e^{0.67} \exp(-4.2/T_e)$	21, 288
115	$e + \mathrm{Ar}^m \rightarrow \mathrm{Ar}^r + e$	0.09	$3.7 \cdot 10^{-13}$	21, 289
116	$e + \mathrm{Ar}^m \rightarrow \mathrm{Ar(4p)} + e$	1.57	$8.9 \cdot 10^{-13} T_e^{0.51} \exp(-1.59/T_e)$	21, 288
117	$e + \mathrm{Ar(4p)} \rightarrow \mathrm{Ar}^+ + 2e$	2.55	$1.8 \cdot 10^{-13} T_e^{0.61} \exp(-2.61/T_e)$	21, 288
118	$e + \mathrm{Ar(4p)} \rightarrow \mathrm{Ar}^r + e$	0.0	$3.0 \cdot 10^{-13} T_e^{0.51}$	21, 250
119	$e + \mathrm{Ar(4p)} \rightarrow \mathrm{Ar}^m + e$	0.0	$3.0 \cdot 10^{-13} T_e^{0.51}$	21, 250
120	$e + \mathrm{Ar(4p)} \rightarrow \mathrm{Ar} + e$	0.0	$3.9 \cdot 10^{-16} T_e^{0.71}$	21, 250
121	$e + \mathrm{Ar}^r \rightarrow \mathrm{Ar} + e$	0.0	$4.3 \cdot 10^{-16} T_e^{0.74}$	21, 250
122	$e + \mathrm{Ar}^r \rightarrow \mathrm{Ar}^m + e$	0.0	$9.1 \cdot 10^{-13}$	21, 289
123	$e + \mathrm{Ar}^r \rightarrow \mathrm{Ar(4p)} + e$	1.48	$8.9 \cdot 10^{-13} T_e^{0.51} \exp(-1.59/T_e)$	21, 288

A.3 Oxygen-oxygen

Table A.3: Oxygen-oxygen reactions. Electron temperature, T_e, in eV and neutral and ion temperature, T_N, in K. $\mu_{A,B} = m_A m_B/(m_A + m_B)$ is the reduced mass of species A and B.

#	Reaction	K_r [$\mathbf{m^3 s^{-1}}$]	Ref.
124	$3O \rightarrow O + O_2$	$3.80 \cdot 10^{-44}(300/T_N)\exp(-170/T_N)$	[114, reaction 92], 290
125	$3O \rightarrow O + O_2(b^1\Sigma_u^+)$	$1.40 \cdot 10^{-42}\exp(-650/T_N)$	[114, reaction 93], 279
126	$2O + O_2 \rightarrow O + O_3$	$4.20 \cdot 10^{-47}\exp(1056/T_N)$	[114, reaction 94], 290, 291
127	$2O + O_2 \rightarrow O + O_3(\nu)$	$9.80 \cdot 10^{-47}\exp(1056/T_N)$	[114, reaction 95], 290, 291
128	$2O + O_2 \rightarrow O_2(a^1\Delta_u) + O_2$	$6.50 \cdot 10^{-45}(300/T_N)\exp(-170/T_N)$	[114, reaction 96], 290, 292
129	$2O + O_2 \rightarrow O_2(b^1\Sigma_u^+) + O_2$	$6.50 \cdot 10^{-45}(300/T_N)\exp(-170/T_N)$	[114, reaction 97], 290, 292
130	$O + O(^1D) \rightarrow 2O$	$2.00 \cdot 10^{-18}$	[114, reaction 98], 293
131	$O + O(^1S) \rightarrow 2O$	$2.50 \cdot 10^{-17}\exp(-300/T_N)$	[114, reaction 99], 294
132	$O + O(^1S) \rightarrow O + O(^1D)$	$2.50 \cdot 10^{-17}\exp(-300/T_N)$	[114, reaction 100], 294
133	$O + 2O_2 \rightarrow O_2 + O_3$	$1.80 \cdot 10^{-46}(300/T_N)^{2.6}$	[114, reaction 101], 291, 295, 296
134	$O + 2O_2 \rightarrow O_2 + O_3(\nu)$	$4.20 \cdot 10^{-46}(300/T_N)^{2.6}$	[114, reaction 102], 291, 295, 296
135	$O + O_2 + O_2(a^1\Delta_u) \rightarrow O + 2O_2$	$1.10 \cdot 10^{-44}$	[114, reaction 103], 291
136	$O + O_2 + O_3 \rightarrow 2O_3$	$1.40 \cdot 10^{-47}\exp(-1050/T_N)$	[114, reaction 104], 291

Continuation of table A.3: Oxygen-oxygen reactions

#	Reaction	K_r [$\mathbf{m^3 s^{-1}}$]]	Ref.
137	$O + O_2 + O_3 \rightarrow O_3 + O_3(\nu)$	$3.27 \cdot 10^{-47} \exp(-1050/T_N)$	[114, reaction 105], 291
138	$O + O_2(a^1\Delta_u) \rightarrow O + O_2$	$1.00 \cdot 10^{-22}$ (E_{th} = -2.14 eV)	[114, reaction 106], 295
139	$O + O_2(b^1\Sigma_u^+) \rightarrow O + O_2(a^1\Delta_u)$	$8.00 \cdot 10^{-20}$ (E_{th} = -0.65 eV)	[114, reaction 107], 295, 296
140	$O + O_3 \rightarrow 2O + O_2$	$1.20 \cdot 10^{-15} \exp(-11400/T_N)$	[114, reaction 108], 290
141	$O + O_3 \rightarrow 2O_2$	$8.00 \cdot 10^{-18} \exp(-2060/T_N)$	[114, reaction 109], 295–298
142	$O + O_3(\nu) \rightarrow 2O_2$	$4.50 \cdot 10^{-18}$	[114, reaction 110], 299
143	$O + O_3(\nu) \rightarrow O_3 + O$	$1.05 \cdot 10^{-17}$	[114, reaction 111], 299
144	$O(^1D) + O_2 \rightarrow O + O2$	$4 \cdot 10^{-17}$	15, 300
145	$O(^1D) + O_2(a^1\Delta_u) \rightarrow O + O_2$	$4 \cdot 10^{-17}$	15, 300[a]
146	$O(^1D) + O_2(b^1\Sigma_u^+) \rightarrow O + O_2$	$4 \cdot 10^{-17}$	15, 300[a]
147	$O(^1D) + O_2 \rightarrow O + O_2(b^1\Sigma_u^+)$	$2.64 \cdot 10^{-17} \exp(55/T_N)$	[114, reaction 112], 295
148	$O(^1D) + O_2 \rightarrow O + O_2(a^1\Delta_u)$	$6.60 \cdot 10^{-18} \exp(55/T_N)$	[114, reaction 113], 295
149	$O(^1D) + O_3 \rightarrow 2O + O_2$	$1.20 \cdot 10^{-16}$	[114, reaction 114], 295, 296, 299
150	$O(^1D) + O_3 \rightarrow 2O_2$	$1.20 \cdot 10^{-16}$	[114, reaction 115], 295, 296, 299

Continuation of table A.3: Oxygen-oxygen reactions

#	Reaction	K_r [$\mathbf{m^3 s^{-1}}$]]	Ref.
151	$O(^1S) + O_2 \rightarrow O + O_2$	$3.00 \cdot 10^{-18} \exp(-850/T_N)$	[114, reaction 116], 279, 301
152	$O(^1S) + O_2(a^1\Delta_u) \rightarrow O + O_2$	$3.00 \cdot 10^{-18} \exp(-850/T_N)$	[114, reactopn 116]279, 301[b]
153	$O(^1S) + O_2(b^1\Sigma_u^+) \rightarrow O + O_2$	$3.00 \cdot 10^{-18} \exp(-850/T_N)$	[114, reactopn 116]279, 301[b]
154	$O(^1S) + O_2 \rightarrow O(^1D) + O_2$	$1.30 \cdot 10^{-18} \exp(-850/T_N)$	[114, reaction 117], 279, 301
155	$O(^1S) + O_2(a^1\Delta_u) \rightarrow 3O$	$3.20 \cdot 10^{-17}$	[114, reaction 118], 302–304
156	$O(^1S) + O_2(a^1\Delta_u) \rightarrow O + O_2(b^1\Sigma_u^+)$	$1.30 \cdot 10^{-16}$	[114, reaction 119], 302–304
157	$O(^1S) + O_2(a^1\Delta_u) \rightarrow O(^1D) + O_2$	$3.60 \cdot 10^{-17}$	[114, reaction 120], 303, 304
158	$O(^1S) + O_3 \rightarrow O + O(^1D) + O_2$	$1.93 \cdot 10^{-16}$	[114, reaction 121], 299
159	$O(^1S) + O_3 \rightarrow 2O_2$	$1.93 \cdot 10^{-16}$	[114, reaction 122], 299
160	$O(^1S) + O_3 \rightarrow 2O + O_2$	$1.93 \cdot 10^{-16}$	[114, reaction 123], 299
161	$2O_2 \rightarrow 2O + O_2$	$6.60 \cdot 10^{-15}(300/T_N)^{1.5} \exp(-59000/T_N)$	[114, reaction 124], 279
162	$O_2 + O_2(a^1\Delta_u) \rightarrow 2O_2$	$3.60 \cdot 10^{-24} \exp(-220/T_N)$	[114, reaction 126], 295
163	$O_2 + O_2(b^1\Sigma_u^+) \rightarrow O_2 + O_2(a^1\Delta_u)$	$3.90 \cdot 10^{-23}$	[114, reaction 128], 295, 305
164	$O_2 + O_3 \rightarrow O + 2O_2$	$7.26 \cdot 10^{-16} \exp(-11435/T_N)$	[114, reaction 130], 299

Continuation of table A.3: Oxygen-oxygen reactions

#	Reaction	K_r [$\mathbf{m^3 s^{-1}}$]]	Ref.
165	$O_2 + O_3(\nu) \rightarrow O_2 + O_3$	$4.00 \cdot 10^{-20}$	[114, reaction 131], 299
166	$2O_2(a^1\Delta_u) \rightarrow O_2 + O_2(b^1\Sigma_u^+)$	$2.70 \cdot 10^{-23}$	[114, reaction 132], 306
167	$O_2(a^1\Delta_u) + O_2(b^1\Sigma_u^+) \rightarrow O_2 + O_2(b^1\Sigma_u^+)$	$2.70 \cdot 10^{-23}$	[114, reaction 133]
168	$2O_2(b^1\Sigma_u^+) \rightarrow O_2 + O_2(b^1\Sigma_u^+)$	$2.70 \cdot 10^{-23}$	[114, reaction 134]
169	$O_2(a^1\Delta_u) + O_3 \rightarrow O + 2O_2$	$5.20 \cdot 10^{-17} \exp(-2840/T_N)$	[114, reaction 135], 295
170	$O_2(a^1\Delta_u) + O_3(\nu) \rightarrow O_2 + O_3$	$5.00 \cdot 10^{-17}$	[114, reaction 136], 299
171	$O_2(b^1\Sigma_u^+) + O_3 \rightarrow O + 2O_2$	$2.40 \cdot 10^{-17} \exp(-135/T_N)$	[114, reaction 137], 295
172	$O_2(b^1\Sigma_u^+) + O_3 \rightarrow O_2 + O_3$	$5.50 \cdot 10^{-18} \exp(-135/T_N)$	[114, reaction 138], 295
173	$O_2(b^1\Sigma_u^+) + O_3 \rightarrow O_2(a^1\Delta_u) + O_3$	$5.50 \cdot 10^{-18} \exp(-135/T_N)$	[114, reaction 139], 295
174	$2O_3 \rightarrow O + O_2 + O_3$	$1.65 \cdot 10^{-15} \exp(-11435/T_N)$	[114, reaction 140], 299
175	$O_3 + O_3(\nu) \rightarrow 2O_3$	$1.00 \cdot 10^{-19}$	[114, reaction 141], 299
176	$O + O^- \rightarrow e + O_2$	$2.30 \cdot 10^{-16}(300/T_N)^{1.3}$	[114, reaction 155], 307, 308
177	$O + O_2^- \rightarrow O^- + O_2$	$8.50 \cdot 10^{-17}(300/T_N)^{1.8}$	[114, reaction 156], 307
178	$O + O_2^- \rightarrow e + O_3$	$8.50 \cdot 10^{-17}(300/T_N)^{1.8}$	[114, reaction 157], 307

Continuation of table A.3: Oxygen-oxygen reactions

#	Reaction	K_r [$\mathbf{m^3 s^{-1}}$]]	Ref.
179	$O + O_3^- \rightarrow e + 2O_2$	$1.00 \cdot 10^{-17}$	[114, reaction 158], 279
180	$O + O_3^- \rightarrow O_2 + O_2^-$	$2.50 \cdot 10^{-16}$	[114, reaction 159], 309
181	$O + O_4^+ \rightarrow O_3 + O_2^+$	$3.00 \cdot 10^{-16}$	[114, reaction 160], 309
182	$O + O_4^- \rightarrow O_2 + O_3^-$	$4.00 \cdot 10^{-16}$	[114, reaction 161], 279, 309
183	$O(^1D) + O^- \rightarrow e + 2O$	$7.40 \cdot 10^{-16}$	[114, reaction 162], 310–312
184	$O(^1D) + O_2^- \rightarrow e + O_3$	$8.50 \cdot 10^{-17}(300/T_N)^{1.8}$	[114, reaction 163]
185	$O(^1D) + O_2^- \rightarrow O^- + O_2$	$8.50 \cdot 10^{-17}(300/T_N)^{1.8}$	[114, reaction 164]
186	$O(^1D) + O_3^+ \rightarrow 2O + O_2^+$	$3.00 \cdot 10^{-16}$	[114, reaction 165], 310, 311, 313
187	$O(^1D) + O_3^- \rightarrow O + O_2 + O^-$	$3.00 \cdot 10^{-16}$	[114, reaction 166], 310, 311, 313
188	$O(^1D) + O_3^- \rightarrow O + O_3 + e$	$3.00 \cdot 10^{-16}$	[114, reaction 167], 310–312
189	$O(^1D) + O_4^+ \rightarrow O + O_2 + O_2^+$	$3.00 \cdot 10^{-16}$	[114, reaction 168], 310–312
190	$O(^1D) + O_4^+ \rightarrow O_3 + O_2^+$	$3.00 \cdot 10^{-16}$	[114, reaction 169], 310–312
191	$O(^1D) + O_4^- \rightarrow e + O + 2O_2$	$2.00 \cdot 10^{-16}$	[114, reaction 170], 310, 311, 313
192	$O(^1D) + O_4^- \rightarrow O + O_2 + O_2^-$	$2.00 \cdot 10^{-16}$	[114, reaction 171], 310, 311, 313

Continuation of table A.3: Oxygen-oxygen reactions

#	Reaction	K_r [$\mathbf{m^3 s^{-1}}$]]	Ref.
193	$O(^1D) + O_4^- \rightarrow 2O_2 + O^-$	$2.00 \cdot 10^{-16}$	[114, reaction 172], 310, 311, 313
194	$O(^1D) + O_4^- \rightarrow O + O_2 + O_2^-$	$7.40 \cdot 10^{-16}$	[114, reaction 173], 310–312
195	$O(^1S) + O_2^- \rightarrow O^- + O_2$	$8.50 \cdot 10^{-17}(300/T_N)^{1.8}$	[114, reaction 174]
196	$O(^1S) + O_2^- \rightarrow e + O_3$	$8.50 \cdot 10^{-17}(300/T_N)^{1.8}$	[114, reaction 175]
197	$O(^1S) + O_3^+ \rightarrow 2O + O_2^+$	$2.00 \cdot 10^{-16}$	[114, reaction 176], 310, 311, 313
198	$O(^1S) + O_3^- \rightarrow e + O + O_3$	$2.00 \cdot 10^{-16}$	[114, reaction 177], 310, 311, 313
199	$O(^1S) + O_3^- \rightarrow 2O + O_2^-$	$2.00 \cdot 10^{-16}$	[114, reaction 178], 310, 311, 313
200	$O(^1S) + O_3^- \rightarrow O + O^- + O_2$	$2.00 \cdot 10^{-16}$	[114, reaction 179], 310, 311, 313
201	$O(^1S) + O_4^+ \rightarrow O + O_2 + O_2^+$	$3.00 \cdot 10^{-16}$	[114, reaction 180], 310–312
202	$O(^1S) + O_4^+ \rightarrow O_2^+ + O_3$	$3.00 \cdot 10^{-16}$	[114, reaction 181], 310–312
203	$O(^1S) + O_4^- \rightarrow e + O + 2O_2$	$2.00 \cdot 10^{-16}$	[114, reaction 182], 310, 311, 313
204	$O(^1S) + O_4^- \rightarrow O + O_2 + O_2^-$	$2.00 \cdot 10^{-16}$	[114, reaction 183], 310, 311, 313
205	$O(^1S) + O_4^- \rightarrow O^- + 2O_2$	$2.00 \cdot 10^{-16}$	[114, reaction 184], 310, 311, 313
206	$O^+ + O + O_2 \rightarrow O_2 + O_2^+$	$4.00 \cdot 10^{-42}(300/T_N)^{2.93}$	[114, reaction 185]

Continuation of table A.3: Oxygen-oxygen reactions

#	Reaction	K_r [$\mathbf{m^3 s^{-1}}$]]	Ref.
207	$O^+ + O_2 \rightarrow O + O_2^+$	$2.10 \cdot 10^{-17}(300/T_N)^{0.4}$	[114, reaction 189], 279, 314
208	$O^+ + O_3 \rightarrow O_2 + O_2^+$	$1.20 \cdot 10^{-15}$	[114, reaction 193], 310, 311, 313
209	$O^- + O_2 \rightarrow O_3 + e$	$1.00 \cdot 10^{-18}$	[114, reaction 198], 309
210	$O^- + O_2 \rightarrow O_2^- + O$	$1.00 \cdot 10^{-18}$	[114, reaction 199], 309
211	$O^- + 2O_2 \rightarrow O_2 + O_3^-$	$1.10 \cdot 10^{-42}$	[114, reaction 200], 279
212	$O^- + O_2(a^1\Delta_u) \rightarrow O + O_2^-$	$7.90 \cdot 10^{-16} \exp(-890/T_N)$	[114, reaction 203], 315
213	$O^- + O_2(a^1\Delta_u) \rightarrow O_3 + e$	$6.10 \cdot 10^{-17}$	[114, reaction 204], 315
214	$O^- + O_2(b^1\Sigma_u^+) \rightarrow O + O_2^-$	$7.90 \cdot 10^{-16} \exp(-890/T_N)$	[114, reaction 205]
215	$O^- + O_2(b^1\Sigma_u^+) \rightarrow O_3 + e$	$6.10 \cdot 10^{-17}$	[114, reaction 206]
216	$O^- + O_3 \rightarrow e + 2O_2$	$3.00 \cdot 10^{-16}$	[114, reaction 209], 309, 316
217	$O^- + O_3 \rightarrow O + O_3^-$	$2.00 \cdot 10^{-16}$	[114, reaction 210], 309, 316
218	$O^- + O_3 \rightarrow O_2 + O_2^-$	$1.00 \cdot 10^{-17}$	[114, reaction 211], 309, 316
219	$2O_2 + O_2^+ \rightarrow O_2 + O_4^+$	$4.00 \cdot 10^{-42}(300/T_N)^{2.93}$	[114, reaction 215], 317
220	$2O_2 + O_2^- \rightarrow O_2 + O_4^-$	$3.50 \cdot 10^{-43}(300/T_N)$	[114, reaction 216], 279

Continuation of table A.3: Oxygen-oxygen reactions

#	Reaction	K_r [$\mathbf{m^3 s^{-1}}$]]	Ref.
221	$O_2 + O_2^- \rightarrow e + 2O_2$	$2.70 \cdot 10^{-16}(T_N/300)^{0.5} \exp(-5590/T_N)$	[114, reaction 217], 279
222	$O_2 + O_2^- \rightarrow O + O_3^-$	$3.50 \cdot 10^{-21}$	[114, reaction 218], 309
223	$O_2 + O_3^+ \rightarrow O_2^+ + O_3$	$6.70 \cdot 10^{-16}$	[114, reaction 221], 310, 311, 313, 318
224	$O_2 + O_4^+ \rightarrow 2O_2 + O_2^+$	$1.00 \cdot 10^{-11}(300/T_N)^{4.2} \exp(-5400/T_N)$	[114, reaction 222], 279, 309
225	$O_2 + O_4^- \rightarrow 2O_2 + O_2^-$	$2.20 \cdot 10^{-11}(300/T_N) \exp(-6300/T_N)$	[114, reaction 227], 279
226	$O_2(a^1\Delta_u) + O_2^- \rightarrow e + 2O_2$	$7.00 \cdot 10^{-16}$	[114, reaction 228], 315
227	$O_2(a^1\Delta_u) + O_4^+ \rightarrow 2O_2 + O_2^+$	$6.00 \cdot 10^{-16}$	[114, reaction 229], 310, 311, 313
228	$O_2(a^1\Delta_u) + O_4^- \rightarrow 3O_2 + e$	$3.00 \cdot 10^{-16}$	[114, reaction 230], 310, 311, 313
229	$O_2(a^1\Delta_u) + O_4^- \rightarrow 2O_2 + O_2^-$	$3.00 \cdot 10^{-16}$	[114, reaction 231], 310, 311, 313
230	$O_2(b^1\Sigma_u^+) + O_2^- \rightarrow e + 2O_2$	$7.00 \cdot 10^{-16}$	[114, reaction 232]
231	$O_2(b^1\Sigma_u^+) + O_3^- \rightarrow O^- + 2O_2$	$6.70 \cdot 10^{-16} \exp(-1300/T_N)$	[114, reaction 233], 310, 311, 313
232	$O_2(b^1\Sigma_u^+) + O_4^+ \rightarrow 2O_2 + O_2^+$	$6.00 \cdot 10^{-16}$	[114, reaction 234]
233	$O_2(b^1\Sigma_u^+) + O_4^- \rightarrow e + 3O_2$	$3.00 \cdot 10^{-16}$	[114, reaction 235], 310, 311, 313
234	$O_2(b^1\Sigma_u^+) + O_4^- \rightarrow 2O_2 + O_2^-$	$3.00 \cdot 10^{-16}$	[114, reaction 236], 310, 311, 313

Continuation of table A.3: Oxygen-oxygen reactions

#	Reaction	K_r [$\mathbf{m^3 s^{-1}}$]]	Ref.
235	$O_2^- + O_3 \rightarrow O_2 + O_3^-$	$6.00 \cdot 10^{-16}$	[114, reaction 247], 309
236	$O_3 + O_4^- \rightarrow 2O_2 + O_3^-$	$8.00 \cdot 10^{-16}$	[114, reaction 251], 310, 311, 313
237	$O_3^- + O_3 \rightarrow e + 3O_2$	$8.50 \cdot 10^{-16}$	[114, reaction 254], 310, 311, 313
238	$O(^3P) + O_2 \rightarrow O + O_2$	$9.4 \cdot 10^{-16}$	319
239	$O(^3P) + O_2(a^1\Delta_u) \rightarrow O + O_2$	$9.4 \cdot 10^{-16}$	319[c]
240	$O(^3P) + O_2(b^1\Sigma_u^+) \rightarrow O + O_2$	$9.4 \cdot 10^{-16}$	319[c]
241	$O(^3P) + O_3 \rightarrow O + O_3$	$9.4 \cdot 10^{-16}$	319[c]
242	$O(^3P) + O \rightarrow O + O$	$9.4 \cdot 10^{-16}$	319[c]
243	$O(^3S) + O_2 \rightarrow O + O_2$	$9.4 \cdot 10^{-16}$	319[c]
244	$O(^3S) + O_2(a^1\Delta_u) \rightarrow O + O_2$	$9.4 \cdot 10^{-16}$	319[c]
245	$O(^3S) + O_2(b^1\Sigma_u^+) \rightarrow O + O_2$	$9.4 \cdot 10^{-16}$	319[c]
246	$O(^3S) + O_3 \rightarrow O + O_3$	$9.4 \cdot 10^{-16}$	319[c]
247	$O(^3S) + O \rightarrow O + O$	$9.4 \cdot 10^{-16}$	319[c]
248	$O(^5P) + O_2 \rightarrow O + O_2$	$1.08 \cdot 10^{-15}$	320

Continuation of table A.3: Oxygen-oxygen reactions

#	Reaction	K_r [$\mathbf{m^3 s^{-1}}$]]	Ref.
249	$O(^5P) + O_2(a^1\Delta_u) \rightarrow O + O_2$	$1.08 \cdot 10^{-15}$	320[d]
250	$O(^5P) + O_2(b^1\Sigma_u^+) \rightarrow O + O_2$	$1.08 \cdot 10^{-15}$	320[d]
251	$O(^5P) + O_3 \rightarrow O + O_3$	$1.08 \cdot 10^{-15}$	320[d]
252	$O(^5P) + O \rightarrow O + O$	$1.08 \cdot 10^{-15}$	320[d]
253	$O(^5S) + O_2 \rightarrow O + O_2$	$1.4 \cdot 10^{-16}$	321
254	$O(^5S) + O_2(a^1\Delta_u) \rightarrow O + O_2$	$1.4 \cdot 10^{-16}$	321[e]
255	$O(^5S) + O_2(b^1\Sigma_u^+) \rightarrow O + O_2$	$1.4 \cdot 10^{-16}$	321[e]
256	$O(^5S) + O_3 \rightarrow O + O_3$	$1.4 \cdot 10^{-16}$	321[e]
257	$O(^5S) + O \rightarrow O + O$	$1.4 \cdot 10^{-16}$	321[e]

[a] The collisional quenching coefficient for $O(^1D) + O_2$ is measured in Ref. 300. Here, the same quenching coefficient is used for the marked reactions, due to a lack of specific data.

[b] The collisional quenching coefficient for $O(^1S) + O_2$ is measured in Refs. 279, 301. Here, the same quenching coefficient is used for the marked reactions, due to a lack of specific data.

[c] The collisional quenching coefficient for $O(^3S) + O_2$ is measured in Ref. 319. Here, the same quenching coefficient is used for the marked reactions, due to a lack of specific data.

[d] The collisional quenching coefficient for $O(^5P) + O_2$ is measured in Ref. 320. Here, the same quenching coefficient is used for the marked reactions, due to a lack of specific data.

[e] The collisional quenching coefficient for $O(^5S) + O_2$ is measured in Ref. 321. Here, the same quenching coefficient is used for the marked reactions, due to a lack of specific data.

A.4 Argon-argon

Table A.4: Argon-argon reactions. Electron temperature, T_e, in eV and neutral and ion temperature, T_N, in K. $\mu_{A,B} = m_A m_B/(m_A + m_B)$ is the reduced mass of species A and B.

#	**Reaction**	K_r $[\mathbf{m^3 s^{-1}}]$	**Ref.**
258	$2\mathrm{Ar}^m \rightarrow 2\mathrm{Ar}$	$2.0 \cdot 10^{-13}$	21
259	$\mathrm{Ar}^m + \mathrm{Ar}^r \rightarrow \mathrm{Ar} + \mathrm{Ar}^+ + e$	$2.1 \cdot 10^{-15}$	21, 322
260	$\mathrm{Ar(4p)} + \mathrm{Ar(4p)} \rightarrow \mathrm{Ar} + \mathrm{Ar}^+ + e$	$5.0 \cdot 10^{-16}$	21, 288
261	$2\mathrm{Ar}^m \rightarrow \mathrm{Ar} + \mathrm{Ar}^+ + e$	$6.4 \cdot 10^{-16}$	21, 289
262	$\mathrm{Ar} + \mathrm{Ar}^m \rightarrow 2\mathrm{Ar}$	$2.1 \cdot 10^{-21}$	21, 322

[a] The reaction is an extension from the reactions in ref. [319].

A.5 Argon-oxygen

Table A.5: Argon-oxygen reactions. Electron temperature, T_e, in eV and neutral and ion temperature, T_N, in K. $\mu_{A,B} = m_A m_B/(m_A + m_B)$ is the reduced mass of species A and B.

#	Reaction	K_r [m^3]	Ref.
263	$O + Ar^m \rightarrow O + Ar$	$4.1 \cdot 10^{-17}$	21, 323
264	$O + Ar^r \rightarrow O + Ar$	$4.1 \cdot 10^{-17}$	21[a]
265	$O_2 + Ar(4p) \rightarrow O + O + Ar$	$2.96 \cdot 10^{-16}$	21
266	$O_2(a^1\Delta_u) + Ar(4p) \rightarrow O + O + Ar$	$2.96 \cdot 10^{-16}$	21[a]
267	$O_2(b^1\Sigma_u^+) + Ar(4p) \rightarrow O + O + Ar$	$2.96 \cdot 10^{-16}$	21[a]
268	$O_2 + Ar(4p) \rightarrow O + O(^1D) + Ar$	$3.34 \cdot 10^{-16}$	21
269	$O_2(a^1\Delta_u) + Ar(4p) \rightarrow O + O(^1D) + Ar$	$3.34 \cdot 10^{-16}$	21[a]
270	$O_2(b^1\Sigma_u^+) + Ar(4p) \rightarrow O + O(^1D) + Ar$	$3.34 \cdot 10^{-16}$	21[a]
271	$O_2 + Ar^+ \rightarrow O_2^+ + Ar$	$4.90 \cdot 10^{-17}(300/T_N)^{0.78}$	21, 324
272	$O_2(a^1\Delta_u) + Ar^+ \rightarrow O_2^+ + Ar$	$4.90 \cdot 10^{-17}(300/T_N)^{0.78}$	21[a]
273	$O_2(b^1\Sigma_u^+) + Ar^+ \rightarrow O_2^+ + Ar$	$4.90 \cdot 10^{-17}(300/T_N)^{0.78}$	21[a]
274	$O + Ar^+ \rightarrow O^+ + Ar$	$6.40 \cdot 10^{-18}$	21, 325
275	$O_2 + Ar^m \rightarrow O + O + Ar$	$1.035 \cdot 10^{-16}$	15, 326, 327
276	$O_2(a^1\Delta_u) + Ar^m \rightarrow O + O + Ar$	$1.035 \cdot 10^{-16}$	15, 326, 327
277	$O_2(b^1\Sigma_u^+) + Ar^m \rightarrow O + O + Ar$	$1.035 \cdot 10^{-16}$	15, 326, 327
278	$O_2 + Ar^m \rightarrow O + O(^1D) + Ar$	$1.17 \cdot 10^{-16}$	15, 326, 327
279	$O_2(a^1\Delta_u) + Ar^m \rightarrow O + O(^1D) + Ar$	$1.17 \cdot 10^{-16}$	15, 326, 327
280	$O_2(b^1\Sigma_u^+) + Ar^m \rightarrow O + O(^1D) + Ar$	$1.17 \cdot 10^{-16}$	15, 326, 327
281	$O_2 + Ar^m \rightarrow O + O(^1S) + Ar$	$4.5 \cdot 10^{-18}$	15, 326, 327
282	$O_2(a^1\Delta_u) + Ar^m \rightarrow O + O(^1S) + Ar$	$4.5 \cdot 10^{-18}$	15, 326, 327
283	$O_2(b^1\Sigma_u^+) + Ar^m \rightarrow O + O(^1S) + Ar$	$4.5 \cdot 10^{-18}$	15, 326, 327
284	$O_2 + Ar^r \rightarrow O + O + Ar$	$1.288 \cdot 10^{-16}$	15, 326, 327

Continuation of table A.5: Argon-oxygen reactions.

#	Reaction	K_r [$\mathbf{m^3 s^{-1}}$]	Ref.
285	$O_2(a^1\Delta_u) + Ar^r \rightarrow 2O + Ar$	$1.288 \cdot 10^{-16}$	15, 326, 327
286	$O_2(b^1\Sigma_u^+) + Ar^r \rightarrow 2O + Ar$	$1.288 \cdot 10^{-16}$	15, 326, 327
287	$O_2 + Ar^r \rightarrow O + O(^1D) + Ar$	$1.456 \cdot 10^{-16}$	15, 326, 327
288	$O_2(a^1\Delta_u) + Ar^r \rightarrow O + O(^1D) + Ar$	$1.456 \cdot 10^{-16}$	15, 326, 327
289	$O_2(b^1\Sigma_u^+) + Ar^r \rightarrow O + O(^1D) + Ar$	$1.456 \cdot 10^{-16}$	15, 326, 327
290	$O_2 + Ar^r \rightarrow O + O(^1S) + Ar$	$5.6 \cdot 10^{-18}$	15, 326, 327
291	$O_2(a^1\Delta_u) + Ar^r \rightarrow O + O(^1S) + Ar$	$5.6 \cdot 10^{-18}$	15, 326, 327
292	$O_2(b^1\Sigma_u^+) + Ar^r \rightarrow O + O(^1S) + Ar$	$5.6 \cdot 10^{-18}$	15, 326, 327
293	$O(^1D) + Ar \rightarrow Ar + O$	$3.0 \cdot 10^{-19}$	15, 294
294	$O(^1S) + Ar \rightarrow Ar + O$	$4.8 \cdot 10^{-24}$	15, 294
295	$O + Ar^m \rightarrow Ar + O(^3P)$	$7.6 \cdot 10^{-17}$	15, 328
296	$O(^3P) + Ar \rightarrow Ar + O(^5P)$	$2.80 \cdot 10^{-18}$	15, 329
297	$O(^3P) + Ar \rightarrow O + Ar$	$1.4 \cdot 10^{-17}$	319
298	$O(^3S) + Ar \rightarrow O + Ar$	$1.4 \cdot 10^{-17}$	319[b]
299	$O(^5P) + Ar \rightarrow O + Ar$	$1.4 \cdot 10^{-17}$	319[b]
300	$O(^5S) + Ar \rightarrow O + Ar$	$1.4 \cdot 10^{-17}$	319[b]

[a] The reaction is an extension from the reactions in Ref. 21.

[b] The collisional quenching coefficient for $O(^3P) + Ar$ is measured in Ref. 319. Here, the same quenching coefficient is used for the marked reactions, due to a lack of specific data.

A.6 Recombination

Table A.6: Recombination reactions. Neutral and ion temperature, T_N, in K.

#	Reaction	K_r [m^3]	Ref.
301	$O^+ + O^- \rightarrow 2O$	$3.10 \cdot 10^{-14}(300/T_N)^{1.1}$	[114, reaction 186], 330
302	$O^+ + O^- + O_2 \rightarrow 2O + O_2$	$1.00 \cdot 10^{-37}(300/T_N)^{2.5}$	[114, reaction 187], 331
303	$O^+ + O^- + O_2 \rightarrow 2O_2$	$1.00 \cdot 10^{-37}(300/T_N)^{2.5}$	[114, reaction 188], 331
304	$O^- + O_2^+ \rightarrow 3O$	$1.61 \cdot 10^{-14}(300/T_N)^{1.1}$	[114, reaction 207], 330
305	$O^- + O_2^+ \rightarrow O + O_2$	$1.61 \cdot 10^{-14}(300/T_N)^{1.1}$	[114, reaction 208], 330
306	$O^- + O_3^+ \rightarrow O + O_3$	$3.07 \cdot 10^{-14}(300/T_N)^{1.1}$	[114, reaction 212], 330
307	$O^- + O_4^+ \rightarrow O + 2O_2$	$1.54 \cdot 10^{-14}(300/T_N)^{0.9}$	[114, reaction 213], 330
308	$O^- + O_4^+ \rightarrow O_2 + O_3$	$1.54 \cdot 10^{-14}(300/T_N)^{0.9}$	[114, reaction 214], 330
309	$O_2^+ + O^- + O_2 \rightarrow O + 2O_2$	$1.00 \cdot 10^{-37}(300/T_N)^{2.5}$	[114, reaction 237], 331
310	$O_2^+ + O^- + O_2 \rightarrow O_2 + O_3$	$1.00 \cdot 10^{-37}(300/T_N)^{2.5}$	[114, reaction 238], 331
311	$O_2^+ + O_2^- + O_2 \rightarrow 3O_2$	$2.00 \cdot 10^{-37}(300/T_N)^{2.5}$	[114, reaction 239], 331
312	$O_2^+ + O_3^- + O_2 \rightarrow 2O_2 + O_3$	$2.00 \cdot 10^{-37}(300/T_N)^{2.5}$	[114, reaction 240], 331
313	$O_2^+ + O_4^- + O_2 \rightarrow 4O_2$	$2.00 \cdot 10^{-37}(300/T_N)^{2.5}$	[114, reaction 241], 331
314	$O_2^+ + O_2^- \rightarrow O_2 + 2O$	$1.60 \cdot 10^{-14}(300/T_N)^{1.1}$	[114, reaction 242], 330
315	$O_2^+ + O_2^- \rightarrow 2O_2$	$1.60 \cdot 10^{-14}(300/T_N)^{1.1}$	[114, reaction 243], 330
316	$O_2^+ + O_3^- \rightarrow 2O + O_3$	$2.90 \cdot 10^{-14}(300/T_N)^{0.9}$	[114, reaction 244], 330
317	$O_2^+ + O_3^- \rightarrow O_2 + O_3$	$2.90 \cdot 10^{-14}(300/T_N)^{0.9}$	[114, reaction 245], 330
318	$O_2^+ + O_4^- \rightarrow 3O_2$	$6.07 \cdot 10^{-14}(300/T_N)^{0.9}$	[114, reaction 246], 330
319	$O_2^- + O_3^+ \rightarrow O_2 + O_3$	$3.29 \cdot 10^{-14}(300/T_N)^{1.1}$	[114, reaction 248], 330
320	$O_2^- + O_4^+ \rightarrow 2O + 2O_2$	$1.60 \cdot 10^{-14}(300/T_N)^{1.1}$	[114, reaction 249], 330
321	$O_2^- + O_4^+ \rightarrow 3O_2$	$1.60 \cdot 10^{-14}(300/T_N)^{1.1}$	[114, reaction 250], 330
322	$O^+ + O_2^- \rightarrow O + O_2$	$3.22 \cdot 10^{-14}(300/T_N)^{1.1}$	[114, reaction 190], 330
323	$O^+ + O_2^- + O_2 \rightarrow O + 2O_2$	$1.00 \cdot 10^{-37}(300/T_N)^{2.5}$	[114, reaction 191], 331

Continuation of table A.6: Recombination reactions.

#	**Reaction**	K_r $[\mathbf{m^3 s^{-1}}]$	**Ref.**
324	$O^+ + O_2^- + O_2 \rightarrow O_2 + O_3$	$1.00 \cdot 10^{-37}(300/T_N)^{2.5}$	[114, reaction 192], 331
325	$O_2 + O_2^- + O_3^+ \rightarrow 2O_2 + O_3$	$2.00 \cdot 10^{-37}(300/T_N)^{2.5}$	[114, reaction 219], 331
326	$O_2 + O_2^- + O_4^+ \rightarrow 4O_2$	$2.00 \cdot 10^{-37}(300/T_N)^{2.5}$	[114, reaction 220], 331
327	$O_3^+ + O_3^- \rightarrow 2O_3$	$5.19 \cdot 10^{-14}(300/T_N)^{0.9}$	[114, reaction 252], 330
328	$O_3^+ + O_4^- \rightarrow 2O_2 + O_3$	$5.37 \cdot 10^{-14}(300/T_N)^{0.9}$	[114, reaction 253], 330
329	$O_3^- + O_4^+ \rightarrow O + 3O_2$	$2.43 \cdot 10^{-14}(300/T_N)^{0.9}$	[114, reaction 255], 330
330	$O_3^- + O_4^+ \rightarrow 2O_2 + O_3$	$2.43 \cdot 10^{-14}(300/T_N)^{0.9}$	[114, reaction 256], 330
331	$O_4^+ + O_4^- \rightarrow 4O_2$	$4.97 \cdot 10^{-14}(300/T_N)^{0.9}$	[114, reaction 257], 330
332	$O^+ + O_3^- \rightarrow O + O_3$	$7.33 \cdot 10^{-14}(300/T_N)^{0.9}$	[114, reaction 194], 330
333	$O^+ + O_3^- + O_2 \rightarrow O + O_2 + O_3$	$2.00 \cdot 10^{-37}(300/T_N)^{2.5}$	[114, reaction 195], 331
334	$O^+ + O_4^- \rightarrow O + 2O_2$	$7.87 \cdot 10^{-14}(300/T_N)^{0.9}$	[114, reaction 196], 330
335	$O^+ + O_4^- + O_2 \rightarrow O + 3O_2$	$2.00 \cdot 10^{-37}(300/T_N)^{2.5}$	[114, reaction 197], 331
336	$O_2 + O_3^+ + O_3^- \rightarrow O_2 + 2O_3$	$2.00 \cdot 10^{-37}(300/T_N)^{2.5}$	[114, reaction 223], 331
337	$O_2 + O_3^+ + O_4^- \rightarrow 3O_2 + O_3$	$2.00 \cdot 10^{-37}(300/T_N)^{2.5}$	[114, reaction 224], 331
338	$O_2 + O_3^- + O_4^+ \rightarrow 3O_2 + O_3$	$2.00 \cdot 10^{-37}(300/T_N)^{2.5}$	[114, reaction 225], 331
339	$O_2 + O_4^+ + O_4^- \rightarrow 5O_2$	$2.00 \cdot 10^{-37}(300/T_N)^{2.5}$	[114, reaction 226], 331
340	$O^- + O_2 + O_3^+ \rightarrow O + O_2 + O_3$	$2.00 \cdot 10^{-37}(300/T_N)^{2.5}$	[114, reaction 201], 331
341	$O^- + O_2 + O_4^+ \rightarrow O + 3O_2$	$2.00 \cdot 10^{-37}(300/T_N)^{2.5}$	[114, reaction 202], 331
342	$O^- + Ar^+ \rightarrow O + Ar$	$4.0 \cdot 10^{-14}(300/T_N)^{0.43}$	21

Table A.7: Oxygen reactions derived from emission cross sections[a,b]. Electron temperature, T_e, in eV. N_r is the number of reactants.

#	Process	K_r [$\mathbf{m}^{3+3(N_r-2)}\mathbf{s}^{-1}$]	Ref.
380	$e + \mathrm{O} \rightarrow e + \mathrm{O}(^5\mathrm{S}) + \lambda_{777.5}$	$1.96 \cdot 10^{-14} T_e^{-0.90} \exp(-15.23/T_e)$	15, 244, 332[c]
381	$e + \mathrm{O}_2 \rightarrow e + 2\mathrm{O} + \lambda_{130.4}$	$4.78 \cdot 10^{-16} T_e^{-0.06} \exp(-15.69/T_e)$	15, 244, 332[d]
382	$e + \mathrm{O}_2(\mathrm{a}^1\Delta_u) \rightarrow e + 2\mathrm{O} + \lambda_{130.4}$	$4.78 \cdot 10^{-16} T_e^{-0.06} \exp(-15.69/T_e)$	15, 244, 332[d,e]
383	$e + \mathrm{O}_2(\mathrm{b}^1\Sigma_u^+) \rightarrow e + 2\mathrm{O} + \lambda_{130.4}$	$4.78 \cdot 10^{-16} T_e^{-0.06} \exp(-15.69/T_e)$	15, 244, 332[d,e]
384	$e + \mathrm{O}_2 \rightarrow e + 2\mathrm{O} + \lambda_{135.6}$	$1.65 \cdot 10^{-15} T_e^{-0.19} \exp(-15.7/T_e)$	15, 244, 332[d]
385	$e + \mathrm{O}_2(\mathrm{a}^1\Delta_u) \rightarrow e + 2\mathrm{O} + \lambda_{135.6}$	$1.65 \cdot 10^{-15} T_e^{-0.19} \exp(-15.7/T_e)$	15, 244, 332[d,e]
386	$e + \mathrm{O}_2(\mathrm{b}^1\Sigma_u^+) \rightarrow e + 2\mathrm{O} + \lambda_{135.6}$	$1.65 \cdot 10^{-15} T_e^{-0.19} \exp(-15.7/T_e)$	15, 244, 332[d,e]
387	$e + \mathrm{O}_2 \rightarrow e + \mathrm{O} + \mathrm{O}(^5\mathrm{S}) + \lambda_{777.5}$	$1.73 \cdot 10^{-16} T_e^{0.77} \exp(-14.69/T_e)$	15, 244, 267[d]
388	$e + \mathrm{O}_2(\mathrm{a}^1\Delta_u) \rightarrow e + \mathrm{O} + \mathrm{O}(^5\mathrm{S}) + \lambda_{777.5}$	$1.73 \cdot 10^{-16} T_e^{0.77} \exp(-14.69/T_e)$	15, 244, 267[d,e]
389	$e + \mathrm{O}_2(\mathrm{b}^1\Sigma_u^+) \rightarrow e + \mathrm{O} + \mathrm{O}(^5\mathrm{S}) + \lambda_{777.5}$	$1.73 \cdot 10^{-16} T_e^{0.77} \exp(-14.69/T_e)$	15, 244, 267[d,e]
390	$e + \mathrm{O}_2 \rightarrow e + \mathrm{O} + \mathrm{O}(^3\mathrm{S}) + \lambda_{844.6}$	$1.00 \cdot 10^{-16} T_e^{0.73} \exp(-14.77/T_e)$	15, 244, 267[d]
391	$e + \mathrm{O}_2(\mathrm{a}^1\Delta_u) \rightarrow e + \mathrm{O} + \mathrm{O}(^3\mathrm{S}) + \lambda_{844.6}$	$1.00 \cdot 10^{-16} T_e^{0.73} \exp(-14.77/T_e)$	15, 244, 267[d,e]
392	$e + \mathrm{O}_2(\mathrm{b}^1\Sigma_u^+) \rightarrow e + \mathrm{O} + \mathrm{O}(^3\mathrm{S}) + \lambda_{844.6}$	$1.00 \cdot 10^{-16} T_e^{0.73} \exp(-14.77/T_e)$	15, 244, 267[d,e]

[a] The cross sections on which these rate constants are based are derived by measuring the corresponding emission lines. Therefore, they include contributions from excitation to higher states which cascade down to the state emitting the measured wavelength, as well as direct electron impact excitation of the corresponding excited state. Further information on what the values of each rate constant represent is given in the relevant footnotes.

[b] All rate constants have been derived from by fitting the data provided in the supplementary information in Ref. 244.

[c] The emission cross section for excitation of the O ground state with emission at 777 nm given in the reference includes both the direct excitation of the $\mathrm{O}(^5P)$ state and excitation of higher levels that cascade down to the same state. The rate constant given here is calculated by subtracting the direct excitation cross section for the $\mathrm{O}(^5P)$ state (reaction 88) from the emission cross section given in the reference. Because of this, that the rate constant for reaction 380 represents only the contribution of cascades from higher levels to the production of emission at 777 nm.

[d] The dissociative excitation cross sections for emission at at 130.4 nm and 135.6 nm, given in the corresponding references, include both dissociative excitation which directly forms the corresponding excited states, as well as excitation processes to higher levels that cascade down to the same states. Because of this, the dissociative excitation cross sections for the emission at at 130.4 nm and 135.6 nm effectively include the cross sections for emission at 844 nm and 777 nm (reactions 390 and 387), respectively. To account for this, the rate constants shown for emission at 130.4 nm and 135.6 nm represent the total rate constant derived from those emission cross sections minus the rate constants derived from the emission cross sections for emission at 844 nm and 777 nm, respectively. This means that the rate constants for dissociative emission at 130.4 nm and 135.6 nm represent the direct excitation of the corresponding excited levels with subsequent emission at the given wavelengths. The rate constants for emission at 844 nm and 777 nm on the other hand represent the direct excitation of the states emitting at those wavelengths, as well as the excitation of higher levels that cascade down to the same excited states.

[e] The rate constants for dissociative excitation followed by emission for $\mathrm{O}_2(\mathrm{a}^1\Delta_u)$ and $\mathrm{O}_2(\mathrm{b}^1\Sigma_u^+)$ are assumed the same as for the O_2 ground state.

Appendix B

Additional global model validation problems

This appendix reproduces some results from the existing literature on Ar/O_2 ICP with the 0D GM model presented in chapter 5.

B.1 Sato et al

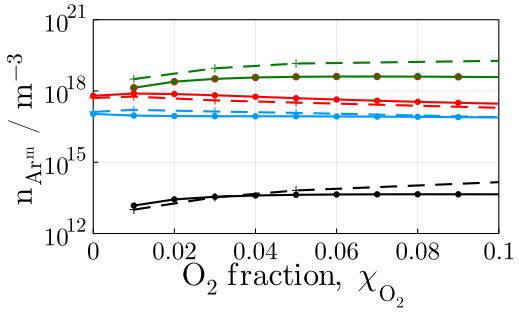

Figure B.1: Ar^m density results of an Ar/O_2 ICP operated at $p_T = 100\,\text{mTorr}$ and $P_{in} = 100\,\text{W}$ investigated in ref. [20] (dashed lines) and reproduced with the GM (solid lines).

The numerical study performed in ref. [20] on an Ar/O_2 ICP has been reproduced to verify the GM results for Ar^m densities. The reactor chamber is cylindrical with $R = 5\,\text{cm}$ and $L = 10\,\text{cm}$, and the operating conditions are $p_T = 13.33\,\text{Pa}$ $= 100\,\text{mTorr}$ and $P_{in} = 100\,\text{W}$. For the GM simulations, the neutral gas temperature is set to $T_N = 740\,\text{K}$. Other simulation parameters and chemistry are as described in section 6.1. The results are shown in figure B.1.

B.2 Gudmundsson et al

The numerical investigation conducted in ref. [21] on an Ar/O_2 ICP has been reproduced to verify the GM results for Ar, A^m, Ar^r and Ar(4p) densities. The reactor

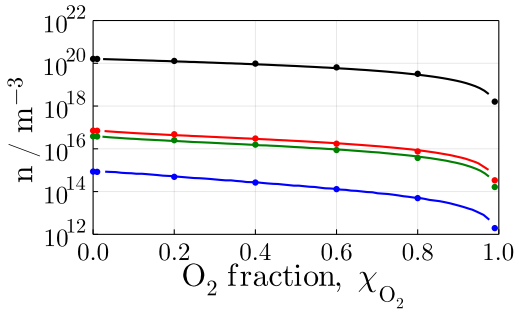

Figure B.2: Ar density results of an Ar/O_2 ICP operated at $p_T = 10\,\text{mTorr}$ and $P_{in} = 500\,\text{W}$ investigated in ref. [21] (dot-dashed lines) and reproduced with the GM (solid lines). Ar in black, Ar^m in red, Ar^r in green and Ar(4p) in blue.

chamber is cylindrical with $R = 10\,\text{cm}$ and $L = 10\,\text{cm}$ and the operating conditions are $p_T = 10\,\text{mTorr} = 1.33\,\text{Pa}$ and $P_{in} = 500\,\text{W}$. For the GM simulations the neutral gas temperature is set to $T_N = 600\text{K}$. Other simulation and chemistry parameters are described in section 6.1. The results are shown in figure B.2.

B.3 Hayashi et al

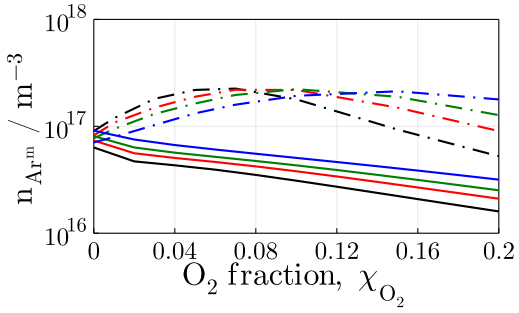

Figure B.3: Ar^m density results of an Ar/O_2 ICP operated at $p_T = 10\,\text{mTorr}$ at different P_{in}. The experimental results of ref. [22] (dotted lines) have been reproduced with the GM (solid lines). $P_{in} = 50\,\text{W}$ in black, 75 W in red, 100 W in green and 150 W in blue.

The experimental results of ref. [22] on an Ar/O_2 ICP have been reproduced to verify the GM results for Ar^m densities. The reactor chamber is cylindrical with $R = 5\,\text{cm}$ and $L = 20\,\text{cm}$, and the operating conditions are $p_T = 100\,\text{Pa} = 13.33\,\text{mTorr}$ and $P_{in} = 50\,\text{W}$. For the GM simulations the neutral gas temperature is set to $T_N = 600\,\text{K}$. Other simulation parameters and chemistry are as described in section 6.1. The results are shown in figure B.2.

Appendix C

Ion flux rates

The figures C.1, C.2 and C.3 show the ion fluxes of Ar^+, O^+, and O_2^+ respectively. The sum of these fluxes corresponds to the total ion flux shown in figure 6.11.

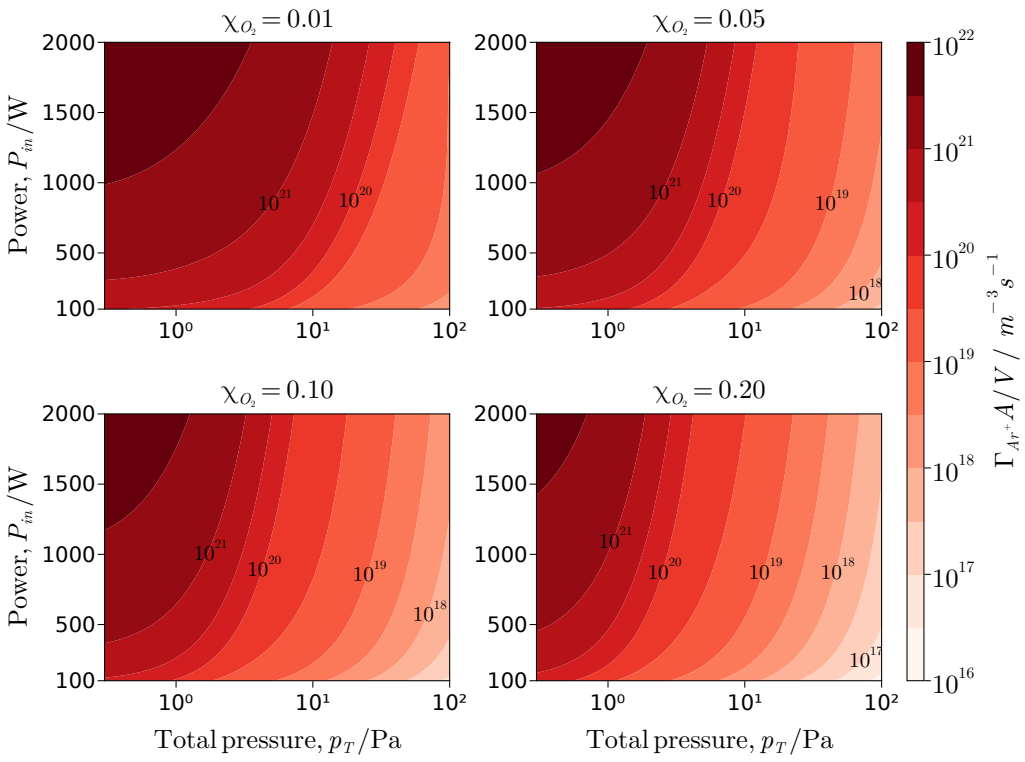

Figure C.1: Ar^+ flux rate.

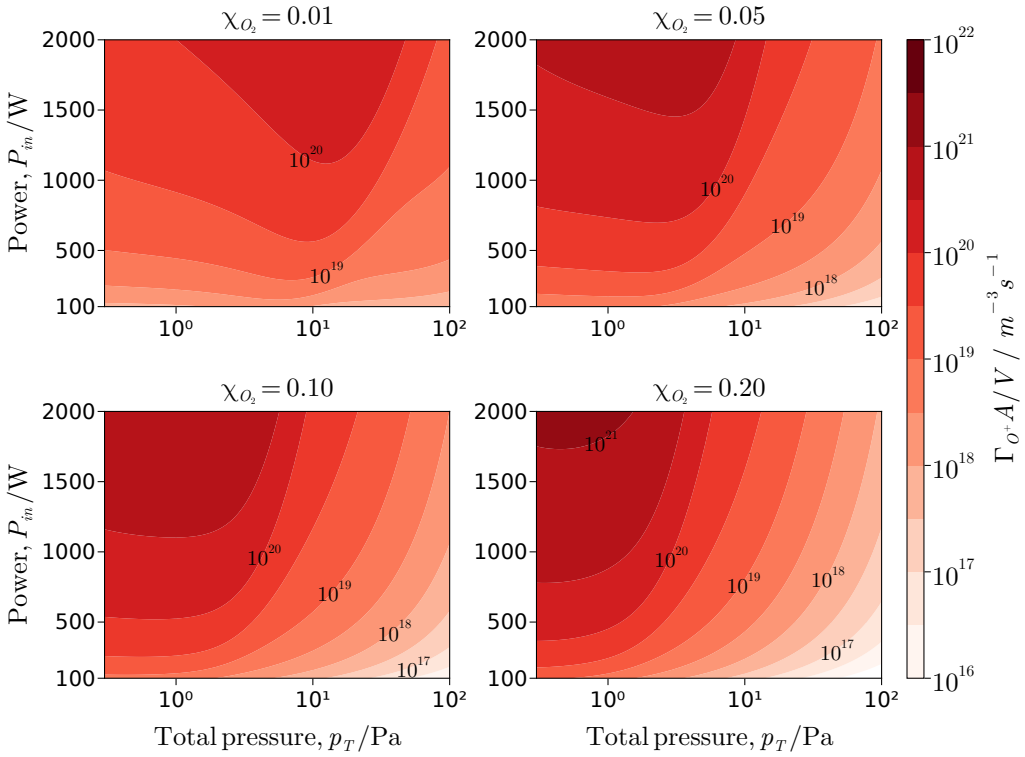

Figure C.2: O^+ flux rate.

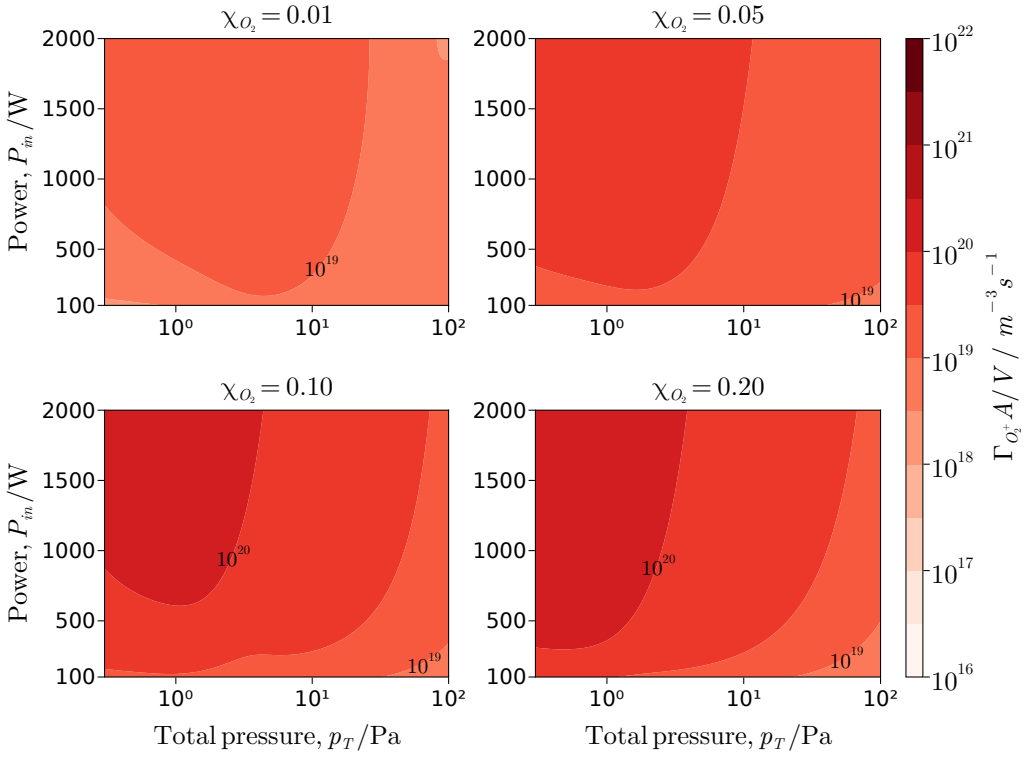

Figure C.3: O_2^+ flux rate.